

Rochester Institute of Technology

RIT Digital Institutional Repository

Theses

2005

Single-phase liquid flow and heat transfer in plain and enhanced silicon microchannels

Mark Steinke

Follow this and additional works at: <https://repository.rit.edu/theses>

Recommended Citation

Steinke, Mark, "Single-phase liquid flow and heat transfer in plain and enhanced silicon microchannels" (2005). Thesis. Rochester Institute of Technology. Accessed from

This Dissertation is brought to you for free and open access by the RIT Libraries. For more information, please contact repository@rit.edu.

**SINGLE-PHASE LIQUID FLOW AND HEAT TRANSFER
IN PLAIN AND ENHANCED SILICON MICROCHANNELS**

by

MARK E. STEINKE

A DISSERTATION

Submitted in partial fulfillment of the requirements for the degree of

Doctor of Philosophy

in

MICROSYSTEMS ENGINEERING

at the

Rochester Institute of Technology

May 2005

Author: _____
Microsystems Engineering Program

Certified by: _____
Satish G. Kandlikar
Advisor, Professor of Mechanical Engineering

Approved by: _____
Mustafa A.G. Abushagur
Director of Microsystems Engineering Program

Certified by: _____
Harvey J. Palmer
Dean Kate Gleason College of Engineering

NOTICE OF COPYRIGHT

© 2005

Mark E. Steinke

REPRODUCTION PERMISSION STATEMENT

Permission Granted

TITLE:

“Single-Phase Liquid Flow and Heat Transfer in Plain and Enhanced Silicon Microchannels”

I, *Mark E. Steinke*, hereby grant permission to the Wallace Library of the Rochester Institute of Technology to reproduce my dissertation in whole or in part. Any reproduction will not be for commercial use or profit.

Signature of Author: _____ Date: _____

Single-Phase Liquid Flow and Heat Transfer in Plain and Enhanced Silicon Microchannels

By

Mark E. Steinke

Approved by:

Dr. Satish G. Kandlikar
(Committee Chair and Dissertation Advisor)

Dr. Stephen Boedo

Dr. Jeffrey D. Kozak

Dr. James E. Moon

Dr. Alan D. Raisanen

Dr. William J. Grande

MICROSYSTEMS ENGINEERING PROGRAM
ROCHESTER INSTITUTE OF TECHNOLOGY
May 2005

ACKNOWLEDGMENTS

There are many people that have contributed to my successful completion of my degree. Some have played small roles and some have played large roles. All are important in achieving my degree and I want to recognize a few of them now.

Professionally speaking, my advisor Dr. Kandlikar has played the largest role. You have given me this wonderful opportunity and I am so deeply grateful that you took the time to take an interest in me. You have a profound affect upon my career and I hope that I can be as inspired by my profession as you are by yours. Continue to inspire and guide others and thank you for opening the door for me.

Dr. Hensel has also given a great deal of support to me and I appreciate the guidance and opportunity to participate in instruction. I realize now that our knowledge as a society only increases if what is learned is taught to others. Dave and Steve have helped me realize my crazy ideas in very tangible ways, thank you. I would also like to thank Dr. Abushagur for providing support during my studies. John and Evan have provided such generous support in the fabrication of devices that this would not have been have been possible. Finally, my lab and office mates have been wonderful in lending a hand, watching an experiment, or acting as a sounding board.

Personally, no one has such a profound impact on my life than my wife, Kate. All of this would not be possible or worth anything with out your support. You have given me so much encouragement, strength and happiness during the course of this pursuit. The door was opened and you have been there to walk though with me. Mere words can not express my gratitude, my appreciation, and my awe of you. I look forward to continuing our journey together.

My parents, Chuck and Mary, have provided me with a wonderful example to live my life. I remember and appreciate the sacrifices you have made to put me where I am today. I hope that this achievement will in some small way remove those things from your mind and give you satisfaction. My other parents, Jon and Rachel, have given me wonderful support during this time and I appreciate all you have done for me. I would also like to thank my siblings Laurel, Eric, Torrie and Will. You have endured long absences and inconveniences and your support is appreciated. Finally, thank you Will for such a generous gift of your time during the final days.

TABLE OF CONTENTS

List of Figures	ix
List of Tables	xiii
List of Symbols	xiv
1.0 INTRODUCTION	1
1.1 Applications of Microscale Heat Transfer and Microfluidics	5
1.2 Hypothesis.....	9
1.3 Approach.....	10
1.4 Objectives	10
2.0 LITERATURE REVIEW	12
2.1 Non-Dimensional Parameters for Fluid Flow and Heat Transfer.....	13
2.2 Literature Database for Single-Phase Liquid Flow in Microchannels.....	15
2.3 Single-Phase Liquid Flow in Microchannels.....	19
2.4 Single-Phase Liquid Heat Transfer in Microchannels	30
2.5 Conventional Single-Phase Liquid Heat Transfer Enhancements	38
2.6 Summary of Literature Reviews.....	41
3.0 THEORETICAL CONSIDERATION FOR MICROCHANNELS	44
3.1 Single-Phase Liquid Flow in Microchannels.....	44
3.2 Single-Phase Liquid Heat Transfer in Microchannels	54
4.0 UNCERTIANTY ANALYSIS	64
4.1 Methodology.....	66
4.2 Geometric Parameters.....	67
4.3 Fluid Flow Parameters	68
4.4 Heat Transfer Parameters.....	70
4.5 Summary	73
5.0 EXPERIMENTAL TEST FACILITY DEVELOPMENT.....	76
5.1 Fluid Flow Circuit.....	76
5.2 Test Section.....	81
5.3 Data Acquisition	81
5.4 Experimental Component Design.....	88

6.0	TEST SECTION DESIGN	92
6.1	Microchannel Test Device	93
6.2	Electrical Connections	99
6.3	Test Device Assembly	100
6.4	Test Fixture	109
7.0	SYSTEM CALIBRATION AND EXPERIMENTAL TECHNIQUES	115
7.1	System Calibration.....	115
7.2	Experimental Procedure.....	118
7.3	Working Fluid Preparation	121
8.0	EXPERIMENTAL RESULTS FOR PLAIN SILICON MICROCHANNELS.....	122
8.1	Single-Phase Water Flow in Microchannels.....	122
8.2	Microchannel Geometry Measurements	126
8.3	Microchannel Surface Roughness Measurements	130
8.4	Normalized Heat Transfer Performance	131
9.0	SINGLE-PHASE LIQUID HEAT TRANSFER ENHANCEMENT TECHNIQUES IN MICROCHANNELS.....	133
9.1	Passive Enhancement Techniques	133
9.2	Active Enhancements Techniques	144
9.3	Design of a Passive Enhancement Device	148
10.0	EXPERIMENTAL RESULTS FOR ENHANCED SILICON MICROCHANNELS	157
10.1	Microchannel Heat Exchanger Thermal Resistance.....	157
10.2	Apparent Pressure Drop.....	162
10.3	f and j Factors.....	164
10.4	Coefficient of Performance Using Pumping Flux	168
11.0	CONCLUSIONS	175
11.1	Reconciliation of Discrepancies in Literature.....	175
11.2	Development of an Experimental Facility	176
11.3	Uncertainty Analysis.....	176
11.4	Single-Phase Liquid Flow.....	177
11.5	Single-Phase Heat Transfer Enhancement.....	178

12.0	REFERENCES	179
13.0	APPENDIX.....	190
13.1	Test Fixture Details.....	190
13.2	Test Section Details	201
13.3	DAQ Details.....	213
13.4	Uncertainty Analysis.....	221

LIST OF FIGURES

- Figure 1.1: Typical Air-Cooled Microprocessor Heat Sink.
- Figure 1.2: Data From ITRS for 2004.
- Figure 1.3: Integrated Microchannel Heat Exchanger and Microprocessor.
- Figure 2.1: Distribution of Data Sets and Data Points for the Range of Hydraulic Diameters Reported in Literature.
- Figure 2.2: Reynolds Number vs. Hydraulic Diameters for the 220 Data Sets.
- Figure 2.3: Schematic of the Microchannel Geometry.
- Figure 2.4: Friction Factor vs. Reynolds Number for all of the Available Data Sets.
- Figure 2.5: Non-dimensional Poiseuille Number vs. Reynolds Number for all of the Available Data Sets.
- Figure 2.6: Friction Factor vs. Reynolds Number for the Reduced Data Sets.
- Figure 2.7: Friction Factor vs. Reynolds Number in the Transitional Regime for the Reduced Data Sets.
- Figure 2.8: Non-dimensional Poiseuille Number vs. Reynolds Number for the Reduced Data Sets.
- Figure 2.9: Non-dimensional Poiseuille Number vs. Reynolds Number for Low Laminar Reynolds Numbers, Papautsky et al. (1999).
- Figure 2.10: Non-dimensional Poiseuille Number vs. Reynolds Number for Laminar Reynolds Numbers, Judy et al. (2002).
- Figure 2.11: Non-dimensional Poiseuille Number vs. Reynolds Number for Transitional Reynolds Numbers, Bucci et al. (2003).
- Figure 2.12: Nusselt Number versus Reynolds Number for All Reported Data Sets.
- Figure 2.13: Colburn j Factor versus Reynolds Number for All Reported Data Sets.
- Figure 2.14: Nusselt Number versus Reynolds Number for Reduced Data Sets.
- Figure 2.15: Colburn j Factor versus Reynolds Number for Reduced Data Sets.
- Figure 2.16: A^* versus Reynolds Number for All Reported Data Sets, Laminar Regime.
- Figure 2.17: A^* versus Reynolds Number for Reduced Data Sets, Laminar Regime.
- Figure 2.18: A^* versus Reynolds Number for Lee and Garimella. (2002).
- Figure 2.19: A^* versus Reynolds Number for Bucci et al. (2003).

Figure 2.20: A^* versus Reynolds Number for Bucci et al. (2003) Including Reported Uncertainties.

Figure 3.1: Components of Pressure When Measuring Δp in Microchannel Manifolds.

Figure 3.2: Apparent Friction Factor Dependence Upon Channel Aspect Ratio, taken from Curr et al. (1972).

Figure 3.3: Fully Developed Hagenbach Factor Dependence Upon Channel Aspect Ratio, Kakaç et al. (1987).

Figure 3.4: Micro-thermocouples Embedded in the Inlet and Outlet Plenums to Microchannel.

Figure 3.5: Fully Developed Nusselt Number versus Channel Aspect Ratio for Four Side Heating.

Figure 3.6: Nusselt number versus Channel Aspect Ratio. For T boundary condition.

Figure 3.7: Nusselt number versus Channel Aspect Ratio. For H1 boundary condition.

Figure 4.1: Dependency of Uncertainty for Calculated Parameter Based Upon Measured Parameters.

Figure 4.2: Experimental Uncertainties Using a Mean Value Calculation. A^* versus Reynolds Number for Bucci et al. (2003) Including Reported Uncertainties.

Figure 5.1: Experimental Flow Circuit.

Figure 5.2: Experimental Test Facility.

Figure 5.3: Virtual Instrument Created for Experimental Test Facility.

Figure 5.4: Section of the VI for Test Facility Monitoring of Temperatures and Pressures.

Figure 5.5: Section of the VI for Test Section Power Supply Control.

Figure 5.6: Section of the VI for Micropump Control.

Figure 5.7: Section of the VI for Data Logging.

Figure 6.1: Schematic of Microchannel Geometry.

Figure 6.2: Model of the Microchannels in Silicon Substrate.

Figure 6.3: Backside of Test Device.

Figure 6.4: Microchannels in Silicon Substrate.

Figure 6.5: SEM Micrograph of a Top View of the Silicon Microchannels.

Figure 6.6: SEM Micrograph of a Side View of the Silicon Microchannels.

Figure 6.7: Model of the Pogo Probe, the Receptacle, and the Assembled unit.

Figure 6.8: Transferred Adhesive Thickness Versus Volume for Different Speeds.

Figure 6.9: Model of and Actual Test Device in Adhesive Bonding Fixture.

Figure 6.10: Model of and Actual Adhesive Bonding Fixture.

Figure 6.11: Model of the Test Fixture Assembly.

Figure 6.12: Installed Test Fixture Assembly.

Figure 6.13: Model and Actual Pictures of the Pogo Probe Block.

Figure 6.14: Model and Actual Pictures of the Main Block.

Figure 6.15: Model of the Device Retaining Plate.

Figure 6.16: Thermocouple Device Supporting Plate.

Figure 7.1: Thermocouple Calibration Curve for the T03 Thermocouple.

Figure 7.2: Temperature Sensing Resistor Calibration Curve for the S1 Sensor.

Figure 7.3: Temperature Sensor Calibration Curve for the P01 Pressure Transducer.

Figure 7.4: Example of Burst Mode DAQ.

Figure 8.1: Friction Factor vs. Reynolds Number Considering Entrance and Exit Losses.

Figure 8.2: Apparent C^* Ratio vs. Reynolds Number Considering Developing Flow.

Figure 8.3: Actual Cross Section of Tested Microchannel.

Figure 8.4: Apparent C^* Ratio vs. Reynolds Number Considering Measured Cross Section.

Figure 8.5: Fin Cross Section of Silicon Microchannel.

Figure 8.6: Surface Roughness in the Microchannels.

Figure 8.7: A^* vs. Reynolds Number.

Figure 8.8: A^* vs. Reynolds Number.

Figure 8.9: A^* vs. Reynolds Number.

Figure 9.1: Sidewall flow obstructions in a microchannel.

Fig. 9.2: Flow obstructions in the channel.

Figure 9.3: Entrance spaces in a microchannel flow network.

Figure 9.4: Re-entrant structures included in a microchannel.

Figure 9.5: Secondary flow channels.

Figure 9.6: Venturi based secondary flow.

Figure 9.7: Three-Dimensional Twisted Microchannel, Bondar and Battaglia (2003).

Figure 9.8: Effect of concentration on single-phase heat transfer coefficient, Hu and Zhang (2002).

Figure 9.9: Microchannel with hydrophilic and hydrophobic surface treatments.

Figure 9.10: Effect of microfin array on heat sink temperature difference, Go, (2003).

Figure 9.11: Piezoelectric enhanced microchannels.

Figure 9.12: Electrostatic forces with insert probe for conventional channel, minichannel, and microchannel.

Figure 9.13: Electrostatic forces with wall integrated probes for a microchannel.

Figure 9.14: Variable roughness structure using actuators.

Figure 9.15: Concept of Using Offset Strip Fin Geometry for Microchannel Enhancement.

Figure 9.16: Enhanced Microchannel Nomenclature.

Figure 9.17: SEM Micrograph of Enhanced Microchannels.

Figure 9.18: SEM Micrograph of a Fin.

Figure 9.19: SEM Micrograph of the Fin Structure.

Figure 9.20: SEM Micrograph of the Surface Roughness Occurring in the Enhanced Microchannels.

Figure 10.1: Thermal Resistance vs. Reynolds Number.

Figure 10.2: Thermal Resistance vs. Reynolds Number.

Figure 10.3: Thermal Resistance vs. Reynolds Number.

Figure 10.4: Heat Flux vs. Reynolds Number.

Figure 10.5: Apparent Pressure Drop vs. Reynolds Number.

Figure 10.6: Apparent Pressure Drop vs. Reynolds Number.

Figure 10.5: Apparent Pressure Drop vs. Reynolds Number.

Figure 10.6: Friction and Colburn j Factors vs. Reynolds Number.

Figure 10.7: Friction and Colburn j Factors vs. Reynolds Number.

Figure 10.8: Friction and Colburn j Factors vs. Reynolds Number.

Figure 10.9: Coefficient of Performance vs. Reynolds Number.

Figure 10.10: Coefficient of Performance vs. Reynolds Number.

Figure 10.11: Coefficient of Performance vs. Reynolds Number.

Figure 10.12: Coefficient of Performance vs. Reynolds Number.

LIST OF TABLES

Table 2.1: Selected Literature for Single-Phase Liquid Flow in Microchannel Passages.

Table 2.2: Selected Literature for Single-Phase Liquid Flow in Microchannel Passages.

Table 2.3. Summary of Enhancement Techniques for Microchannels and Minichannels.

Table 4.1. Measured Parameters.

Table 6.1: Channel Geometries of the Test Device.

Table 6.2: Summary of Bonding Technologies for Use in Microsystems.

Table 6.3: Summary of Adhesive Application Methods for Use in Microsystems.

Table 9.1: Enhanced Microchannel Nominal Geometries.

LIST OF SYMBOLS

a	channel width	m
A	area	m^2
A^*	non-dimensional Nusselt number	$= Nu_{\text{exp}} / Nu_{\text{theory}}$
b	channel height	m
B	systematic error	
B^*	non-dimensional Colburn j factor	$= j_{\text{exp}} / j_{\text{theory}}$
Br	Brinkman number	$= \mu V^2 / k \Delta T$
c	volumetric concentration of microcapsules,	$L L^{-1}$
C^*	non-dimensional Poiseuille number	$= fRe_{\text{exp}} / fRe_{\text{theory}}$
Ca	Capillary number	$= \mu V / \sigma$
C_p	specific heat	$J \text{ kg}^{-1} \text{ K}^{-1}$
D	diameter	m
D_h	hydraulic diameter	m
e	roughness height	m
f	Fanning friction factor	$= \rho \Delta p D_h / 2 L G^2$
G	mass flux	$\text{kg m}^{-2} \text{ s}^{-1}$
h	convective heat transfer coefficient	$\text{W m}^{-2} \text{ K}^{-1}$
\bar{h}	average heat transfer coefficient	$\text{W m}^{-2} \text{ K}^{-1}$
I	current	A
j	Colburn j factor	$= St Pr^{2/3}$
k	thermal conductivity	$\text{W m}^{-1} \text{ K}^{-1}$
K	loss coefficient	
L	channel length	m
L_h	hydrodynamic entrance length	m
L^+	non-dimensional entrance length	

m	exponent = -0.58 for present work	
n	number of channels	
N	number of measurements in sample	
Nu	Nusselt number	$= h D_h / k$
p	pressure	kPa
P	power	W
P_w	wetted perimeter	m
Po	Poiseuille number	$= f * Re$
Pr	Prandtl number	$= \mu C_p / k$
q	heat transfer rate	W
q''	heat flux	$W m^{-2}$
Q	volumetric flow rate	$mL min^{-1}$
R	thermal resistance	$^{\circ}C W^{-1}$
r_h	hydraulic radius	m
r_0	duct radius	m
Re	Reynolds number	$= G D_h / \mu$
s	fin thickness	m
St	Stanton number	$= Nu / Re Pr$
T	temperature,	$^{\circ}C$
u	uncertainty of parameter i	
U	uncertainty	
V	velocity,	$m s^{-1}$
\bar{V}	mean velocity	$m s^{-1}$
x	axial location	m

x^+	non-dimensional flow distance
x^*	non-dimensional thermal flow distance

Greek

α_c	microchannel aspect ratio	$= a / b$
α_c	fin aspect ratio	$= s / b$
Δ	difference	
ε	roughness height	m
K	Hagenbach factor	
η	degree of heat transfer enhancement	$\eta = h / h_{single}$
μ	viscosity	N s m^{-2}
ρ	density	kg m^{-3}
σ	surface tension	N m^{-1}
	standard deviation	
θ	unit thermal resistance	$^{\circ}\text{C cm}^2 \text{W}^{-1}$
τ_w	wall shear stress	Pa

Subscripts

app	apparent
avg	average
b	bulk or mean
c	cross section
cp	constant property
FD	fully developed

h	heater
ht	heat transfer
i	inlet
LMTD	log mean temperature difference
m	mean
o	outlet
s	surface
tot	total
w	wall

CHAPTER 1

INTRODUCTION

The use of small passages to increase the overall heat transfer in a heat exchanger is not a new practice. As the passage size is decreased, the heat transfer performance increases. Unfortunately, the pressure drop increases sharply when the passage size is reduced. Therefore, a condition is reached where the design engineer must balance the heat transfer augmentation with the increased pressure penalty.

That balance was found earlier by the automotive community when they utilized passages only a few millimeters in diameter to develop compact heat exchangers for use in engine cooling. The small overall size and light weight created the necessary conditions for them to be beneficial in automotive as well as aerospace applications.

The next logical step would be to further decrease the size of the passage to increase the heat transfer. This is indeed what has occurred. Unfortunately, the fabrication technology for microchannels with diameters less than 1 mm has far outpaced the fundamental understanding of heat transfer and fluid flow for those scales. All of a sudden, microchannels became the hot research topic. Researchers quickly realized that if the fluid undergoes a phase change, in other words boiling, in the microchannels the heat transfer performance can be increased yet again. As a result, the majority of researchers did not concern themselves with fundamental understanding of the physics occurring in microchannels and moved into the heat transfer regime that gave them the quickest benefit.

However, an opportunity to explore and develop single-phase liquid flows in microchannels is being missed. There are some papers regarding the single-phase liquid flow

and heat transfer in microchannels that came out in the early stages of this field. Currently, all of the high profile laboratories are conducting the two-phase research for microprocessor cooling. It does not make sense to proceed without first resolving the issues that have been presented in literature for microchannel flows and heat transfer. This is where the study of single-phase flow and heat transfer in microchannels would be very beneficial. The single-phase liquid flow would be simpler to study than the two-phase flow. As a result, the fundamental physics could be investigated and determined to build a base to approach the two-phase flow. While there are tremendous advances in the understanding of two-phase flows and heat transfer in microchannels, the question remains unanswered of why there is still a belief that the fundamental physics is different in microchannels. A single-phase liquid investigation could possibly shed some light and give a definite conclusion.

Once again, there is a great discussion in the microscale heat transfer and microfluidics community as to whether the conventional theories apply in the microscale. Because of the proliferation of microchannel fabrication and the appeal of finding novel physics, a larger number of researchers have entered this field. A great deal of experimental data has been generated. Unfortunately, there are data sets that show over-prediction of both heat transfer and pressure drop parameters by conventional theories, data sets that show under-prediction by conventional theories, completely different trends from conventional theories, and a few data sets that show agreement with conventional theories. This leads to confusion and a questioning of the physics occurring in microchannels.

The most common thought is that the physics of heat transfer and fluid flow in microchannels is completely different from conventional theory. The main question should be “Why should it be different?”. What is different about microchannels that cannot be captured by

conventional theory? The author will concede that microchannel gas flows can be different if the microchannel dimensions are small relative to the free mean path of the fluid or that the base assumptions of the conventional theories (Newtonian fluid, no-slip boundary condition, etc...) are violated. However, a liquid flow should not suffer from those same problems. There should be no deviations from theory if all of the base assumptions are not violated.

However, one must consider forces that are weak in macroscale systems and much stronger in the microscale. An electric field can be used to drive flow through a microchannel. This adds a new motive force to conventional theories. In addition, a Poiseuille flow of a polar fluid occurring in a microchannel with a polar surface can generate an electrokinetic force due to the motion of the polar molecules over a polar surface. This force can become quite large in the microscale and is usually neglected in the macroscale.

Therefore, the discussion of heat transfer and fluid flow in microchannels in the present work will pertain to a liquid flow that is not in violation of the base assumptions of a Newtonian fluid, conservation of mass, momentum and energy equations are applicable, and the fluid behaves as a continuum, and no electrokinetic flow behavior.

Researchers have reported deviations from conventional theories. They specifically point to deviations in magnitude and trend for such non-dimensional parameters as Nusselt number and friction factor. The entire purpose of the non-dimensional number is to properly capture the physics involved and make it independent of dimension or, in other words, geometry. Therefore, the researchers conclude that the physics must be different. Perhaps the better argument should be what physics is not captured by the parameters we are using.

For example, consider the forces acting upon the fluid elements. One force that becomes more important in the microscale is surface tension. This force can become dominating in the

microscale when the fluid interacts with a surface, for example a capillary tube. How about gravity? This tends to have a smaller effect due to very small heights in a microsystem. However, it can play an important role depending upon the application and should be included for completeness. Despite these issues, there are non-dimensional parameters that pertain to each of those forces and can be included as parameters. An all-liquid flow will not exhibit the surface to liquid interface. So again, what is different?

There should be nothing that is different for liquid microchannel flows. Once all of the important physics is identified and the assumptions are validated, the non-dimensional parameters describing the heat transfer and fluid flow should scale with the non-dimensional parameters. It is also important to identify the microchannel roughness because it can become quite large for microchannels and could lead to complications in predicting flow behavior.

However, there is one main problem remaining: how do we reconcile the vast available data for liquid heat transfer and fluid flow in microchannels. This is no easy task given the wide variety of microchannel geometries, flow rates, and heat transfer parameters utilized. All of that work cannot be invalid. Therefore, there must be an explanation for all of the data sets reporting discrepancies from conventional theories. What did those previous researchers miss that causes the discrepancies to exist and send the community as a whole into mass confusion?

The present work is undertaken to determine with certainty if the conventional theories for liquid flow in passages applies to microchannels. In doing that, the previous literature will be carefully evaluated and possible root causes for deviation will be identified. Also, new experimental data will be generated to supply evidence of agreement with conventional theory and provide a procedure for proper data reduction. Finally, some ways to further the heat transfer performance of microchannels will be identified.

1.1 Applications of Microscale Heat Transfer and Microfluidics

The knowledge gained from a fundamental understanding of microchannel liquid flow and microscale heat transfer has several promising applications. Many possible applications meet pressing needs of several research and industrial communities. For example, the development of very small, portable, and self contained biological agent detection systems for military personnel would find immediate implementation. A small DNA unit that uses very small sample volumes with very high throughput would allow for more efficient study of DNA and also aid in the detection of individual genes and other DNA analysis. Also, the cooling of very high heat fluxes can be achieved using microchannels and this could aid in the development of faster microprocessors and integrated silicon laser microsystems.

Water is the main medium for the vast majority of biological processes. Many microsystems are developed to perform biological analyses. Proper handling of fluid samples is critical to their success. The development of micro fuel cells to provide on-board power generation for microsystems is dependent upon finding the proper balance in water management. This function is dependent upon the microchannels' ability to control the flow of water from the fuel stack. The cooling of high heat flux microprocessors has become a critical limitation in the development of future microprocessors. Microchannels can be utilized here to provide efficient heat transfer and maintain microprocessors at their working temperature. The present work will focus on just that, the direct cooling of microprocessors using liquid flow in microchannels.

The fundamental understanding of fluid flows and heat transfer mechanisms in microchannels is critical to the development of devices that utilize these channels for cooling passages. The combination of microfluidics and microscale heat transfer presents new sets of engineering challenges and opportunities.

The scheme that dominates microprocessor cooling is air-cooling with an extended surface heat sink. Figure 1.1 shows a typical microprocessor air-cooling scheme. The silicon device is oriented device side down and the backside of the chip is used to dissipate the heat generated in the device. The microprocessor is attached to the cooling solution with something called a thermal interface material (TIM). This is a material that provides contact to the heat spreader plate. This plate increases the heat transfer area from the very small die size of the microprocessor to a more manageable area for the heat sink. There are a total of four thermal resistances between the device temperature and the ambient temperature. Heat must move through this path in order to be dissipated from the device. The physical distance is long and the thermal resistances can be quite large.

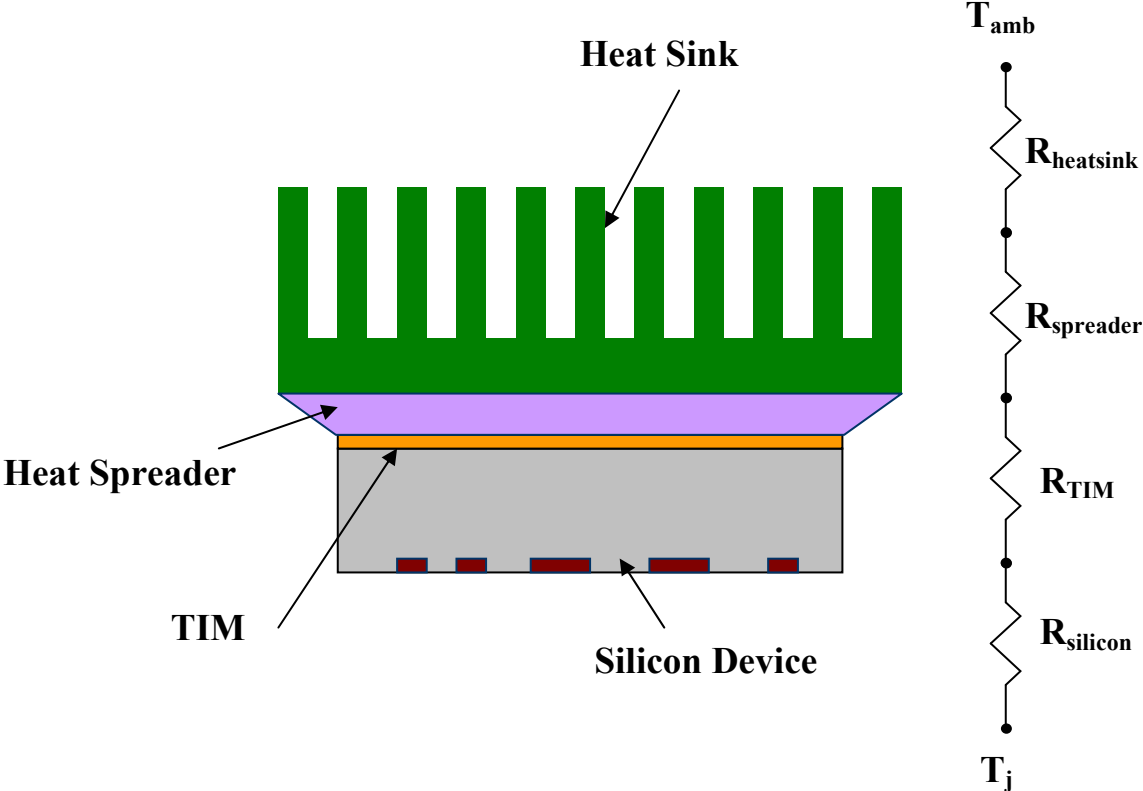


Figure 1.1: Typical Air-Cooled Microprocessor Heat Sink.

To further compound the difficulties in cooling of microprocessors, the number of transistors that fit on a single die is ever increasing, and doubles every 18 months. This is commonly referred to as Moore's law. The International Technology Roadmap for Semiconductors (ITRS) is output of a consortium of companies that predict the future path of semiconductor products. Each year, they publish a report that attempts to predict future requirements for microprocessors. Figure 1.2 shows the prediction from the 2004 report. It demonstrates the increasing trend in heat flux, shown as solid points for low and high performance microprocessors, which must be dissipated from the microprocessor. In 2009, it is predicted that the production microprocessors will approach 100 W/cm². This heat flux is above what can be effectively dissipated using air-cooling. At present, there is no cooling scheme that will reliably dissipate this level of heat flux. An alternative to the dominant cooling scheme is needed.

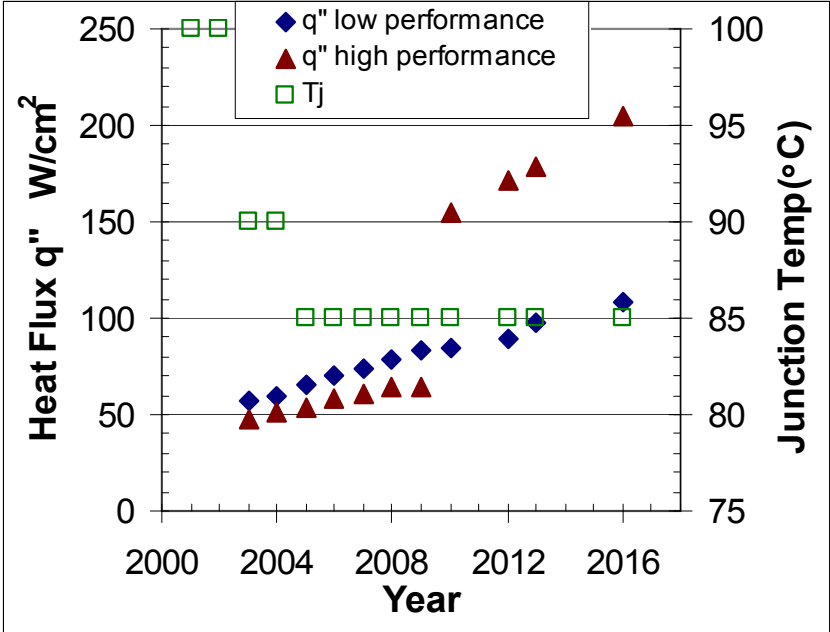


Figure 1.2: Data From ITRS for 2004.

Enter the microchannel heat exchanger. If a heat exchanger that utilizes microchannel and higher heat capacity fluid could be integrated into the microprocessor cooling scheme, the heat fluxes that could be dissipated are at least an order of magnitude larger than the air-cooled heat sink. Integrating the microchannel heat exchanger (MCHX) into the microprocessor would greatly reduce the overall thermal resistance.

Figure 1.3 shows the integrated microchannel heat exchanger. The microchannels are fabricated on the backside of the microprocessor. As a result, the overall thermal resistance is greatly reduced. There are several perturbations to this basic concept. Arguing that the added heat capacity dominates the added thermal resistance, the MCHX can be bonded to the microprocessor and still have superior performance over air-cooled heat sinks.

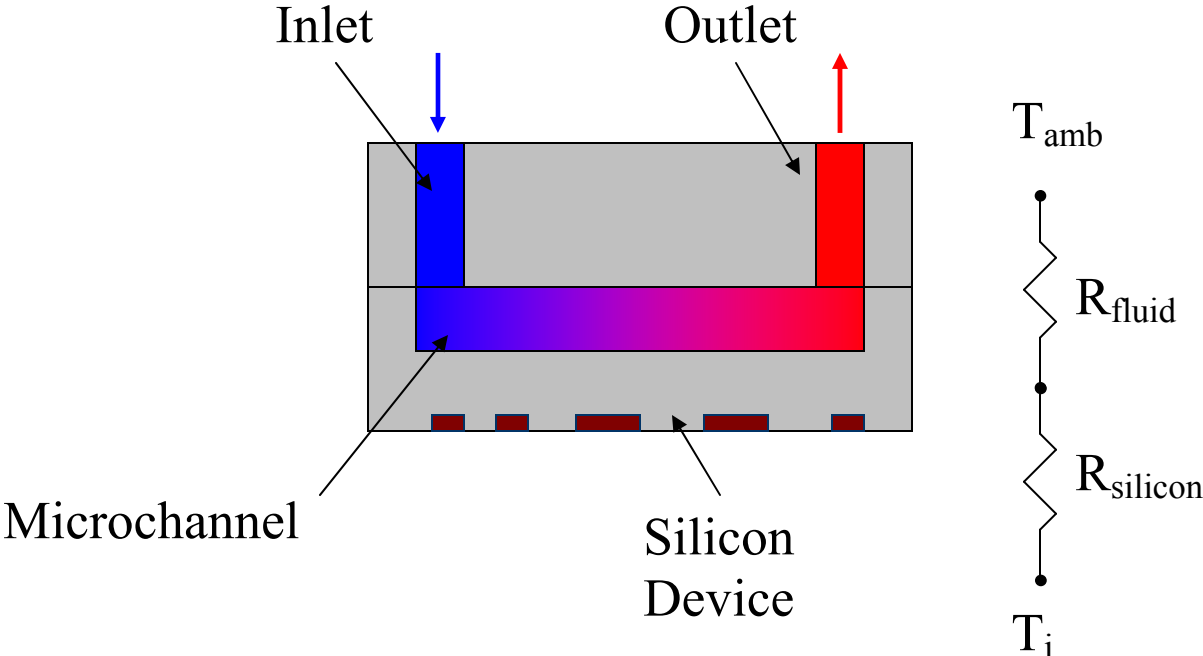


Figure 1.3: Integrated Microchannel Heat Exchanger and Microprocessor.

If evaporation occurs in the cooling fluid (ie, two-phase flow), the heat transfer is enhanced further than the single-phase flow. The heat transfer improvement gained by a two-

phase system (given the same heat flux and mass flux) over a single-phase system is well documented in conventional sized channels, and current research is ongoing in the microchannel region. In fact, the majority of new research is in the field of microchannel flow boiling. However, the total pressure drop, pumping requirements and system complexity are greatly increased in a two-phase flow system.

Therefore, a paradigm shift from traditional air-cooling schemes to liquid cooling schemes is required to meet the increasing demands of heat flux for future microprocessors. The shift to two-phase flow immediately may not be needed until the liquid cooling limit is reached. The two-phase system could be reserved for very, very high heat fluxes when those are achieved. However, there is the possibility to satisfy the heat flux requirements utilizing a single-phase flow and provide some method of heat transfer augmentation.

The present work will conduct a study of liquid flow and heat transfer in microchannels. The design aspects of the test section used for experimental studies will keep the application of high heat flux microprocessor cooling in mind. The goals of practical implementation, reasonable pressure drop, and high heat flux cooling are very much on the mind of a thermal designer when concerned with that application.

1.2 Hypothesis

There is no significant difference in physics for single-phase liquid heat transfer and fluid flow in microchannels from conventionally scaled systems when all of the base assumptions are not violated. Those assumptions are a Newtonian fluid, conservation of mass, momentum and energy equations are applicable, the fluid behaves as a continuum, and no electrokinetic flow

behavior. Once all of the important forces are identified, the same non-dimensional parameters for macroscale systems are valid for use in microchannels.

1.3 Approach

The hypothesis will be tested using several different metrics. First, a critical review of the available literature on single-phase liquid flow in microchannels will be conducted. The results of each work will be analyzed to determine what possible oversights were made that lead to discrepancies from conventional theories. Then, a new experimental facility will be developed to allow for accurate experimental studies of microchannel fluid flow and heat transfer. Finally, new experimental data will be generated in support of the claims indicated previously.

1.4 Objectives

There are several major objectives of the present work. Each one will further substantiate the claims of the hypothesis. The major objectives are as follows:

- Determine the applicability of single-phase liquid flows in microchannel for high heat flux cooling and identify the design issues facing a thermal designer in direct microprocessor cooling.
- Generate a database of available literature on single-phase liquid flow in microchannels. Then, critically evaluate the available literature and identify possible reasons for the reported discrepancies. Identify common problems for the literature as a whole.

- Develop an experimental facility that is capable of accurately assessing the thermal and hydraulic performance of a wide variety of microchannel geometries. Generate new experimental data to provide a method to correct for the causes of deviation from conventional theory.
- Perform a detailed uncertainty analysis that determines the effect of actual measured parameters on the calculated parameters used in microscale heat transfer and microfluidics.
- Develop new techniques based upon the previous results that could enhance the heat transfer performance of single-phase liquid flow in microchannels to dissipate high heat fluxes.
- Identify the appropriate parameters and metrics for use in microscale heat transfer and microfluidics with liquid flows and generate new parameters if necessary.

CHAPTER 2

LITERATURE REVIEW

It is widely accepted that the field of microchannel heat transfer for microprocessor cooling was started by Tuckerman and Pease (1981). They applied the very efficient mode of heat transfer resulting from the use of very small passages to the cooling of very large scale integration integrated circuits (VLSI IC). Since that pioneering work, the field of microchannel heat and mass transfer has grown exponentially.

However, many researchers have reported discrepancies from conventional theory for their experimental studies. There are studies that report that the theories under-predict the experimental data while others report that they over-predict the data, while others report good agreement between the conventional theories and the experimental data. All of the deviations have forced the research community to question the validity of theories based upon conventional geometries for microchannel geometries. As stated in Chapter 1, the author believes that there is no physical significance of the microchannel geometry upon the fundamental physics. Therefore, there should be no deviation of the experimental data from conventionally based theories.

However, in order for the research community to move past this hurdle, definitive answers to the validity of conventional theories in microchannel flows must be given. To that end, the previous literature must be reconciled for microchannel liquid flow and heat transfer in terms of what causes those discrepancies and how to correct for them. As a result, a large database is generated containing the experimental data for all of the available literature in order to create a base of knowledge and gain understanding into the important issues in generating reliable experimental data for liquid flow and heat transfer in microchannels.

2.1 Non-Dimensional Parameters for Fluid Flow and Heat Transfer

In order to more efficiently evaluate the previous literature, the commonly reported non-dimensional parameters used in heat transfer and fluid dynamics are presented. There are several non-dimensional parameters that can describe the pressure drop and heat transfer that occurs in passages. First, the hydraulic diameter is used to relate the non-circular shaped passages to circular passages. A direct comparison of microchannel geometries can be performed when using the hydraulic diameter shown in Eq. (2.1).

$$D_h = \frac{4 A_c}{P} \quad (2.1)$$

where A_c is the cross sectional area of the passage and P is the wetted perimeter. The flow regime of the fluid in the channel is described by the Reynolds number seen in Eq. (2.2).

$$\text{Re} = \frac{G D_h}{\mu} \quad (2.2)$$

where G is the mass flux and μ is the viscosity.

The pressure drop in the microchannel can be represented by the non-dimensional friction factor, f . However, there is one complication for determining the friction factor. Darcy and Fanning friction factors are two different methods for determining the friction factor. For the present work, the Fanning definition of friction factor will be utilized. The Fanning friction factor is more convenient when performing diabatic experiments. It can take the same form of the Colburn j factor equation. Therefore, a link between the heat transfer performance and the pressure drop performance through the f factor and the j factor. The Fanning friction factor is defined as the ratio of the wall shear stress to the flow kinetic energy per unit volume and is found using Eq. (2.3).

$$f = \frac{\tau_w}{\frac{1}{2} \rho \bar{V}^2} \quad (2.3)$$

where f is the Fanning friction factor, τ_w is the wall shear stress, ρ is the fluid density, and \bar{V} is the average channel velocity. The friction factor can be rewritten in terms of the mass flux, Eq. (2.4).

$$f = \frac{\rho \Delta p D_h}{2 L G^2} \quad (2.4)$$

where Δp is the pressure drop and L is the microchannel length. The Fanning friction factor for a smooth tube, Eq. (2.4), can be related to the Colburn j factor via Eq. (2.5).

$$j \cong \frac{f}{2} \quad (2.5)$$

This equation provides a link between the forced convection heat transfer and the fluid flow, via Nusselt and Reynolds numbers. This link is typically referred to as the Reynolds analogy, Reynolds (1874).

In regards to heat transfer, the first useful non-dimensional group is the Nusselt number which describes the non-dimensional temperature gradient at the heated surface and is given by Eq. (2.6)

$$Nu = \frac{h D_h}{k_f} \quad (2.6)$$

where Nu is the Nusselt number, D_h is the hydraulic diameter, k_f is the thermal conductivity of the fluid, and h is the heat transfer coefficient. In this equation, the microchannel hydraulic

diameter is used as a length scale. The Prandtl number gives the ratio of the momentum and the thermal diffusivities, Eq (2.7).

$$\text{Pr} = \frac{C_p \mu}{k_f} \quad (2.7)$$

where C_p is the specific heat of the fluid and μ is the viscosity. A modified Nusselt number, called the Stanton number, is also very common, Eq. (2.8).

$$\text{St} = \frac{\text{Nu}}{\text{Re Pr}} \quad (2.8)$$

Finally the Colburn j factor is given in Eq. (2.9).

$$j = \text{St Pr}^{2/3} = \frac{\text{Nu Pr}^{1/3}}{\text{Re}} \quad (2.9)$$

This parameter has a close relationship to the friction factor and allows for the link between hydrodynamic and thermal performance.

2.2 Literature Database for Single-Phase Liquid Flow in Microchannels

The available literature on single-phase liquid flows in microchannel flows is reviewed. There are over 150 papers that directly deal with the heat transfer or pressure drop measurements in microchannels. These papers can be classified into review papers, experimental works and numerical works. The papers containing experimental data are reviewed in depth, for the present study. As a result, approximately forty papers remain that contain the detailed experimental data required to complete this analysis.

The researchers typically include data for more than microchannel geometry. A single occurrence of a diameter is considered to be an individual data set in the present work. As a result, there are approximately 220 data sets and over 5,000 individual data points in the papers that have been reviewed. The total number of data sets and data points can be used to normalize the respective quantities. Figure 2.1 shows the percentage of data sets and the percentage of data points reported for each sub-range of hydraulic diameters.

It is important to know what is included in the database to determine the distribution of the data. The most common range of hydraulic diameters is 100 to 200 μm , with 60 data sets. The most data points also fall within the 100 to 200 μm hydraulic diameter range.

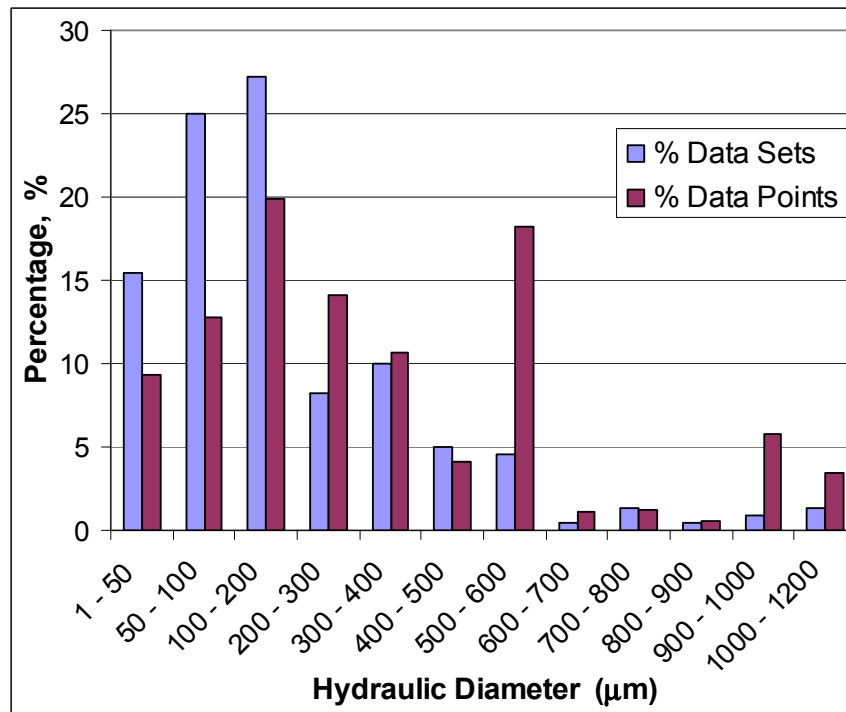


Figure 2.1: Distribution of Data Sets and Data Points for the Range of Hydraulic Diameters Reported in Literature.

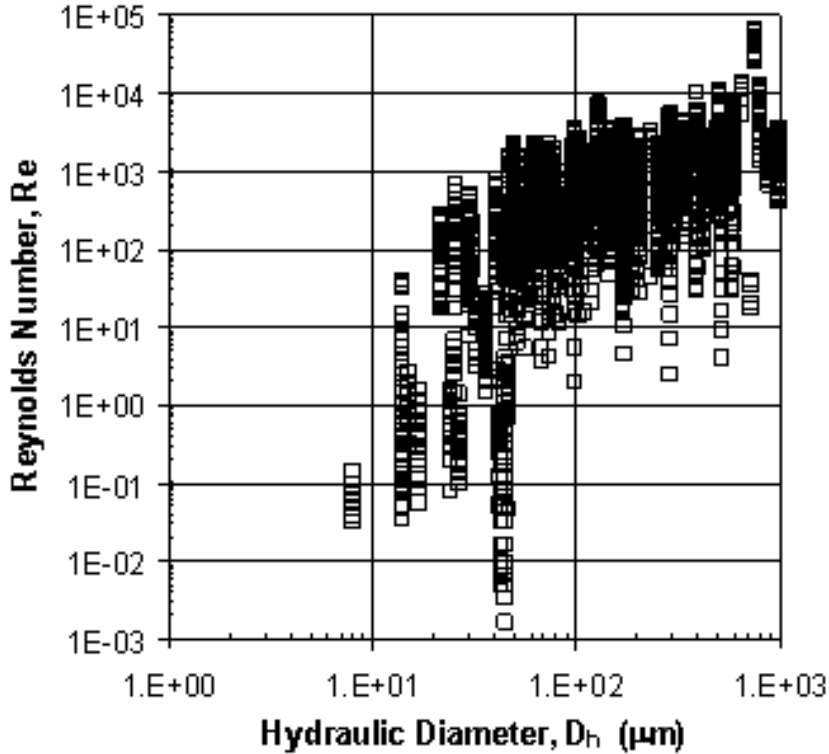


Figure 2.2: Reynolds Number vs. Hydraulic Diameters for the 220 Data Sets.

The Reynolds numbers investigated versus the hydraulic diameters reported are plotted in Fig. 2.2. The general trend seen in the figure is that as the hydraulic diameter decreases, the Reynolds number is also decreased. This makes sense because the pressure drop increases sharply as the hydraulic diameter is reduced and lower flow rates are employed. The laminar flow regime is the main choice for microchannel flows due to lower pressure drops. There are very few data points in the turbulent regime.

It is convenient to identify the nomenclature used in the present work. Figure 2.3 shows a schematic of a microchannel with the associated variables. The microchannel width is a , depth is b , fin thickness is s , and the microchannel length is L .

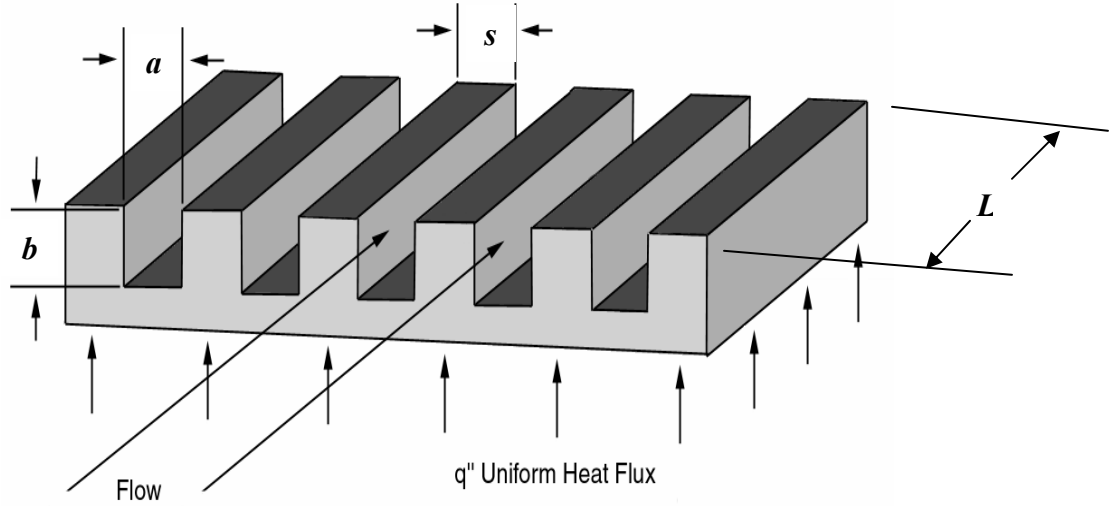


Figure 2.3: Schematic of the Microchannel Geometry.

Another parameter used to describe the microchannel geometry is the aspect ratio. It is a ratio of characteristic channel dimensions. Unfortunately, there have been several different definitions for channel aspect ratio in the literature. A clear definition and consistency is required for comparison of other experimental works. For the present work, the channel aspect ratio, α_c is defined by Eq. (2.10).

$$\alpha_c = \frac{a}{b} \quad (2.10)$$

It is defined as the channel width divided by the microchannel height. The orientation of the geometry and the applied boundary conditions are crucial for heat transfer. It would be desirable to have several deep, narrow (ie $\alpha_c < 1.0$) microchannels than to have a few wide, shallow microchannels from a heat transfer perspective. Another ratio used in the present work is the fin aspect ratio and it is defined as the fin thickness divided by the microchannel fin height, Eq. (2.11).

$$\alpha_f = \frac{s}{b} \quad (2.11)$$

where s is the fin thickness. This ratio is a measure of the geometry of the fin structure. It is desirable to have tall, thin fins as opposed to short, wide fins.

An additional geometric parameter will be introduced in this work. The fin spacing ratio is defined as the fin aspect ratio divided by the channel aspect ratio, seen in Eq. (2.12).

$$\alpha_s = \frac{\alpha_f}{\alpha_c} = \frac{s}{w} \quad (2.12)$$

This ratio is developed because it relates the spacing or the pitch of the fins to the width of the microchannel. This would allow the microchannel to be optimized with respect to the fin thickness and the microchannel width. It is therefore desirable to have all three ratios less than 1.0.

2.3 *Single-Phase Liquid Heat Transfer in Microchannels*

The papers used in the present work are shown in Table 2.1. The ranges of the important microchannel fluid flow parameters are reported. Not all of the parameters were reported by the authors. Many of those parameters are calculated by the present author to determine the values using the data from the paper. The most common working fluid for the papers presented is water. This working fluid is an excellent choice to develop fundamental data. It is also the most common working fluid for chemical processes, such as those used in micro-total analysis systems. The present work includes both adiabatic and diabatic works. The difference is noted in the table, along with the channel geometry.

As stated previously, the present work will focus on the flow of single-phase liquids in microchannel passages. Compressibility effects, slip boundary condition and rarefied flow concerns do not apply for single-phase liquid flows. There is no such term like Knudsen number

in gas flows to quantify the validity of the continuum assumption for fluid flow. It will be assumed that the continuum assumption will be valid for microchannels larger than $1.0\ \mu\text{m}$ in hydraulic diameter. This is also experimentally verified using some investigation in lubricated bearing systems.

The non-dimensional measure for pressure drop is the friction factor, f . One complication for determining the friction factor is the two different definitions for f , Darcy and Fanning. For the present work, the Fanning definition of friction factor will be utilized. The Fanning friction factor is more convenient when performing diabatic experiments. It can take the same form of the Colburn j factor equation. Therefore, a link exists between the heat transfer performance and the pressure drop performance through the f factor and the j factor.

The Fanning friction factor was determined for the cases that presented sufficient data. The Fanning friction factors versus the Reynolds number for all of the data sets are shown in Fig. 2.4. The most common observation noted by researchers is an early departure from the laminar theory that suggests a lower critical Reynolds number.

Table 2.1: Selected Literature for Single-Phase Liquid Flow in Microchannel Passages.

Author	Year	Fluid / Shape*	D_h (μm)	α_c = a/b	Re	$f\text{Re}$	C^*	L/D_h	Adiab/ Diab**	Account Losses	Agree Laminar
Tuckerman & Pease	1981	water / R	92 - 96	0.17 - 0.19	291 - 638	14.0 - 20.8	0.73 - 1.06	104 - 109	D	N	Y
Missaggia et al.	1989	water / R	160	0.25	2350	611.6	33.54	6	D	N	N
Riddle et al.	1991	water / R	86 - 96	0.06 - 0.16	96 - 982	15.8 - 80.6	0.79 - 4.06	156 - 180	D	N	N
Rahman & Gui	1993a	water / R	299 - 491	3.00 - 6.00	275 - 3234	2279.8 - 8720.2	121.89 - 507.10	94 - 154	D	N	N
Rahman & Gui	1993b	water, R11 / R	299 - 491	3.00 - 6.00	275 - 3234	2279.8 - 8720.2	121.89 - 507.10	94 - 154	D	N	N
Gui & Scaringe	1995	water / Tr	338 - 388	0.73 - 0.79	834 - 9955	18.4 - 76.8	1.28 - 5.33	119 - 136	D	N	N
Peng et al.	1995	methanol / R	311 - 646	0.29 - 0.86	1530 - 13455	ID	ID	70 - 145	D	N	N
Peng & Peterson	1995	water / R	311	0.29	214 - 337	ID	ID	145	D	N	N
Cuta et al.	1996	R124 / R	425	0.27	101 - 578	7.0 - 36.6	0.39 - 2.04	48	D	Y	Y
Peng & Peterson	1996	water / R	133 - 200	0.5 - 1.0	136 - 794	192.1 - 394.1	13.50 - 27.70	25 - 338	D	N	N
Jiang et al.	1997	water / C, Tr	8 - 68	0.38 - 0.44	0.032 - 26.1	3.6 - 48.9	0.22 - 3.05	69 - 276	D	N	Y
Tso & Mahulikar	1998	water / C	728	NA	16.6 - 37.5	ID	ID	76 - 89	D	Y	N
Vidmar & Barker	1998	water / C	131	NA	2452 - 7194	28.4 - 89.2	1.77 - 5.58	580	D	Y	Y
Adams et al.	1999	water / Tr	131	ID	3899 - 21429	ID	ID	141	D	Y	Y
Mala & Li	1999	water / C	50 - 254	NA	132 - 2259	22.2 - 321.2	1.38 - 20.07	150 - 490	A	Y	Y
Papautsky et al.	1999	water / R	44 - 47	5.69 - 26.42	0.002 - 4	19.8 - 32.1	0.98 - 1.41	164 - 177	A	Y	Y
Pfund et al.	2000	water / R	253 - 990	19.19 - 78.13	55.3 - 3501	21.9 - 40.7	0.01 - 1.81	101 - 396	A	Y	Y
Qu et al.	2000a	water / Tr	51 - 169	1.54 - 14.44	6.2 - 1447	9.2 - 36.7	0.55 - 1.68	165 - 543	A	Y	Y

Author	Year	Fluid / Shape*	D_h (μm)	α_c = a/b	Re	fRe	C^*	L/D_h	Adiab/ Diab**	Account Losses	Agree Laminar
Qu et al.	2000b	water / Tr	62 - 169	2.16 - 11.53	94 - 1491	ID	ID	178 - 482	D	N	N
Rahman	2000	water / R	299 - 491	3.00 - 6.00	275 - 3234	9119.2 - 34880.6	487 - 2028	94 - 154	D	N	N
Xu et al.	2000	water / R	30 - 344	0.58 - 24.53	5 - 4620	9.1 - 46.2	0.53 - 3.18	145 - 1070	A	Y	Y
Chung et al.	2002	water / C	100	NA	1.9 - 3237	41.2 - 33.3	0.89 - 2.08	875	A	Y	Y
Judy et al.	2002	water, methanol, isopropyl / C, R	14 - 149	1.00	7.6 - 2251	12.9 - 20.3	0.83 - 1.27	1203 - 5657	A	Y	Y
Lee et al.	2002	water / R	85	0.25	119 - 989	19.4 - 43.6	1.06 - 2.39	118	D	Y	Y
Qu & Mudawar	2002	water / R	349	0.32	137 - 1670	12.1 - 33.4	0.70 - 1.94	128	D	Y	Y
Bucci et al.	2003	water / C	172 - 520	NA	2 - 5272	14.0 - 51.9	0.87 - 3.24	ID	D	Y	Y
Jung & Kwak	2003	water / R	100 - 200	1.00 - 2.00	50 - 325	10.7 - 33.4	0.69 - 2.15	75 - 150	D	Y	Y
Lee & Garimella	2003	water / R	318 - 903	0.17 - 0.22	558 - 3636	ID	ID	28 - 80	D	Y	Y
Park et al.	2003	water / R	73	4.44	4.2 - 19.1	ID	ID	654	D	-	-
Tu & Hrnjak	2003	R134a / R	69 - 305	4.11 - 11.61	112 - 3500	17.6 - 50.5	0.89 - 2.35	131 - 288	D	Y	Y
Wu & Cheng	2003a	water / Tr, Ti	26 - 291	ID	11.1 - 3060	11.7 - 31.6	0.73 - 1.98	ID	A	Y	Y
Wu & Cheng	2003b	water / Tr	169	1.54 - 26.20	16 - 1378	8.6 - 34.1	0.58 - 1.88	192 - 467	D	N	Y
Baviere et al.	2004	water / R	14 - 593	83.33	0.1 - 7985	21.5 - 71.8	0.91 - 3.04	138 - 429	D	Y	Y
Hsieh et al.	2004	water / R	146	1.74	45 - 969	14.6 - 51.2	0.96 - 3.39	164	D	Y	Y
Owhaib & Palm	2004	R134a / C	800 - 1700	NA	1262 - 16070	ID	ID	191 - 406	D	Y	Y

NA = Not Applicable ID = Insufficient Data * C = circular, R = rectangular, Tr = trapezoid, Ti = triangle ** A = Adiabatic, D = Diabatic *** Y = Yes, N = No

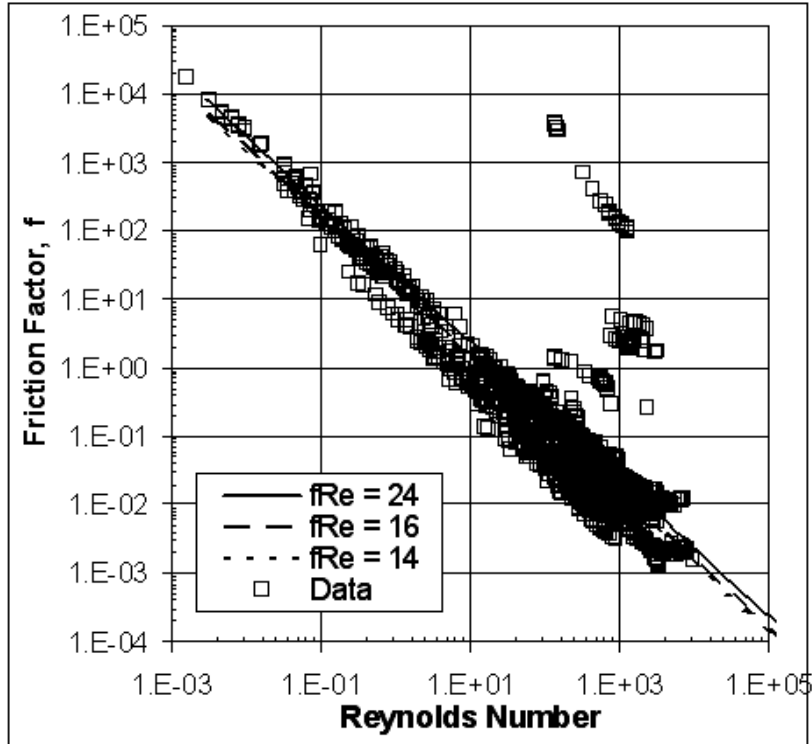


Figure 2.4: Friction Factor vs. Reynolds Number for all of the Available Data Sets.

The friction data should follow the $fRe = \text{Constant}$ line in the laminar region. Lines representing the flat parallel plate value of $fRe = 24$, the circular tube value of $fRe = 16$, and the square channel value of $fRe = 14$ are plotted for reference. The Poiseuille number is a constant whose value is geometry dependent and the value of 16 will not universally apply and plotting the friction factor for a variety of geometries is not appropriate. Therefore, the fRe number is normalized using the theoretical value of fRe and is given by:

$$C^* = \frac{(fRe)_{\text{exp}}}{(fRe)_{\text{theory}}} \quad (2.13)$$

where fRe_{exp} is the experimentally determined value and fRe_{theory} is the theoretical value determined by the channel geometry. It would be more appropriate to evaluate the C^* ratio for each geometry. A value of 1.0 for C^* would give a perfect match between experimental data and

the theoretical prediction. Figure 2.5 shows the ratio versus Reynolds number for all of the available data sets.

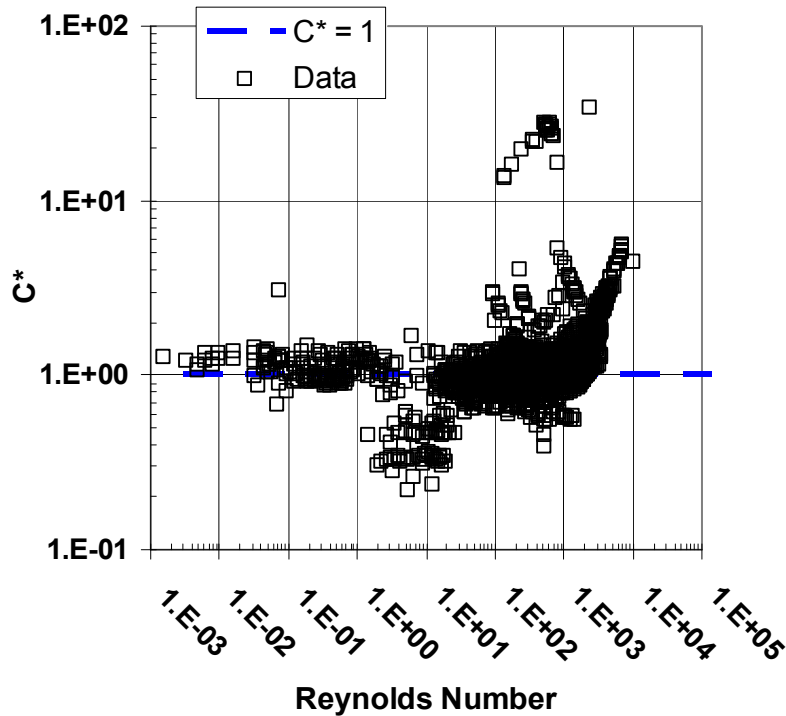


Figure 2.5: Non-dimensional Poiseuille Number vs. Reynolds Number for all of the Available Data Sets.

There is a common thread between all of the papers that have reported some form of discrepancy between the experimental data and the predicted theoretical value. Those authors that have not discussed the entrance or exit losses or the developing length are the same authors reporting the discrepancies. The authors that have removed the added losses for the entrance and exit and the added friction factor for the developing region also report good agreement with the predicted theory. Table 2.1 presents a column that indicates if the authors have accounted for the losses or the developing region in their test sections. However, there are a few exceptions. It is possible to have an entrance condition and a flow case that would give good agreement with theoretical predictions. Nevertheless, it seems that this is the common occurrence.

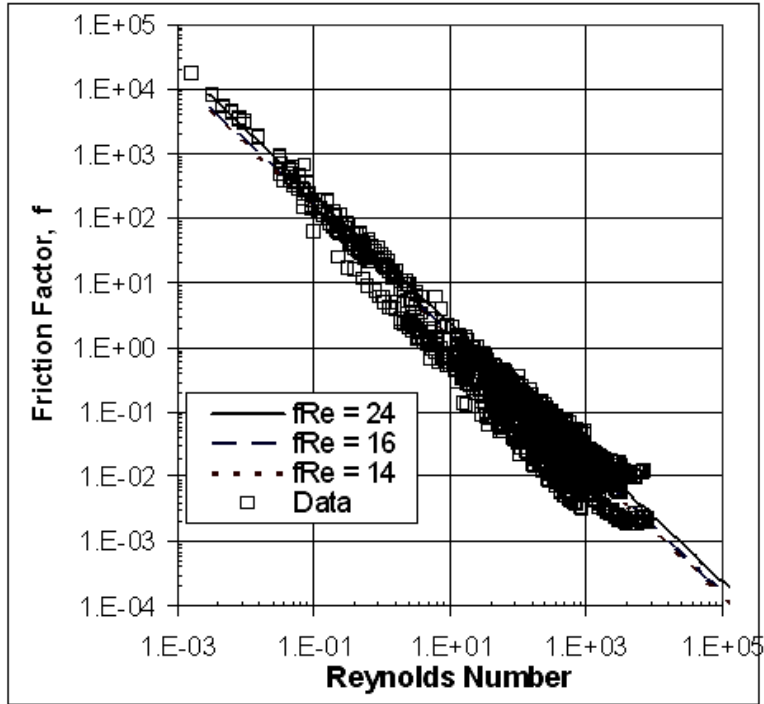


Figure 2.6: Friction Factor vs. Reynolds Number for the Reduced Data Sets.

If the papers that do not account for these effects on friction factor are removed, the data that are now reduced show very good agreement with predicted theory. Figure 2.6 shows the friction factors versus Reynolds number for the reduced data set. There still exists some deviation in the form of an offset from the predicted values of fRe . However, it is important to note that the general trends are present. Every data set exhibits the classical decreasing trend with a constant slope in the laminar region.

Figure 2.7 shows the transitional region in detail for the reduced data set. Even though there is some difference in the slope of the predicted line, the predicted linear decreasing trend is present. In addition, it can be seen that the critical Reynolds number is just where classical theory predicts it to be, $Re_{cr} \approx 2,300$. Furthermore, the data seem to begin to follow the lines that demonstrate the effect of surface roughness, as the Reynolds number moves into the transition

region. However, there are no data sets in the turbulent region to confirm the surface roughness behavior. The lines in the turbulent region represent the turbulent region friction factors with the surface roughness effect included.

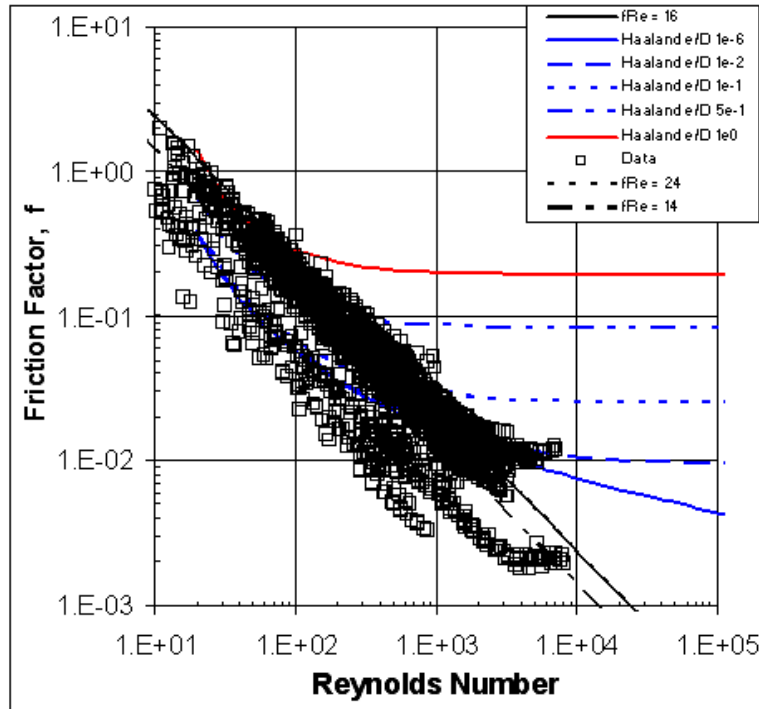


Figure 2.7: Friction Factor vs. Reynolds Number in the Transitional Regime for the Reduced Data Sets.

Figure 2.8 shows the C^* ratio for the reduced data set. As seen in Fig. 2.5, the very high values of f are removed from the data when losses and developing flow is considered. This makes sense because both would be components of pressure drop that would serve to add to the overall pressure drop and artificially increase the friction factor. However, there is still some significant deviation from the desired value of $C^* = 1.0$. If some error bounds are applied to Fig. 2.7, the vast majority of the data falls between $0.6 < C^* < 1.4$. An explanation of this behavior could come from experimental uncertainties, which will be described in the next section.

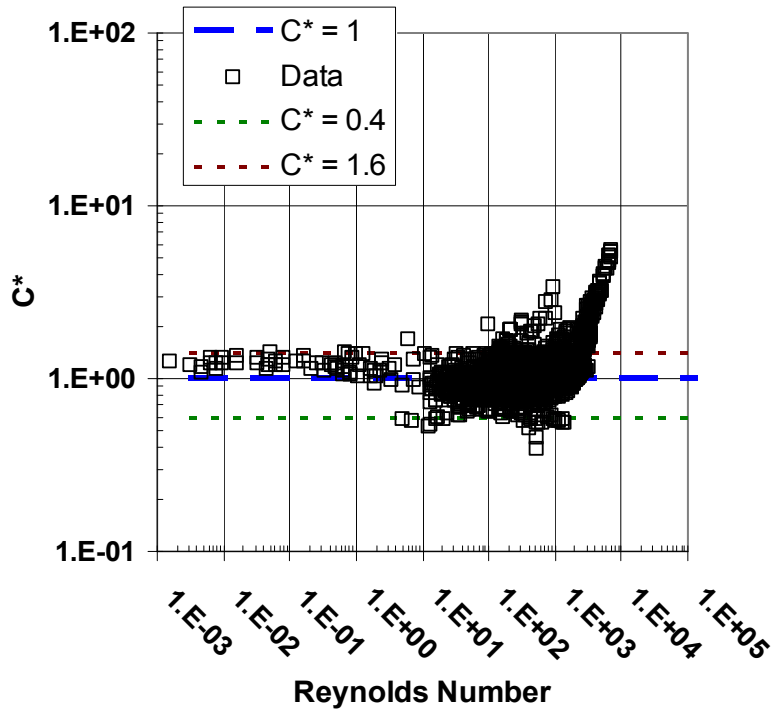


Figure 2.8: Non-dimensional Poiseuille Number vs. Reynolds Number for the Reduced Data Sets.

Three papers have been identified to demonstrate agreement with theory over the range of Reynolds numbers and a variety of shapes. Beginning with very low flow rates, Papautsky et al. (1999) investigated water flow in rectangular channels of hydraulic diameters between 44 and 47 μm , shown in Fig. 2.9. Judy et al. (2002) used water flowing through circular and rectangular tubes with hydraulic diameters between 14 to 149 μm . Figure 2.10 shows the C^* for laminar Reynolds numbers. Finally, Bucci et al. (2003) used water flowing in circular tubes with hydraulic diameters ranging between 172 and 520 μm . Figure 2.11 shows the C^* ratio for transitional Reynolds numbers.

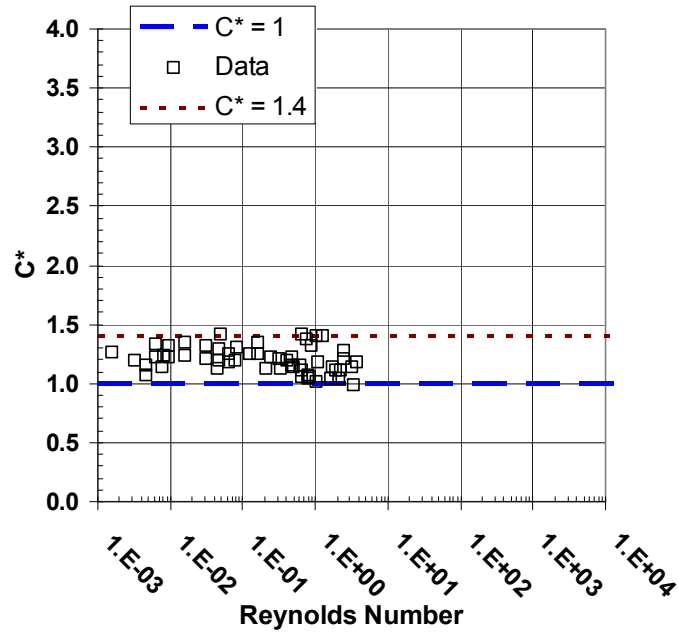


Figure 2.9: Non-dimensional Poiseuille Number vs. Reynolds Number for Low Laminar Reynolds Numbers, Papautsky et al. (1999).

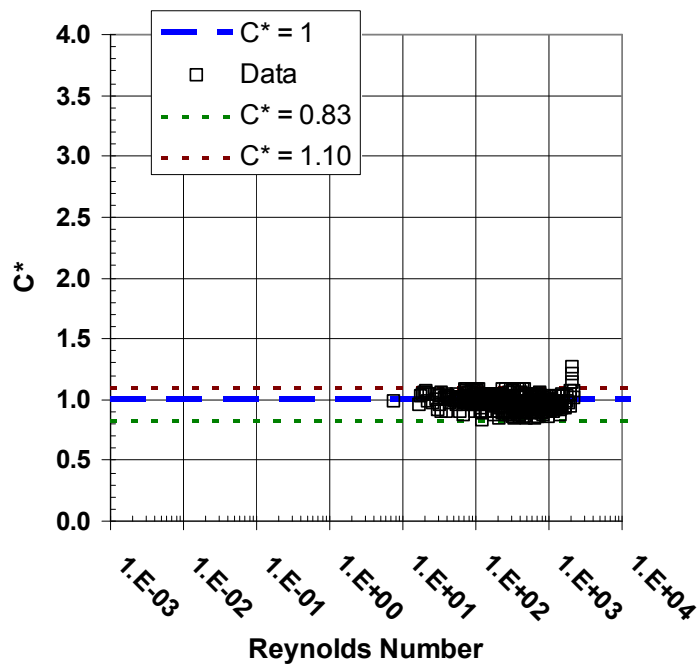


Figure 2.10: Non-dimensional Poiseuille Number vs. Reynolds Number for Laminar Reynolds Numbers, Judy et al. (2002).

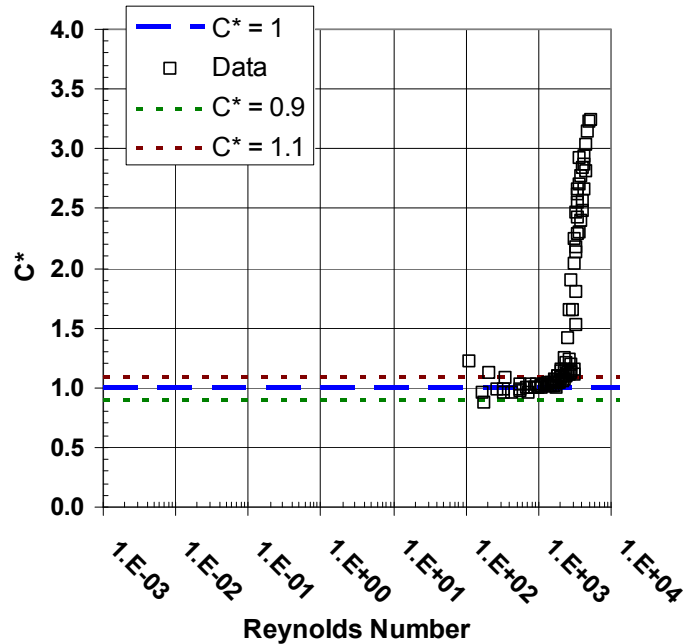


Figure 2.11: Non-dimensional Poiseuille Number vs. Reynolds Number for Transitional Reynolds Numbers, Bucci et al. (2003).

Figure 2.9 shows the data from Papautsky et al. (1999). The C^* ratio is bounded by the range $1.0 < C^* < 1.4$, which translates into an uncertainty of +40%. The channel diameter is very small and the Reynolds numbers are very low. This is perhaps the most extreme case. The experimental uncertainties will be quite large in this region. Figure 2.10 shows data from Judy et al. (2002) and the laminar Reynolds number range. There is excellent agreement with the C^* ratio being bounded by -15% and +10%. The Reynolds numbers and the channel hydraulic diameters are larger here and the uncertainty is improving. Finally, Fig. 2.11 shows the data from Bucci et al. (2003) and the transitional Reynolds number region. Here, the C^* ratio is bounded by $\pm 10\%$. The channel diameters here are greater than $500 \mu\text{m}$ at times with very larger Reynolds numbers. There is excellent agreement, until the critical Reynolds number is achieved, as expected.

2.4 Single-Phase Liquid Heat Transfer in Microchannels

The papers that contain heat transfer data are shown in Table 2.2. The ranges of the important microchannel heat transfer parameters are reported. Not all of the parameters were reported by the authors. As a result, some of the parameters are calculated by the present author using the data from the paper. The present work includes both adiabatic and diabatic works with several different channel geometries.

The papers listed in Table 2.2 are carefully reviewed to determine the Nusselt numbers for each data set. The Nusselt number versus the Reynolds number plot from the data is shown in Fig. 2.12. Conventional theory predicts a constant Nusselt number in the laminar range. This does not appear to be the case with the reported data. It is interesting to note that there are no data sets that show the constant Nusselt number behavior in the laminar region. In addition, there are a few data sets that show a decreasing trend in Nusselt number for the laminar region.

In the transition regime, there seems to be a better general agreement. The conventional theory predicts a dependency upon Reynolds number in the turbulent regime. The actual slope of the line is dependent upon which correlation is used. The trends generally follow the predicted increase in Nusselt number, although the Reynolds numbers reported here are actually in the transitional flow regime. There is not a general correlation for use in this regime. However, it seems that the turbulent theory may apply in this regime.

Figure 2.13 shows the Colburn j factor versus the Reynolds number. Conventional theory predicts a decreasing trend with an increasing Reynolds number. All of the data in the laminar region should collapse on a line corresponding to a constant value dependent upon the channel aspect ratio. However, there are several data sets that exhibit different slopes.

Table 2.2: Selected Literature for Single-Phase Liquid Flow in Microchannel Passages.

Author	Year	Fluid / Shape*	D_h (μm)	$\alpha_c = a/b$	Re	q'' (W/cm^2)	Nu	j	L/D_h	Account Losses	Agree Laminar
Tuckerman & Pease	1981	water / R	92 - 96	0.17 - 0.19	291 - 638	187 - 790	ID	ID	104 - 109	N	N
Missaggia et al.	1989	water / R	160	0.25	2350	100	ID	ID	6	N	N
Riddle et al.	1991	water / R	86 - 96	0.06 - 0.16	96 - 982	100 - 2500	4.9 - 17.7	ID	156 - 180	N	N
Gui & Scaringe	1995	water / Tr	338 - 388	0.73 - 0.79	834 - 9955	12 - 112	9 - 31	$6.19 \times 10^{-4} - 5.77 \times 10^{-3}$	119 - 136	N	N
Peng et al.	1995	methanol / R	311 - 646	0.29 - 0.86	1530 - 13455	0.2 - 10	0.2 - 4.3	$4.38 \times 10^{-5} - 6.40 \times 10^{-4}$	70 - 145	N	N
Peng & Peterson	1995	water / R	311	0.29	214 - 337	5 - 45	0.6 - 1.6	$1.10 \times 10^{-3} - 3.68 \times 10^{-3}$	145	N	N
Cuta et al.	1996	R124 / R	425	0.27	101 - 578	ID	4.1 - 12.8	$8.97 \times 10^{-3} - 3.22 \times 10^{-2}$	48	Y	Y
Peng & Peterson	1996	water / R	133 - 200	0.5 - 1.0	136 - 794	ID	0.2 - 0.7	$1.69 \times 10^{-4} - 1.39 \times 10^{-3}$	25 - 338	N	N
Tso & Mahulikar	1998	water / C	728	NA	16.6 - 37.5	0.5 - 0.8	0.3 - 1.1	$7.35 \times 10^{-3} - 1.59 \times 10^{-2}$	76 - 89	Y	Y
Vidmar & Barker	1998	water / C	131	NA	2452 - 7194	506 - 2737	ID	ID	580	Y	NA
Adams et al.	1999	water / Tr	131	ID	3899 - 21429	ID	15.7 - 91.7	ID	141	Y	NA
Qu et al.	2000	water / Tr	62 - 169	2.16 - 11.53	94 - 1491	ID	0.6 - 2.3	$6.29 \times 10^{-4} - 5.70 \times 10^{-3}$	178 - 482	N	N
Lee et al.	2002	water / R	85	0.25	119 - 989	35	3.2 - 9.9	$5.54 \times 10^{-3} - 1.69 \times 10^{-2}$	118	Y	Y
Qu & Mudawar	2002	water / R	349	0.32	137 - 1670	100 - 200	402 - 1788	$5.65 \times 10^{-1} - 1.63 \times 10^0$	128	Y	Y
Bucci et al.	2003	water / C	172 - 520	NA	2 - 5272	ID	4.8 - 50.6	$9.33 \times 10^{-3} - 1.08 \times 10^0$	ID	Y	Y
Lee & Garimella	2003	water / R	318 - 903	0.17 - 0.22	558 - 3636	ID	7.1 - 35.4	$3.19 \times 10^{-3} - 8.03 \times 10^{-3}$	28 - 80	Y	Y
Wu & Cheng	2003	water / Tr	169	1.54 - 26.20	16 - 1378	ID	0.2 - 4.1	$1.01 \times 10^{-3} - 1.73 \times 10^{-2}$	192 - 467	N	N
Owhaib & Palm	2004	R134a / C	800 - 1700	NA	1262 - 16070	ID	11.5 - 922.2	$9.23 \times 10^{-3} - 1.05 \times 10^{-1}$	191 - 406	Y	Y

NA = Not Applicable ID = Insufficient Data * C = circular, R = rectangular, Tr = trapezoid, Ti = triangle ** A = Adiabatic, D = Diabatic *** Y = Yes, N = No

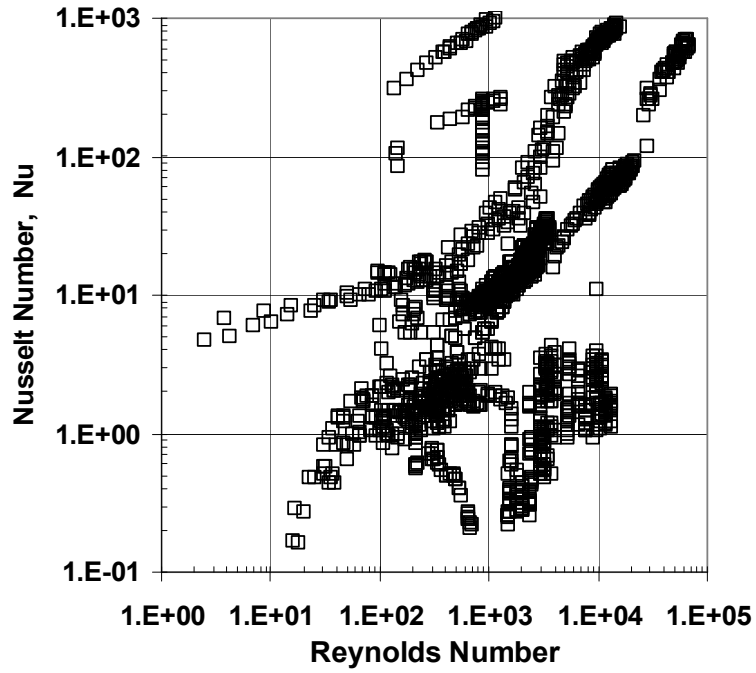


Figure 2.12: Nusselt Number versus Reynolds Number for All Reported Data Sets.

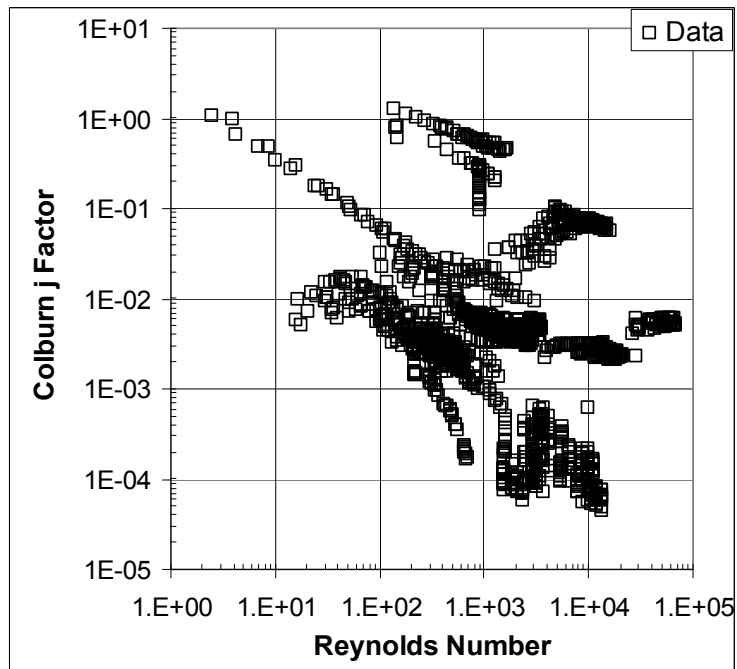


Figure 2.13: Colburn j Factor versus Reynolds Number for All Reported Data Sets.

There are several different trends seen in the data shown in Figs. 2.12 and 2.13. There are simultaneously occurring increasing and decreasing trends in Nusselt number shown in Fig. 2.12. However, some data sets present good general agreement with conventional theory. The data in Fig. 2.12 and Fig. 2.13 represents data collected in test sections where the developing regions might be quite long or covering the majority of the flow length. Therefore, the data sets that do not account for or address the developing length issue are removed from the database.

Figure 2.14 shows the Nusselt number for the data sets that have been reduced by including only those that account for developing lengths. There is still a trend that has some dependence upon Reynolds number in the laminar region. The trend has a much larger slope in the turbulent region, as expected.

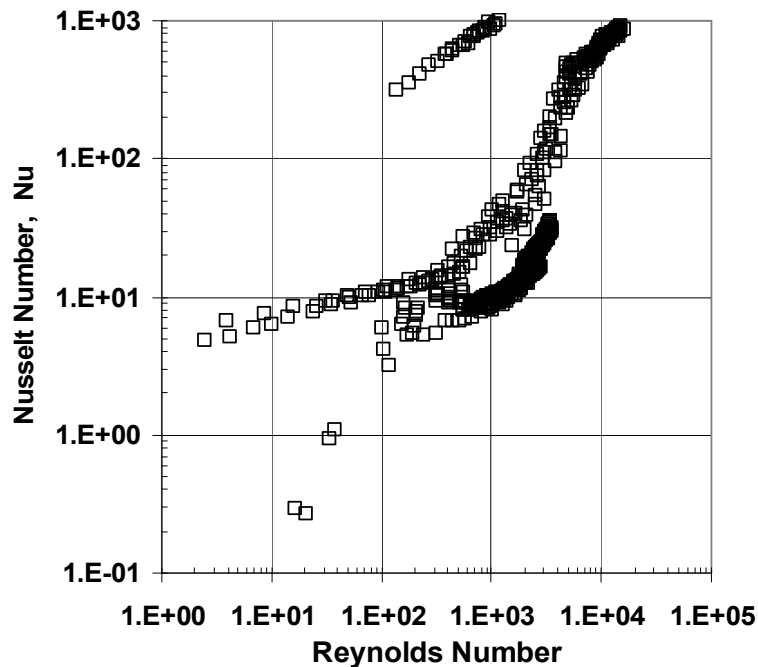


Figure 2.14: Nusselt Number versus Reynolds Number for Reduced Data Sets.

The Colburn j factor versus the Reynolds number for the reduced data sets is shown in Fig. 2.15. The general trend of decreasing j with Re in the laminar region is present here. The

constant value the Nusselt number achieves in the laminar region is dependent upon the boundary conditions. This makes a direct comparison for all of the data sets very difficult.

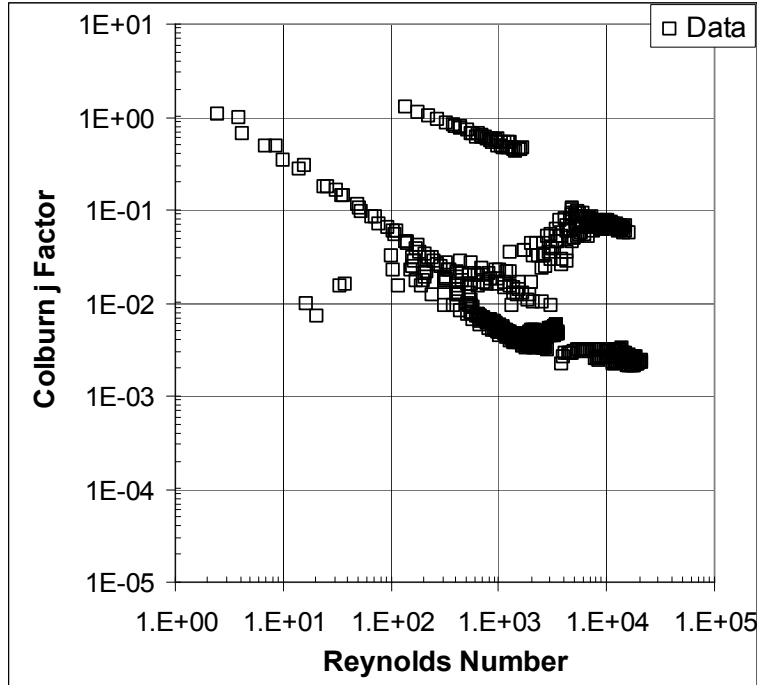


Figure 2.15: Colburn j Factor versus Reynolds Number for Reduced Data Sets.

Therefore, a parameter is used to provide a metric for how well the experimental data compares to the predicted value. A similar parameter C^* is utilized in comparing the theoretical and experimental friction factors. C^* is the ratio of the experimental fRe product to the predicted fRe product. The same method is utilized in the present work. The ratio of the experimental Nusselt number to the theoretical fully developed Nusselt number is given by A^* , Eq. (2.14).

$$A^* = \frac{Nu_{exp}}{Nu_{theory}} \quad (2.14)$$

The proper Nusselt number for each data set is carefully determined from the information contained in the respective paper. This is a difficult process for many data sets as the boundary conditions are not clearly defined in many experiments. Only the experimental data sets with

clearly defined boundary conditions are included in Fig. 2.15. The theoretical Nusselt numbers for all three boundary conditions are calculated and the boundary condition that gives the best agreement is chosen to represent that data set.

The present work will mainly focus on laminar flow. Therefore, the A^* ratio is calculated using the appropriate laminar Nu for each data set. Figure 2.16 shows the A^* ratio for all of the data sets. A value of 1.0 would indicate a perfect match between experimental data and theoretical prediction. The sharp rise in A^* in the transition region is due to the use of laminar Nusselt numbers and is expected. There are seemingly many different transition points indicated by the sharp rise in A^* .

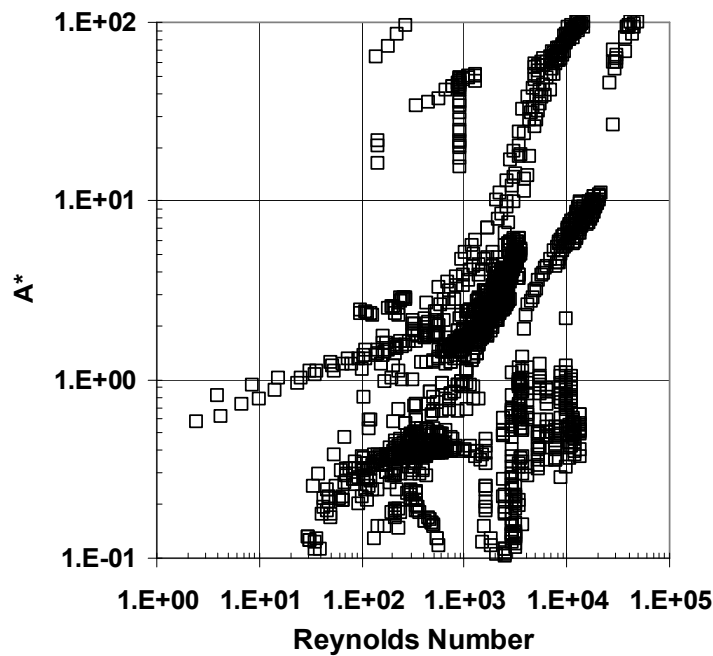


Figure 2.16: A^* versus Reynolds Number for All Reported Data Sets, Laminar Regime.

Once again, the only the data sets that address the developing flows are used in plotting Fig. 2.17. A large number of data sets are removed and only a few data sets remain. There seems to be good general agreement in the laminar region.

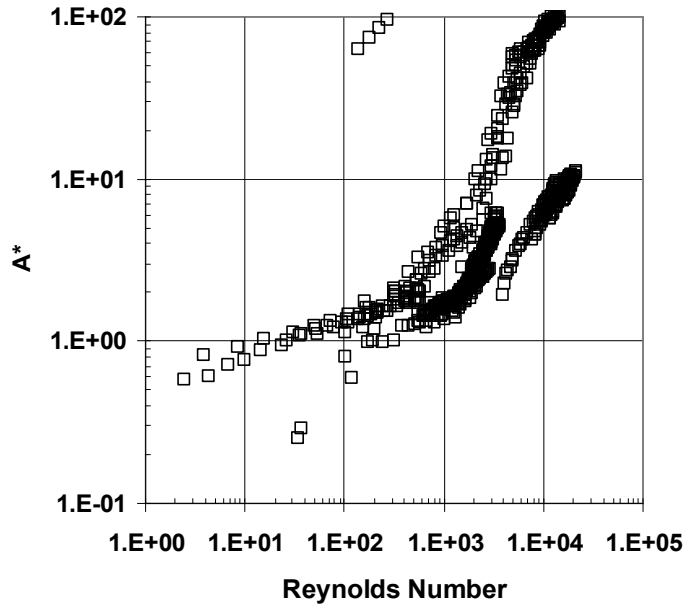


Figure 2.17: A^* versus Reynolds Number for Reduced Data Sets, Laminar Regime.

Figure 2.18 shows the A^* data from Lee and Garimella (2002). They investigated high laminar and transitional Reynolds numbers. There is generally good agreement with the laminar Nusselt number.

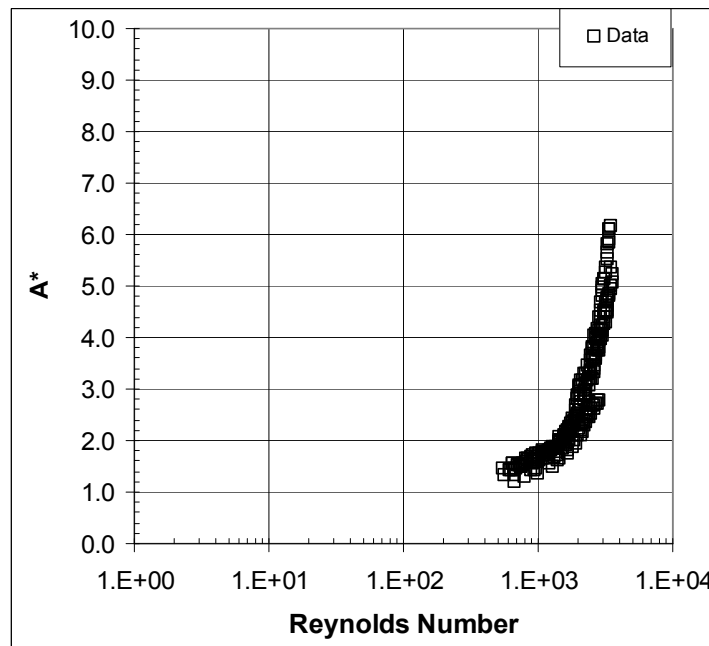


Figure 2.18: A^* versus Reynolds Number for Lee and Garimella. (2002).

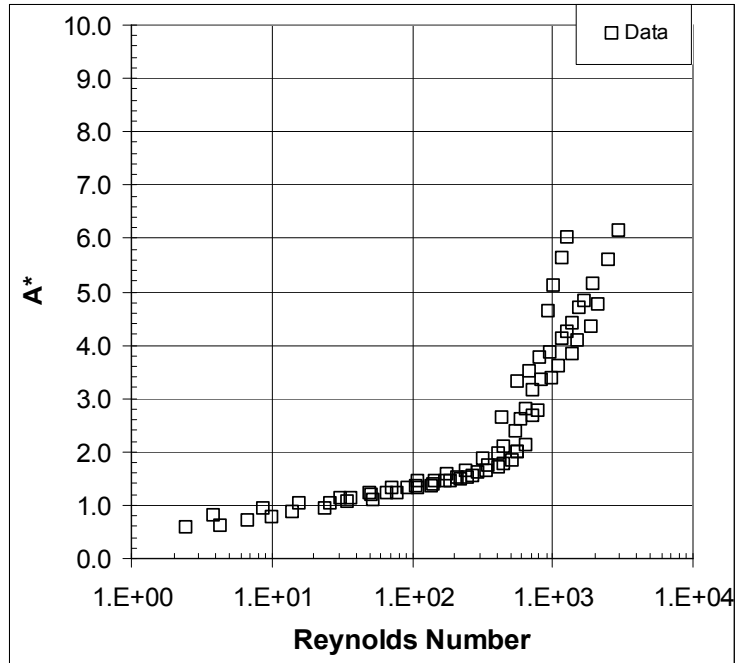


Figure 2.19: A^* versus Reynolds Number for Bucci et al. (2003).

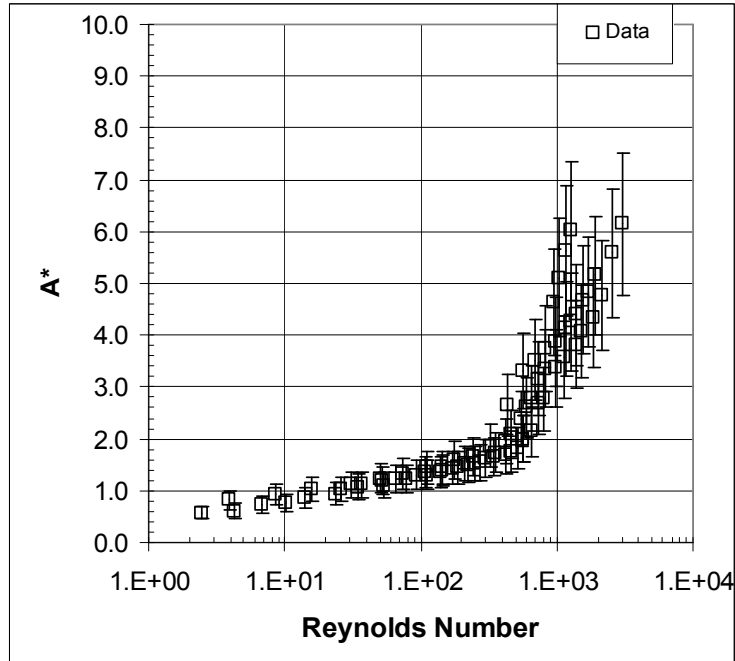


Figure 2.20: A^* versus Reynolds Number for Bucci et al. (2003) Including Reported Uncertainties.

Figure 2.19 shows only the A^* versus Reynolds number data from Bucci et al. (2003). There is a suggested dependency upon Reynolds number in the laminar region. Bucci et al. conclude that there is good agreement with Hausen (1959) for the laminar region and Gnielinski (1976) for the transition region. Furthermore, the critical Reynolds number occurs at the conventional location but the actual value is greatly dependent upon flow and heat transfer conditions. The authors reported the experimental uncertainty for the Nusselt number to be 22.25%. This allows the majority of the laminar data to fall into agreement with the constant Nusselt number theory, as seen in Fig. 2.20.

2.5 Conventional Single-Phase Liquid Heat Transfer Enhancements

Study of heat transfer augmentation began as early as the 1920s and the work continues to the present day. In the 1980s, the benefits of this field began to emerge in industry and also in open literature, Bergles (1997). There are several thousand papers that have been published on the subject of heat transfer enhancement or augmentation. There have been several researchers that have presented reviews of the state of the art. Bergles et al. (1996) have compiled the available literature on convective heat transfer. They sampled several journals, conferences and patents to generate a database of over five thousand papers. Bergles has classified the augmentation techniques into two categories, passive and active. In addition, Bergles has presented reviews of this topic in (1997, 1999, 2002). In his latest work, Bergles (2002) presents the fourth generation of heat transfer enhancement using a combination of different techniques. He suggests that the field can be extended and heat transfer coefficients further increased by combining different individual techniques. The use of multiple techniques in single-phase flows is an attractive possibility.

A summary of the techniques discussed is presented in Table 2.3. The techniques are described according to their application in a conventional channel, minichannel, and microchannel. Each technique will be described respectively in detail in another chapter.

Table 2.3. Summary of Enhancement Techniques for Microchannels and Minichannels.

ENHANCEMENT TECHNIQUE	CONVENTIONAL $D_h > 3 \text{ mm}$	MINICHANNEL $3 \text{ mm} \geq D_h > 200 \text{ }\mu\text{m}$	MICROCHANNEL $200 \text{ }\mu\text{m} \geq D_h > 1 \text{ }\mu\text{m}$
<i>Passive Techniques</i>			
Surface Roughness	Roughness structure remains in boundary layer; provides early transition to turbulence	Use different surface treatments, roughness structures can remain in boundary layer and protrude into bulk flow	Can achieve with various etches; roughness structures may greatly influence flow field
Flow Disruptions	Using twisted tape, coiled wires, offset strip fins; fairly effective	Can extend conventional methods here; offset strip fins, some twisted tapes, small gauge wire	Can use sidewall or in channel; optimize geometry for minimal impact on flow
Channel Curvature	Not practical due to large radius of curvature; has been demonstrated in $D_h = 3.33 \text{ mm}$	More possible than conventional; incorporate return bends for compact heat exchangers	Most practical; achievable radius of curvature; large number of serpentine channels
Re-entrant Obstructions	Effect not as prevalent; bulk flow reaches fully developed flow quickly; harder to return flow to developing state	Can incorporate structures to interrupt flow; header design could contribute to pre-existing turbulence	Short paths make for dominant behavior; can incorporate opportunities to maintain developing flows
Secondary Flows	Flow obstructions can generate secondary flows; combination of inserts and obstructions	Could use jets to aid in second flow generation; combination of inserts and obstructions	Can fabricate geometries to promote mixing of fluid in channel
Out of Plane Mixing	Not very effective; space requirements prohibitive	Possible use; three dimensional mixing may not be that effective	Greatest potential; fabricate complex 3D geometries very difficult
Fluid Additives	PCMs dominate	PCMs possible; fluid additives possible	Fluid additives; micro- and nanoparticles possible
<i>Active Techniques</i>			
Vibration	Surface and fluid vibration utilized currently	Possible to implement; can use in compact heat exchangers	External power is a problem; integrate piezoelectric actuators
Electrostatic Fields	Electrohydrodynamic forces currently used; integrated electrodes	Could be easier to integrate into compact heat exchanger; external power not as problematic	Can integrate electrodes into channel walls; power consumption problematic
Flow Pulsation	Established work showing enhancement	Can implement in compact heat exchangers fluid delivery	Possible to implement, could make fluid delivery simpler
Variable Roughness Structures	Difficult to integrate very small variable structures into a conventional channel	Difficult to integrate into compact heat exchangers	Possible to integrate; piezoelectric actuators change roughness structure

Balaras (1990) reviewed augmentation techniques and classified them as surface, fluid, combined and compound methods. The surface methods included modifications to the heated surface such as extended surfaces, roughened surfaces, swirl-flow devices, and surface vibration. The fluids methods involved external fluid vibration, additives and electrostatic forces. The combined and compound methods use suction, injection and a combination of the other methods.

Based upon other research and their own, Tao et al (2002) have presented three possible mechanisms for the single-phase heat transfer enhancement. These three mechanisms are: 1) Decreasing the thermal boundary layer, 2) Increasing flow interruptions, and 3) Increasing the velocity gradient near the heated surface. It is the manipulation of these three mechanisms that results in heat transfer augmentation.

The channel classification used for the present study was presented in Kandlikar and Grande (2003). A conventional sized flow passage has a hydraulic diameter larger than 3.0 mm. A minichannel passage has a hydraulic diameter between 3.0 mm and 200 μm . A microchannel has a hydraulic diameter of less than 200 μm . The classification is meant for a guideline in describing the size of a flow passage.

The present work will focus on applying heat transfer augmentation in conventional sized passages to the minichannel and microchannel passages. The following discussion closely follows the classification of passive and active enhancement techniques as outlined by Bergles (1996).

2.6 Summary of Literature Reviews

This section describes the summary results of the literature reviews. There are several different topics addressed in the present work. For ease of discussion, they will be separated into several sub-sections in order to focus on the topics.

2.6.1 Pressure Drop

There are several papers on the topic of pressure drop in microchannel passages. The deviations from classical theory have been identified and classified. The researchers' not accounting for entrance and exit losses and not accounting for the developing flows is believed to be responsible for the discrepancies reported in literature. Those researchers who have accounted for these two complications report good agreement with conventional theory.

In several recent papers, the researchers have been more careful with the additional losses seen in complicated flow structures used in microchannels, and as a result, are reporting better agreement with conventional theory. However, it is important to explain the discrepancies that exist in the previous literature.

The microchannel geometry and surface roughness do not influence the laminar friction factor. A few researchers have begun to address this issue in the transitional flow regime. However, there are very limited data in the transitional flow regime and almost none in the turbulent regime in microchannels. More experimental data are required here to determine the effect of microchannel roughness in the transitional and turbulent flow regimes.

Finally, the experimental uncertainties for the friction factor and the fRe number should be carefully evaluated. Figures 2.8, 2.9, and 2.10 each show the C^* ratio for three selected works over different ranges of Reynolds numbers. The error bars, as calculated by the present

author, tend to decrease as the Reynolds number range is increased. This behavior is attributed to the decrease in experimental uncertainties as the Reynolds number magnitude is increased. It is critical to report experimental uncertainties along with experimental data so that discrepancy in theory is not mistaken as large experimental uncertainties.

2.6.2 Heat Transfer

There still can be some major errors associated with heat transfer measurements in microchannels. Some of the deviations still seen in the data can be attributed to a number of factors. The following is a list of the possible complications that are believed to be the source of the remaining discrepancy.

- Hard to determine boundary conditions
- More complex developing flows
- Fin efficiency not accounted for
- Large experimental errors

Another source of error can come from the separating walls in a microchannel heat exchanger. Typically, these would be referred to as fins. The fin efficiency can have an effect on the experimentally derived heat transfer coefficients in the microchannels. Very few authors have discussed this issue and any correction seems to be missing to account for this aspect.

Finally, the microchannel heat exchanger is a complex system. More accurate modeling could involve describing the conjugate heat transfer that is occurring in these systems. It is strongly recommended to consider microchannel heat transfer as a conjugate problem instead of a purely convective one.

2.6.3 Heat Transfer Enhancement

There are several thousand papers that address the topic of heat transfer enhancement in conventional passages. Several excellent review papers exist that give good descriptions of the techniques employed to perform heat transfer augmentation. The identified enhancement techniques need to be carefully evaluated in order to determine their applicability to microchannel heat transfer.

CHAPTER 3

THEORETICAL CONSIDERATIONS FOR PRESSURE DROP AND HEAT TRANSFER IN MICROCHANNELS

Now that the discrepancies have been identified in the previous literature, the theory and correlations that are useful in microchannels can be described. This chapter will describe in detail the theoretical considerations to determine pressure drop and heat transfer in a microchannel. The non-dimensional groups that are utilized for comparison purposes will first be identified. Then, the equations that utilize these groups will be explained. Finally, some microchannel specific complications such as pressure and temperature measurements will be presented.

3.1 *Single-Phase Liquid Heat Transfer in Microchannels*

The pressure drop occurring in a microchannel will be described in this section. The components of the pressure drop that constitute the overall pressure drop in a microchannels heat exchanger will be described. The correct prediction of the pressure drop is critical for the design of the entire microchannel heat exchanger system.

3.1.1 Pressure Drop Measurements in Microchannels

The measurement of pressure drop in a microchannel heat exchanger is not a trivial task. There are several issues that need to be addressed when performing pressure drop measurements in microchannel flows. The inlet and exit losses need to be quantified for the microchannel. In

addition, the overall lengths of microchannels tend to be very short. Therefore, the hydrodynamic developing length needs to be carefully evaluated. The entrance length can be as long as the total flow length of the microchannel. Finally, the remaining length will have the fully developed frictional loss.

Typically, there are several microchannel passages in one microchannel heat exchanger. The pressure drop is usually measured inside the inlet and outlet manifolds. In addition, the physical size of the passage can be limiting in attempting to make measurements inside a channel.

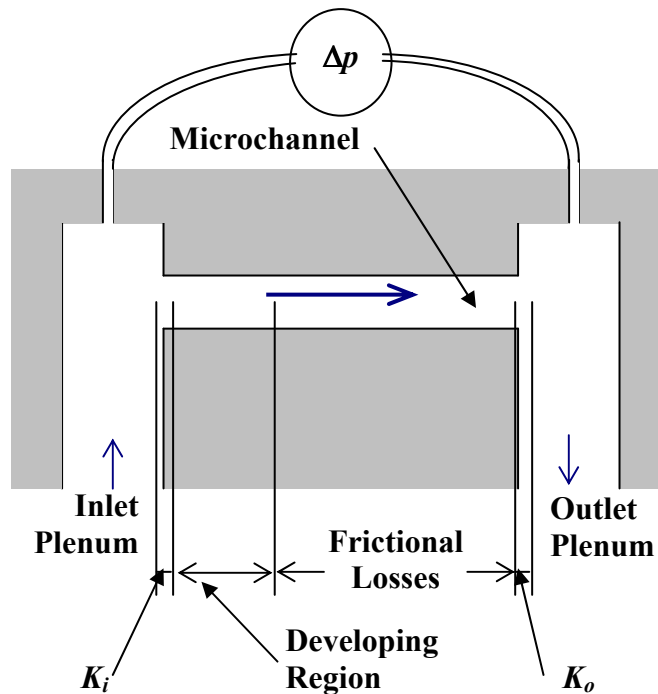


Figure 3.1: Components of Pressure When Measuring Δp in Microchannel Manifolds.

The most common method to measure the pressure drop involves making pressure measurements inside the inlet and outlet manifolds. The different components of pressure that make up the entire pressure drop are shown a schematically in Fig. 3.1. There are three main

components that contribute to the overall pressure drop. The inlet and outlet loss coefficients are represented by K_i and K_o . The friction factor is also increased in the developing region. Finally, the friction loss region should follow the conventional theory. The components of the total pressure drop can be seen in Eq. (3.1).

$$\Delta p = 2 \rho \bar{V}^2 \left[K_i + K_o + \frac{f L}{D_h} \right] \quad (3.1)$$

where K_i is the inlet loss coefficient and K_o is the outlet loss coefficient. Remember that this equation is valid for incompressible flow. This equation is commonly found in literature. However, there is still another component that can become quite large for microchannels. The entrance region must also be accounted for. Therefore, the f in Eq. (3.1) would actually be an apparent friction factor, f_{app} . Equation (3.2) reflects the actual total pressure drop equation to use in microchannels.

$$\Delta p = 2 \rho \bar{V}^2 \left[K_i + K_o + \frac{f_{app} L}{D_h} \right] \quad (3.2)$$

The determination of f_{app} can become quite complicated. It is therefore very important to be able to account for the entrance and exit losses and the developing flow lengths in order to properly measure and predict the total pressure drop.

Fortunately, the entrance and exit losses can be eliminated to obtain the data for the frictional pressure drop in the microchannels. Several researchers have addressed this issue. The unknown entrance and exit losses can be eliminated by using two different flow lengths. Bucci et al. (2003) measured the overall pressure drop in stainless steel capillary tubes. They used a short length and a long length of tube with the same entrance conditions. Therefore, the entrance

and exit losses are the same for each flow case. The only component left to account for the difference in pressure drop is the added frictional loss from the added length of tube. They demonstrated agreement with conventional theory.

Local static pressure measurements in the microchannel would be the best situation to determine the pressure drop occurring inside the microchannel. This becomes very difficult in practical system. However, there are several researchers that have been able to successfully make local measurements in the microchannel.

Tu and Hrnjak (2003) fabricated a test section from clear polyvinylchloride (PVC). There were two pressure taps located over the microchannel and away from the inlet and exit manifolds. Baviere et al. (2004) fabricated a microchannel with local pressure channels away from the inlet and exit plenums in a silicon substrate. The pressure transducers, fabricated from a thin silicon membrane, were also incorporated into the silicon substrate. Each of these works reported agreement with conventional theory. Kandlikar et al. (2005) also made local pressure measurements in an aluminum channel. However, they reported agreement with conventional theory for the smooth channels. The channels with highly ordered roughness structures showed early transition.

There is one more complication with the pressure drop measurements located in the plenums. For a conventional system, the inlet and exit plenums are sufficiently large in area to cause the flow to reach stagnation or attain a very low velocity relative to the channel velocity. A uniform flow can now enter the channel. This case may not be satisfied for microchannel heat exchangers. The entrance condition could be considerably more complex. There maybe an added component of dynamic pressure included in the pressure drop measurements if the plenums are not properly sized. A verification of the losses in the plenum would be appropriate.

3.1.2 Fully Developed Laminar Flow

For a laminar flow, the Poiseuille number, $Po = fRe$, is constant. The fRe is 16 for a round tube. The Poiseuille number is a function of aspect ratio for a rectangular passage. It can be determined using Eq. (3.3) from Shah and London (1978).

$$f Re = 24 \left(1 - 1.3553\alpha_c + 1.9467\alpha_c^2 - 1.7012\alpha_c^3 + 0.9564\alpha_c^4 - 0.2537\alpha_c^5 \right) \quad (3.3)$$

where α_c is the channel aspect ratio, for four side heated channels. One constraint for this equation is that the aspect ratio must be less than one. If the channel aspect ratio is greater than 1.0, the inverse is taken to use with Eq. (3.3).

3.1.3 Fully Developed Turbulent Flow

The turbulent regime has several possible correlations to choose from. In the turbulent regime, the friction factor begins to demonstrate a dependence upon the surface roughness ratio, e/D . For a very smooth passage, the Blasius equation can be used and is given by:

$$f = \frac{0.0791}{Re^{1/4}} \quad (3.4)$$

This correlation is valid for the range of $2,100 < Re < 10^5$ and for e/D ratios $< 1 \times 10^6$. Moody (1944) arranged his widely accepted Moody diagram to present an easy method to determine the friction factor in terms of the Reynolds number and surface roughness for a circular tube. On that plot, the constant Poiseuille number for laminar flow is easily identified. In addition, the line for an e/D ratio of 1×10^6 is actually that of the Blasius equation. The remainder of the lines in the turbulent regime can be determined by using the implicit Colebrook (1938) equation shown in Eq. (3.5).

$$\frac{1}{\sqrt{f}} = -2 \log \left\{ \frac{e}{3.7D} + \frac{2.51}{\text{Re} \sqrt{f}} \right\} \quad (3.5)$$

The complication with this equation is that it is in an implicit form. After all, this was the motivation for the Moody diagram. There are several explicit correlations that demonstrate good agreement with the Colebrook equation. Each have different accuracies and intended ranges. However, the available correlations are derived using rough circular tubes.

The first work to recognize the effect of surface roughness on fluid flow for the turbulent region was by Nikuradse (1933). He varied the roughness of the pipes using sand adhered to the walls using a lacquer and determined the dependence of friction factor upon a non-dimensional wall roughness as seen in Eq. (3.6).

$$\frac{1}{\sqrt{f}} = 3.48 - 1.737 \ln \left(\frac{e}{D} \right) \quad (3.6)$$

This is a good place to start with explicit form of the Colebrook equation. For the present work, two correlations have been used. First, the Churchill (1977) correlation shown in Eq. (3.7) is used.

$$f = 2 \cdot \left[\left(\frac{8}{\text{Re}} \right)^{12} + \frac{1}{(A+B)^{1.5}} \right]^{\frac{1}{12}} \quad (3.7)$$

$$A = \left\{ 2.457 \cdot \ln \left[\frac{1}{\left(\frac{7}{\text{Re}} \right)^{0.9} + \left(\frac{0.27e}{D} \right)} \right] \right\}^{16}$$

$$B = \left(\frac{37530}{\text{Re}} \right)^{16}$$

The advantage of this correlation is that it is valid for almost all Reynolds numbers from laminar, transitional, and turbulent. The agreement with the Colebrook equation is approximately 5%. A limitation to this equation is that its critical Reynolds Number is 3,000 and should not be used for Reynolds numbers below that value.

As a result, a second correlation is utilized to extrapolate into the laminar regime. Equation (3.8) shows the Haaland (1983) correlation.

$$f = \left\{ 1.81 \cdot \log \left[\frac{6.9}{\text{Re}} + \left(\frac{e}{3.7D} \right)^{1.11} \right] \right\}^{-2} \quad (3.8)$$

This equation is a good approximation, within approximately 2%, for the implicit Colebrook equation and is valid for $\text{Re} > 2,300$.

3.1.4 Hydrodynamically Developing Flow

The hydrodynamicly developing flow in microchannels will be discussed. First, the definition of a non-dimensional flow distance is defined in Eq. (3.9).

$$x^+ = \frac{x}{D_h \text{Re}} \quad (3.9)$$

where x^+ is the non-dimensional flow distance and x is the axial flow direction location. It is commonly accepted that for a value of $x^+ = 0.05$, the flow can be considered fully developed.

The non-dimensional entrance length is given by Eq. (3.10).

$$L^+ = \frac{L_h}{D_h \text{Re}} \quad (3.10)$$

where L^+ is the non-dimensional entrance length and L_h is the hydrodynamic entrance length.

The entrance length can be determined using the classically accepted equation given by:

$$\frac{L_h}{D_h} = 0.05 \text{ Re} \quad (3.11)$$

Another accepted correlation for a circular channel is given by Chen (1973) and is seen in Eq. (3.12).

$$L^+ = 0.056 + \frac{0.60}{\text{Re} (1 + 0.035 \text{Re})} \quad (3.12)$$

As mentioned previously, the pressure drop measurement technique that utilizes the pressure measurements must take into account three main components. Suppose that the inlet and exit losses have been removed from the pressure drop measurement. The remaining pressure drop now only has the developing flow component and the frictional losses in the fully developed region. The pressure drop is now related to an apparent friction factor and is seen in Eq. (3.13), Kakaç et al. (1987).

$$\Delta p = \frac{2 (f_{app} \text{Re}) \mu \bar{V} x}{D_h^2} \quad (3.13)$$

where f_{app} is the apparent friction factor. If the entire length of the microchannel is considered, the x term can be the microchannel length. Figure 3.2 shows the dependence of f_{app} upon non-dimensional flow distance and channel aspect ratio, taken from Curr et al. (1972).

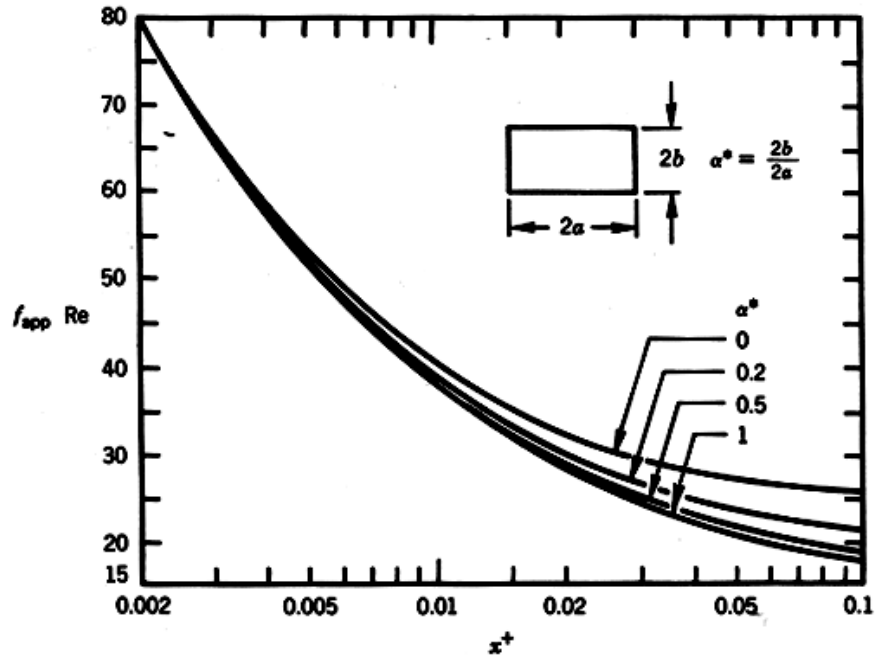


Figure 3.2: Apparent Friction Factor Dependence Upon Channel Aspect Ratio, taken from Curr et al. (1972).

The apparent friction factor consists of two components. The first is the friction factor from fully developed theory and the second is the pressure defect (aka Hagenbach factor), Eq. (3.14).

$$\Delta p = \frac{2 (f \text{Re}) \mu \bar{V} L}{D_h^2} + \frac{K(x) \rho \bar{V}^2}{2} \quad (3.14)$$

where $K(x)$ is the Hagenbach factor given by:

$$K(x) = (f_{app} - f_{FD}) \frac{x}{r_h} \quad (3.15)$$

where r_h is the hydraulic radius that is equal to $\frac{1}{4}D_h$. The Hagenbach factor will begin at a value of zero and increase to some constant value $K(\infty)$. For a circular channel, the fully developed Hagenbach factor is given by Chen (1972):

$$K(\infty) = 1.20 + \frac{38}{Re} \quad (3.16)$$

However, $K(\infty)$ also has a dependence upon channel aspect ratio for rectangular channels, as seen in Fig. 3.3, Curr et al. (1972). The data from the figure can be used to generate the following equations. Equations 3.3 are for the channel aspect ratios of 1.0, 0.5, 0.2, and 0.0, respectively.

$$f_{app} Re = 5.8198 \alpha_c^{-0.4134} \quad (\alpha_c = 1.0) \quad (3.17)$$

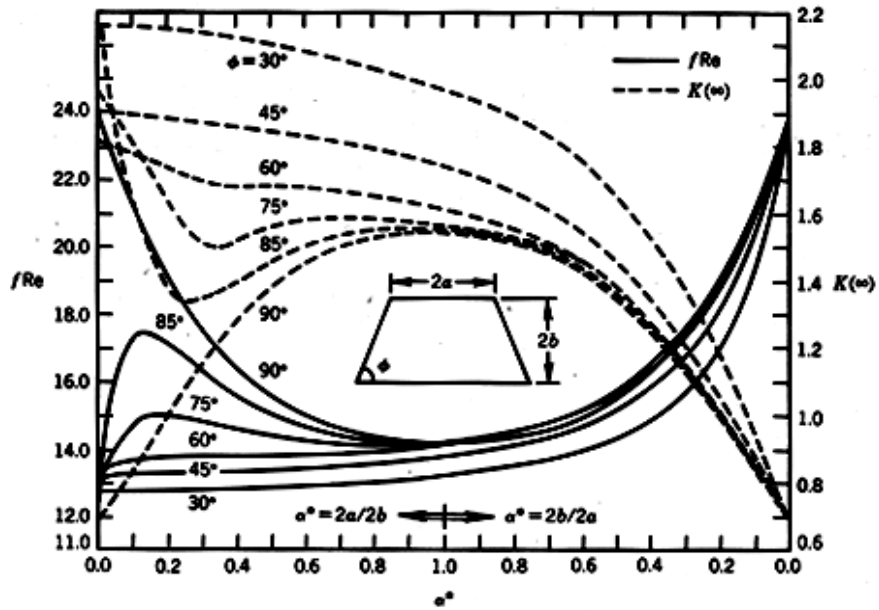


Figure 3.3: Fully Developed Hagenbach Factor Dependence Upon Channel Aspect Ratio, Kakaç et al. (1987).

Figure 3.3 shows the dependence of $K(\infty)$ upon channel aspect ratio. If one considers the case with t equal to 90, the curve would be for a rectangular shape. The $K(\infty)$ can then be read from the graph or calculated using Eq. (3.18).

$$K(\infty) = (0.6796 + 1.2197 \cdot \alpha_c + 3.3089 \cdot \alpha_c^2 - 9.5921 \cdot \alpha_c^3 + 8.9089 \cdot \alpha_c^4 - 2.9959 \cdot \alpha_c^5) \quad (3.18)$$

In addition, it also shows the dependence of $K(\infty)$ upon aspect ratio for rectangular channels. The above equation has an R^2 value of 0.9996.

3.2 Single-Phase Liquid Heat Transfer in Microchannels

The present work focuses on the flow of single-phase liquids in microchannel passages. Compressibility effects, slip boundary condition, and the rarefied flow concerns do not apply for these single-phase liquid flows in microchannels. For the present work, it will be assumed that the continuum assumption is valid for microchannels larger than 1.0 μm in hydraulic diameter.

The starting point for this discussion is the basic convective heat transfer equation shown in Eq. (3.19).

$$q = \bar{h} A_{ht} (T_s - T_m) \quad (3.19)$$

where q is the heat transfer rate, \bar{h} is the average heat transfer coefficient, A_{ht} is the heat transfer area, T_s is the surface temperature, and T_m is the mean temperature. This equation can be rewritten in terms of the local parameters to give the local heat transfer coefficients. The heat transfer rate can be more accurately described using a log mean temperature difference, as is used in conventional heat exchangers, Eq. (3.20).

$$q = \bar{h} A_{ht} \Delta T_{LMTD} \quad (3.20)$$

where ΔT_{LMTD} is the log mean temperature difference given by Eq. (3.21).

$$\Delta T_{LMTD} = \frac{(T_s - T_i) - (T_s - T_o)}{\ln\left(\frac{T_s - T_i}{T_s - T_o}\right)} \quad (3.21)$$

where T_s is the surface temperature, T_i is the inlet fluid temperature, and T_o is the outlet fluid temperature.

3.2.1 Boundary Conditions

The boundary conditions used in heat transfer analysis are crucial to the solution of the problem. The boundary conditions will cause the solution of the temperature profiles and heat transfer coefficients to take on a specific form. This is no different in the microchannel regime.

For the present work, three boundary conditions will be used, as defined in Kakaç et al. (1987). The constant temperature boundary condition, T, is defined as the wall having a constant temperature that is both circumferentially and axially uniform and constant. There are two constant heat flux boundary conditions used here. First, the H1 boundary condition is defined as having a circumferentially constant heat flux, constant wall temperature, and a axially constant heat flux. Secondly, the H2 boundary condition is defined as having a circumferentially and axially uniform heat flux.

All three boundary conditions may have application in microchannels. If one is modeling a microprocessor, the H1 boundary condition would allow for local “hot spots” where the local heat flux is higher than the mean. Finally, the T boundary condition could be applicable to a micro-total analysis system, where the wall temperature is desired to be at a constant temperature

to aid in a chemical reaction. However, the H2 boundary condition is more common across a wide variety of test sections and will be the primary focus here.

Furthermore, the location of the boundary conditions is a major complication in microchannel heat transfer. A four side heated passage is the most common assumption when deriving correlations. However, this case is not that common in practical microchannels. The microchannels usually are only heated from three sides with an adiabatic top. This leads to some difficulty in comparing results from many researchers and predicted results.

3.2.2 Temperature Dependent Properties

The mean temperature of the fluid will be utilized to calculate properties. This temperature is also referred to as the bulk temperature or the mixing cup temperature and is given in Eq. (3.22).

$$T_m = \frac{1}{A_c \bar{V}} \int_{A_c} V T dA_c = \frac{T_o + T_i}{2} \quad (3.22)$$

where T_m is the mean temperature, \bar{V} is the mean velocity, and T_i and T_o are the inlet and outlet fluid temperatures, respectively. Using this parameter to calculate fluid properties is more accurate than using the inlet temperature alone.

In addition to simply measuring the temperatures of desired quantities, the property used to calculate the parameters are temperature dependent. There are sometimes large temperature gradients in the flow and this can greatly affect the fluid properties. A property correction method shown in Eq. (3.36), Kakaç et al. (1987), will correct the Nusselt number for the

variations in fluid viscosity. The viscosity property has a much greater dependency upon temperature than the other properties.

$$\frac{Nu}{Nu_{cp}} = \left(\frac{\mu_b}{\mu_w} \right)^n \quad (3.23)$$

where Nu_{cp} is the constant property Nusselt number, Nu is the property corrected Nusselt number, μ_b is the viscosity of the fluid calculated at the bulk fluid temperature, μ_w is the viscosity of the fluid calculated at the wall temperature, and $n = 0.14$ for laminar heating in a fully developed, circular duct.

3.2.3 Temperature Measurements in Microchannels

The fluid properties depend upon properly measuring temperatures of the inlet and outlet of the fluid, the heater, and the surface. This can become quite difficult for a microchannel heat exchanger. One method is to measure the inlet and outlet fluid temperatures. A complication here is that traditional thermocouples can be large by comparison and must be placed a certain distance from the actual inlet and outlet of the microchannel.

Micro-thermocouples are very small in physical size and can be integrated into the inlet and outlet plenums. Figure 3.4 shows two very small thermocouples embedded in the plenums. The sensing bead on the thermocouple can be the approximate size of the microchannel however. This would be more appropriate for a multiple pass manifold versus a single channel. In addition, extreme care must be taken to ensure that the bead does not interfere with the flow distribution in the manifold.

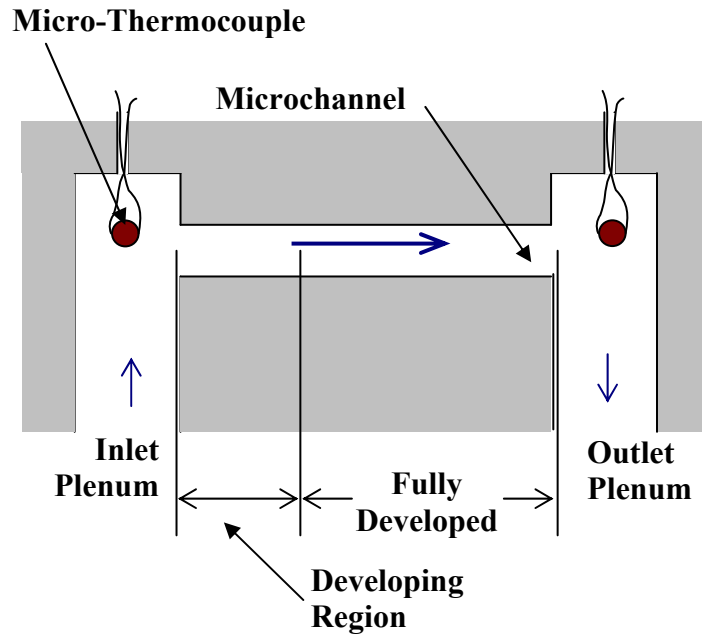


Figure 3.4: Micro-thermocouples Embedded in the Inlet and Outlet Plenums to Microchannel.

Another method for temperature measurement is to incorporate thermocouples into the test section or microchannel heat exchangers. Several researchers have been exploring this possibility. Typically, these test sections utilize silicon microchannels and take advantage of the microelectronics industry to fabricate on board temperature sensing devices. One device is simply a p-n junction. The voltage across the p-n junction is a function of the temperature.

Another method is to use a metal or a metal oxide and rely on the thermal coefficient of resistance. For this device, the resistance of the metal is a function of temperature. This is a well known and often used property. The present work utilizes very thin resistors intertwined within a heater on the backside of the test section. Further details are provided in the chapter discussing the test section.

3.2.4 Fully Developed Laminar Flow

This flow case is usually the beginning point for most analysis. It is the simplest of all flow cases. The major commonly accepted result for this flow case is that the Nusselt number is constant in the laminar region and a function of Reynolds number in the turbulent region.

The Nusselt number is constant in this flow case. The values for a circular tube are; 3.66 for T and 4.36 for H2. The Nusselt number for a rectangular channel has a dependency upon channel aspect ratio. Shah and London (1978) presented data for that dependency. Figure 3.5 shows the fully developed Nu for the three boundary conditions with four side heating.

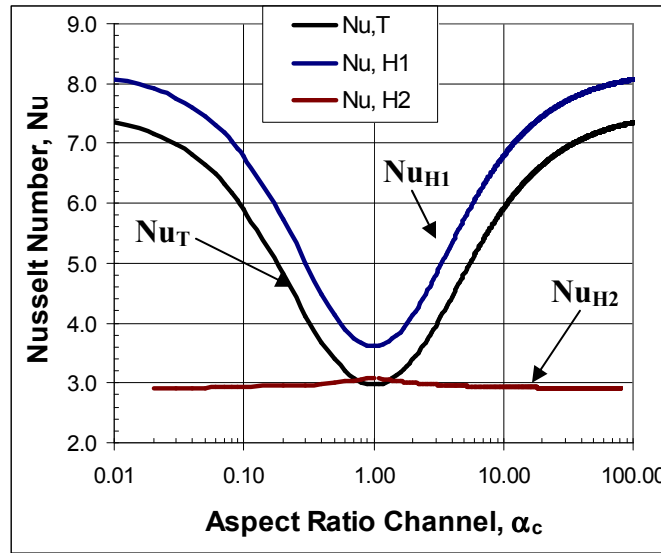


Figure 3.5: Fully Developed Nusselt Number versus Channel Aspect Ratio for Four Side Heating.

Equation (3.24, 3.25, 3.26) shows the Nusselt number for T, H1, and H2, respectively.

$$Nu_T = 7.541(1 - 2.610\alpha_c + 4.970\alpha_c^2 - 5.119\alpha_c^3 + 2.702\alpha_c^4 - 0.548\alpha_c^5) \quad (3.24)$$

$$Nu_{H1} = 8.235(1 - 2.0421\alpha_c + 3.0853\alpha_c^2 - 2.4765\alpha_c^3 + 1.0578\alpha_c^4 - 0.1861\alpha_c^5) \quad (3.25)$$

$$Nu_{H_2} = 8.235(1 - 10.6044\alpha_c + 61.1755\alpha_c^2 - 155.1803\alpha_c^3 + 176.9203\alpha_c^4 - 72.9236\alpha_c^5) \quad (3.26)$$

If the channel aspect ratio is greater than 1.0, then the reciprocal of the channel aspect ratio is used in the above equations. Remember that the above equations are for fully developed, laminar flow with four side heating. Figure 3.6, from Kakaç et al. (1987), shows the fully developed Nu for several different heating arrangements for a T boundary condition.

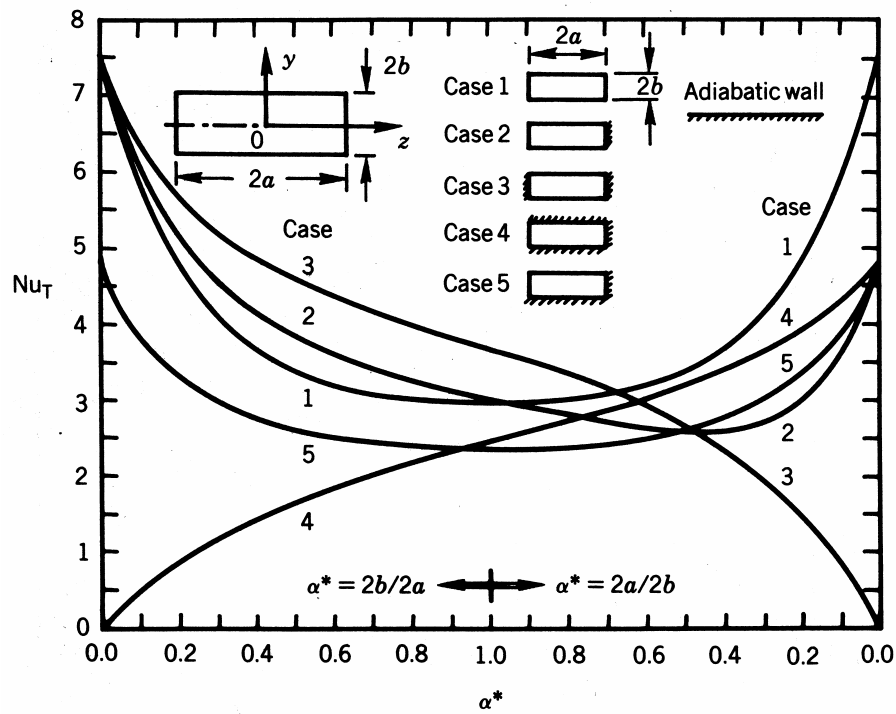


Figure 3.6: Nusselt number versus Channel Aspect Ratio. For T boundary condition, Kakaç et al. (1987).

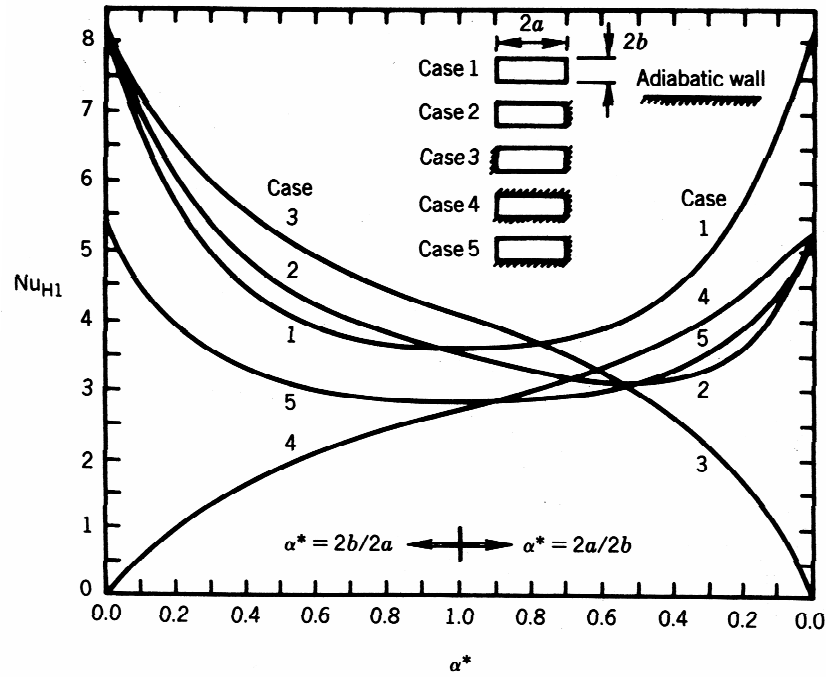


Figure 3.7: Nusselt number versus Channel Aspect Ratio. For H1 boundary condition, Kakaç et al. (1987).

Figure 3.7, from Kakaç et al. (1987), shows the fully developed Nu for several different heating arrangements for a H1 boundary condition.

3.2.5 Fully Developed Turbulent Flow

There are several correlations available for heat transfer in the turbulent flow regime. One of the first correlations began with Reynolds (1874), Eq. (3.40).

$$Nu = \left(\frac{f}{2} \right) Re Pr \quad (3.27)$$

for $Pr = 1.0$, $Re > 2,300$. Dittus and Boelter (1930) presented a correlation with two different exponents for heating and cooling, Eq. (3.28).

$$Nu = 0.023 Re^{4/5} Pr^n \quad (3.28)$$

where n is 0.4 for heating and 0.3 for cooling, for $0.7 \leq Pr \leq 120$ and $2,500 \leq Re \leq 1.24 \times 10^6$.

Petukhov and Popov (1963) presented a correlation, Eq. (3.29), that has a dependency upon friction factor as well.

$$Nu = \frac{\left(\frac{f}{2}\right) Re Pr}{1.07 + \frac{900}{Re} - \left[\frac{0.63}{(1+10 Pr)}\right] + 12.7 \left(\frac{f}{2}\right)^{1/2} \left(Pr^{2/3} - 1\right)} \quad (3.29)$$

where f is given by Filonenko (1954), Eq. (3.30), for $0.5 \leq Pr \leq 10^6$ and $4,000 \leq Re \leq 5 \times 10^6$.

$$\frac{1}{\sqrt{f}} = 1.58 \ln(Re) - 3.28 \quad (3.30)$$

The Petukhov and Popov (1963) equation can be quite complex. Gnielinski (1976) used a simplified version of Eq. (3.42) and extended the Reynolds number range to the critical Reynolds number of 2,300, seen in Eq. (3.31).

$$Nu = \frac{\left(\frac{f}{2}\right) (Re - 1,000) Pr}{1 + 12.7 \left(\frac{f}{2}\right)^{1/2} \left(Pr^{2/3} - 1\right)} \quad (3.31)$$

where f is still given by Eq. (3.30), for $0.5 \leq Pr \leq 10^6$ and $2,300 \leq Re \leq 5 \times 10^6$.

The previous equations are among the most commonly accepted correlations for turbulent Nusselt number. There are many other correlations that other researchers have presented. Sobhan and Garimella (2001) presented an excellent summation of the Nusselt number correlations in literature until that point. More or less, the other correlations take on the general

forms of the ones presented here. It is interesting to note that the correlations are irrespective of the boundary conditions. Therefore, they are valid for any of the boundary conditions discussed here. In addition, the vast majority of correlations have been developed using circular passages. It would be important to investigate their application to non-circular passages.

3.2.6 Thermally Developing Flow

In this flow regime, the flow is considered to be hydrodynamically fully developed and thermally developing. A flow can be considered thermally fully developed when the local Nusselt number reaches 1.05 times the fully developed Nusselt number. The non-dimensional, thermal axial flow length is given in Eq. (3.32).

$$x^* = \frac{x}{D_h \cdot \text{Re} \cdot \text{Pr}} \quad (3.32)$$

where x^* is the non-dimensional, thermal axial flow location. As in x^+ , the flow is fully developed when x^* is 0.05.

3.2.7 Simultaneously Developing Flow

This is the most complex flow case. The flow is simultaneously developing hydrodynamically and thermally. The Nusselt number is dependent upon the hydrodynamic and thermal axial locations. In addition, the Prandtl number influences the value of Nusselt number as well. It is very difficult to arrive at a general equation for this case, due to the dependency upon Re , Nu , x^+ , x^* , and Pr . Much more data is need for this flow regime.

CHAPTER 4

UNCERTAINTY ANALYSIS

The analysis of experimental uncertainties is critical to any work that contains experimental data. Unfortunately, many researchers take a simplistic approach or ignore it completely. In a microchannel flow, these uncertainties can become quite large given the small magnitudes of measurements. As seen in Chapter 2, the experimental uncertainty can be a contributing factor or the reason for discrepancies from conventional theories. As the Reynolds number is decreased, the observed fluctuations increase and could suggest an increase in experimental uncertainty. However, a number of authors listed in Tables 2.1 and 2.2 did not address the uncertainty in such detail.

Therefore, the experimental uncertainty will be carefully analyzed in the present work. However, there are several complications in a microsystem that cause some difficulty. First, the propagation of errors in the system can become troublesome. Second, the physical size of the system being measured is a complication. It is very difficult to fabricate a thermocouple small enough to have any significant size resolution. Finally, the magnitudes of some of the measurements are very small in value and can be problematic. The heat transfer in microchannels is very efficient. Therefore, the changes in temperature or the temperature difference can be very small. The ΔT can be on the order of unity or a few degrees. A typical experimental uncertainty value for temperature is ± 0.5 °C on a two point calibration. An experimental uncertainty of ± 0.04 °C can be achieved, with very careful control and a multipoint calibration scheme. Unfortunately, this is still a $\pm 20\%$ uncertainty with a 1 °C temperature difference.

Several researchers have begun to address this issue. Judy et al. (2002) demonstrated that with some assumptions about the flow and flow regime, the uncertainty is dominated by four times the hydraulic diameter, compared to other measurements. There are others that have drawn similar conclusions. However, they are still using calculated parameters such as velocity and hydraulic diameter in those results. It would be much more beneficial to gain understanding into how actual measured parameters such as volumetric flow rate and microchannel geometries affect the experimental uncertainties. Therefore, the following sections will present, for the first time, the experimental uncertainties for several key calculated parameters in terms of the actual measured parameters shown in Table 4.1.

Table 4.1. Measured Parameters.

Parameter	Symbol	Units
microchannel width	a	m
microchannel depth	b	m
microchannel fin thickness	s	m
microchannel length	L	m
flow length	x	m
volumetric flow rate	Q	$\text{m}^3 \text{s}^{-1}$
viscosity	μ	N s m^{-2}
density	ρ	kg m^{-3}
thermal conductivity	k	$\text{W m}^{-1} \text{K}^{-1}$
pressure drop	Δp	Pa
temperature	T	$^{\circ}\text{C}$
Prandtl number	Pr	-
pressure loss factor	K	-
voltage	V	V
current	I	A
fin efficiency	η	-

4.1 Methodology

Fortunately, several of the standards for experimental uncertainties still apply for a microsystem. The two best standards for determining experimental uncertainties are ASME PTC 19.1 (1998) and NIST Technical Note 1297 (1994). However, there are many similarities between these standards. The primary standard discussed here will be the ASME standard. In general, the total uncertainty is comprised of two parts; systematic error and random error as given by:

$$U = 2\sqrt{\left(\frac{B}{2}\right)^2 + \left(\frac{\sigma}{\sqrt{N}}\right)^2} \quad (4.1)$$

where U is the total uncertainty, B is the systematic error, σ is the standard deviation, N is the total number of samples. The bias error is a measure of the systematic error and the precision error is a measure of the random errors in the system.

There are several rules to follow when propagating errors from measured variable to calculated values. In general, Eq. (4.2) gives the uncertainty of a calculated parameter.

$$U_p = \sqrt{\sum_{i=1}^n \left(\frac{\partial p}{\partial a_i} u_{ai}\right)^2} \quad (4.2)$$

where U_p is the uncertainty in the calculated parameter p , u_{ai} is the uncertainty of measured parameter a_i . The uncertainty in any parameter is the sum of the uncertainties of the components used to calculate that parameter. The method of partial sums will be used to propagate the experimental uncertainties into calculated parameters. In general, the addition of all of the parametric partials will give the uncertainty of the calculated parameter. A listing of the most commonly used propagation laws is given in Appendix 13.4.

4.2 Geometric Parameters

There are several key geometry parameters to consider with microchannels. This is the most simplistic set of parameters and a good way to start. A primary calculated parameter is the hydraulic diameter. Equation 4.3 shows the hydraulic diameter formula for a rectangular microchannel of width a and depth b used to calculate the uncertainty. Equation 4.4 shows the hydraulic diameter uncertainty.

$$D_h = \frac{4 a b}{2 (a + b)} \quad (4.3)$$

$$\frac{U_{D_h}}{D_h} = \left[\left(\frac{U_a}{a} \right)^2 + \left(\frac{U_b}{b} \right)^2 + \left(\frac{U_a}{a+b} \right)^2 + \left(\frac{U_b}{a+b} \right)^2 \right]^{1/2} \quad (4.4)$$

The hydraulic diameter is only dependent upon the microchannel geometries. There are 4 terms in the uncertainty expression. However, the microchannel width and height appear twice. The microchannel aspect ratio formulas are shown in Eq. (4.5, 4.7, and 4.9) and the uncertainty in the microchannel aspect ratios are shown in Eqs. (4.6, 4.8, 4.10).

$$\alpha_c = \frac{a}{b} \quad (4.5)$$

$$\frac{U_{\alpha_c}}{\alpha_c} = \left[\left(\frac{U_a}{a} \right)^2 + \left(\frac{U_b}{b} \right)^2 \right]^{1/2} \quad (4.6)$$

$$\alpha_f = \frac{s}{b} \quad (4.7)$$

$$\frac{U_{\alpha_f}}{\alpha_f} = \left[\left(\frac{U_s}{s} \right)^2 + \left(\frac{U_b}{b} \right)^2 \right]^{1/2} \quad (4.8)$$

$$\beta = \frac{\alpha_f}{\alpha_c} = \frac{s}{a} \quad (4.9)$$

$$\frac{U_\beta}{\beta} = \left[\left(\frac{U_s}{s} \right)^2 + \left(\frac{U_a}{a} \right)^2 \right]^{1/2} \quad (4.10)$$

As expected, the microchannel measurements affect the uncertainty in a predicted manner. There is only a single dependence upon each of the measured parameters in these formulations.

4.3 Fluid Flow Parameters

There are several key uncertainties when it comes to the fluid flow parameters. The first parameter is the Reynolds number shown in Eq. (4.11). The uncertainty in the Reynolds number is seen in Eq. (4.12).

$$\text{Re} = \frac{\rho Q D_h}{\mu A_c} \quad (4.11)$$

$$\frac{U_{\text{Re}}}{\text{Re}} = \left[\left(\frac{U_\rho}{\rho} \right)^2 + \left(\frac{U_\mu}{\mu} \right)^2 + \left(\frac{U_Q}{Q} \right)^2 + 2 \cdot \left(\frac{U_a}{a} \right)^2 \right. \\ \left. + 2 \cdot \left(\frac{U_b}{b} \right)^2 + \left(\frac{U_a}{a+b} \right)^2 + \left(\frac{U_b}{a+b} \right)^2 \right]^{1/2} \quad (4.12)$$

The geometric parameters are present along with the volumetric flow rate and the fluid properties. However, the microchannel geometry parameters have 3 times more importance in the total uncertainty than any other parameter.

The friction factor is another important parameter for fluid flow. For the present work, the Fanning formulation of the friction factor will be used, Eq (4.13). The uncertainty for the Fanning friction factor is shown in Eq. (4.14).

$$f = \frac{\Delta p D_h A_c^2}{2 \rho L Q^2} \quad (4.13)$$

$$\frac{U_f}{f} = \left[\left(\frac{U_\rho}{\rho} \right)^2 + \left(\frac{U_{\Delta p}}{\Delta p} \right)^2 + \left(\frac{U_L}{L} \right)^2 + 2 \cdot \left(\frac{U_Q}{Q} \right)^2 + 3 \cdot \left(\frac{U_a}{a} \right)^2 \right. \\ \left. + 3 \cdot \left(\frac{U_b}{b} \right)^2 + \left(\frac{U_a}{a+b} \right)^2 + \left(\frac{U_b}{a+b} \right)^2 \right]^{1/2} \quad (4.14)$$

Finally, one of the most important calculated parameters is the Poiseuille number or the fRe number, Eq. (4.15). The uncertainty for this parameter is seen in Eq. (4.16).

$$f Re = \frac{\Delta p D_h A_c^2 Re}{2 \rho L Q^2} \quad (4.15)$$

$$\frac{U_{f Re}}{f Re} = \left[2 \cdot \left(\frac{U_\rho}{\rho} \right)^2 + \left(\frac{U_\mu}{\mu} \right)^2 + \left(\frac{U_{\Delta p}}{\Delta p} \right)^2 + \left(\frac{U_L}{L} \right)^2 + 3 \cdot \left(\frac{U_Q}{Q} \right)^2 + \right. \\ \left. 5 \cdot \left(\frac{U_a}{a} \right)^2 + 5 \cdot \left(\frac{U_b}{b} \right)^2 + 2 \cdot \left(\frac{U_a}{a+b} \right)^2 + 2 \cdot \left(\frac{U_b}{a+b} \right)^2 \right]^{1/2} \quad (4.16)$$

Something very interesting emerges from this result. The fRe number was thought to be dominated by the measured pressure drop. As a result, many researchers take great pains in determining very, very accurate pressure drop measurements. Carefully reviewing the experimental uncertainty reveals that the uncertainty in the Poiseuille number is greatly dominated by the microchannel geometries. The microchannel width and height have 7 times more importance than the pressure drop. Even the volumetric flow rate has 3 times the importance of pressure drop. Therefore, greater detail and accuracy should be used when determining the microchannel geometry. A clear picture of the channel geometry is more important than an extremely accurate pressure drop measurement.

4.4 Heat Transfer Parameters

The calculated heat transfer parameters in heat transfer are well established. However, they tend to be more complex than the fluid flow parameters. There are several methods for determining heat transfer performance. The method of comparison is also greatly dependent upon the type of boundary conditions used in the experiment. As a result, it is very difficult to cover every possibility. So, a general form of some parameters will be presented followed by some parameter formulations that are specific to the present work.

The general form of the average heat transfer coefficient is given in Eq. (4.17). This is a general form of the convective heat transfer equation. The resulting uncertainty of the average heat transfer coefficient is given by Eq. (4.18).

$$q = \bar{h} A_{HT} \Delta T \quad (4.17)$$

$$\frac{U_{\bar{h}}}{\bar{h}} = \left[\left(\frac{U_q}{q} \right)^2 + \left(\frac{U_{A_{HT}}}{A_{HT}} \right)^2 + \left(\frac{U_{\Delta T}}{\Delta T} \right)^2 \right]^{1/2} \quad (4.18)$$

The heat transfer area can be written in terms of the measured geometric parameters and the ΔT term is dependent of the form of the ΔT chosen. Assume that the heat transfer rate is given by a resistance heat using the voltage and current. The general from of the average Nusselt number is given by Eq. (4.19) and the uncertainty is given in Eq. (4.20).

$$\bar{Nu} = \frac{\bar{h} D_h}{k_f} \quad (4.19)$$

$$\frac{U_{\bar{Nu}}}{\bar{Nu}} = \left[\left(\frac{U_k}{k_f} \right)^2 + \left(\frac{U_a}{a} \right)^2 + \left(\frac{U_b}{b} \right)^2 + \left(\frac{U_a}{a+b} \right)^2 + \left(\frac{U_b}{a+b} \right)^2 + \left(\frac{U_{\bar{h}}}{\bar{h}} \right)^2 \right]^{1/2} \quad (4.20)$$

Finally, the general form of the Colburn j factor is given in Eq. (4.21) and the uncertainty in Eq. (4.22).

$$j = \frac{Nu \ Pr^{1/3}}{Re} \quad (4.21)$$

$$\frac{U_j}{j} = \left[\left(\frac{U_\rho}{\rho} \right)^2 + \left(\frac{U_\mu}{\mu} \right)^2 + \left(\frac{U_Q}{Q} \right)^2 + 2 \cdot \left(\frac{U_a}{a} \right)^2 + 2 \cdot \left(\frac{U_b}{b} \right)^2 + \left(\frac{U_a}{a+b} \right)^2 + \left(\frac{U_b}{a+b} \right)^2 + \frac{1}{3} \cdot \left(\frac{U_{Pr}}{Pr} \right)^2 + \left(\frac{U_{Nu}}{Nu} \right)^2 \right]^{1/2} \quad (4.22)$$

After the uncertainty for the most general forms of the parameters is determined, some further assumptions can be determined based upon the measured parameters and can lead to more useful uncertainties. First, the heat transfer area that takes into account the fin efficiency can be seen in Eq. (4.23) and the uncertainty in Eq. (4.24).

$$A_{HT,\eta} = (a + 2\eta b) n L \quad (4.23)$$

$$\frac{U_{A_{HT,\eta}}}{A_{HT,\eta}} = \left[\left(\frac{U_L}{L} \right)^2 + \left(\frac{U_a}{a + 2 \cdot \eta \cdot b} \right)^2 + 2 \cdot \left(\frac{b \cdot U_\eta}{(a + 2 \cdot \eta \cdot b)} \right)^2 + 2 \cdot \left(\frac{\eta \cdot U_b}{(a + 2 \cdot \eta \cdot b)} \right)^2 \right]^{1/2} \quad (4.24)$$

The ΔT in the heat transfer coefficient can be calculated using the log mean temperature difference (LMTD). The general form of the LMTD is shown in Eq. (4.25) and the uncertainty Eq. (4.26).

$$\Delta T_{LMTD} = \frac{\Delta T_2 - \Delta T_1}{\ln\left(\frac{\Delta T_2}{\Delta T_1}\right)} \quad (4.25)$$

$$\frac{U_{\Delta T_{LMTD}}}{\Delta T_{LMTD}} = \left[\left(\frac{U_{\Delta T_2}}{\Delta T_2 - \Delta T_1} \right)^2 + \left(\frac{U_{\Delta T_1}}{\Delta T_2 - \Delta T_1} \right)^2 + \left(\frac{U_{\frac{\Delta T_2}{\Delta T_1}}}{\frac{\Delta T_2}{\Delta T_1} \cdot \ln\left(\frac{\Delta T_2}{\Delta T_1}\right)} \right)^2 \right]^{1/2} \quad (4.26)$$

It can be further assumed that the LMTD formulation can be based upon the H1 boundary condition for the present work. This would allow for the LMTD to be recast into Eq. (4.27)

$$\frac{U_{\Delta T_{LMTD}}}{\Delta T_{LMTD}} = \left[\left(\frac{U_{T_{so}-T_i}}{(T_{s,i} - T_i) - (T_{s,o} - T_o)} \right)^2 + \left(\frac{U_{T_{si}-T_o}}{(T_{s,i} - T_i) - (T_{s,o} - T_o)} \right)^2 \right]^{1/2} + \left(\frac{U_{\frac{T_{si}-T_i}{T_{so}-T_o}}}{\frac{(T_{s,i} - T_i)}{(T_{s,o} - T_o)} \cdot \ln\left(\frac{(T_{s,i} - T_i)}{(T_{s,o} - T_o)}\right)} \right)^2 \quad (4.27)$$

Finally, all of the previous results can be utilized to determine the uncertainty for an average Nusselt number with the assumptions of laminar, H1 boundary condition (constant heat flux), average heat transfer coefficient, LMTD, and including fin efficiency, Eq. (4.28).

$$\frac{U_{\bar{Nu}}}{\bar{Nu}} = \left[\begin{aligned} & \left(\frac{U_k}{k_f} \right)^2 + \left(\frac{U_a}{a} \right)^2 + \left(\frac{U_b}{b} \right)^2 + \left(\frac{U_a}{a+b} \right)^2 + \left(\frac{U_b}{a+b} \right)^2 \\ & + \left(\frac{U_V}{V} \right)^2 + \left(\frac{U_I}{I} \right)^2 + \left(\frac{U_L}{L} \right)^2 + \left(\frac{U_a}{a+2 \cdot \eta \cdot b} \right)^2 \\ & + 2 \cdot \left(\frac{b \cdot U_\eta}{(a+2 \cdot \eta \cdot b)} \right)^2 + 2 \cdot \left(\frac{\eta \cdot U_b}{(a+2 \cdot \eta \cdot b)} \right)^2 \\ & + \left(\frac{U_{T_{s,o}-T_o}}{(T_{s,i}-T_i)-(T_{s,o}-T_o)} \right)^2 + \left(\frac{U_{T_{s,i}-T_i}}{(T_{s,i}-T_i)-(T_{s,o}-T_o)} \right)^2 \\ & + \left(\frac{U_{\frac{T_{s,i}-T_i}{T_{s,o}-T_o}}}{\left(\frac{T_{s,i}-T_i}{T_{s,o}-T_o} \right) \cdot \ln \left(\frac{T_{s,i}-T_i}{T_{s,o}-T_o} \right)} \right)^2 \end{aligned} \right]^{1/2} \quad (4.28)$$

The resulting equation has quite a complex form. However, it now demonstrates the dependency of the Nusselt number uncertainty upon measured parameters. The most dominant parameter is the temperature difference. In addition, the microchannel width occurs 3 times and the microchannel height occurs 4 times.

4.5 Summary

The experimental uncertainties of important calculated parameters have been determined. A surprising result has been discovered. The microchannel geometries have a much more significant influence on the Poiseuille number than was previously thought. The microchannel

geometries also have a propionate effect upon the Nusselt number as well. This makes the case for extra care in determining the microchannel geometry for experimental works.

A figure has been generated in order to highlight the dependency of measured parameters. Figure 4.1 shows that dependency. The number of occurrences of the measured parameter in an uncertainty equation is given on the x axis. The measured parameters are given on the x axis and the calculated parameters are shown in the legend. The most important parameter overall is the microchannel geometry measurements. The surface temperature measurements are the second most important parameter. It is concluded that when conducting experiments, there needs to be much more accurate measurements of the microchannel geometry and surface temperature measurements.

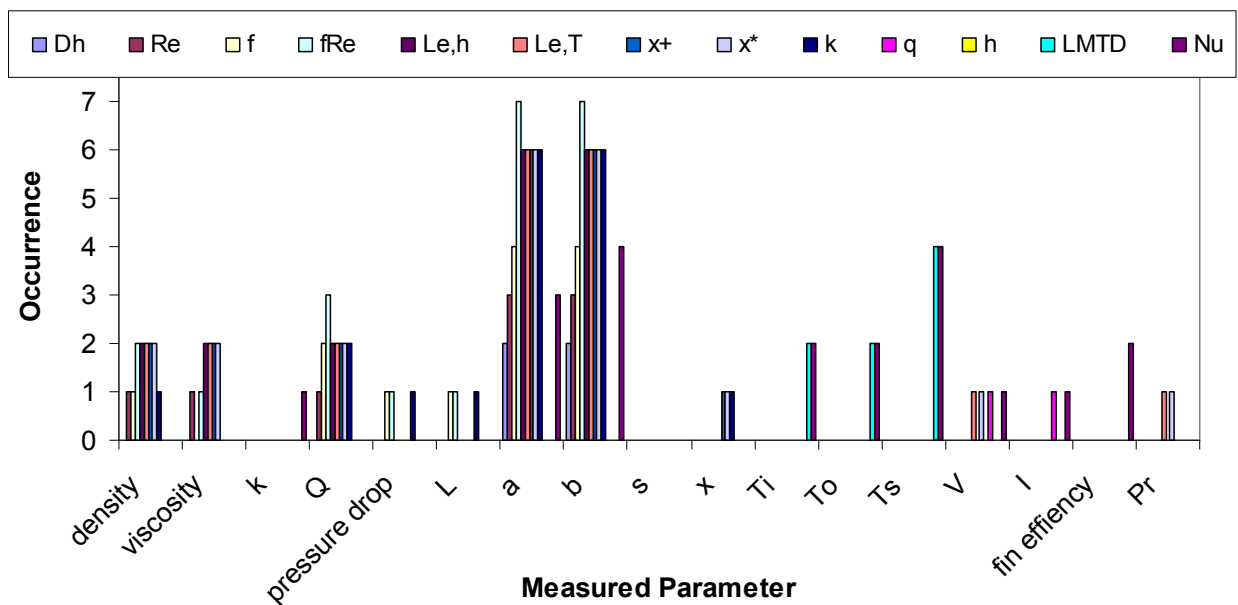


Figure 4.1: Dependency of Uncertainty for Calculated Parameter Based Upon Measured Parameters.

Furthermore, many researchers have presented the uncertainties at a mean parameter range and assumed that that is characteristic of the entire range of parameters. This practice should no longer be utilized. For example, Bucci et al. (2003) performed experiments with water

in circular tubes reported experimental uncertainty for the Nusselt number is 22% at a mean value and applied that to the entire data set as seen in Fig. 4.2.

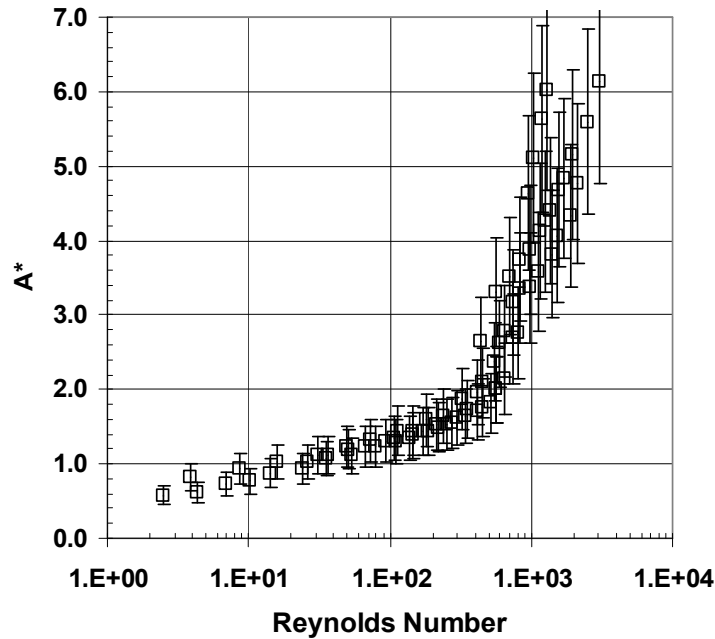


Figure 4.2: Experimental Uncertainties Using a Mean Value Calculation. A^* versus Reynolds Number for Bucci et al. (2003) Including Reported Uncertainties.

As seen in here the experimental uncertainties can change greatly for different Reynolds number ranges. The uncertainty increases with an increase in Reynolds number. This is actually opposite of what happens in an experimental system. As a result, the uncertainty will change for each individual data point and a mean value will lead to false representation. Point by point uncertainty analyses where the uncertainty for each specific data point is represented is a much improved method. This is more representative of what actually occurs in an experimental system. It is recommended that the uncertainty for each individual point is represented. Further explanation and demonstration of this method will be presented later.

CHAPTER 5

EXPERIMENTAL TEST FACILITY DEVELOPMENT

A major objective of the present work is to develop an experimental facility to provide accurate data describing the fluid flow and heat transfer performance of microchannels. In this section, the components of the fluid flow circuit will be described in detail. In addition, the data acquisition (DAQ) equipment used to collect, control and process signals from the experimental system will be described. Finally, some important details of the individual components will be presented.

5.1 Fluid Flow Circuit

The experimental test facility contains all of the supporting equipment that supplies metered working fluid to the test section and the measurement of heat transfer and pressure drop. Figure 5.1 shows the design schematic for the experimental system and Fig. 5.2 shows an actual picture of the experimental facility. The main components are the test section, the DAQ, the fluid pump, the flow meter bank, and the inlet heat exchanger.

The flow loop can be operated in an open-system or a closed-system fashion. For different experiments, it might be desirable to switch between the two configurations. The system represented in Fig. 5.1 is an open flow loop. The fluid begins in a polycarbonate supply tank. Polycarbonate is chosen to minimize the different materials that come into contact with the working fluid, as polycarbonate is used in the test section as well.

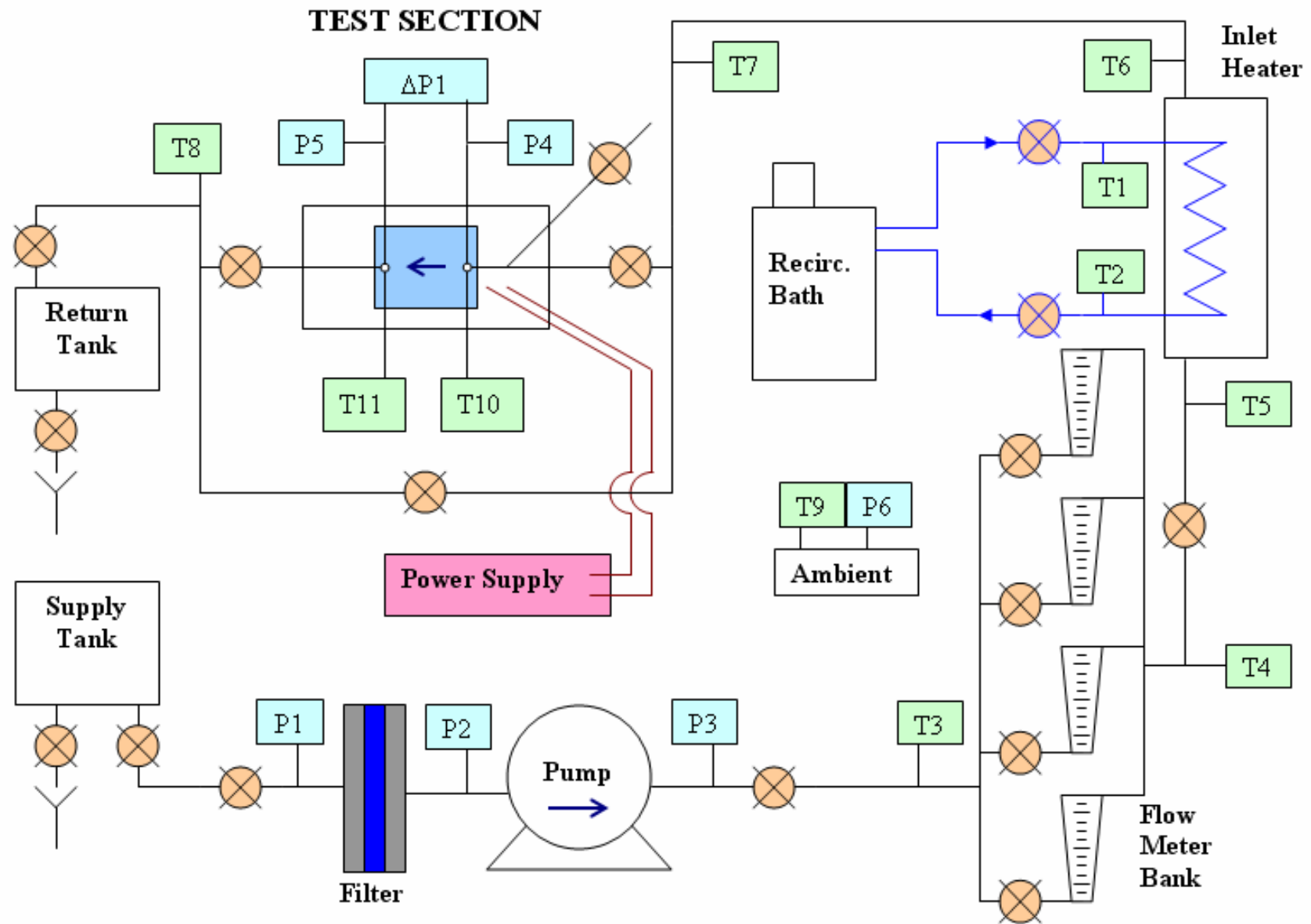


Figure 5.1: Experimental Flow Circuit.

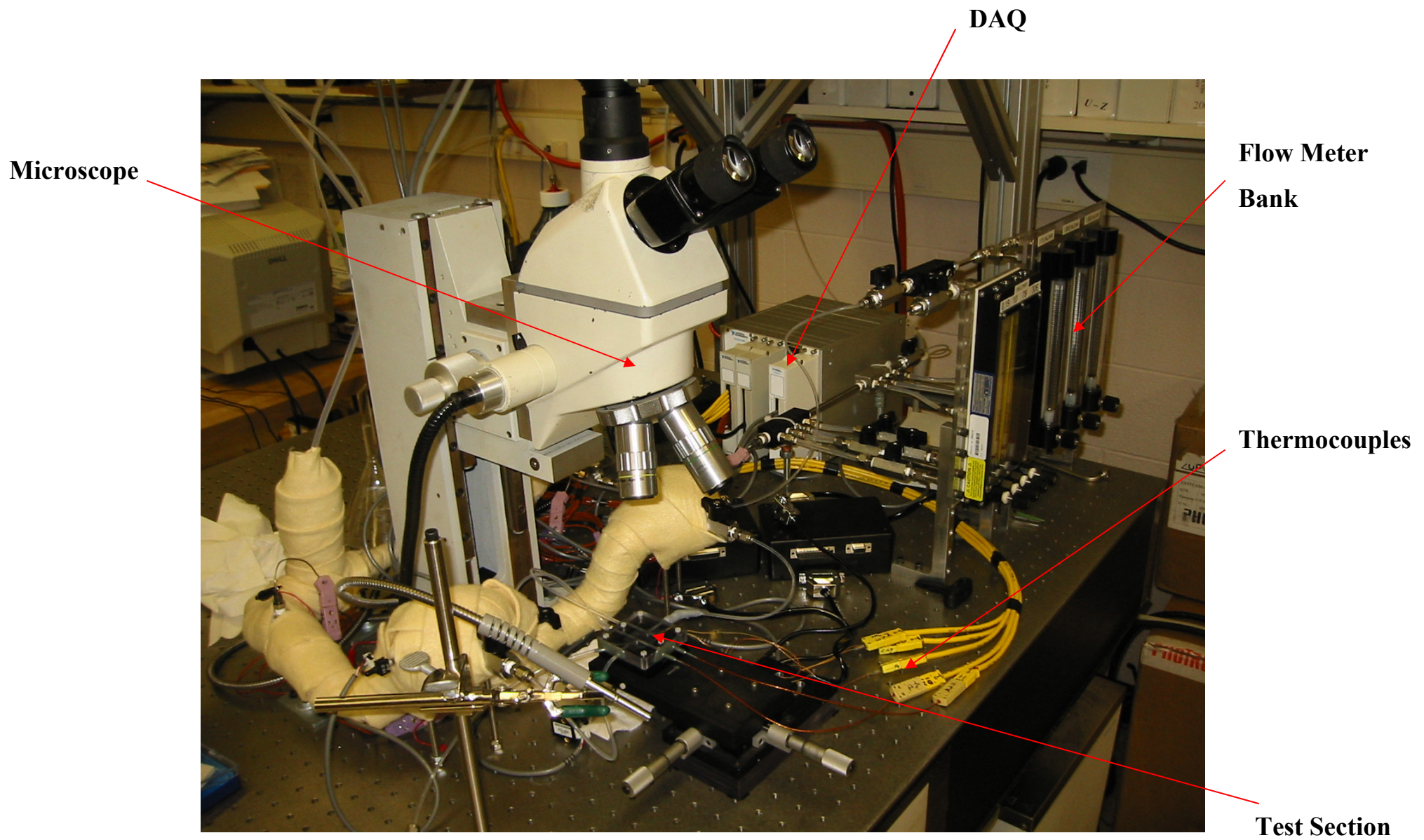


Figure 5.2: Experimental Test Facility.

A positive displacement, micro-gear pump drives the flow through the loop. The gear pump is a Micropump brand device that delivers 1 to 300 mL/min of flow at a maximum pressure of 4.8 bars. This style of pump is chosen to give a constant flow rate for the test section regardless of the pressure drop in the test section. That pressure drop could change significantly due to different microchannel geometries being tested. The micropump is chosen because of its small footprint, accurate flow rates, and ability to dispense small volumes.

Next, a membrane filter follows the pump. The filter is housed in a stainless steel casing that can maintain high pressures and temperatures. The membrane used in the filter housing is a standard 47 mm diameter replaceable filter. There are a number of filters available with diameters ranging from 0.2 μm to 25 μm . Typically, a 1.0 μm pore size is utilized in the filter for experimentation.

The flow loop continues with a flow meter bank with several flow meters in a parallel arrangement with different flow rate ranges. Each flow meter has a different range to improve the accuracy of the flow measurement. The flow meters are a rotameter style flow meter. Given the flow range of the pump, the rotameter gives reasonable accuracy at a moderate cost. When operating at low flow rates, a coriolis flow meter is utilized to improve the accuracy. The flow meters in the flow meter bank have an overall flow range of 0.01 to 4,000 mL/min. Each successive flow meter range increases by an order of magnitude from the previous one. In other words, one flow meter would have a 3 to 75 mL/min flow range and the next available flow meter would have a 30 to 300 mL/min flow range.

A miniature shell and tube heat exchanger and a recirculation bath are used to control the fluid temperature entering the test section. The tube diameters are 3 mm and the entire heat

exchanger is constructed from stainless steel. The inlet heater is designed to heat the working fluid up to 90 °C. A typical load for the heat exchanger is 100 W.

The experimental system is capable of measuring temperatures, pressures and flow rates. Resistors on the backside of the test device are used to measure the heater temperatures. The sense resistors are custom fabricated with the test device. The system thermocouples are commercially available thermocouple. They are inserted into a compression fitting to make a water proof seal. E type and K type thermocouples are chosen for their accuracy and the operating temperature of the system. Pressure is measured using a differential pressure transducer from Omega. There is more information presented in Section 5.4.7 on the thermocouples and the pressure transducers. The pressure transducer range is chosen to give the highest level of accuracy. The pressure transducers used for the experiment ranged from 0.02 to 6.8 bars. The experiments are started at the lowest flow rate and pressure drop and moved to higher flow rates and pressure drops.

Finally, the next item in the flow loop is the test section. It consists of a supporting fixture, pogo probes for the electrical connections, and a test chip. The last item in the flow loop is the polycarbonate collection tank.

Figure 5.2 shows the physical layout of the experimental test facility. However, the DAQ system and the recirculation chiller is not pictured in this figure. The test fixture is located in the bottom center, below the microscope. The yellow felt insulation is seen surrounding the inlet heat exchanger and the test fixture junctions.

5.2 Test Section

The test section subsystem is of primary importance in this fluid flow circuit. This is where the microchannels are located in the test devices. The purpose of the entire loop is to ensure that proper data collection occurs in the test section. The test section and its design of the test section will be discussed in detail in Chapter 6.

5.3 Data Acquisition

The data acquisition (DAQ) system monitors several thermocouples, pressure transducers, and sensing resistors. In addition, the DAQ controls the pump and the flow rate through the system. The DAQ is based upon the signal conditioning SCXI system from National Instruments. This system provides signal conditioning all incoming signals and gives the ability to have high channel counts.

The DAQ card is a model PCI-MIO-16XE-10 card that can sample at a rate of 10,000 samples per second. This system uses a SCXI-1000 chassis to contain the different functioning modules. The first module is a model SXCI-1100 that receives the millivolt input from the heater sensing resistors of the test section. A SXCI-1303 terminal block to facilitate the electrical connections is also employed. The other modules used in the DAQ include a SXCI-1102 design for thermocouple input and a SXCI-1520 strain gage module for excitation and signal reading for the pressure transducers.

Another DAQ card used is the PCI-6704. This card supplies constant milliamp current to the heater sensing resistors on the test chip. In addition, the card provides the drive current for

the micropump. This DAQ card uses a shielded SCB-68 accessory block for the electrical connections.

The DAQ system uses LabVIEW as the controlling software. It is a visual basic based program that allows for the monitoring, measurement, and logging of sensors as well as analog control of devices. A virtual instrument (VI) is created to interface the software and hardware. Figure 5.3 shows the VI used for the experimental test facility. It would be very difficult to represent the Visual Basic that goes into programming the VI. This is not the main focus of the present work so it has been omitted. There are several features to see in the VI. It is used to monitor the system temperatures and pressures, control the test section power supply, control the micropump and log data. It will be beneficial to break this figure into the respective parts.

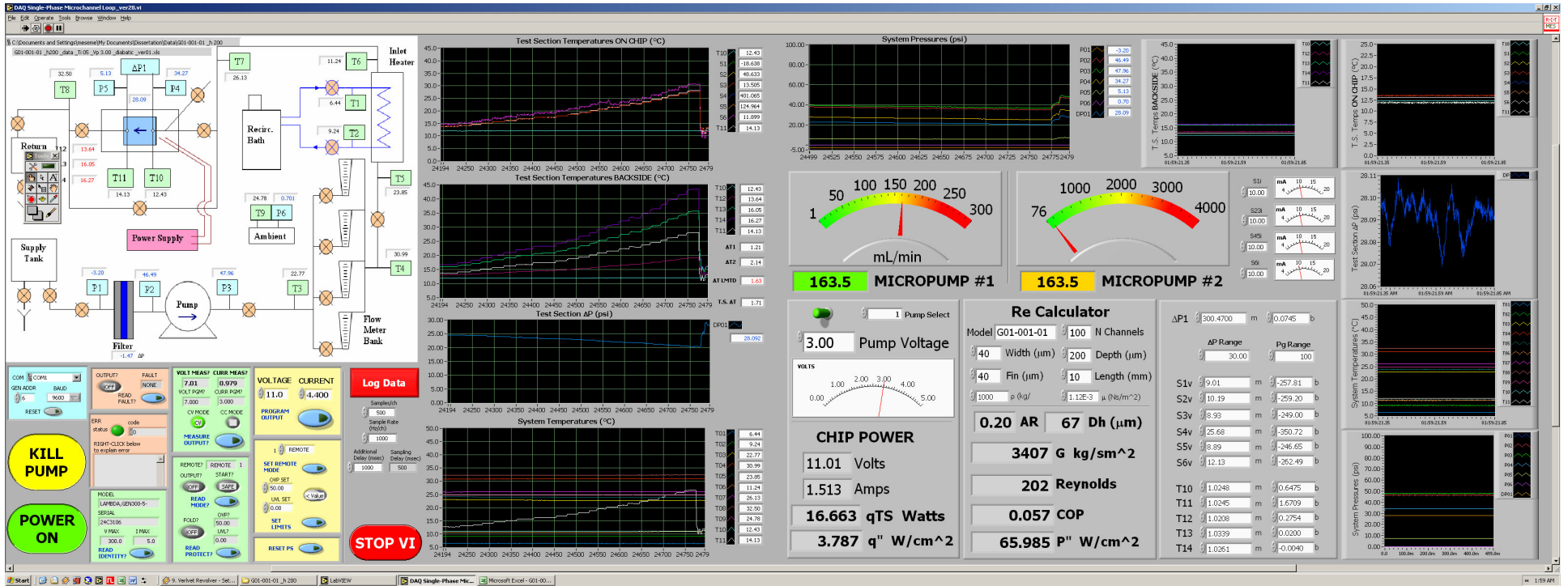


Figure 5.3: Virtual Instrument Created for Experimental Test Facility.

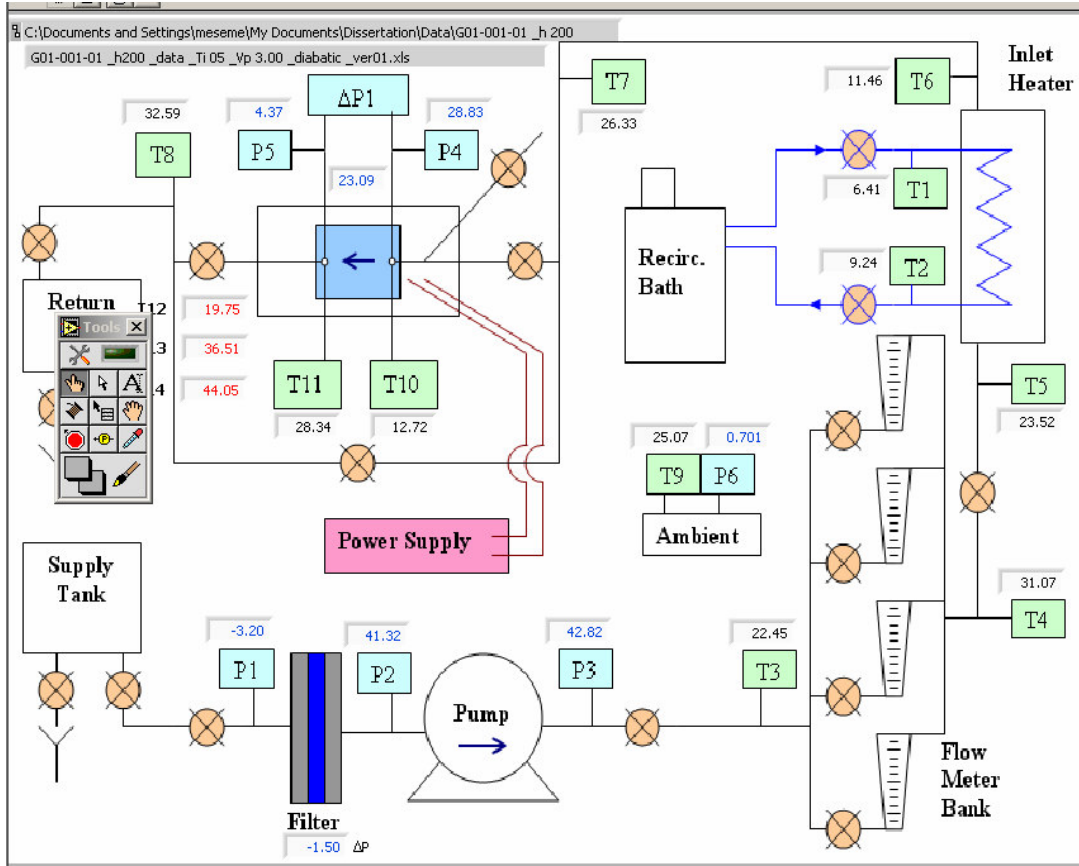


Figure 5.4: Section of the VI for Test Facility Monitoring of Temperatures and Pressures.

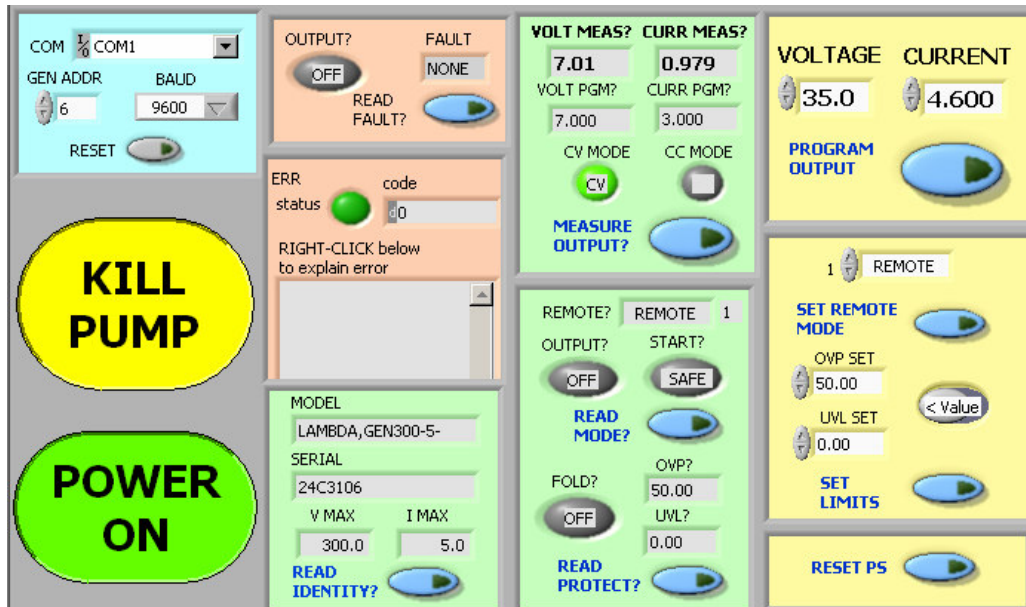


Figure 5.5: Section of the VI for Test Section Power Supply Control.

Figure 5.4 shows the portion of the VI concerned with monitoring the various temperatures and pressures in the experimental test facility. A schematic of the flow loop is represented with the individual monitors located where they occur in the flow loop. Using this section, things like monitoring the temperature of the recirculation chiller and the flow meter bank can be easily seen. In addition, the pressure drop across the filter can be monitored for increases in Δp that would indicate a need for a filter change.

Figure 5.5 shows the portion of the VI concerned with controlling the power supply for the test section. The VI communicates to the power supply by sending commands through a RS232 port and a custom sub-VI, or in other words an embedded VI. The VI can control, monitor, and report errors from the power supply. The controlling features are located in the yellow boxes. The power supply voltage and current, over voltage protection and upper voltage limit can be set. In addition, the output can be switched off or on. The monitoring or feedback features are located in the green boxes. All of the items that can be controlled can also be remotely read using these queries. Finally, the error reporting features are located in the red boxes. They will indicate if a problem has occurred in the power supply.

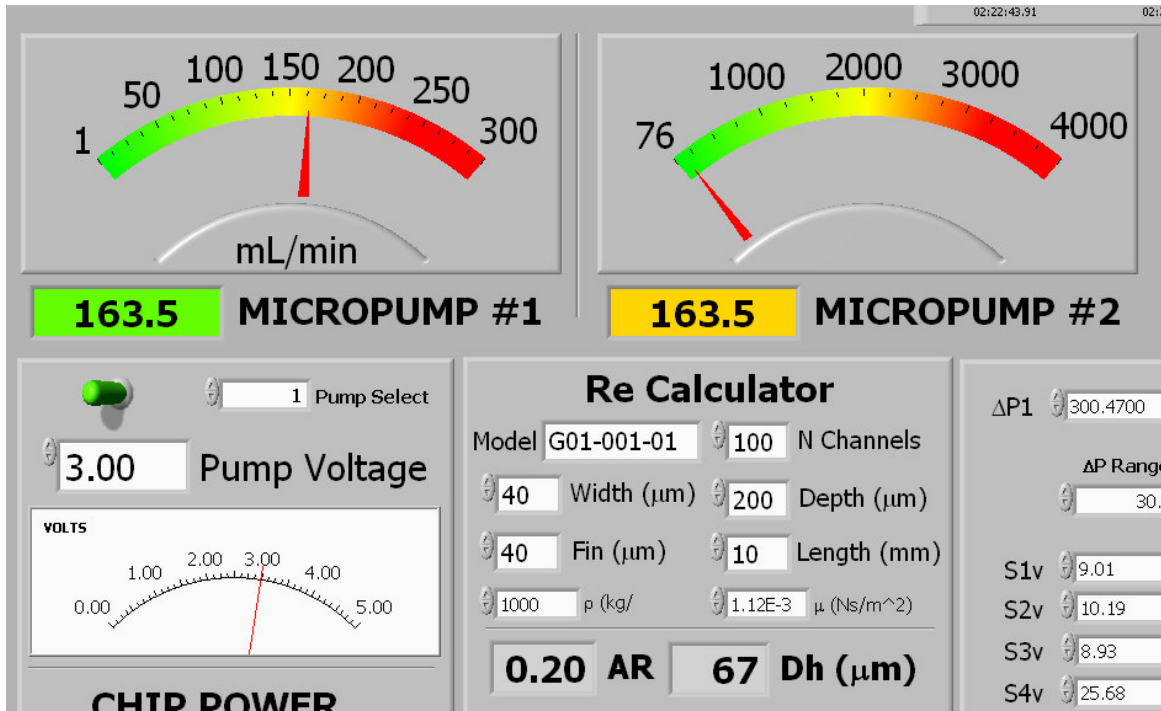
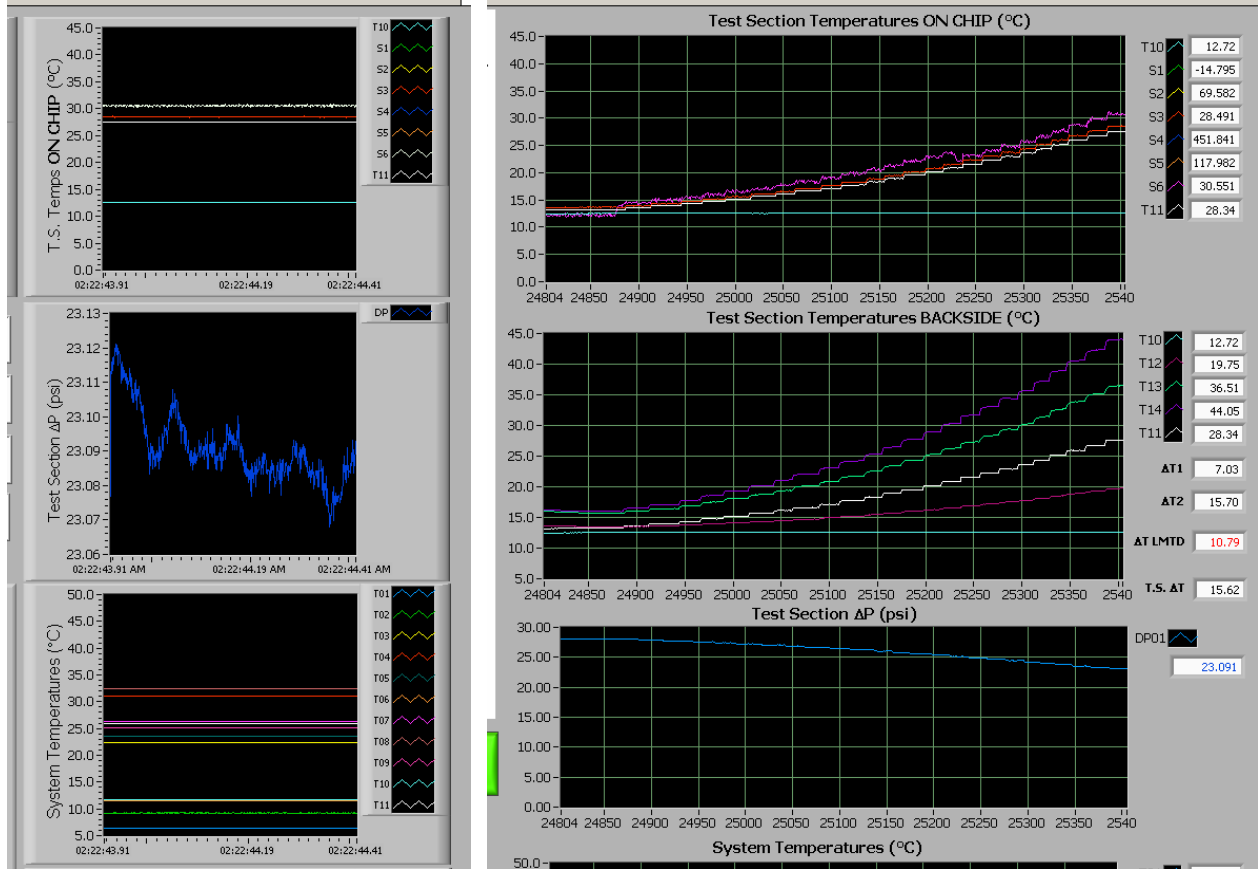


Figure 5.6: Section of the VI for Micropump Control.

Figure 5.5 shows the portion of the VI concerned with controlling micropump for flow rate control. The micropump is controlled using a 0 to 5 volt analog output channel in the SCXI system. Basically, the varying the voltage supplied the revolutions per minute of the micropump motor and thus varies the flow rate in the system. There is a low and a high flow rate pump that can be selected. In addition, the item labeled as “Re Calculator” simply takes the geometry of the test device being tested and calculates some parameters like microchannel aspect ratio and hydraulic diameter.



Waveform Data

Calibrated Data

Figure 5.7: Section of the VI for Data Logging.

Figure 5.7 shows the portion of the VI concerned with the logging of the experimental data. The raw signals from the sensors throughout the system are actually in the form of a waveform. The waveform data can be seen in the right hand side of the figure. They are meaningful for each sampling cycle. However, they do not provide history of measurement data and the raw signals are not useful when monitoring the system. Therefore, the calibration equations are used, the waveform is converted into an array, and the calibrated data is plotted to the history behavior of the system, as seen on the left side of the figure.

5.4 Experimental Component Design

In this section, the individual components that comprise the experimental system will be described in greater detail. The major components that will be described are the working fluid, the test chip, test section power supply, the test fixture, fluid pump, the filtration, flow meter bank, the inlet heat exchanger, and the instrumentation.

5.4.1 Working Fluid

The working fluid for all of the experimental investigations is water. This fluid is chosen for several reasons. When the fundamental phenomenon is poorly understood, most researchers will begin their experiments with in order to simplify the fluid interactions. The properties and behavior of water are well known and is a basic solvent for a vast majority of industrial and biological systems. Although the latter does not have direct bearing on the present work, the more fundamental information on single-phase liquid flow of water in small passages is beneficial to the research community.

The water used is de-ionized with a resistance of 18 M Ω . The water is then degassed according to the procedure described by Steinke and Kandlikar (2003). Using the procedure described in Steinke and Kandlikar (2003), the concentration of oxygen in the water is 3.2 parts per million (ppm) and is sufficient to eliminate the effect of dissolved gases. The resulting water will not experience out-gassing as long as the surface temperatures do not exceed 121 °C.

This procedure was originally developed to generate reliable flow boiling data. It prevents out-gassing than can mask sub-cooled nucleation. The primary reason for using this procedure in the present work is to remove as many variables as possible and give a good comparison with the previously published data.

5.4.2 Test Section Power Supply

The electric resistance heaters in the test device supply the power to be dissipated via the microchannels. The heaters are controlled with a dedicated power supply. It is a Genesys model 300-5 from Lambda-EMI. The power supply can operate in either a constant voltage or constant current mode. The power supply operates in a constant voltage mode for the experimental investigations reported here. The power supply has an upper limit of 300 volts and 5 amps.

5.4.3 Fluid Pump

The working fluid is driven through the system using a positive displacement gear pump. A micropump GA-V23-J9-SSG is the specific model of pump utilized. It is capable of delivering from 1 to 300 mL/min at a maximum differential pressure of 4.8 atm. It consists of two independent gears intermesh to form the pumping cavity. It produces repeatable and steady flow rates during the course of the experiments. The flow rate from the pump is controlled via a signal from the DAQ.

5.4.4 Filtration

Filtration occurs just before the inlet to the micropump. The filter membrane holder is a stainless steel housing for a membrane filter that can sustain 20 atms and 125 °C from Fisher Scientific. The model number is 09-753-13C. The 47 mm diameter membrane is used with the housing. A model R50SP04700 Magna nylon membrane filter is used with the process fluid. The filter membrane has an overall diameter of 47 mm and a pore size of 5.0 micrometers.

5.4.5 Flow Meter Bank

The flow meter bank contains four variable area flow meters encompassing different ranges. This type of flow meter is also referred to as a rotameter. The ranges of the flow meters are 0.020 to 0.194 mL/min, 0.39 to 9.96 mL/min, 5.0 to 77.8 mL/min and 8 to 306 mL/min. The four ranges are chosen to maximize the accuracy in each flow range. Each flow meter has a separate throttle control valve to provide fine adjustment and isolation of the flow entering the flow meter bank. For higher flow applications, three additional flow meters are used. One flow meter has a maximum flow rate of 515 mL/min and the other two have a maximum flow rate of 1,950 mL/min. The exit of each flow meter is tied into a common line that supplies the inlet heat exchanger.

5.4.6 Inlet Heat Exchanger

The inlet temperature of the test section is controlled using a heat exchanger. The heat exchanger is a miniature shell and tube heat exchanger model 00268-3 from Exergy. The heat exchanger is rated for 300 watts at a flow rate of 100 mL/min and is constructed of stainless steel.

On the shell side of the heat exchanger is a recirculation chiller. The chiller uses water as a working fluid and regulates the temperature of the heat exchanger thus regulating the inlet fluid temperature. It can control the heat exchanger temperature from 5 °C to 90 °C. However, the temperature of the chiller is typically at 5 or 20 °C for the experiments conducted in this work.

5.4.7 Instrumentation

The experimental system is instrumented to measure temperatures, pressures and flow rates. The flow meters were previously discussed. The system uses two different measurement techniques to monitor temperature.

Resistors on the device are used to measure temperature, since the resistance is a function of temperature. Thermocouples are also used to measure temperatures because the generated electromagnetic field is a function of temperature. The heater sensing resistors are custom fabricated with the test device. The system thermocouples are commercially available thermocouples from Omega, model HGEMQSS-062G-6. The test section thermocouples are custom made using K type wire.

Pressure is measured using a differential pressure transducer. The pressure transducer is a PX-26 series from Omega. The transducer is a silicon diaphragm that uses a wheat-stone bridge resistor network to measure the deflection. The excitation voltage is 10 VDC and the output is from 0 to 100 mV. The pressure transducer range is selected to give the highest level of accuracy, with a range of 0 to 6.8 atms.

CHAPTER 6

TEST SECTION DESIGN

The test section for the present work will serve as experimental verification of the conclusions based upon the results from the literature review in Chapter 2 and the theoretical considerations for microchannels in Chapter 3. It was concluded that the fundamental theories for fluid flow and heat transfer in conventionally scaled passages will be valid in microchannel passages. The test section will be used to provide experimental justification of those conclusions.

It would be advantageous to design the test section with a very long flow length in order to achieve fully developed flow for study. This type of microchannel geometry would not be used in a practical system. It would be more useful from an integration aspect to develop a test geometry that would mimic a microchannel geometry that could be used in microprocessor cooling. This would mean short lengths with a large number of microchannels.

This arrangement presents more challenges investigating the fundamentals of fluid flow and heat transfer. However, if such geometry was used and could achieve agreement with conventional theory, it could serve as a design method to allow greater understanding of the fundamental physics occurring in liquid flows. This would ultimately lead to improved predictive correlations. Therefore, a short multiple passage silicon microchannel test section will be utilized.

6.1 Microchannel Test Device

The test device is the primary item in the experimental system. It contains the microchannels, the heater and the temperature resistance sensors. The microchannels are fabricated on the front side of a silicon substrate. Copper is used on the back side to form a heater and temperature resistance sensors. The heater mimics an integrated circuit on the opposite side of the microchannels. A uniform heat flux can now be applied to the microchannels. Figure 6.1 shows a schematic of the microchannel geometry. The microchannel width is a , the depth is b and the fin thickness is s . This is a three side heated heat exchanger because the top wall is formed with an adiabatic material.

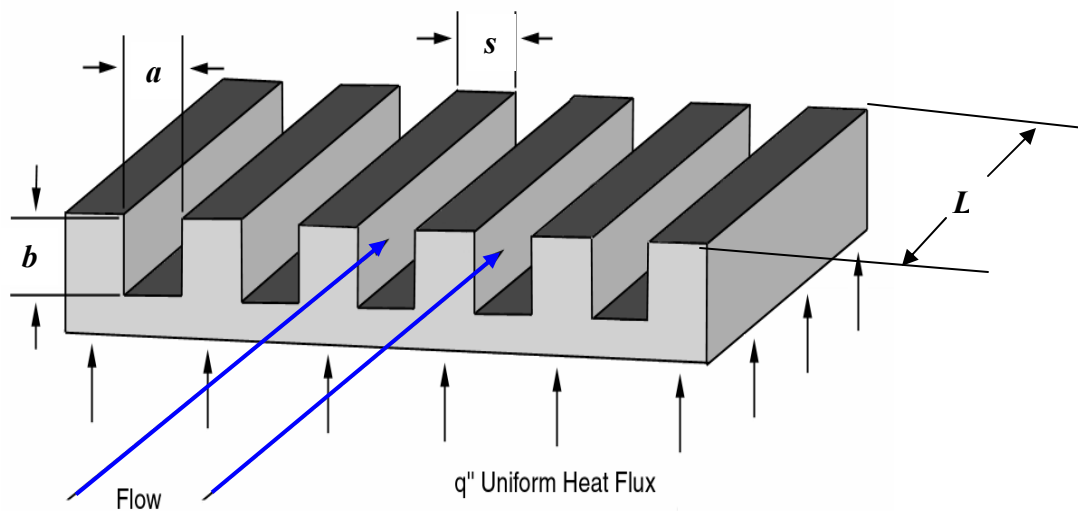


Figure 6.1: Schematic of Microchannel Geometry.

The geometries of the microchannels vary throughout the course of the experimental study and are listed in Table 6.1. There are twelve different geometries given in this table. Each microchannel geometry is given a unique identification number relating to the test section generation and the specific geometry. The channel width range from 40 to 250 μm and the fin

thickness ranges from 40 to 200 μm . The pitch of the microchannel geometry refers to the distance to repeated points in the microchannel. For example, from left edge of one microchannel to the left edge of the neighboring microchannel would be the pitch. The microchannel length, L , is fixed at 10 mm.

Table 6.1: Channel Geometries of the Test Device.

Number	a μm	s μm	Pitch μm	n	L μm
G1-001	40	40	80	100	10000
G1-002	40	100	140	57	10000
G1-003	70	40	110	73	10000
G1-004	70	100	170	47	10000
G1-005	100	40	140	57	10000
G1-006	100	100	200	40	10000
G1-007	200	40	240	33	10000
G1-008	200	100	300	27	10000
G1-009	200	200	400	20	10000
G1-010	250	40	290	28	10000
G1-011	250	100	350	23	10000
G1-012	250	200	450	18	10000

The heater area is fixed for all of the geometries. As a result, the number of microchannels varies with geometry to fill the entire heater area. The larger width microchannels will have fewer microchannels than the smaller width microchannels.

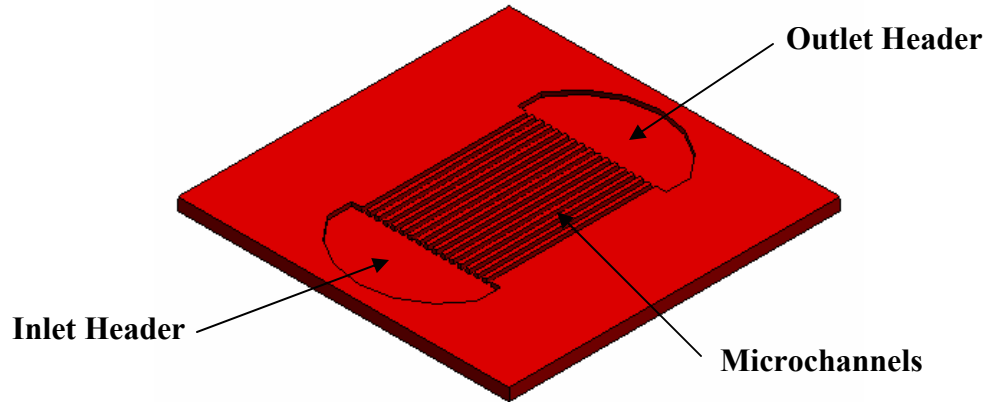


Figure 6.2: Model of the Microchannels in Silicon Substrate.

The inlet and outlet manifolds are designed to deliver the fluid to the microchannels. The furthest side from the microchannels is curved in order to help direct the flow. The manifolds are etched to the same depth as the microchannels.

The microchannels are fabricated by IBM T.J. Watson Research Center using deep reactive ion etching (DRIE). DRIE has become a standard silicon micromachining process since it was developed by the Robert Bosch Company (1988). The substrate to be etched is exposed to two different gas formulations during this process. Typically the etching step is performed with F^- reactive ions from a SF_6 gas. A polymer passivation layer is formed on the surfaces using a mixture of trifluoromethane (CHF_3) and Argon. Then, only the SF_6 gas is used and the ions are absorbed at the surface and combine to form volatile compounds that remove the newly formed polymer layer and silicon substrate on horizontal surfaces. The vertical sidewalls remain virtually untouched. As a result, very high aspect ratios with very straight sidewalls can be achieved. Figure 6.2 shows a model of the microchannels etched into silicon. Also shown is an inlet and outlet header formed in the silicon for the microchannels. The entrance to each channel is rounded to reduce the pressure drop at the entrance.

An insulating layer of nitride is deposited on the backside of the device. Then, a layer of copper is deposited and patterned on the backside to form the heater and sense resistors. Finally, a nitride cap is deposited to help minimize corrosion of the copper. The heater used to mimic a microprocessor is an electric resistance heater. The copper is patterned into a long serpentine resistor. The total length is 82 mm with a resistance of 9.7 ohms. The resistance is controlled to allow for the introduction of 200 W/cm² of power to be dissipated.

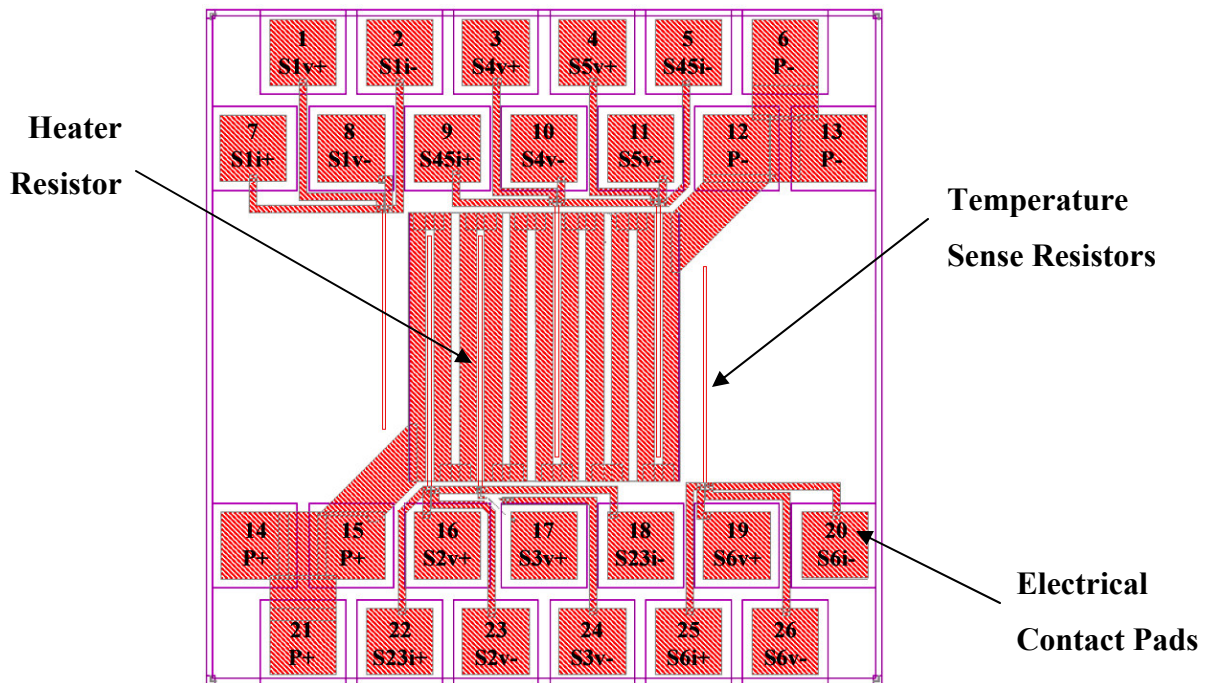


Figure 6.3: Backside of Test Device.

The temperature sensors are also resistors. These resistors are kept very small to obtain high spatial resolution along the channels. A constant current is supplied to the temperature sense resistors. The resistance of the sensors is a function of temperature. Therefore, the potential drop across the resistor will be a function of temperature. Each sense resistor requires four connections, two for supply current and two for voltage reading. The sensors return a line

averaged temperature along the length of the resistor. Figure 6.3 shows the backside of the device with the heater, sensors, and the bonding pads.

Figure 6.4 shows actual images of the front side and the backside of the microchannel test section. The origin is located at the center of the 20 mm by 20 mm device. There are six temperature sensors located on the backside of the device. The location of the sensors is at -4.750 mm, -3.375 mm, -1.875 mm, +0.375 mm, +3.375 mm, and +4.750 mm. The first and last sensor is placed beneath the inlet and outlet plenums. The remaining sensors are interlaced within the serpentine of the heater to obtain temperatures along the flow length.

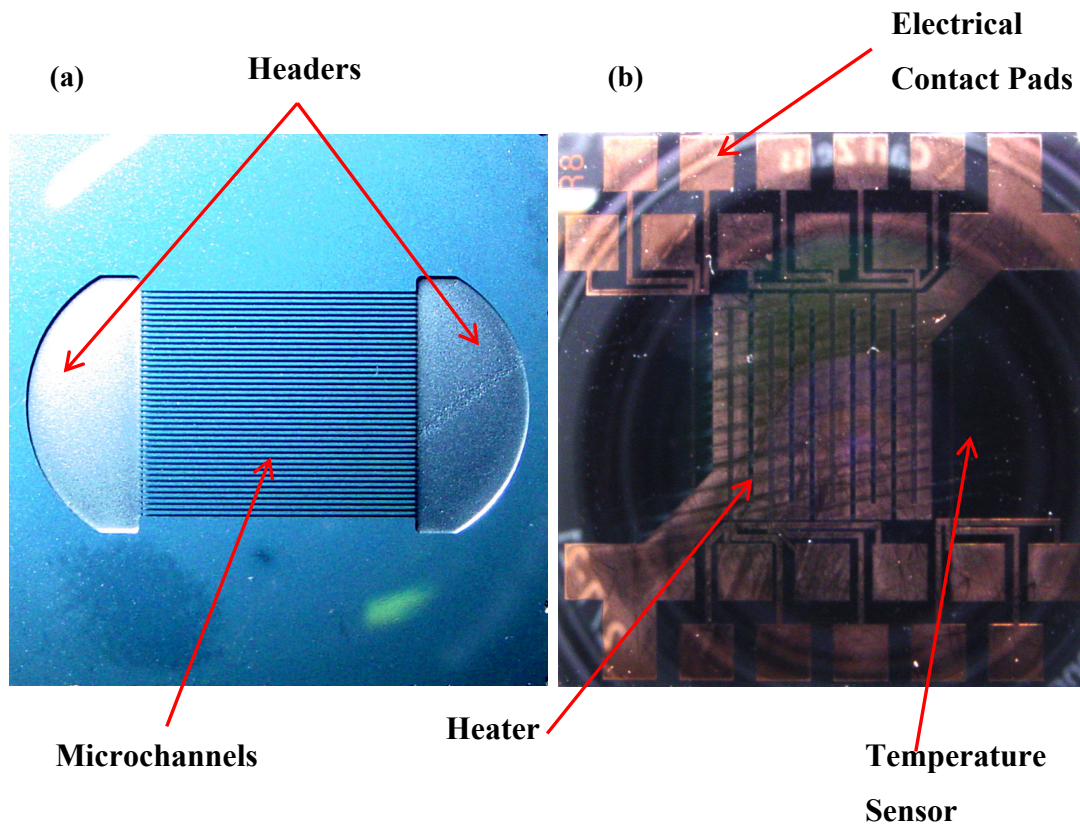


Figure 6.4: Microchannels in Silicon Substrate. (a) microchannels etched into front side of silicon, (b) copper heater and temperature sensors on the back side.

A scanning electron microscope (SEM) can be used to get a closer look at the microchannel. This will aid in the visualization of the microchannel geometry. A LEO model EVO50 SEM is used to image the microchannel test section. Figure 6.5 shows a top view of the microchannels with the plenum area identified. The geometry represented is a G01-008 with a width of $200\ \mu\text{m}$, a depth of $250\ \mu\text{m}$, and a fin thickness of $100\ \mu\text{m}$. Figure 6.6 shows a SEM micrograph at another angle. This view is more like one was standing inside the plenum area.

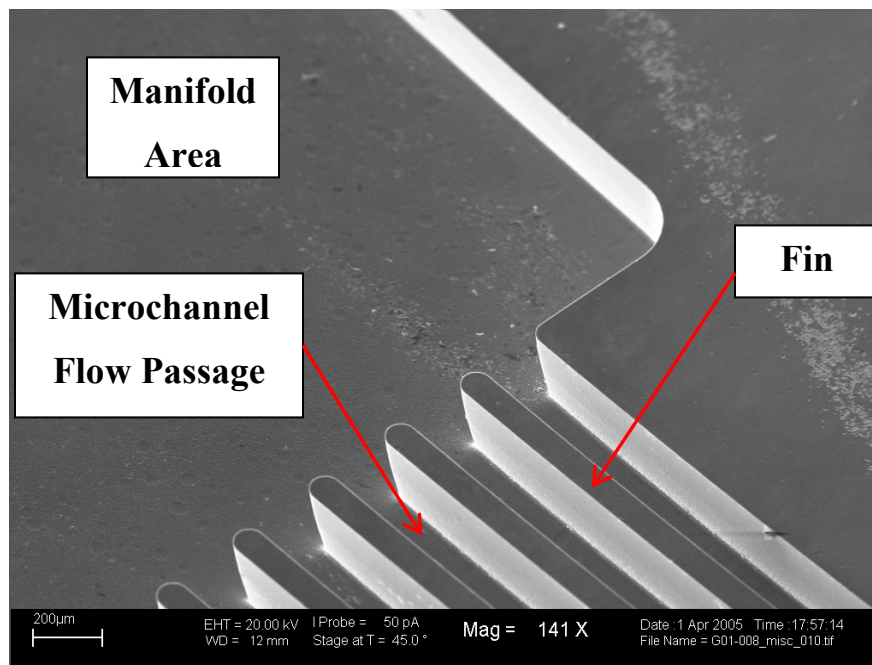


Figure 6.5: SEM Micrograph of a Top View of the Silicon Microchannels. G01-008 $a = 200\ \mu\text{m}$, $b = 250\ \mu\text{m}$, and $s = 100\ \mu\text{m}$.

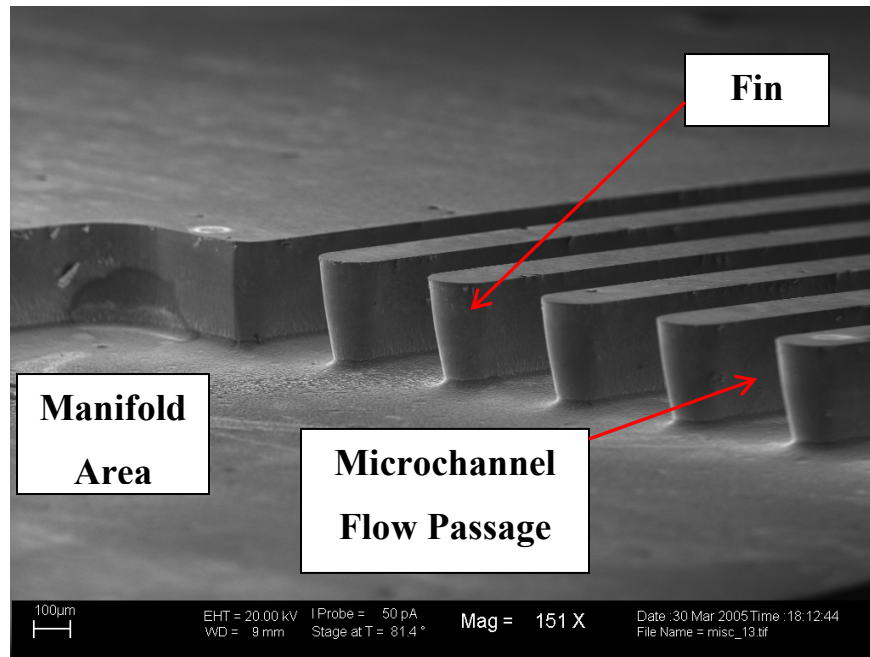


Figure 6.6: SEM Micrograph of a Side View of the Silicon Microchannels. G01-008 $a = 200 \mu\text{m}$, $b = 250 \mu\text{m}$, and $s = 100 \mu\text{m}$.

In each figure, the microchannel flow passages and the fins that separate them are visible. Notice that the edges are very well defined and from sharp boundaries. The curvature in the manifolds is visible. In addition, the radius at the end of the fins can be seen. They are designed to reduce the entrance pressure drop into the microchannel passage from the manifold. The clearly defined boundaries will aid in characterizing these geometries.

6.2 Electrical Connections

The electrical connections for the test device are achieved using a spring loaded device called a pogo probe. The device is made of two parts, the receptacle and the probe, shown in Fig. 6.7. A hole is drilled into the supporting delrin and the receptacle is inserted to be flush with the

surface. Then, the probe is inserted into the receptacle. The pogo probe is a model SHE-25-B-4.0-G from Interconnect Devices. The probe is gold plated probe with a spring force of 4.0 oz. This type of probe is rated for high current, up to 10 amperes and the model number RH-25-SC. The receptacle is also gold plated and has a solder termination for wire connections.

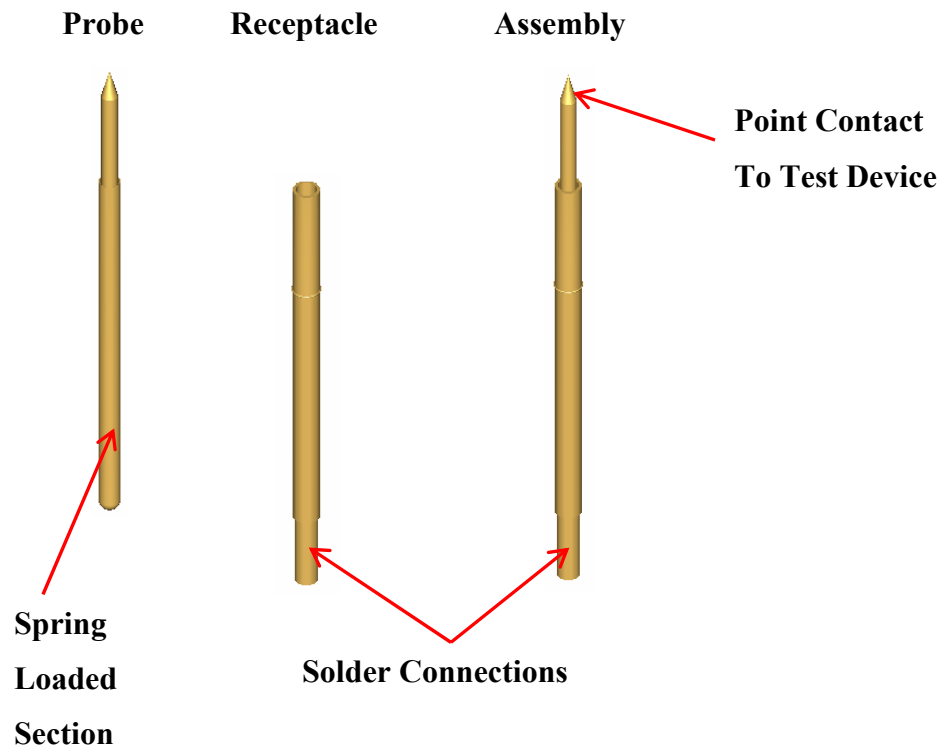


Figure 6.7: Model of the Pogo Probe, the Receptacle, and the Assembled unit.

6.3 Test Device Assembly

The test device is a three-sided microchannel structure. In order to form a complete channel, a cover must be attached to the microchannel substrate. There are a variety of methods for use in microsystems that allow for the attachment of devices. The technologies include:

direct bonding, thermocompression bonding, anodic bonding, adhesive bonding, glass frit bonding, eutectic bonding, ultrasonic weld bonding, and plasma bonding.

Table 6.2: Summary of Bonding Technologies for Use in Microsystems.

Technology	Advantages	Disadvantages
Direct	simplistic , strong bond realized, chemically resistant	must have angstrom level surface roughness, must be extremely clean, requires annealing step
Thermo-compression	bond strength increases, chemically resistant	added process step, requires controlled oven environment
Anodic	strongest bond strength, chemically resistant	added process step, requires controlled oven environment, high potential required
Eutectic	good thermal and electrical conduction, wide range of temperatures and materials, good for packaging	high stresses can result from differing thermal expansion, must remove and start again if failure occurs
Adhesive	more forgiving with surface prep, very low thermal cost	outgassing, leaching, can be chemically sensitive, poor thermal and electrical conductor
Ultrasonic Welding	can provide highly selective locations	must use external power supply, not always reliable with different materials
Plasma	can provide improved surface energy at low temperatures	adds complicated processing step

There are additional bonding technologies available. However, this list includes the most appropriate for microsystems or microelectromechanical systems (MEMS). A summary of the advantages and disadvantages of each technology, with respect to the microfluidics and microscale heat transfer applications at hand, is presented in Table 6.2.

Adhesive bonding is the option chosen from this table because of the following reasons. First, the test devices have bare silicon on the front side, which is desirable, and a silicon nitride layer and cap on the backside, which is not desirable. The silicon nitride prevents a good electrical contact to the silicon. In order for anodic bonding to work properly, it is critical to have a good electrical contact between the bonding substrates. This would not occur given the present test devices.

Secondly, adhesive bonding tends to be a more forgiving when it comes to bonding interfaces. The two surfaces can have flatness tolerances up to a several micrometers and still get successful bonding. The adhesive bonding will be explored for the present work. This one makes the most sense and would be more easily integrated into a production setting.

After several successful experimental runs, it was realized that there was a great deal of time required for bonding of the test devices. A second method of sealing was devised that allowed for quicker test device changes in the test fixture. A thin silicone membrane and a pure mechanical compression technique are utilized for later experimental runs, with no difference between the two sealing techniques. Both of these methods will now be described in detail.

6.3.1 Adhesive Bonding

Adhesive bonding is the method chosen to attach the silicon substrate and the Pyrex cover. This method provides the most latitude with the surface preparation as well as surface

roughness. However, both parameters are still important in the success of the bond interface. The adhesive used is M-Bond 610, a two-component, solvent thinned, epoxy-phenolic adhesive. The operational temperature range is from -269 °C to 370 °C for a short period and the long term temperature range is -269 °C to 260 °C. The approximate composition is 60% Tetrahydrofuran, 30% Bisphenol F epoxy resin, 10% Methyl Ethyl Ketone.

There are several methods for applying adhesive available for microsystems. The majority of the methods are related or derived from conventional sources. These methods include; brushing, roller coating, nozzle dispensing, spraying, and screen printing. Table 6.3 discusses some of the advantages and disadvantages of the application method. In addition, a new method is presented in the table.

A very thin and uniform coating is desired. The thickness is typically a few fractions of a micrometer to a few micrometers. The uniformity of the film should also be on the order of a few fractions of a micrometer. The best method to apply the adhesive using prior techniques is spray coating. This method can give repeatable films on the order of a few micrometers with good uniformity. Unfortunately, this method is not very efficient in the amount of adhesive used. A great deal of energy is used to atomize the adhesive. It also takes a carrier gas to apply. In addition, the environment is filled with particles of adhesive that never attach to the desired area.

Therefore, another method has been developed to provide a uniform, thin and repeatable film of adhesive. The method of spin transfer is a novel application to provide a thin film of adhesive to selected locations on a device. The process begins with attaching a Kapton polyimide film with a thickness of 51 μm to a 100 mm wafer. The wafer and film is secured in the vacuum chuck of a hand spin coater.

Table 6.3: Summary of Adhesive Application Methods for Use in Microsystems.

Method	Advantages	Disadvantages
Brushing	very simplistic, no special tools or process parameters	easily contaminated, not very uniform thicknesses, very thick layers, hard to implement in production
Roller Coating	improved consistency, can implement in a production line	exposed adhesive can be contaminated, large physical size of roller compared to device size
Nozzle Dispensing	improved volume control, reduced size of coating, more precise placement, implement in production line	clogging, more difficult process controls required to control volume, contact line between surface-liquid-gas dominates coating behavior
Spraying	can coat a large area simultaneously, can generate very uniform films	more complex process variables, coat more than what is desired, need carrier gas, introduces adhesive particles to environment
Screen Printing	highly selective, inexpensive, repeatable, can add to production line	fixed film thickness as a function of stencil thickness, added process steps of adding and removing screen, can cause transfer contaminates
Spin Transfer	repeatable, uniform thickness, very thin films, independent of operator, apply only where desired with transfer	several process parameters, four process steps, adhesive property dependent, limit on adhesive viscosity that can be used

The speed, ramp, and time can all be independently controlled on the hand spinner. Once all of these parameters are determined, a specific amount of adhesive is applied with a dropper to the center of the film. The spin recipe is run to allow the fluid to spread out and create a thin film. The resulting adhesive film thickness is a function of the speed, time, ramping conditions, and viscosity of the adhesive.

After an adhesive film is created on the polyimide, the polyimide is removed from the carrier wafer. A test device is placed on a special vacuum fixture to secure it. The adhesive film is inspected to ensure uniformity and then placed on the test device. A hard plastic roller is used to make good contact between the device and the adhesive layer. The roller also removes any air bubbles that might form. The polyimide film is then peeled from the device wafer that remains secured on the vacuum fixture.

The result is a thin film of epoxy that has been transferred to the device surface. In addition, the adhesive film is left only where there was direct contact between the device and the polyimide film. Therefore, no epoxy can coat the sidewalls or the bottom surface of the channels and plenums.

The thickness of the adhesive film referred to will be the resulting transferred thickness after the peel of the polyimide film. The thickness of the adhesive is determined for several process parameters. Figure 6.7 shows the thickness versus the speed of the wafer and the volume of the fluid added.

There are several different adhesive volumes and spin speeds represented in Fig. 6.8. The trend of the data seems to be independent of speed when the uncertainty bars in both the volume and film thickness are added. However, the volume of adhesive used has an effect. As the volume is increased, the uniformity of the film is improved. This is demonstrated by the

reduction in the error bars seen for the speed equal to 4000 rpm case. As the volume increases, the variation in measured thickness decreases. Therefore, a speed of 4000 rpm and a volume of 0.246 mL are chosen to give a film thickness of 1.2 μm . The curing schedule is 200 $^{\circ}\text{C}$ for 60 minutes, with an applied torque of 2.8 N.

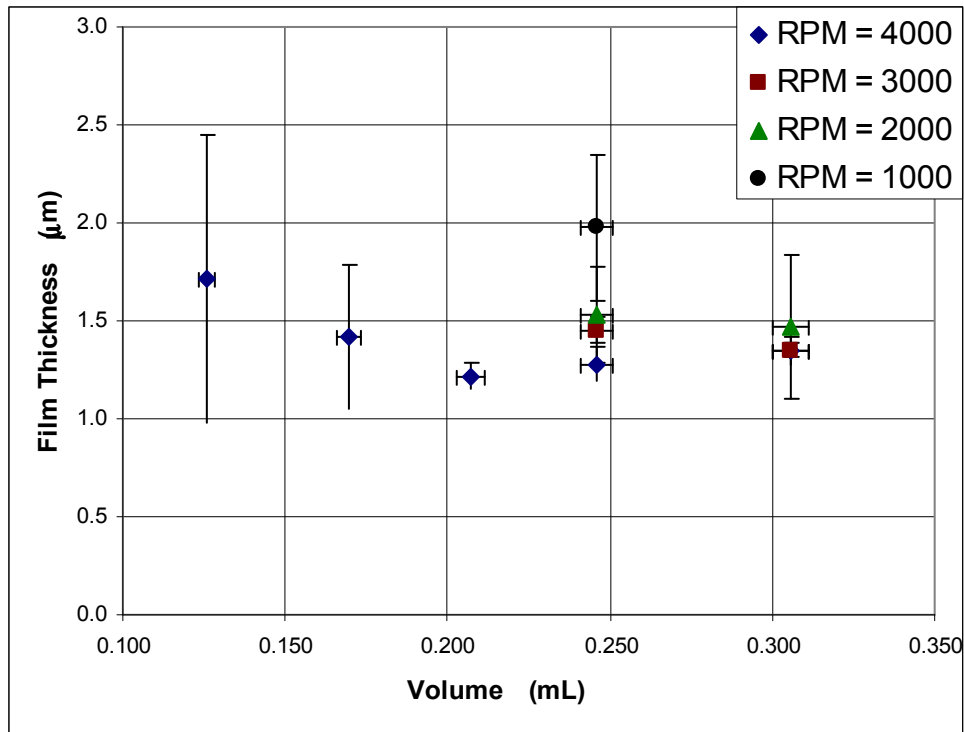


Figure 6.8: Transferred Adhesive Thickness Versus Volume for Different Speeds.

A fixture is developed to support the adhesive bonding of the substrate and Pyrex. Individual pieces are cleaned, prepared and the adhesive is applied. The test device is ready for assembly. The bonding fixture is design to aid in alignment, provide even applied pressure and provide easy transport for high temperature curing. This bonding fixture can be used for adhesive, anodic, thermocompression, and direct bonding.

Stainless steel is chosen for the plate material in contact with the test device. Three locating pins are used with the plates. The pins are made of Macor and are also electrically insulated. Figure 6.9 shows the model and actual picture of the test device located in the bonding fixture, respectively. As can be seen in the figures, the plates are larger than the die size of the test device. This allows for even distribution of applied pressure.

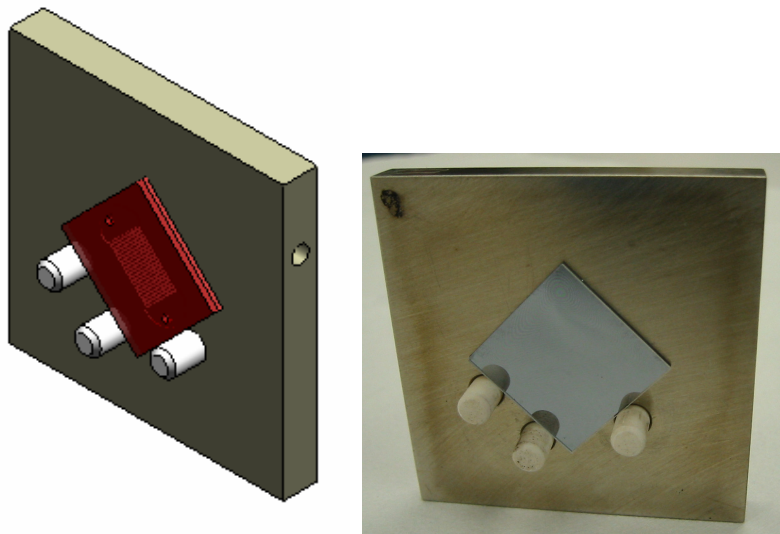


Figure 6.9: Model of and Actual Test Device in Adhesive Bonding Fixture.

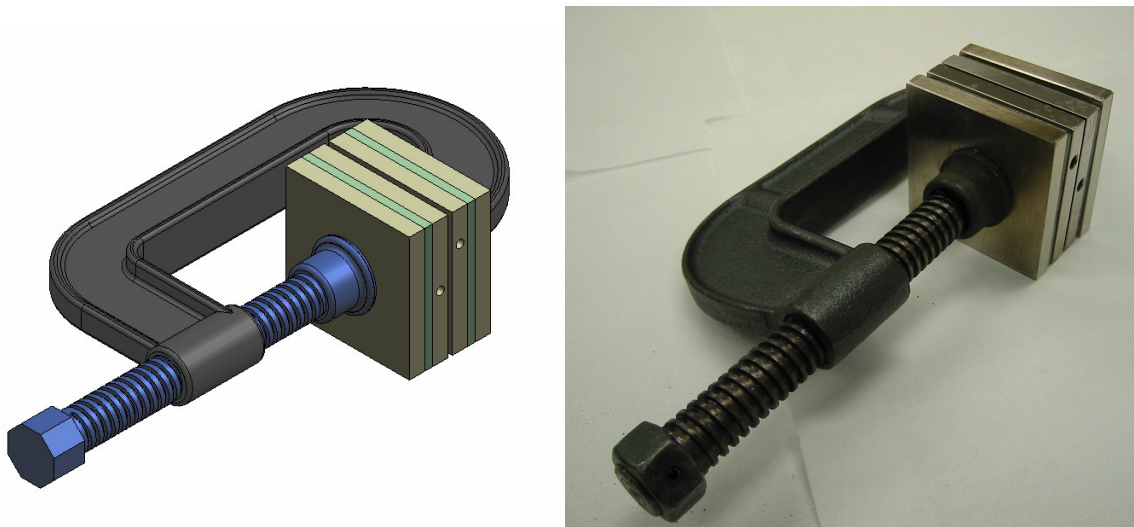


Figure 6.10: Model of and Actual Adhesive Bonding Fixture.

The test device is loaded into the base plate. A Pyrex cover is applied in the proper orientation. The top plate is aligned to the base plate. A clamp is used to hold the plates together and apply a pressure to the test device. The clamp is a standard c style clamp. The typical bar is removed and a hex nut is pinned at the end. A torque wrench can be used to apply different pressures to the test device. Figure 6.10 show the bonding fixture model and the actual bonding fixture, respectively.

6.3.2 Mechanical Compression

The alternative method for sealing the microchannels is using a thin silicone membrane and mechanical compression. The test fixture is adjusted in order to place the test device in pure mechanical compression without any bending stresses.

The silicone membrane is a flexible rubber membrane with a total thickness of 508 μm . One concern using this method is that the membrane would flex too much and enter the microchannel. This was addressed by pinning the membrane on the device retaining plate in such a way to cause it to have some amount of tension. When the pieces of the test device are applied, the membrane is already pre-stretched and compresses in to place thus eliminating excess material from encroaching into the microchannel. A thickness measurement of the stack was also conducted using highly accurate micrometers to verify that the sum of the individual parts match the total of the stack. Additionally, images of the test device in compression are used to provide secondary assurance.

Finally, an experiment with the two different sealing techniques are conducted to compare the results. The same mass flux was used in two test devices with the same geometry. It was found that there is no noticeable difference in overall pressure drop between the devices

sealed with these two methods. There is no encroachment into the microchannel by the silicone membrane. Therefore, the mechanical compression method will be the primary means of sealing the microchannel.

6.4 Test Fixture

The test fixture is the part of the test section that provides the overall mechanical support structure for the test device. In addition, the fixture houses the electrical and fluidic connections. The material used for the test fixture is black delrin. Delrin is an acetal resin from DuPont. It is a lightweight plastic that is very stable and does not experience any major creep. The test fixture is comprised of the following distinct parts; the pogo probe block, main block, bottom retaining plate, device retaining plate, and X-Y stage mounting plate. Figure 6.11 shows the model of the test section assembly. The complete dimensioned drawings are in Appendix Section 13.1.

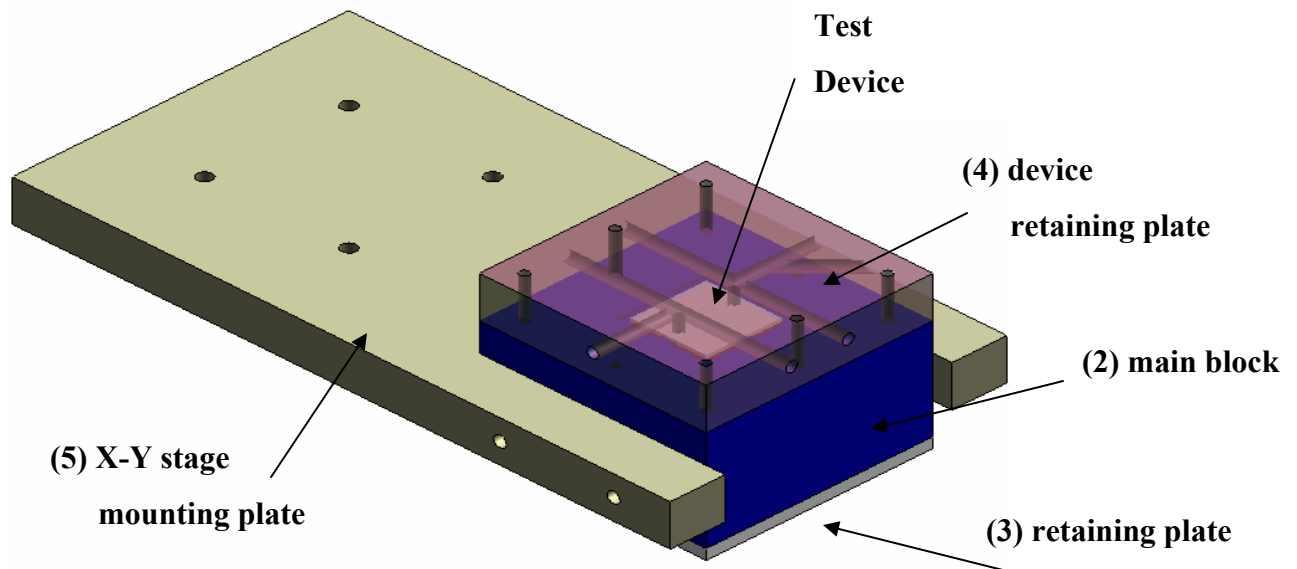


Figure 6.11: Model of the Test Fixture Assembly. (1) pogo probe block (not shown), (2) main block, (3) retaining plate, (4) device retaining plate, and (5) X-Y stage mounting plate.

The actual test fixture assembled and in the experimental test facility can be seen in Fig. 6.12.

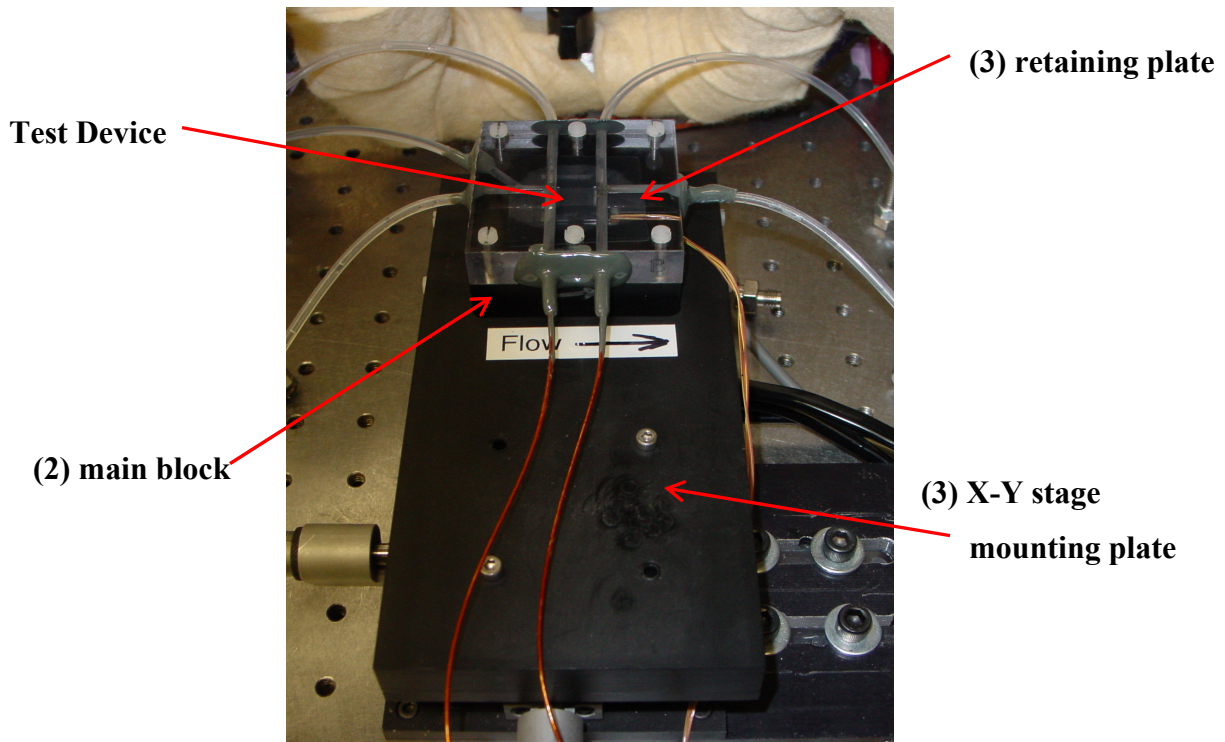


Figure 6.12: Installed Test Fixture Assembly. (1) pogo probe block (not shown), (2) main block, (3) retaining plate, (4) device retaining plate, and (5) X-Y stage mounting plate.

Figure 6.13 shows both the model and the actual pogo probe block. The pogo probe block supports the pogo probes, or in other words the electrical connections. The block is designed to receive the pogo probes with a spacing of 2.54 mm. The length of the block is determined by the amount of force engagement required. The through holes are drilled to a diameter to give the probes interference fit and the probe receptacle is pressed into position. The bottom retaining plate serves to secure the pogo probe block in the main block.

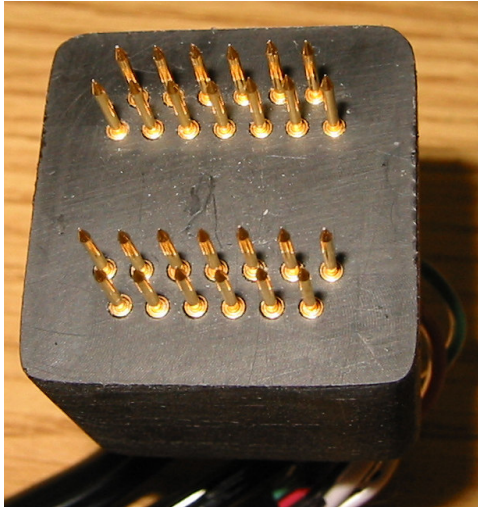
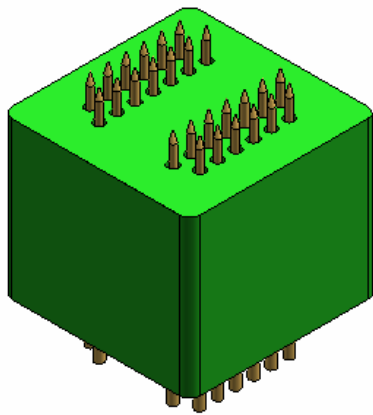


Figure 6.13: Model and Actual Pictures of the Pogo Probe Block.

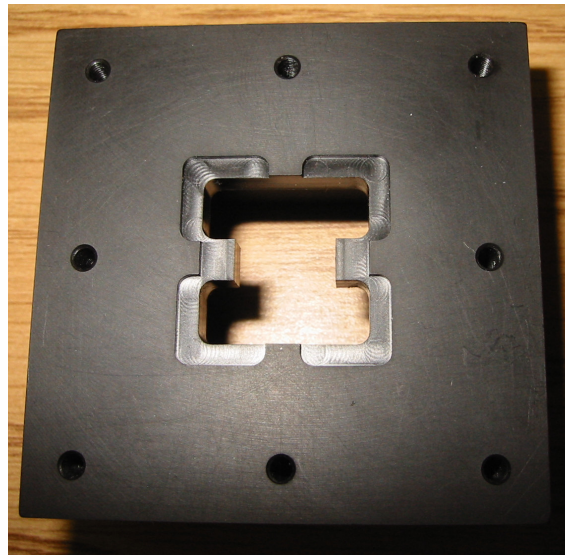
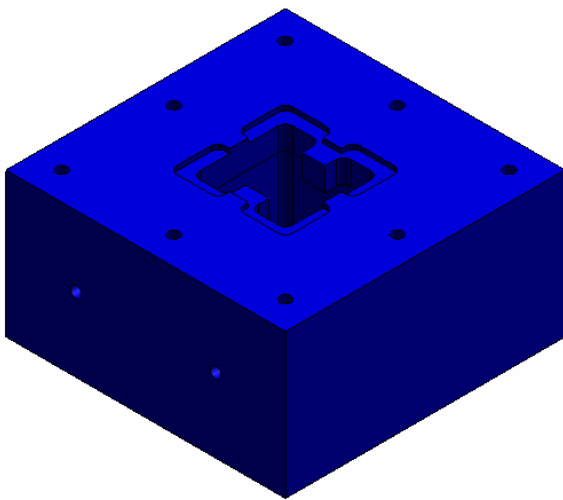


Figure 6.14: Model and Actual Pictures of the Main Block.

The model and the actual pictures of the main block are shown in Fig. 6.14. This part in the assembly supports the test device as well as providing alignment between the test device and the pogo probes. The bottom of the block contains a hole to receive the pogo probe block. The

top of the main block contains a recess to receive the test device. The design of this feature also includes two surfaces to support the backside of the test device.

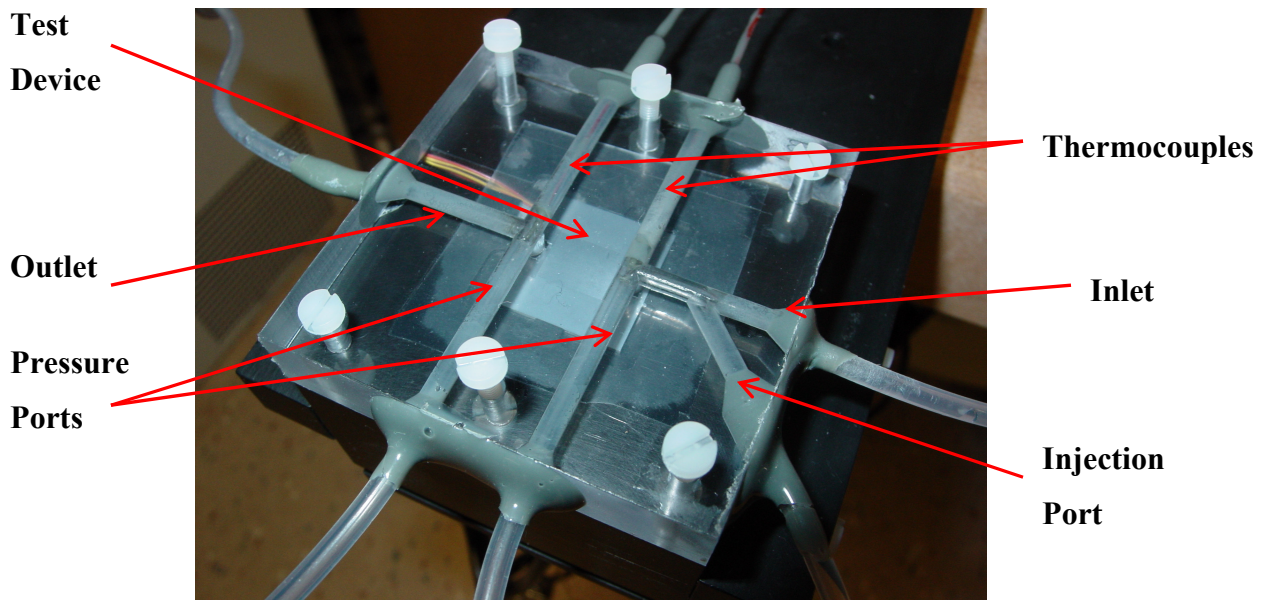
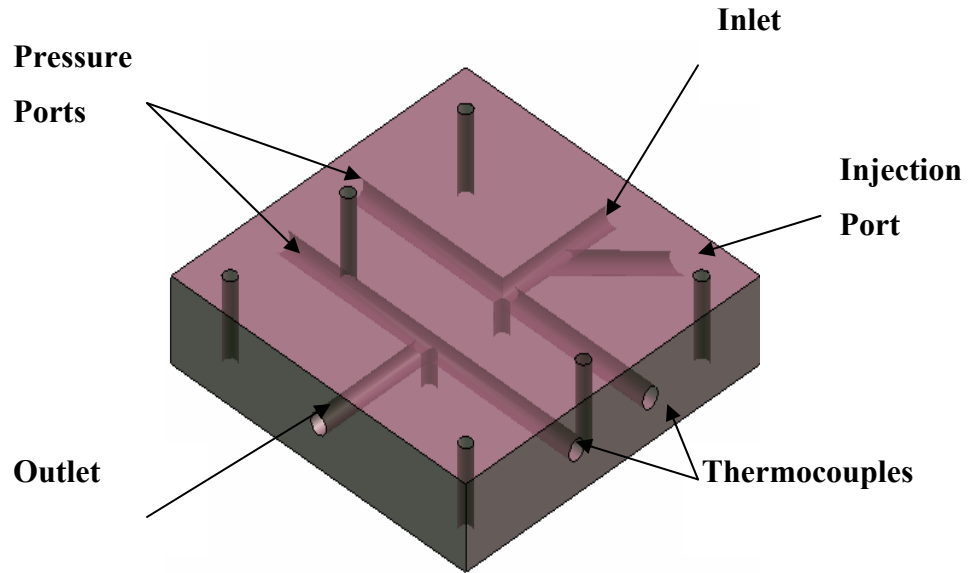


Figure 6.15: Model of the Device Retaining Plate.

The final part in the test fixture assembly is the device retaining plate shown in Figure 6.15. This part provides a clamping force on the test device and the fluidic connections. The piece is made of a clear polycarbonate material to allow for flow visualization. The fluid enters the piece and moves into an inlet plenum. The fluid then enters the test device and goes into the exit plenum. There is a pressure port located in each of the plenums to get the pressure drop across the test device. In addition, there are very small thermocouples located in the inlet and outlet plenums. An injection port is located in the inlet. This port gives the ability to inject particles into the flow. Air bubbles or polymer spheres can be injected to study the reliability of the microchannels. Very small polymer spheres used in micro-Particle Image Velocimetry (μ PIV) experiments will allow for the visualization of the flow field.

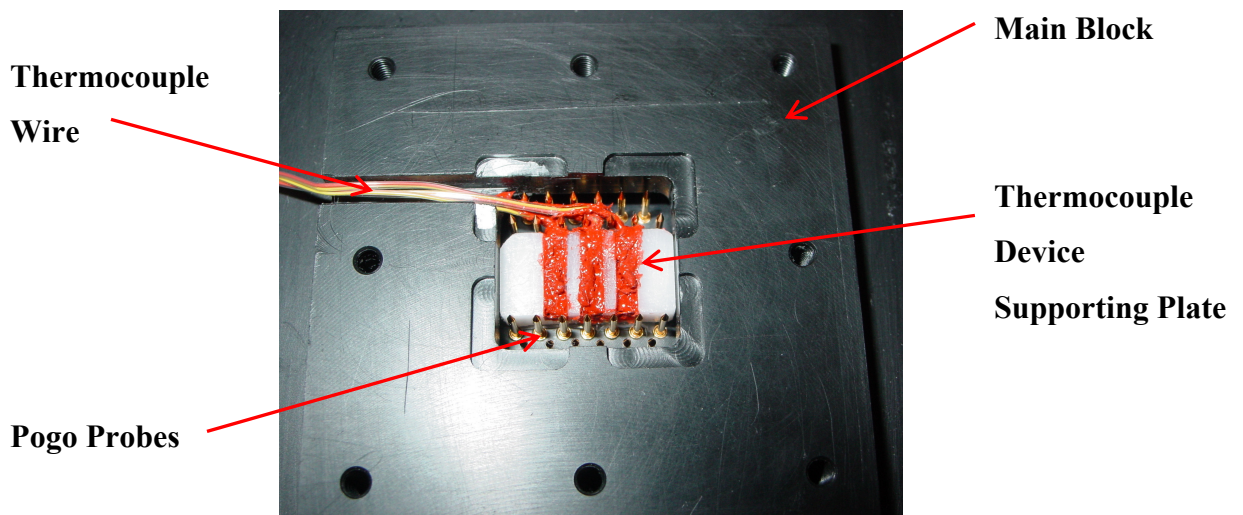


Figure 6.16: Thermocouple Device Supporting Plate.

Finally, a thermocouple device supporting plate made from Teflon is made to house three backside thermocouples. These thermocouples are used to provide additional heater surface temperatures. Figure 6.16 shows the white supporting plate with the thermocouples installed in

the main block with the pogo probes above and below it. The thermocouples are actually coated in a red high temperature epoxy to protect them and the test device from corrosion. The thermocouples are located on the centerline in the y direction and located at -4 mm, 0 mm, and +4 mm in the x or flow direction.

Now, the test device is located in the test fixture and all of the electrical and fluidic connections are made. The next step is to calibrate the test device in order to generate accurate data. Chapter 7 will describe the system and test section calibration process.

CHAPTER 7

SYSTEM CALIBRATION AND EXPERIMENTAL TECHNIQUES

The method utilized for the system calibration and the experimental procedure will be described in this chapter. The three main topics include the system calibration, the experimental procedure, and the preparation of the working fluid.

7.1 *System Calibration*

An experimental system requires calibration and some specific data acquisition techniques to generate the most accurate data possible for a given system configuration. The elements considered in the present calibration scheme are: thermocouples, temperature sensors, pressure transducers, flow meters, and the pump.

The thermocouples are calibrated using a heated block and an ice bath. The ice bath gives a reference temperature of 0 °C. A model CL950-110 calibrated hot block from Omega is used to give the higher values of known temperature. The range of operation for the thermocouple calibrator is 45 °C to 480 °C. The only constraint for the thermocouple calibrator is that the lowest temperature it can read is 20 °C above ambient. To be conservative, the lowest point used on the calibrator is 45 °C.

The experimental system is calibrated over a temperature range of 0 °C to 200 °C. The ice point is utilized to give the low range of temperature readings and the hot calibrator block is used to obtain the rest of the temperatures from 45 °C up to 200 °C. The thermocouples are calibrated using at least twenty points chosen within the 0 °C to 200 °C range. A linear curve fit is applied to the collected points to determine the equation for the thermocouple. Figure 7.1

shows the calibration curve for a thermocouple T03 which is located at the flow meter bank inlet. The data are represented by points and the linear curve fit can be seen as a line. The calibration equation is displayed with the R^2 value.

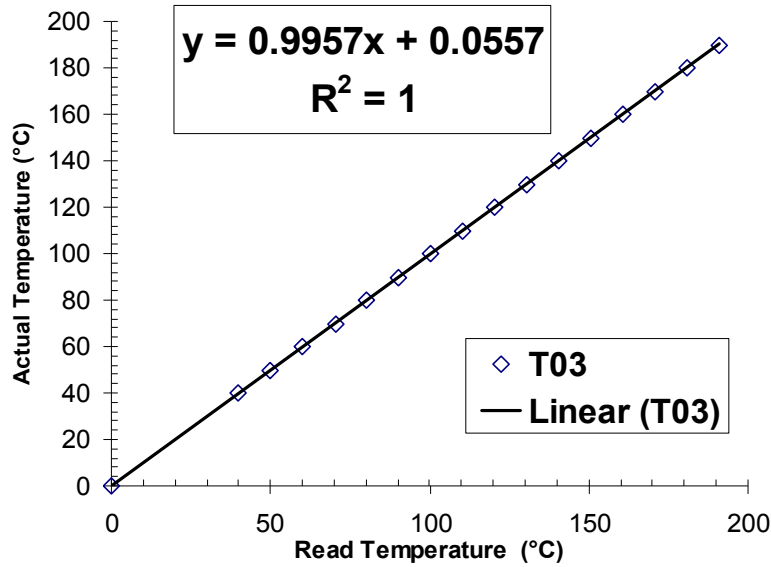


Figure 7.1: Thermocouple Calibration Curve for the T03 Thermocouple.

Each thermocouple is calibrated in this manner. Once all of the calibrations are performed, the thermocouples are exposed to the exact same known values of temperature to test the calibration. The thermocouples show excellent agreement and are all within ± 0.05 °C of each other and the known temperature. It can be concluded that the thermocouples have an accuracy of ± 0.05 °C.

The temperature sensors on the test device are calibrated by applying a known temperature to the device. Recall that these sensors are actually resistors and the resistance is a function of temperature. The efficient heat transfer that occurs in the microchannels will be used to our advantage. Temperature controlled water is passed through the test device at a moderate flow rate. A sufficient amount of time is allowed to let the test device reach the fluid

temperature, within ± 0.05 °C. Several external thermocouples are used to ensure that accurate steady state temperatures are achieved. Finally, the resistance and the potential are measured for that applied temperature. A linear curve fit for the calibration is assumed and applied to the data. Figure 7.2 shows the calibration curve for the S1 sensor located under the inlet manifold on the test device.

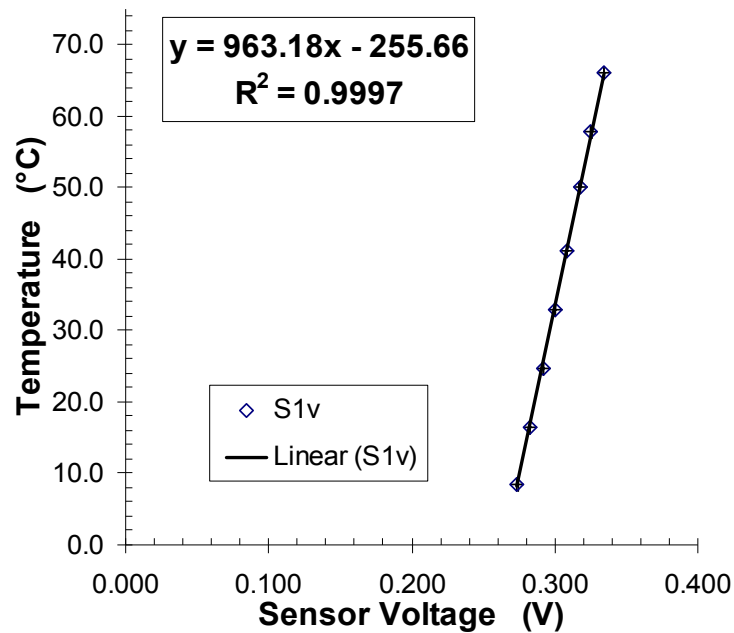


Figure 7.2: Temperature Sensing Resistor Calibration Curve for the S1 Sensor.

The pressure transducers are calibrated using known pressures and the measured response of the transducer. A pressure calibrator from Omega is used to apply a known value of pressure. The range of the pressure calibrator is -100 to 200 kPa. The high side pressure port on the differential pressure transducer is exposed to the known values of pressure. Over twenty points are taken within the range of the specific pressure transducer. A linear curve fit is assumed and used to generate the calibration equation. If the range of the pressure transducer is 690 kPa, the transducer is calibrated up to 200 kPa and linear behavior is assumed throughout the remainder of

the range. Figure 7.3 shows the calibration curve for the P01 pressure transducer located at the outlet of the filter housing.

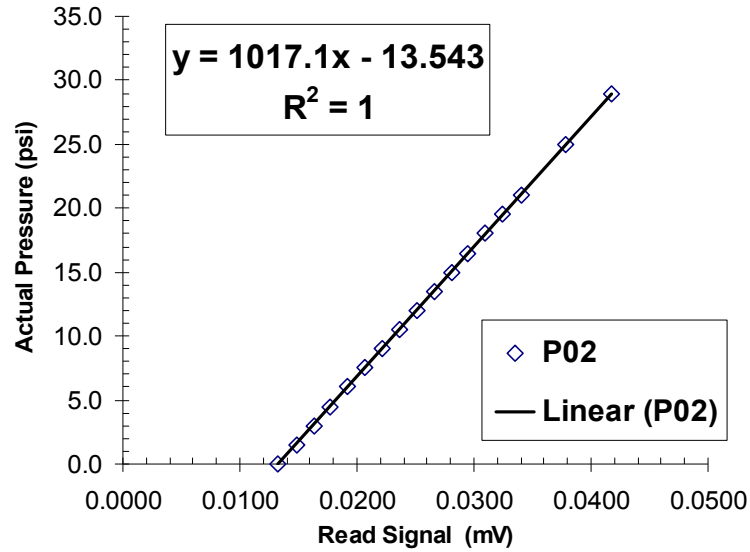


Figure 7.3: Temperature Sensor Calibration Curve for the P01 Pressure Transducer.

The flow meters and pump are calibrated simultaneously. The pump is set for a specific flow rate. The fluid is collected in a flask and timed. Then, the mass of the fluid is measured for that period of time and the mass flow rate is determined. At the same time, the measurement on the flow meters is recorded. Several points are taken over the range of operation of the pump and for each of the flow meter ranges. A polynomial curve fit is applied to get the calibration equation for the pump and flow meters.

7.2 Experimental Procedure

A data acquisition (DAQ) system monitors several thermocouples, pressure transducers, and sensing resistors. In addition, the data acquisition system controls the pump used to drive

flow in the system. The DAQ is based upon the signal conditioning SCXI system from National Instruments. This system conditions all incoming signals and gives the ability to have high channel counts for measuring accuracy.

The DAQ system used in the experimental system is capable of sampling at a rate of 100,000 samples per second. The present work is only focused on steady state performance but such a high sampling rate will eliminate the chance of under sampling the signal.

The method used for data collection is called a burst mode DAQ. This is a mode where several samples are collected at a very fast sampling rate, a burst of sampling. Then, a period of time elapses and several more samples are collected. These two steps are repeated for a long period of time. The individual bursts of data are analyzed online to determine the mean and the standard deviation, σ . Then, several of the individual bursts can be compiled to determine the overall mean and standard deviation for the entire set of bursts collected. Figure 7.4 illustrates this DAQ mode of operation. The black lines represent the calculations based upon the individual bursts. The red lines represent the calculations based upon the entire data population.

The procedure for data collection uses a sampling rate of 500 Hz. The actual data collected by the DAQ is in a waveform type. The channel information contains both amplitude and frequency information. A typical set of data contains a thousand samples for each channel obtained at the sampling frequency. The calibration for each measurement is applied offline of the data collection.

When setting up a test device for a data run, it is first loaded in the test fixture. Then, the top retaining plate is used to create the fluidic connections. Next, the electrical connections are made via the pogo probes. The flow loop is brought to the desired inlet temperature by using a test section bypass. Next, the flow enters the test device and the input power is applied to the

test device. After all of the data has been collected at the specified heat flux, the input power is changed while the flow rate remains constant. Therefore, the data collection is achieved by varying the heat flux for a fixed mass flow rate.

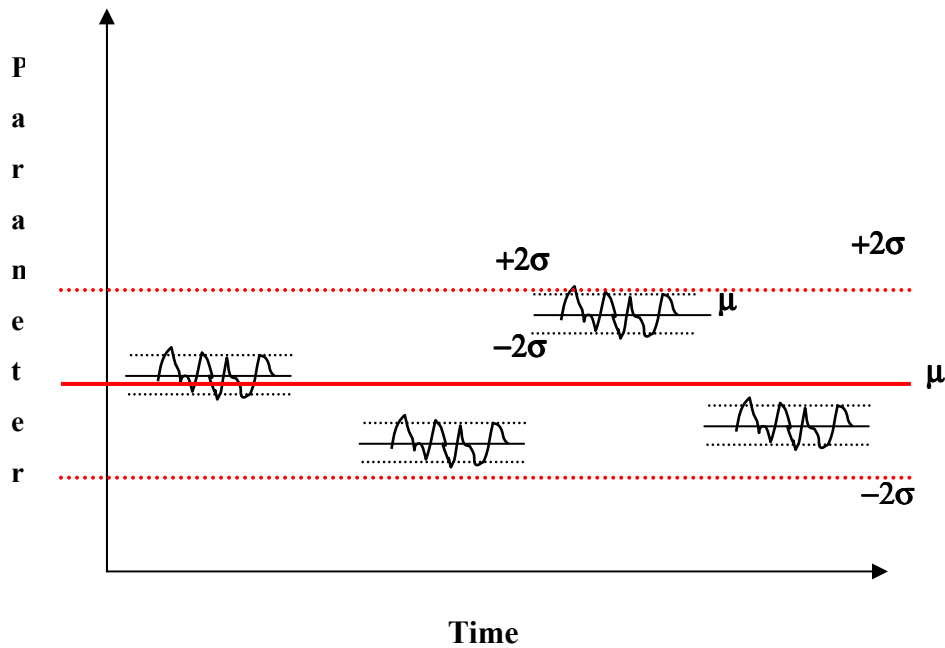


Figure 7.4: Example of Burst Mode DAQ.

The system reaches steady state before the data collection begins. The measured values are considered to be at steady state if the values do not fluctuate more than the uncertainty in the measurements. Typically, the data collection begins 5 minutes after the system reaches steady state.

7.3 Working Fluid Preparation

The working fluid for the present work is distilled, de-ionized and degassed water. The present work is focused on generating fundamental, single-phase flow data for a variety of microchannel geometries. It is therefore important to eliminate all of the interfering variables. The amount of dissolved gas in the water will affect the heat transfer performance. The non-condensables can outgas during the experiments and cause enhanced heat transfer.

CHAPTER 8

EXPERIMENTAL RESULTS FOR PLAIN SILICON MICROCHANNELS

New experimental data for single-phase water flowing in plain silicon microchannels has been obtained. The experimental test facility described in Chapter 5 is utilized to generate pressure drop and heat transfer data with the variety of silicon microchannels shown in Table 6.1. The purpose of the data is mainly to provide a reconciliation of the previous literature.

The new experimental data generated here serves to provide evidence of the effects of the items identified in Chapter 2, such as inlet and exit losses, which have lead to the reported discrepancies in previous experimental data sets. Once those items are determined using the present work, one may be able to reconcile the previous data to provide a wealth of experimental data for single-phase flow and heat transfer in microchannels. To that end, the following sections on single-phase water flow and heat transfer in silicon microchannels are used to substantiate the conclusions drawn for the literature reconciliation. The main items to be identified experimentally are the effect of inlet and exit losses, developing flows, experimental uncertainties, and microchannel geometry measurements.

8.1 *Single-Phase Water Flow in Microchannels*

The experimental data are used to investigate the various issues that have been identified in Chapter 2 as reasons for discrepancies between experimental data and conventional theories. The issues addressed here are accounting for the inlet and exit pressure losses, the developing flow regions within the microchannel, and the experimental uncertainties. The experimental data

for one of the channel geometries in Table 6.1 will be processed completely to illustrate the proper procedure for reporting experimental data for microchannel flows.

A test section with a G01-009 silicon microchannel geometry will be used to reduce the experimental data. It has a width of 200 μm , a depth of 250 μm , and a length of 10 mm is used to provide new experimental data to illustrate the different components of the total pressure drop measurement. The data presented is for adiabatic, single-phase degassed water and covers the range of Reynolds numbers from 14 to 789. There are 26 parallel channels connected to a common header. The inlet plenum and outlet plenums are in a polycarbonate cover plate. The temperature and pressure are measured in the plenums. The plenum areas are sufficiently large to ensure measurement of only the static pressure.

The friction factor is calculated from the measured pressure drop. It is plotted versus Reynolds number in Fig. 8.1. It is compared to the conventional friction factor theory for laminar flow. The data points uncorrected for entrance and exit losses are shown as squares. The experimental uncertainty is calculated and the error bars are included.

There is deviation from the laminar flow theory as observed in the data in the low Reynolds number range. However, the experimental uncertainties are quite large for this flow regime. As the Reynolds number increases, the data begins to show good agreement with the theory. Finally, the data begins to depart from the predicted f/Re approximately at a Reynolds number of 300. This would suggest early transition to turbulent if a regular friction factor versus Reynolds number plot exhibited this behavior. This is not an accurate representation of the measured pressure drop.

The entrance and exit losses are calculated and subtracted according to Eq. (3.2). These losses are found using the conventional constriction and expansion area theory. The area ratio

changes are used to determine the loss coefficients. The corrected data shows little difference to the uncorrected data in the low Reynolds number region and a more significant change in the higher Reynolds number region. However, this component alone does not correct enough to demonstrate good agreement with the theory.

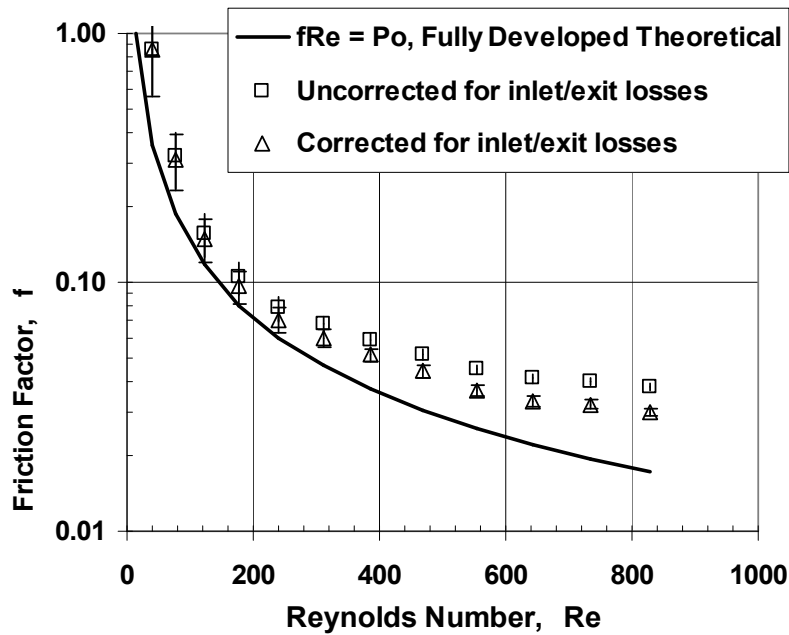


Figure 8.1: Friction Factor vs. Reynolds Number Considering Entrance and Exit Losses.

Line = theoretical prediction of f , square points = uncorrected data, triangle points = corrected data; Adiabatic, G01-009, $a = 200 \mu\text{m}$, $b = 250 \mu\text{m}$, $L = 10 \text{ mm}$.

The entrance lengths at the higher Reynolds numbers become quite significant. For example, the last data point shown in Fig. 8.2 has an x^+ of 0.048 at the exit. This means that the entrance length is 9.8 mm and the flow in the microchannel is not quite fully developed at the exit and the entire flow length is developing flow. This must be taken into account when comparing to the theoretical value. Therefore, the apparent friction factor, f_{app} , must be utilized to compare with theory.

The C^* ratio versus Reynolds number is shown in Fig. 8.2. The C^* ratio would be more appropriate to report for a microchannel geometry of this nature. It will also avoid confusion between the regular friction factor and the apparent friction factor. For comparison purposes, the C^* ratio for the uncorrected data and the C_{app}^* ratio for the data corrected to account for the developing flow portion are presented together.

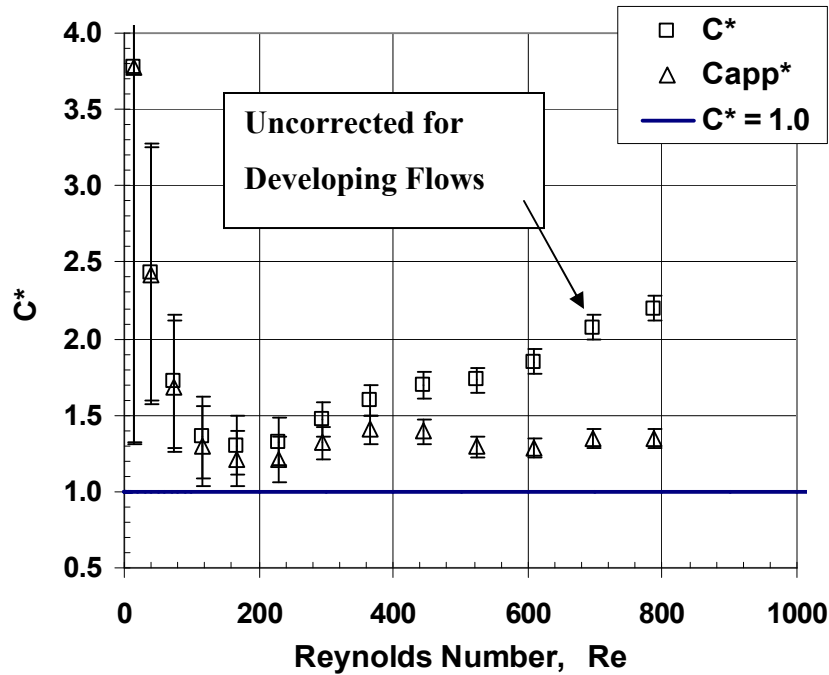


Figure 8.2: Apparent C^* Ratio vs. Reynolds Number Considering Developing Flow. Line = theoretical prediction, square points = uncorrected data, triangle points = corrected data;

Adiabatic, G01-009, $a = 200 \mu\text{m}$, $b = 250 \mu\text{m}$, $L = 10 \text{ mm}$.

The uncorrected data begins to rise in value after a Reynolds number of 300. However, the data that is calculating C^* based upon the apparent friction factor continues to show good agreement, within approximately 25% error. Although the data does not match perfectly, there is good general agreement and the trend is properly predicted.

8.2 Microchannel Geometry Measurements

The channel dimensions have a major effect on the friction factor calculations as seen from Eq. (4.16). The measurements for the microchannels tested were first made using non-destructive measurement techniques. The dimensions resulting from the optical measurement technique yield a microchannel width of $201 \pm 5 \mu\text{m}$ and a microchannel depth of $247 \pm 5 \mu\text{m}$. At the completion of the testing, the microchannel test sections are cleaved in order to facilitate accurate cross sectional measurements. Upon destruction, the profile of the supposed rectangular microchannels is actually found to be trapezoidal in shape as seen in Fig. 8.3.

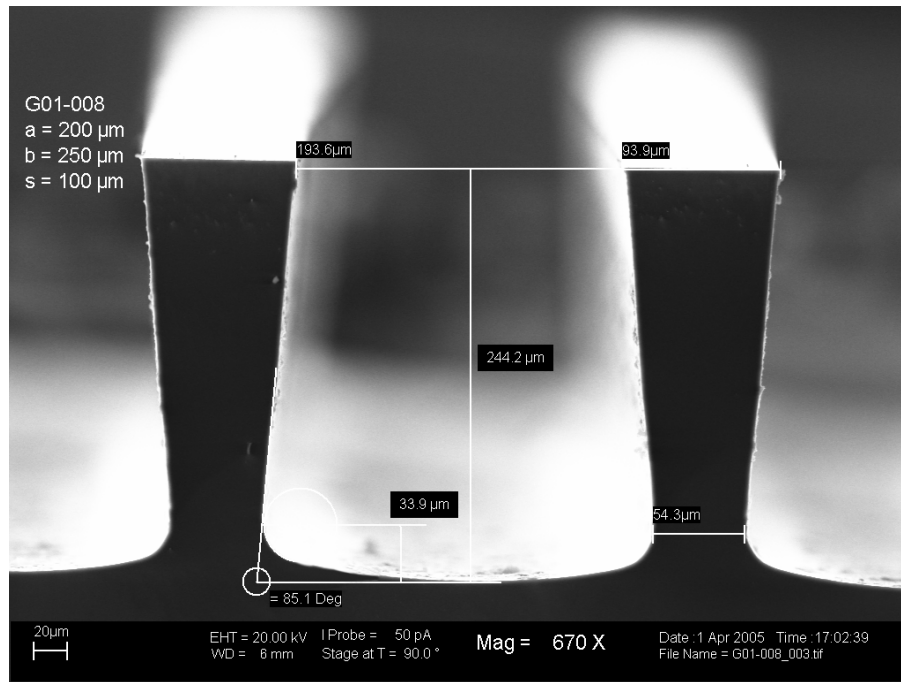


Figure 8.3: Actual Cross Section of Tested Microchannel. G01-009, $a = 194 \mu\text{m}$, $b = 244 \mu\text{m}$, $L = 10 \text{ mm}$, $\theta = 85 \text{ degrees}$, $D_h = 227 \mu\text{m}$.

Figure 8.3 shows an SEM image of the microchannel geometry tested. It can be seen that there is significant undercutting of the fin area in these microchannels. The width at the top is

$194 \pm 1 \mu\text{m}$. The depth is $244 \pm 1 \mu\text{m}$ with a sidewall angle of 85 degrees. This profile could not be obtained from non-destructive measurement techniques.

The microchannel cross section is not a true trapezoid. However, careful measurements are made to determine the cross sectional area and the proper hydraulic diameter is calculated. The equivalent trapezoid has an angle of 85 degrees. The corresponding fRe number is 14.5 for trapezoidal ducts with that side wall angle and aspect ratio.

Unfortunately, there is no available correlation that gives the Nusselt number for a three side heat trapezoid with rounded corners. The four side heated trapezoid correlation should be utilized in determining the Nusselt number until improved correlations are available.

Now consider the effect of these measurements upon the experimental data. For example, the friction factor can now be improved using the corrected geometry for the new trapezoidal cross section. The apparent C^* is shown in Fig. 8.4. It can be seen that the data now shows improved agreement with theory when the inlet and exit losses and developing flows are accounted for. Notice that the data shifts in the x axis. This is due to the slight change in Reynolds number from the change in hydraulic diameter. Using the non-destructive measurement method, the remaining error in the higher Reynolds number range is 33%. After the cross section has been measured using a cut of the test section, the resulting hydraulic diameter is $227 \mu\text{m}$ and the error is reduced to 24%. In addition to identifying the channel as a trapezoid, the area reduction resulting from the rounded corners was accounted for while calculating the equivalent hydraulic diameter.

The remaining discrepancies can be attributed to using fRe_{app} values for a true trapezoidal duct, as no data is available for the trapezoidal geometry with rounded corners. Also, the first

order K factors used for inlet and exit losses based upon conventional empirical data can be attributed to the remaining discrepancies.

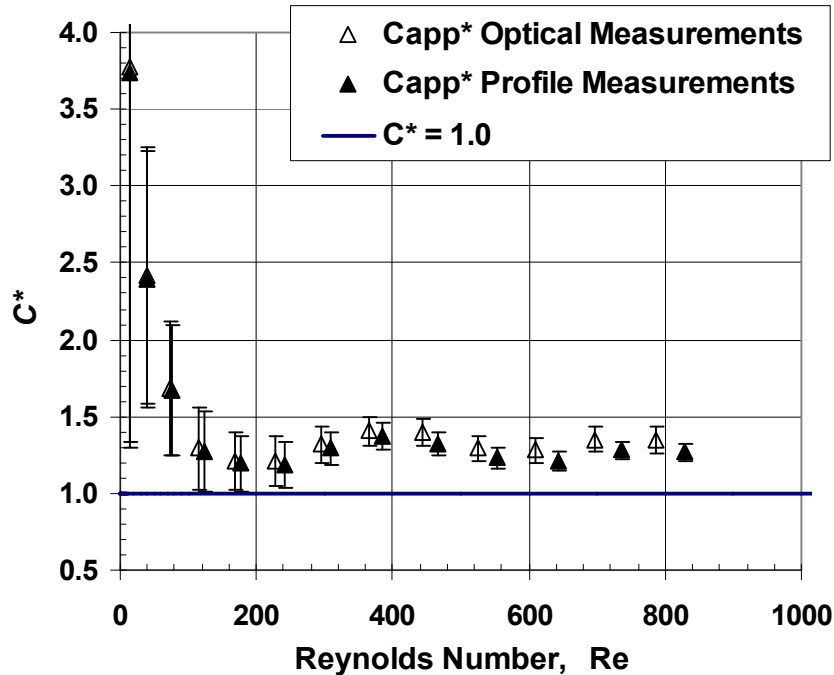


Figure 8.4: Apparent C^* Ratio vs. Reynolds Number Considering Measured Cross Section. Line = theoretical prediction, points = rectangular data, triangle points = trapezoid data; Adiabatic, trapezoid top width = 194 μm , height = 244 μm , $L = 10$ mm, $\theta = 85$ degrees.

The fin geometry is also of concern with heat transfer calculations. Figure 8.5 shows the fin geometry for the fabricated microchannels. The fin thickness is narrower at the base of the fin than at the top (93.9 μm at the top against 54.3 μm at the fin base). The undercutting resulting from the fabrication can become substantial. The heat flux through the fin area will not be uniform. This leads to a severe reduction in the fin efficiency. It is therefore recommended that the thickness of the fin at the base should be used in determining fin performance. More work is needed in this area to characterize the thermal performance of microchannels fabricated in silicon.

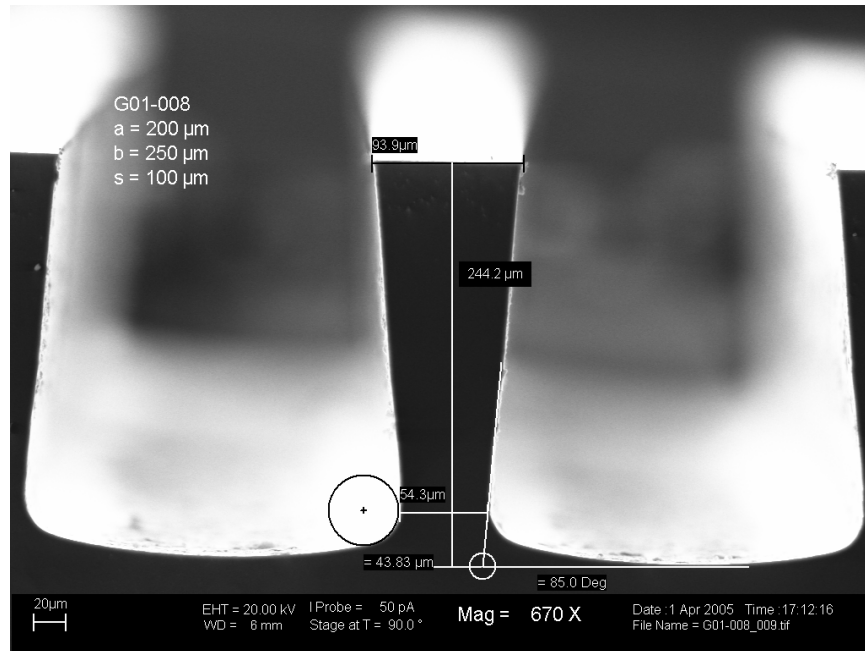


Figure 8.5: Fin Cross Section of Silicon Microchannel. $s_{top} = 94 \mu\text{m}$, $s_{bottom} = 54 \mu\text{m}$, $\theta = 85$ degrees.

8.3 Microchannel Surface Roughness Measurements

The surface roughness of the microchannel walls is another important parameter. In conventional sized channels, the surface roughness has been identified to play a dominate role only in the turbulent region. The data reduced from previous literature suggest the same trend for microchannels. However, this is still an open topic of discussion. It would be important for researchers to report the surface roughness in their work in order to build confidence in that statement.

Figure 8.6 shows the nature of the surface roughness in the present microchannel test sections. The pictures of the side wall and bottom wall surfaces showing surface roughness features are obtained using scanning electron microscope (SEM) and are shown in the figure. The majority of the surface has a very small e/D_h ratio, approximately 0.002. The bottom wall

does have some roughness features seen in the bottom inset. The average size of those features is $1.5\ \mu\text{m}$, making the e/D_h ratio approximately 0.007. The side wall has larger roughness features due to the method of fabrication. These features are an artifact of the deep reactive ion etching processes used. The average roughness feature for the side wall is $2.5\ \mu\text{m}$ and the resulting e/D_h ratio is 0.01. The measurement of the surface roughness for future microchannel works should be carefully evaluated. However, it should be noted that a much smoother sidewall can be achieved for DRIE microchannels which would result in lower e/D_h ratios.

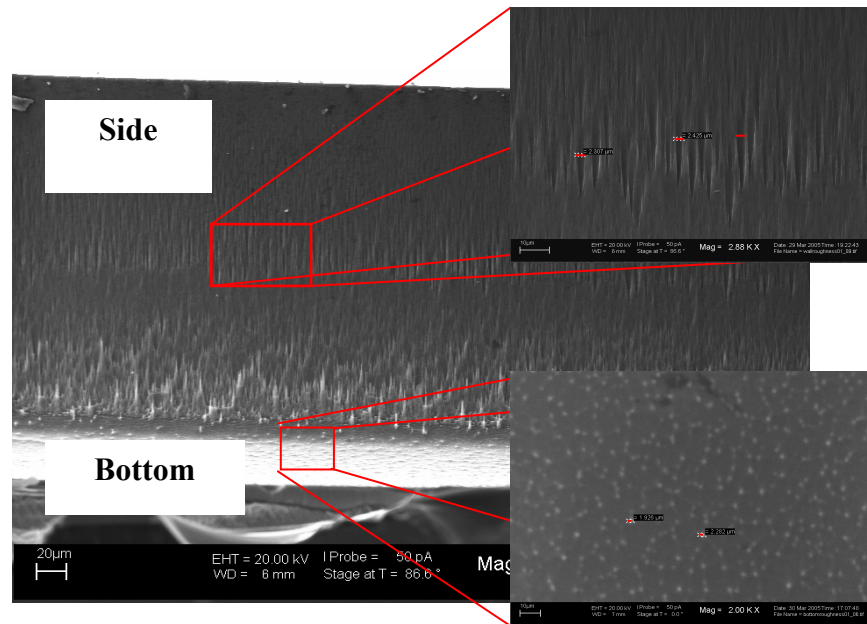


Figure 8.6: Surface Roughness in the Microchannels. Side wall $e/D_h = 0.01$, Bottom wall $e/D_h = 0.007$.

8.4 Normalized Heat Transfer Performance

As determined in Chapter 2, the normalized A^* parameter is proposed to compare the thermal performance of the microchannels to the theoretical values. For each of three flow cases, the A^* parameter has been calculated for three plain microchannel geometries of G01-001, G01-003, and G01-005.

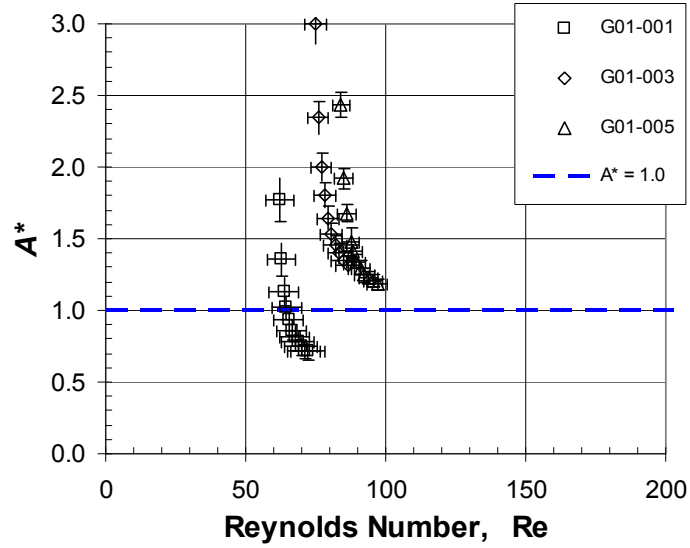


Figure 8.7: A^* vs. Reynolds Number. For $Q = 39$ mL/min; Plain = G01-001, G01-003, G01-005; $b = 200$ μ m; $T_i = 20$ $^{\circ}$ C.

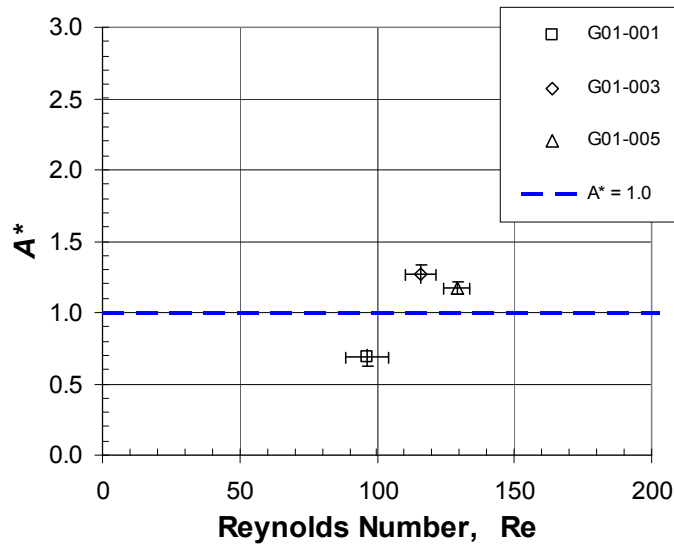


Figure 8.8: A^* vs. Reynolds Number. For $Q = 53$ mL/min; Plain = G01-001, G01-003, G01-005; $b = 200$ μ m; $T_i = 20$ $^{\circ}$ C.

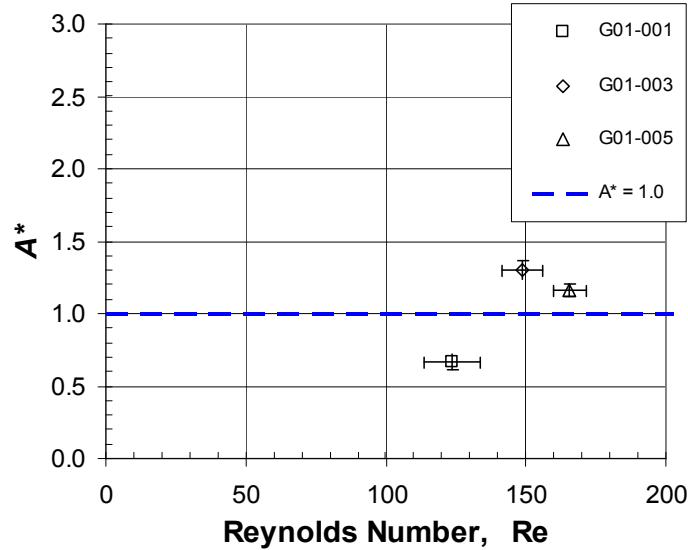


Figure 8.9: A^* vs. Reynolds Number. For $Q = 69$ mL/min; Plain = G01-001, G01-003, G01-005; $b = 200$ μm ; $T_i = 20$ $^\circ\text{C}$.

Figure 8.7 shows A^* versus Reynolds number for a flow rate of 39 mL/min. For each individual data set, A^* decreases as the heat flux increases. One explanation is the increase in the ΔT for larger heat fluxes. The experimental uncertainty will be decreased and the data will be more accurate when the ΔT is larger. Another explanation for some error is the boundary condition determination. The present work used a one-dimensional conduction assumption for the microchannel test sections.

To simply the confusion resulting from displaying all of the heat fluxes recorded for the data sets, only the maximum heat flux achieved for each case is reported in Figs. 8.8 and 8.9. Once again, there is good general agreement in value. A second order model that accounts for the conjugate heat transfer condition may lend improved agreement. However when compared to the scatter in the data from the previous literature, the present work shows good agreement. It can be concluded that the present work's test section are valid and the data is reasonable.

CHAPTER 9

SINGLE-PHASE LIQUID HEAT TRANSFER ENHANCEMENT IN MICROCHANNELS

The single-phase liquid heat transfer enhancement techniques that can be incorporated into microchannels and minichannels will be presented in this chapter. After reviewing the general field of conventional heat transfer enhancement, the following concepts have been identified for inclusion into a microchannel heat exchanger. The augmentation techniques can be separated into two categories; passive and active. Finally, the design of one passive technique is presented.

9.1 *Passive Enhancement Techniques*

The passive enhancement techniques used in single-phase flow augmentation will be discussed in this section. Some of the basic techniques used for the passive enhancement include flow disruption, secondary flows, surface treatments, and entrance effects. Several of these techniques can be easily implemented into a microchannel or a minichannel.

9.1.1 Flow Disruptions

The inclusion of flow interruptions is perhaps the most attractive technique for microchannels. The flow disruptions provide increased mixing and also can serve to break up the boundary layer causing flow transition. In conventional sized passages, the flow interruption can be achieved using flow inserts, flow disruptions along the sidewalls, and offset strip fins.

These techniques are strong candidates for implementation in minichannels. The ability to manufacture smaller diameter wire has progressed enough to manufacture a thin wire, such as those for surgical applications, and tightly coil the wire to insert it into a minichannel.

The use of flow inserts in a microchannel may be impractical due to the confined space requirements. Microchannel dimensions prove to be the limiting factor for the wire diameter currently available. However, the basic concept of flow inserts can be applied to microchannels. The flow disruption technique could find easy integration into microchannels using carefully constructed geometries. The feature size and geometry of objects improve as the achievable critical dimension is decreased. The sidewalls of the microchannel could contain flow obstacles that disrupt the boundary layer. Figure 9.1 shows sidewall obstructions in a microchannel. The triangular obstruction seen in Fig. 9.1a would serve to cause swirl flow. The steps shown in Fig. 9.1b would break up the boundary layer and change the thermal and hydraulic gradients.

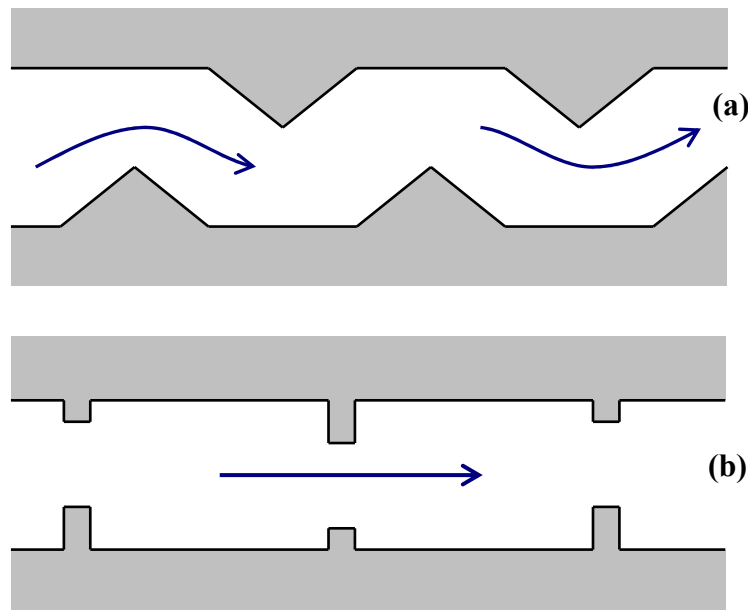


Figure 9.1: Sidewall flow obstructions in a microchannel. a) triangular obstructions, b) square obstructions.

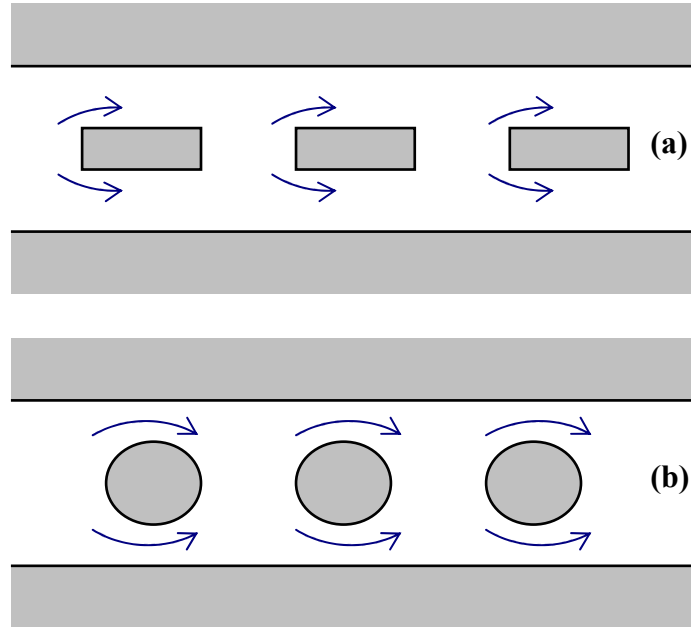


Fig. 9.2: Flow obstructions in the channel. a) simple rectangular geometry, b) circular profile.

Another possibility is to use flow obstacles in the bulk area of the microchannel. Figure 9.2 shows some channel flow obstructions. Figure 9.2a shows some obstructions with simple rectangular geometries. Figure 9.2b shows some obstructions with circular geometries. The heights of these structures could vary to increase the secondary flows in the flow field. As the achievable critical dimensions in lithography are reduced, a more refined circular profile can be achieved. These geometries can be optimized and intermixed to achieve the maximum amount of heat transfer enhancement with the lowest pressure drop penalty.

9.1.2 Channel Curvature

Several researchers have demonstrated that heat transfer enhancement can be achieved by creating a curved flow path. The traditional parabolic velocity profile becomes skewed due to

the additional acceleration forces, causing the angle between the gradients to decrease and facilitate enhancement.

Sturgis and Mudawar (1999) demonstrated the enhancement in a curved channel. The radius of curvature was 32.3 mm and the channel had a cross section of 5.0 x 2.5 mm. The resulting hydraulic diameter is 3.33 mm. The enhancement reached as much as 26% for the curved channel versus a straight channel.

This technique is not really practical in a large sized conventional passage. The application is, however, a possibility in minichannels for using return bends for compact heat exchangers. However, the greatest potential lies in a microchannel. The radius of curvature can be approximately a few millimeters to a few centimeters but, considered to be large compared to the channel diameter. The compact nature of the microchannel flow network could allow for serpentine flow channels to utilize the curvature enhancement. This concept can be seen in the work involved in fabricating a microsystem gas chromatography column.

9.1.3 Re-entrant Obstructions

The entrance region of channels can also provide heat transfer enhancement. There are a few researchers that have reported the enhancement gained in the entrance region of a microchannel, Gui and Scaringe (1995). This technique could also find application in minichannels. However, short lengths and low Reynolds numbers found in microchannel flows seem to be more appropriate. Gui and Scaringe reported heat transfer enhancement in microchannel heat sinks. The hydraulic diameters range from 221 μm to 388 μm . They suggested that the high heat transfer coefficients resulted from the decreased sizes, entrance effects, pre-existing turbulence at the inlets, and wall roughness.

The short lengths in a microchannel could allow a designer to build in entrance spaces in the flow network. The sudden expansion and contractions in flow area would generate entrance effects. This would cause the flow to be in a perpetual state of development, thus causing greater heat transfer enhancement. Figure 9.3 demonstrates such an arrangement. The cavities could also be used for pressure measurements and possible mixing sites.

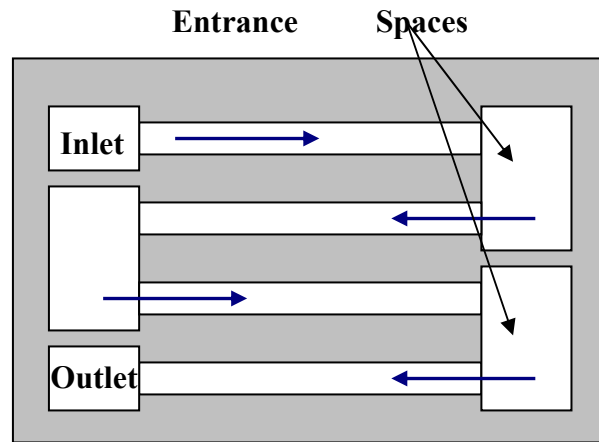


Figure 9.3: Entrance spaces in a microchannel flow network.

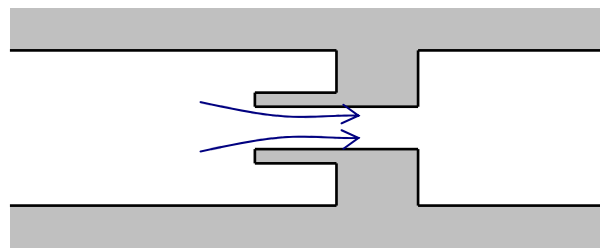


Figure 9.4: Re-entrant structures included in a microchannel.

Another possibility utilizing entrance effects is shown in Fig. 9.4. In this case, a re-entrant structure is incorporated into the channel. Structures such as this could eventually be optimized to provide the maximum entrance effects with the minimal pressure drops. These structures could be arranged in a repeating array along the length of a channel, causing

continually developing flow. Similar structures could be included in a minichannel as well. However, the design of these structures might be limited to simple geometries such as orifices due to manufacturing constraints. However, the pressure drop penalties in these apparatuses need to be carefully evaluated.

9.1.4 Secondary Flows

Many researchers have demonstrated that secondary flows within the flow field provide enhancement. This can be seen in conventional channels. The technique can be applied in minichannels by incorporating offset strip fins, chevron plates and other similar refinements for minichannels are possible. Optimizing the shape and pitch of such devices will continue to improve heat transfer enhancement.

The generation of secondary flows or swirl flows also has potential in microchannels. Microchannel geometries can be manipulated to produce secondary flow within the flow field. Figure 9.5 shows a simple geometry that can generate secondary flows. Smaller channels are added between the main flow channels. Secondary flow will move from one channel to another via these channels.

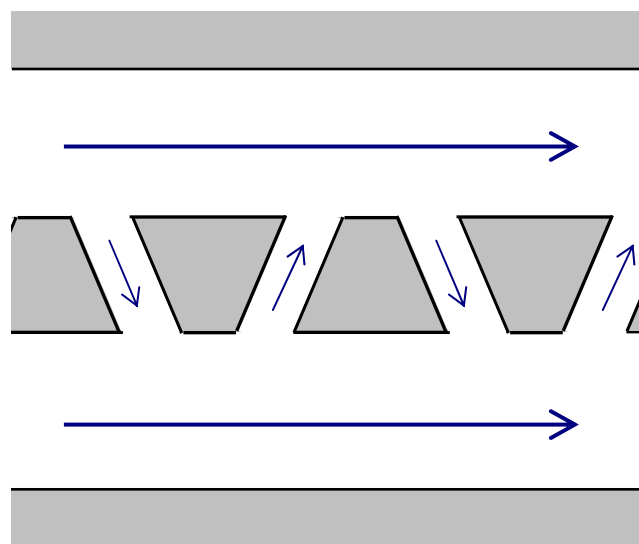


Figure 9.5: Secondary flow channels.

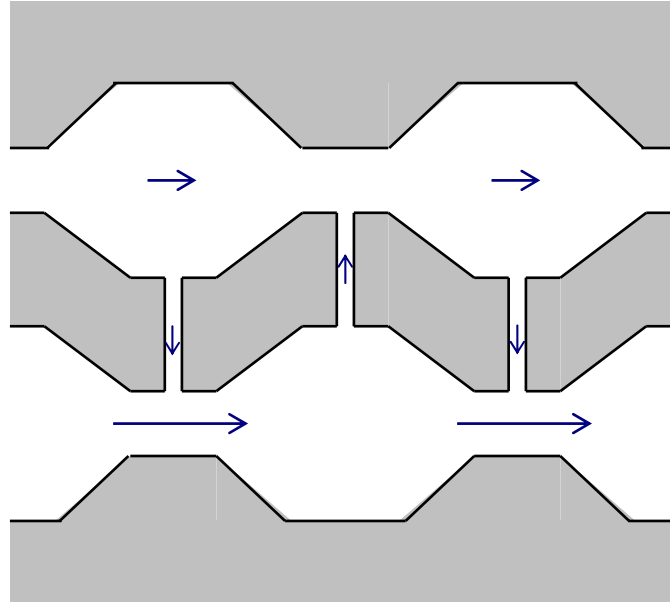


Figure 9.6: Venturi based secondary flow.

A second method for generating secondary flow is derived from a conventional device. A venturi can be manipulated to generate secondary flow without external power or a major increase in pressure drop. Figure 9.6 shows a venturi based secondary flow apparatus. The throat area is connected to the larger area section of an adjacent microchannel. The reduction in pressure at the throat area seen from the reduction in area will draw flow in from the larger area of the adjacent channel. This technique could also be utilized to increase fluid mixing and the addition of another flow stream to the main flow stream while eliminating the need for secondary flow pumping power. Once again, the pressure drop penalties could be a limiting factor for these devices.

9.1.5 Out of Plane Mixing

A technique being developed to increase binary fluid mixing could also be applied to the heat transfer enhancement in microchannels. Bondar and Battaglia (2003) have studied the effect of out-of-plane or three-dimensional mixing of two-phase flows in microchannels. They have achieved a high degree of fluid mixing. An example of a three-dimensional twisted microchannel is shown in Fig. 9.7. This work could provide a path to follow for single-phase

heat transfer. The rotation of the fluid will promote mixing and therefore change the hydrodynamic and thermal gradients.

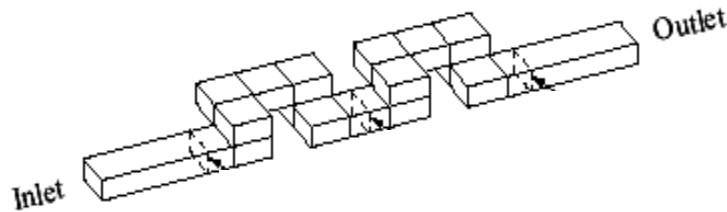


Figure 9.7: Three-Dimensional Twisted Microchannel, Bondar and Battaglia (2003).

9.1.6 Fluid Additives

The addition of small particles to the fluid can sometimes provide heat transfer enhancement. The use of small particles containing a phase change material (PCM) to achieve heat transfer enhancement has been studied. The particles begin in the solid state. As the fluid temperature increases, the particles reach their melting point and begin to melt. The latent heat of fusion involved with the melting of the PCM creates an enhancement. In other words, the effective heat capacity of the fluid has changed due to the presence of the PCM.

Hu and Zhang (2002) studied the effect of microcapsules containing a PCM. The radius of the particles used was $50\ \mu\text{m}$ in a $1.57\ \text{mm}$ radius duct. Figure 9.8 shows the effect of particle concentration on the heat transfer enhancement. The figure shows the degree of heat transfer enhancement versus the non-dimensionalized axial coordinate, using the duct radius. This method works well in conventional channels. Smaller particles are being developed for use in minichannels and may possibly extend to microchannels.

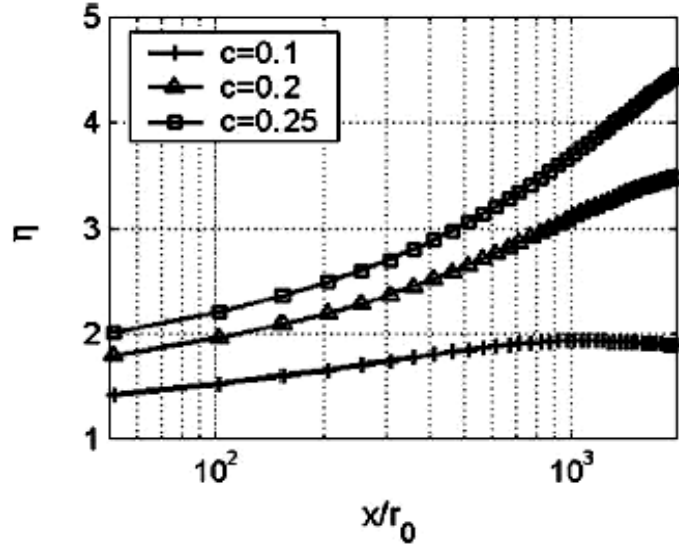


Figure 9.8: Effect of concentration on single-phase heat transfer coefficient, Hu and Zhang (2002); $r_o = 1.57$ mm.

Small quantities of another liquid can be added to the working fluid to achieve enhancement. The concentration of the secondary substance affects the amount of enhancement obtained. A good example is seen in Peng and Peterson (1996). They used water as the working fluid and methanol as the additive. Technically, this would be considered a two-phase mixture. However, Peng and Peterson reported the results in terms of single-phase heat transfer enhancement. The present work will also consider the mixture in such a context. It should be noted that the mixing of these additives typically does not achieve a perfect mixture. Therefore, the use of this technique can provide heat transfer enhancement in a very specific range of operation. Due to the imperfect mixture the heat transfer coefficients can decrease outside this range.

The recent development of nanoparticles, such as those used with Microscale Particle Image Velocimetry (μ PIV), provides some possibilities for microchannel heat transfer

enhancement. The particles could be included to augment the heat transfer without presenting a major clogging issue.

9.1.7 Surface Roughness

One passive technique is to alter the characteristics of the heated surface. This method reduces the thermal boundary layer thickness and also aids in early transition into turbulent flow. The conventional way to alter the surface is to increase the roughness of the surface. The effective roughness e/D ratio is increased to create a boundary layer influence. The roughness ratio can be very large in a microchannel. Therefore, the roughness structure could approach the channel diameter and cause adverse flow behavior. This issue is a very active area of current research. Kandlikar et al. (2003) studied the effect of surface roughness in a minichannel flow. They determined that the e/D ratio has a larger effect in smaller diameter channel than the same e/D ratio in a conventional channel. Further information on the microfluidic physics is required for implementation.

Champagne and Bergles (2001) presented an interesting work to develop a variable roughness enhancement structure. The idea utilized an insert constructed from a shape memory alloy (SMA), specifically Nickel Titanium. As the change in temperature increased, the insert would expand and increase the heat transfer enhancement. This concept could be expanded to minichannels and microchannels. Some SMAs could be inserted into the channels to provide a similar function.

9.1.8 Surface Treatment

The surface of the microchannels can also be treated to change the behavior of the fluid to surface interaction. The surface can be manipulated to make it hydrophilic or hydrophobic. Sections of different surface behavior can be fabricated. Figure 9.9 shows a channel that has the surfaces coated to create hydrophilic and hydrophobic sections.

The fluid sees a hydrophilic section first. The fluid is highly wetting in this region. The next section is hydrophobic and the contact angles will change. The alternating surface regions will cause changes in the contact angles and therefore influence the flow field. The capillary number seen in equation (1) would give insight into the effect of contact angle.

$$Ca = \frac{\mu V}{\sigma} \quad (9.1)$$

There are several other applications of this technique in microfluidics. This technique will have a greater impact for two-phase flow systems. The contact line between the liquid-vapor-surface will be affected by the wetting behavior of the surface. This technique could also be used in a micro-total analysis system to control the local behavior of the liquid surface interface.

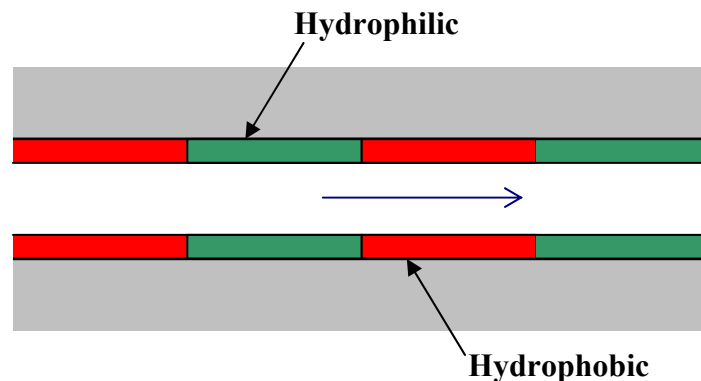


Figure 9.9: Microchannel with hydrophilic and hydrophobic surface treatments.

9.2 Active Enhancement Techniques

The active enhancement techniques used in single-phase flow augmentation will be discussed in this section. Generally, these techniques require additional, external input into the system. The input to the system could be in the form of power, electricity, RF signals, or external pumps.

9.2.1 Vibration

Vibration in the fluid or surface is another active technique that has been applied to conventional channels. The tubes in some conventional heat exchangers can vibrate, providing heat transfer enhancement. This technique could easily be applied to a minichannel heat exchanger. The smaller more compact nature of the tube bundles would allow for easier access for tube vibration.

Recently, Go (2003) studied the effect of microfins oscillating due to flow-induced vibration. The working fluid was air at velocities of 4.4 m/s and 5.5 m/s. A microfin array was fabricated on a heat sink. As the fluid moves over the microfins, a vibration was induced that caused heat transfer enhancement. Figure 9.10 shows the temperature difference for both a microfin array and a plain heat sink. It was determined that the microfins provided up to an 11.5% enhancement over a plain heat sink.

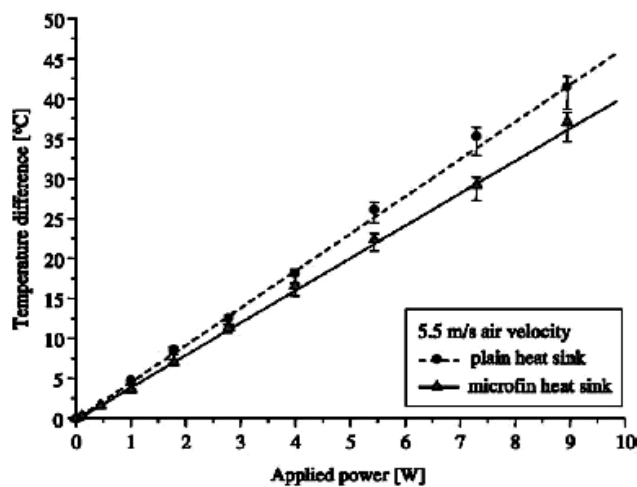


Figure 9.10: Effect of microfin array on heat sink temperature difference, Go, (2003).

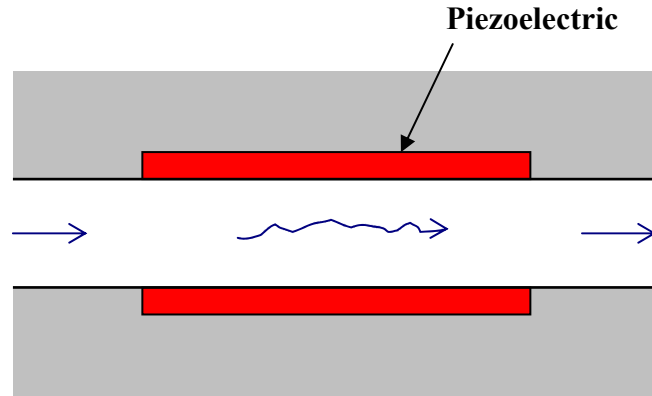


Figure 9.11: Piezoelectric enhanced microchannels.

The use of conventional external vibration generators in a microchannel is impractical due to the large sizes and the large power requirements. However, a vibrating source could be integrated in a microchannel wall. The same technology that generates piezoelectric actuators could find application here. If a piezoelectric material can be embedded, deposited, or placed to act on the microchannel walls, the piezoelectric can be made to oscillate at different frequencies. This would generate surface vibrations and cause enhancement. Figure 9.11 shows the piezoelectric enhanced microchannel.

9.2.2 Electrostatic Fields

The enhancement achieved from exposing a flow to an electrical field has been studied by a large number of researchers. They have demonstrated the enhancement for conventional sized heat exchangers as well as minichannel flows. An excellent paper by Allen and Karayiannis (1995) presents a review of the literature on electrohydrodynamic enhancement. The governing equations, working mechanisms, and existing correlations are presented with some experimental work. It is concluded that the corona wind and electrophoresis contribute the most to single-phase heat transfer enhancement.

This technique could also be applied to microchannel flows. In a conventional or a minichannel application, a small insert electrode is present in the flow field. A potential is applied between the insert probe and the channel surface. The electric field that results will

provide a moving corona effect and enhance the heat transfer. Figure 9.12 shows this arrangement for all three channel sizes: conventional, minichannel and microchannel.

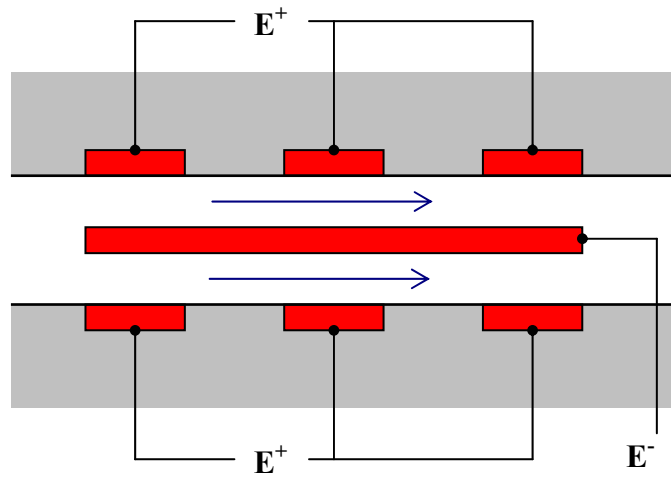


Figure 9.12: Electrostatic forces with insert probe for conventional channel, minichannel, and microchannel.

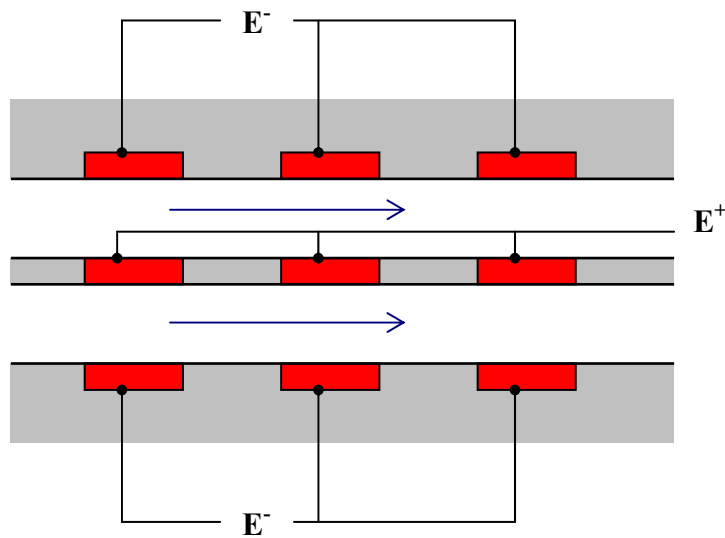


Figure 9.13: Electrostatic forces with wall integrated probes for a microchannel.

The possibility of incorporating the electrodes in the walls of a microchannel is quite attractive. The doped region, which forms the electrode, could easily be formed directly in the wall. The electrical connection can be achieved through the substrate of a cover wafer. Figure 9.13 shows an integrated electrostatic apparatus that incorporates the electrodes in the microchannel walls.

9.2.3 Flow Pulsation

The variation of the mass flow rate through the channel can also provide heat transfer enhancement. Several researchers have demonstrated the mixing enhancement provided by a pulsating flow. Hessami et al. (2003) studied the effect of flow pulsation on a two-phase flow in a 25 mm pipe. They determined that the enhancement could be as much as 15% depending upon the frequency. This technique could be applied in a microchannel. The requirement of delivering constant mass flow rates to a cooling device could be eliminated by utilizing the flow pulsations.

9.2.4 Variable Roughness Structures

Another possibility exists for a variable roughness structure in a microchannel flow. With a variable roughness structure, the heat transfer enhancement could become variable as well. Piezoelectric actuators could be used to control the local surface roughness along the wall. Therefore, the heat transfer enhancement could be customized.

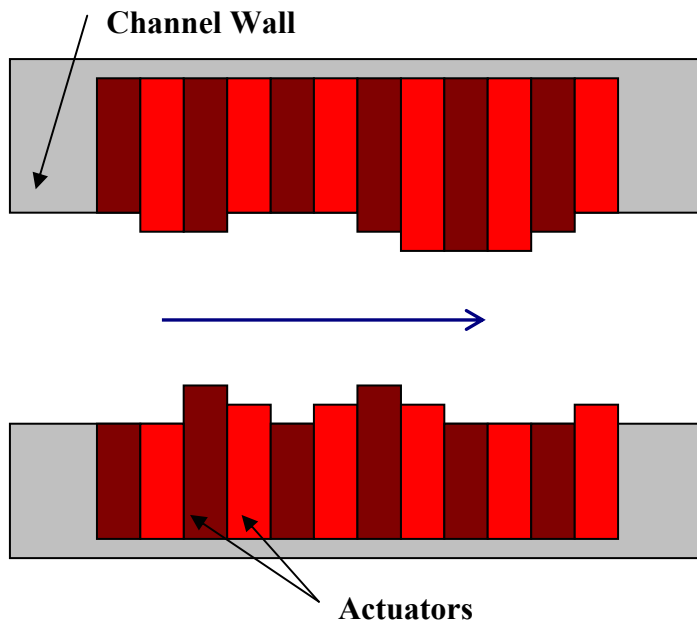


Figure 9.14: Variable roughness structure using actuators.

Figure 9.14 shows a possible variable roughness structure using actuators of some generic type. The actuators could be placed adjacent to each other or within close proximity. These actuators could be controlled independently or in groups to adjust the local roughness of the channel.

9.3 *Implementation of a Passive Enhancement Device*

Several possible heat transfer enhancement techniques have been identified that could be implemented into a microchannel heat exchanger to give improved thermal performance. There are both passive and active techniques described. Some of the technologies could be integrated with today's technology while others need to have further technology developments in order to be realized. Returning to the application of high heat flux microprocessor cooling, let us consider an enhancement technique that could give immediate benefit to this application. A passive flow obstruction enhancement technique will be realized in the silicon microchannel previously used in this work. The design of this enhancement device will be described.

9.3.1 *Design of Enhanced Geometry*

The desire here is to fabricate an enhanced microchannel heat exchanger that can be fabricated with today's technology and can be easily integrated for microprocessor cooling. The most obvious choice is using passive flow obstructions to create heat transfer enhancement. The process should not include any additional process steps and it should be inline the traditional silicon micromachining.

The idea is simply to replace the traditional continuous microchannel walls with short fins that also alternate in position. This is very similar to the concept of offset strip fins in

compact plate heat exchangers. Figure 9.15 shows the concept of using microchannel offset strip fins.

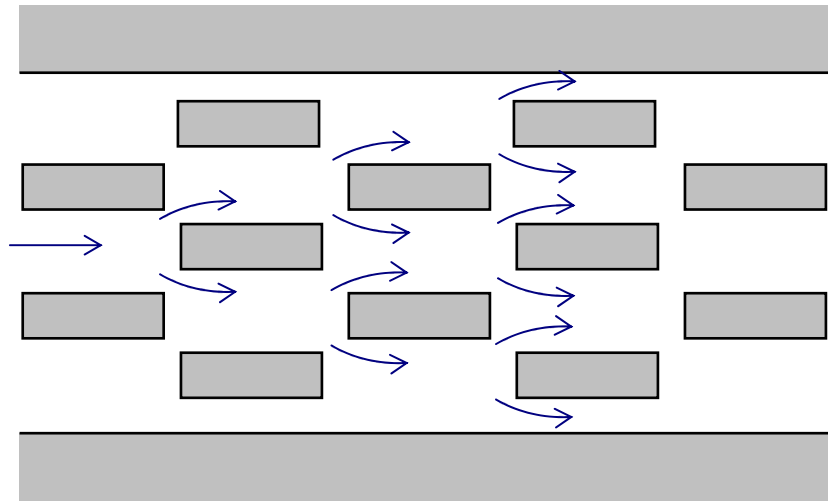


Figure 9.15: Concept of Using Offset Strip Fin Geometry for Microchannel Enhancement.

The fluid enters a flow passage and travels in the flow direction a short distance. Next, the fluid encounters a flow obstruction in the form of another fin. The fluid must separate and move around the next fin. It then travels the length of the second fin and encounters another fin obstruction. The entire process is repeated as the fluid moves down the entire flow length.

As a result, the fluid never enters into a fully developed state and must split and move around the next fin. This device will make use of the enhancement found in developing flows. In addition, the resulting mixing will force the fluid to have more interaction with the heated walls and also provide heat transfer enhancement.

Unfortunately, this heat transfer enhancement will come at the price of added pressure drop for the entire microchannel heat exchanger. The added heat transfer performance must be carefully weighed with the added pressure penalty.

Due to the continually developing flow in the enhanced microchannels, the pressure drop and heat transfer performance will be difficult to compare to conventional theory. This device should be treated as a compact heat exchanger. For a conventional compact heat exchanger, the friction factor and the Colburn j factor are used as the main metrics of performance. These parameters are used to describe the overall performance of the compact heat exchanger. They are used due to the wide variety of complex geometries that occur in current compact heat exchangers. It should be noted that the friction factor for compact heat exchangers is referring to the apparent friction factor and not the purely frictional flow losses friction factor in conventional theory. For the present work, they will be utilized to describe the overall performance of the microchannel heat exchangers and provide a basis of comparison.

A new expression for the hydraulic diameter for the offset strip fin is needed to compare the enhanced microchannels to the plain microchannels. Figure 9.16 shows the nomenclature for the enhanced microchannels. A unit cell is defined in the flow geometry and seen by the dashed lines.

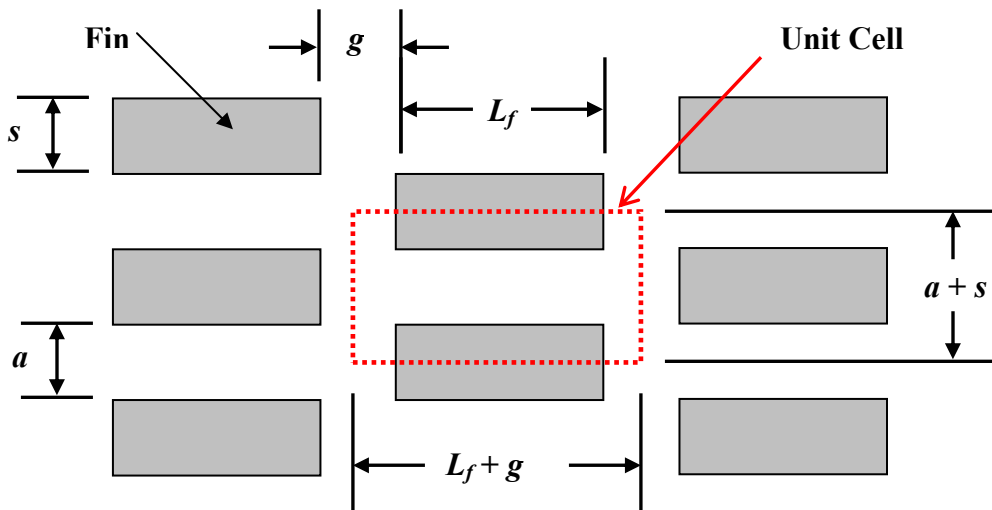


Figure 9.16: Enhanced Microchannel Nomenclature.

The flow passage width is a , the fin thickness is s , L_f is the fin length, and g is the gap between successive fins. The unit cell length is the length of the fin plus the gap distance and the unit cell width is the flow passage width plus the fin thickness. The hydraulic diameter can be derived based upon the compact heat exchanger formulation given in Eq. (9.2)

$$D_h = \frac{4 A_{Free Flow} L_{Unit Cell}}{A_{HT}} \quad (9.2)$$

where $L_{Unit Cell}$ is the unit cell length and $A_{Free Flow}$ is the minimum free flow area. The minimum free flow area is given by Eq. (9.3) and the heat transfer area is given by Eq. (9.4).

$$A_{flow} = b a \quad (9.3)$$

$$A_{HT} = 2 L_f b + 2 s b + (L_f + g)(a + s) - L_f s \quad (9.4)$$

$$A_{HT} = 2 b s + g s + a g + a L_f + 2 b L_f$$

The resulting expression for the offset strip enhanced microchannel geometry is given by Eq. (9.5).

$$D_h = \frac{4 A_{Free Flow} L_{Unit Cell}}{A_{HT}}$$

$$D_h = \frac{4 (a \cdot b) (L_f + g)}{2 b s + g s + a g + a L_f + 2 b L_f} \quad (9.5)$$

$$D_h = \frac{2 a b (L_f + g)}{s \left(b + \frac{g}{2} \right) + \frac{a g}{2} + \frac{L_f}{2} (a + 2 b)}$$

In this formulation, the length of the fin and gap dimensions plays a role in the resulting hydraulic diameter. For the present work, there is no gap used in the reported geometries.

The ends of the fin structures are tapered to form a tip. The reason for this detail is to assist the flow in separating as it moves around the obstruction. The flow should be in continually developing state. However, the fluid could separate from the fin and the

enhancement would be lost if the ends are too blunt. An 80 degree included angle is used to perform this function. The geometries in the present work do not include a gap between the successive rows of fins. The sharpened ends give enough free area in order to allow the fluid to pass the fin. Figure 6.17 shows an SEM micrograph of the enhanced microchannel geometry. This image is taken at the inlet header and the sidewall flow obstructions are also present.

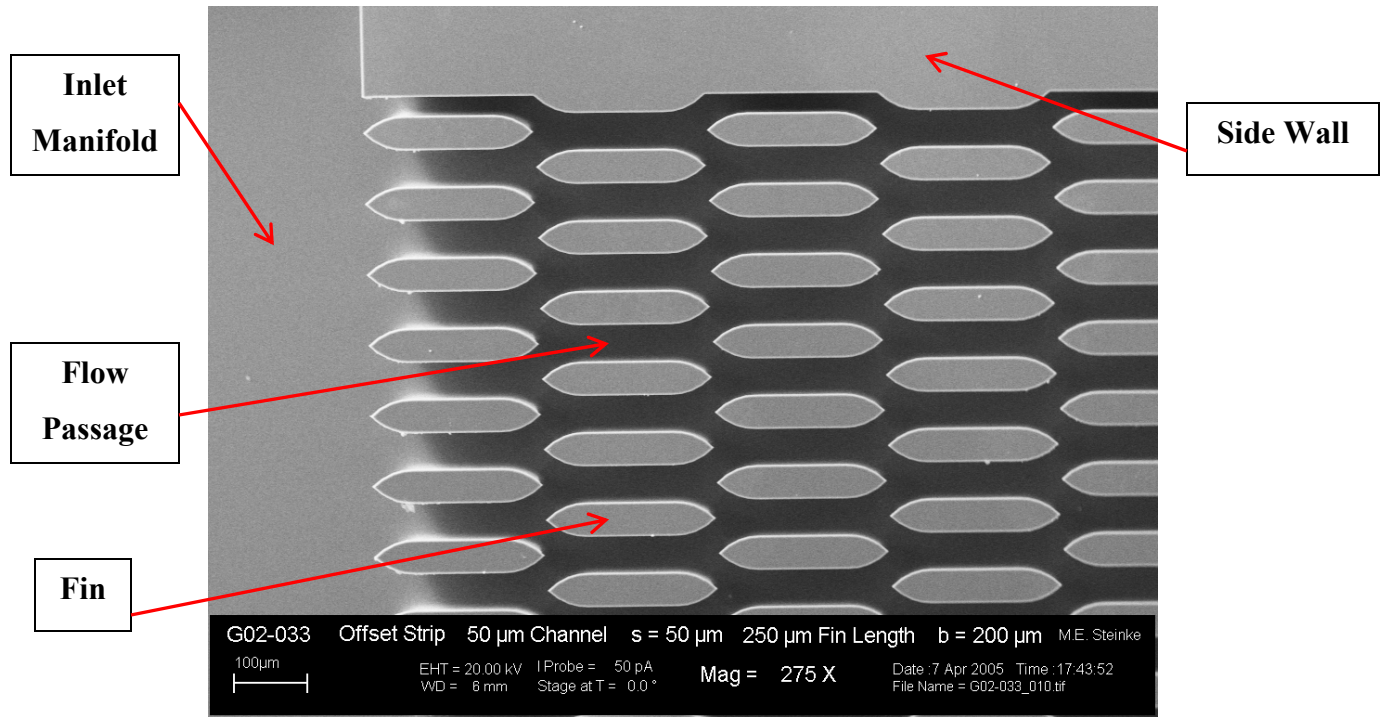


Figure 9.17: SEM Micrograph of Enhanced Microchannels. G02-033, $b = 200 \mu\text{m}$.

There are four different enhanced microchannel nominal geometries seen in Table 9.1. The pitch is fixed at $100 \mu\text{m}$ for all of the geometries. The flow passage width is either 50 or $60 \mu\text{m}$ and the fin thickness is either 50 or $40 \mu\text{m}$, respectively. The fin lengths are also varied to achieve different levels of flow development on the fin surfaces. The equivalent hydraulic diameters range from 76 to $98 \mu\text{m}$.

Figure 9.18 provides a closer look at the fin geometry. As previously stated the ends of each fin are sharpened in order to reduce the pressure loss from blunt end and to allow fluid to pass through each successive layer. Notice that the fin shape is clearly defined and the edges are very sharp.

Table 9.1: Enhanced Microchannel Nominal Geometries.

Number	a μm	s μm	L_f μm	D_h μm	n	L μm
G02-033	50	50	250	76	100	10000
G02-034	50	50	500	82	57	10000
G02-035	60	40	250	92	73	10000
G02-036	60	40	500	98	47	10000

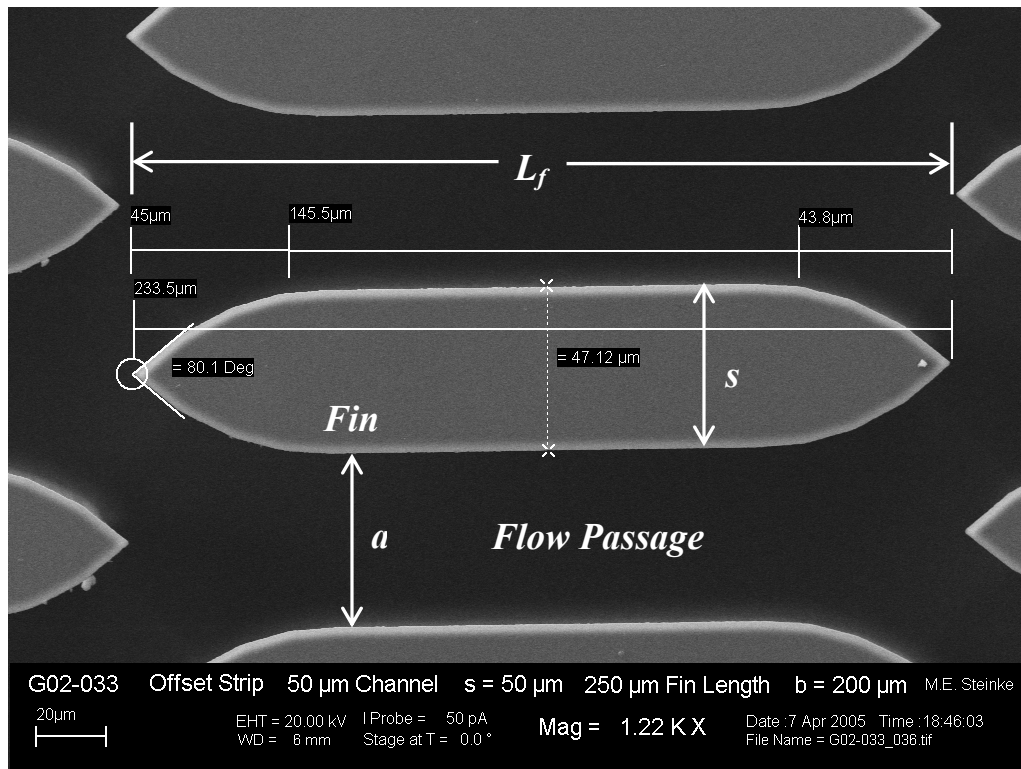


Figure 9.18: SEM Micrograph of a Fin. G02-033, $b = 200 \mu\text{m}$.

The profile of the fin is a complex geometry. Figure 9.19 is an SEM micrograph of a close up look at the fin structure. This view is looking at the beginning row of fins as seen from the manifold. The cross-section of the fin is decreasing in the etch direction. Starting at the top, the cross sectional area of the fin decreases as we move towards the bottom surface. For the G02-033 geometry, the reduction is $7\ \mu\text{m}$ for a single sidewall. The area reduction makes it very difficult to characterize the temperature profile in the fins. A more advanced measurement system would need to be utilized to get any meaningful values for the temperature profiles. For the present work, minimum fin thickness at the base will be used as all of the heat dissipated by the fin must move through that minimum area. Also, notice the slight sculpting of the fin surface due to ruminates of the mask.

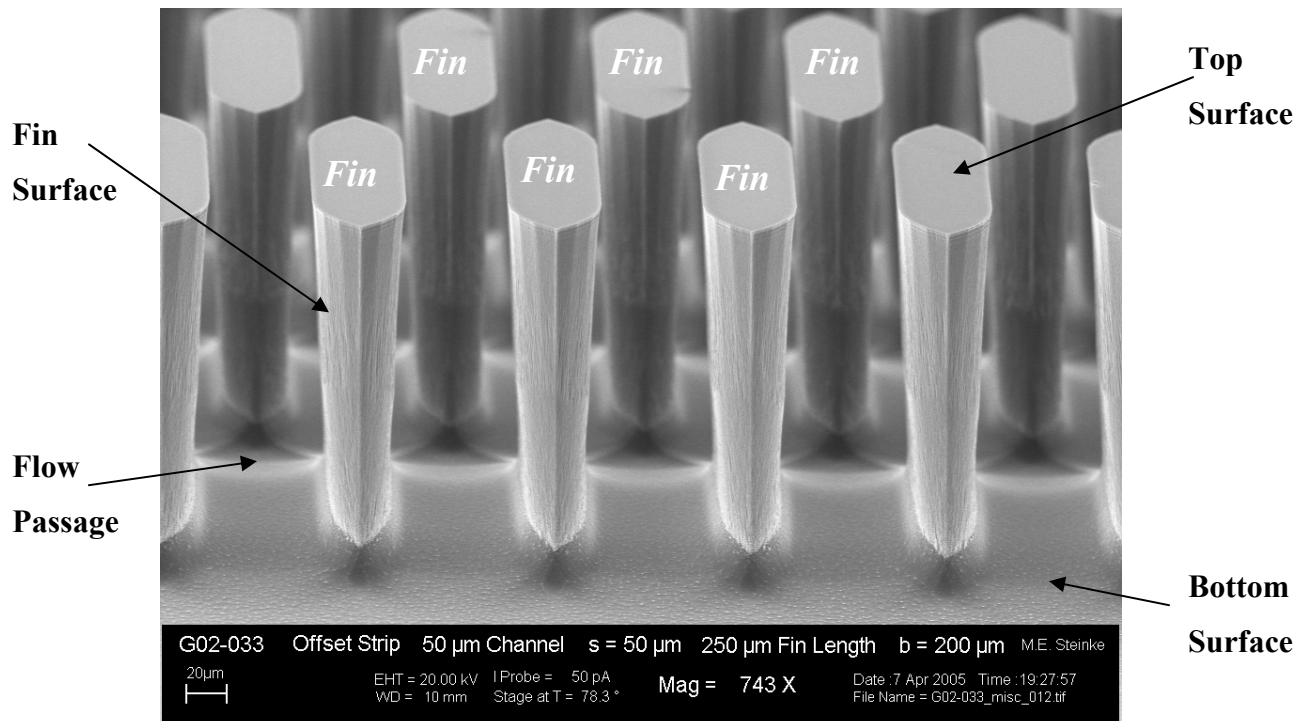


Figure 9.19: SEM Micrograph of the Fin Structure. G02-033, $b = 200\ \mu\text{m}$.

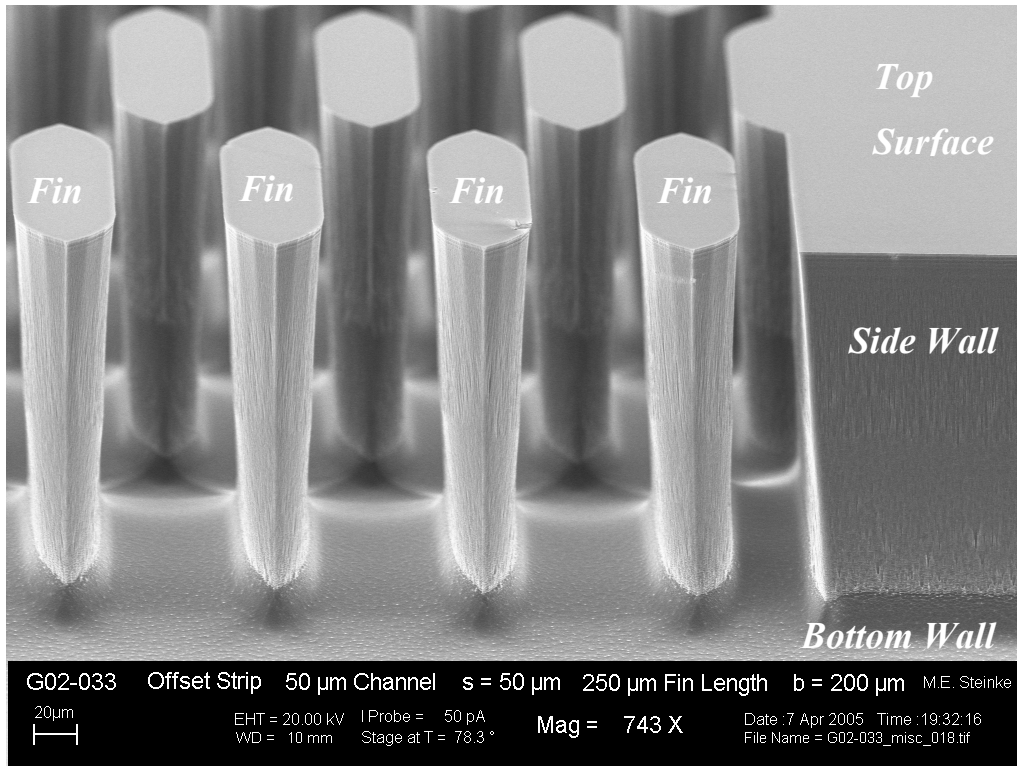


Figure 9.20: SEM Micrograph of the Surface Roughness Occurring in the Enhanced Microchannels. G02-033, $b = 200 \mu\text{m}$.

As discussed in Chapter 8 section 8.4, the surface roughness of microchannel may take on a more dominate role. Although this will have little to no effect upon laminar flow, it will become critical to determine the surface roughness of the flow passages for a turbulent flow case. The surface roughness was also measured for the enhanced microchannels. Figure 9.20 shows a SEM micrograph of the inlet to the microchannels as seen from the manifold area. The side wall roughness is the same as the plain silicon microchannels previously discussed and has a e/D_h ratio of 0.01. The walls of the fins have a rougher texture with an e/D_h ratio of 0.03. The bottom wall seems to have a slightly rougher surface than the plain microchannels with an e/D_h ratio of 0.007. Once again, it would be difficult to predict exactly which surface roughness

values dominates the flow behavior without experimental data. However, one could speculate that the surface with the most fluid contact and area would tend to dominate over the others. Therefore, it is believed that the surface roughness of the fin walls would dominate because of the large total surface area and the high fluid interaction.

CHAPTER 10

EXPERIMENTAL RESULTS FOR ENHANCED SILICON

MICROCHANNELS

The experimental results for the passive enhancement device described in Chapter 9, section 9.3 will be presented in this chapter. The thermal performance is evaluated under the scope of the microprocessor cooling application. Therefore, the results will be presented in terms of the thermal resistances. One must carefully evaluate the added pressure drop the enhancement features create and will be seen using the apparent pressure drop across the microchannel test section.

The enhanced microchannels will be treated as a compact heat exchanger. As a result, the friction factors and the Colburn j factors will be presented for the data sets presented. This allows for the evaluation of the heat transfer and pressure drop performance to be performed simultaneously.

Finally, a new parameter called the pumping flux will be introduced. It is used to provide a direct comparison between plain and enhanced microchannels. Using this parameter, a coefficient of performance is introduced concerning a microchannel heat exchanger.

10.1 *Microchannel Heat Exchanger Thermal Resistance*

The main parameter utilized in microprocessor cooling is the thermal resistance. It is simply a measure of the resistance of the heat exchanger to dissipate the input power. An advantage of using this parameter is that it reduces the complication of local behavior and provides an overall metric of the performance. The unit thermal resistance is given in Eq. (10.1).

$$R = \frac{(T_j - T_i) A_{HT}}{q} \quad (10.1)$$

where R is the unit thermal resistance, T_j is the junction temperature, and T_i is the inlet fluid temperature. The heat transfer area for a unit cell is given by Eq. (9.4). The total heat transfer area is calculated counting the number of unit cells that occur in the microchannel heat exchanger and is used as the total heat transfer area.

To investigate the effect of the offset strip fin enhancement, several experiments are conducted with the plain geometries and the enhanced geometries. The volumetric flow rate into the test section is fixed at three different levels to create three flow cases. The three flow rates are 39 mL/min, 53 mL/min, and 69 mL/min. This causes the mass flow rates to be equivalent for comparison purposes. The actual Reynolds numbers may vary slightly due to geometry and temperature dependent property variations. However, the comparison can still be made on a quantitative basis.

The plain microchannel geometries of G01-001, G01-003, and G01-005, as seen in Table 6.1, will be used for a base performance case. These microchannel geometries are chosen because they all have a fin thickness of 40 μm which is the same or close to the fin thickness of 40 μm and 50 μm in the enhanced microchannels. Finally, a microchannel depth of 200 μm for both the plain and the enhanced microchannels is used.

Figures 10.1, 10.2 and 10.3 shows the thermal resistance verses Reynolds number for the flow rates of 39, 53, and 69 mL/min, respectively. The plain microchannel geometries are represented by open points and the enhanced microchannel geometries are represented by closed points. The prefix G01 refers to the plain microchannels and G02 refers to the enhanced microchannels. The microchannel depth is 200 μm for each of the microchannel geometries.

The inlet water temperature is set to 20 °C for all of the experiments. The uncertainty bars are included for completeness, although they are difficult to see due to the large range represented.

All three figures show that the enhanced microchannel heat exchanger has a much lower thermal resistance than the plain microchannel heat exchanger. For the second and third flow rates, only the maximum point is shown for clarity. The plain microchannels seem to have a thermal resistance near 0.1 °Cm²/W. However, the enhanced microchannels seem to reach a thermal resistance of approximately 0.001 °Cm²/W, irrespective of microchannel geometry. This change can be attributed to the flow never becoming fully developed, promoting mixing, and increased fluid surface interaction which lead to an increase in the conduction at the walls.

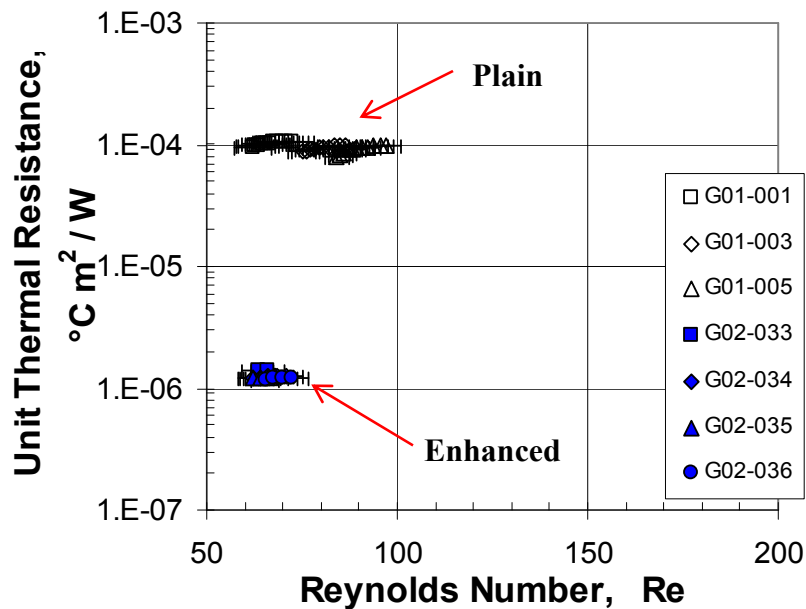


Figure 10.1: Thermal Resistance vs. Reynolds Number. For $Q = 39$ mL/min; Plain = G01-001, G01-003, and G01-005; Enhanced = G02-033, G02-034, G02-35, and G02-036; $b = 200$ μ m; $T_i = 20$ °C.

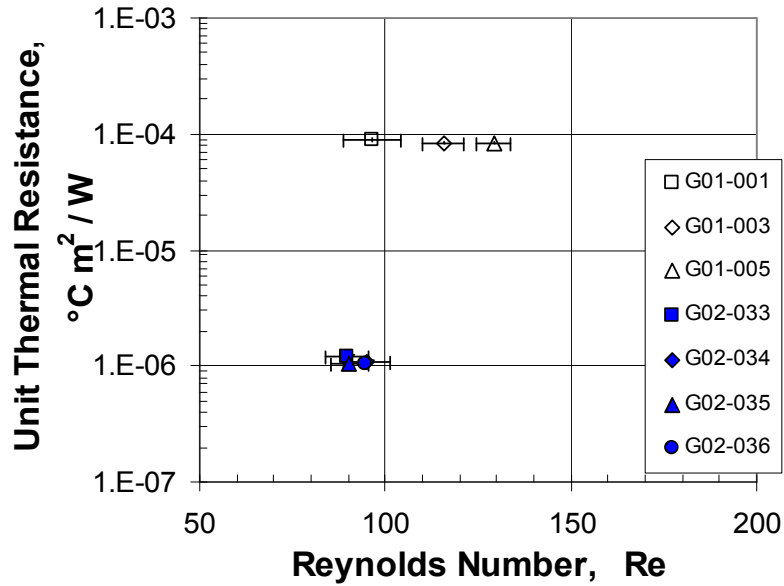


Figure 10.2: Thermal Resistance vs. Reynolds Number. For $Q = 53$ mL/min; Plain = G01-001, G01-003, and G01-005; Enhanced = G02-033, G02-034, G02-35, and G02-036; $b = 200$ μm ; $T_i = 20$ $^{\circ}\text{C}$.

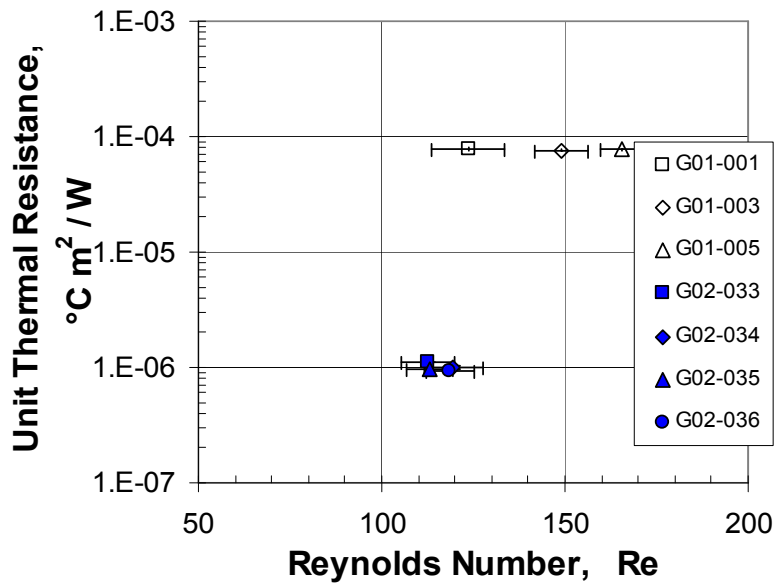


Figure 10.3: Thermal Resistance vs. Reynolds Number. For $Q = 69$ mL/min; Plain = G01-001, G01-003, and G01-005; Enhanced = G02-033, G02-034, G02-35, and G02-036; $b = 200$ μm ; $T_i = 20$ $^{\circ}\text{C}$.

As mentioned, the Reynolds numbers vary for each of the geometries. One reason is the variation of the fluid properties based upon the temperature changes occurring in the microchannel. The water can rise as much as 30 °C for the higher heat flux cases causing significant variation in viscosity, which has been accounted for using Eq. (3.36). After seeing the very large magnitude change in thermal resistance demonstrated by the enhanced microchannels, the small differences in the Reynolds number would not account for the change and therefore is not of concern.

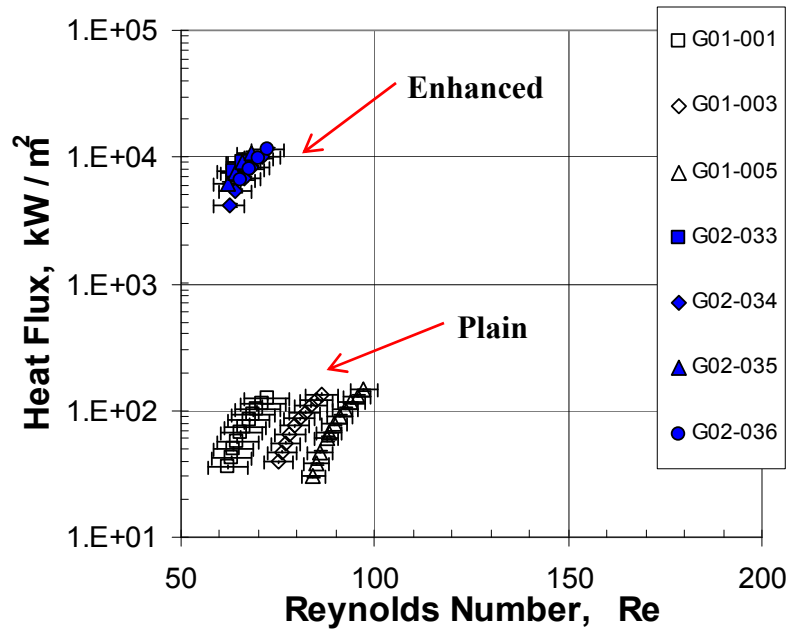


Figure 10.4: Heat Flux vs. Reynolds Number. For $Q = 69$ mL/min; Plain = G01-001, G01-003, and G01-005; Enhanced = G02-033, G02-034, G02-35, and G02-036; $b = 200$ μ m; $T_i = 20$ °C.

To understand the amount of heat that is being dissipated, the heat flux versus the Reynolds number for a flow rate of 38 mL/min is shown in Fig. 10.4. In this figure the uncertainty bars are more readily seen and once again, cannot account for differences seen. As expected, the enhanced microchannels are dissipating substantially more heat than the plain

microchannels. In order to match this performance, the plain microchannels would need to operate at much higher flow rates. The design point of the present work is 200 W/cm^2 . Current microprocessors are operating around 200 W/cm^2 . The plain microchannels operating at approximately 200 W/cm^2 would easily support this heat flux. The enhanced microchannels are dissipating around $1,000 \text{ W/cm}^2$ and become competitive with the heat flux of a two-phase microchannel system. However, the enhanced microchannels come with added pressure drop of only a few tens of kilopascals versus the plain microchannels.

10.2 Apparent Pressure Drop

It is important to investigate the added pressure drop in the enhanced microchannels. The added pressure penalty must be carefully considered when designing an entire liquid cooling system. It is critical to measure the overall pressure drop in order to properly size a fluid pump. For the remainder of this discussion, the pressure drop referred to is actually the apparent pressure drop. The measured pressure drop in the inlet and outlet plenums includes some inlet and exit losses. Those losses are removed and the remaining pressure drop is the apparent pressure drop.

For the enhanced microchannels, it is very difficult to separate the pressure drop due to frictional losses from those due to developing flows since the flow never reaches the fully developed condition. Keeping the pressure drop in the apparent form is also in agreement with traditional compact heat exchanger analysis. Figures 10.5, 10.6, and 10.7 show the apparent pressure drop for the three different flow rates. In each case, the enhanced microchannels have a substantially higher pressure drop than the plain microchannels. This is an expected result due to the added flow blockage presented by the inclusion of the fin structures.

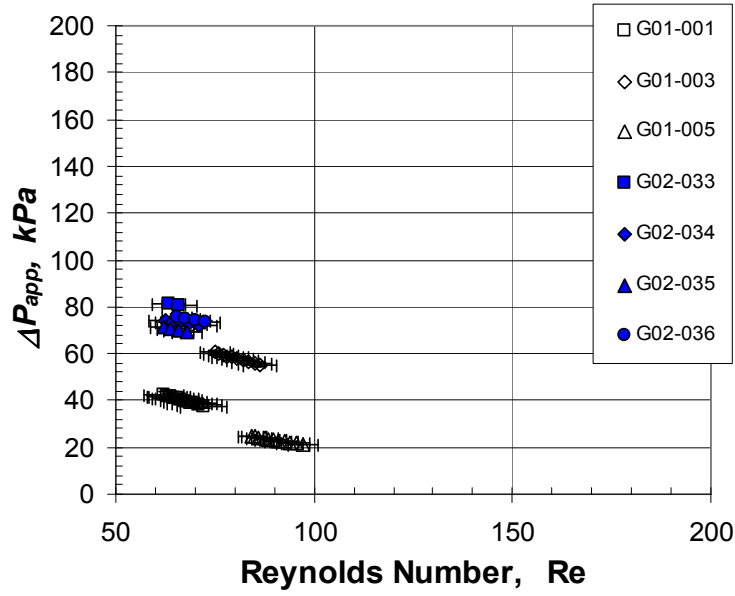


Figure 10.5: Apparent Pressure Drop vs. Reynolds Number. For $Q = 39$ mL/min; Plain = G01-001, G01-003, and G01-005; Enhanced = G02-033, G02-034, G02-35, and G02-036; $b = 200 \mu\text{m}$; $T_i = 20^\circ\text{C}$.

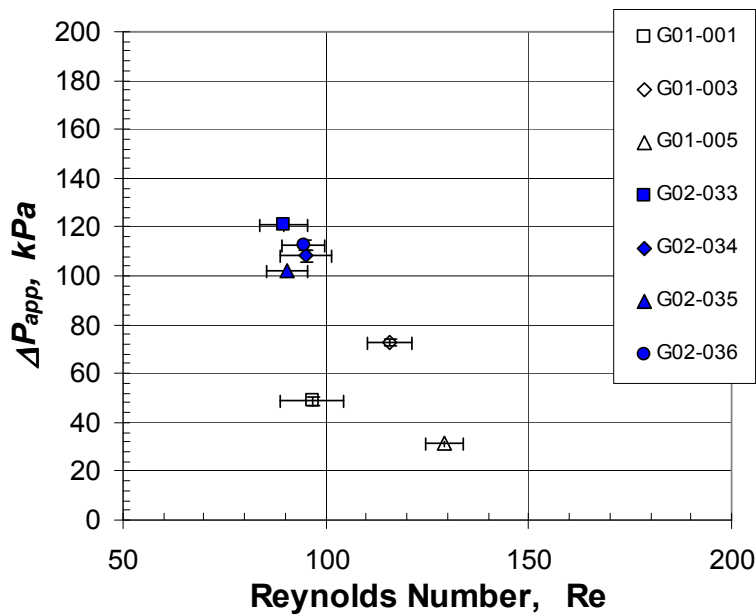


Figure 10.6: Apparent Pressure Drop vs. Reynolds Number. For $Q = 53$ mL/min; Plain = G01-001, G01-003, and G01-005; Enhanced = G02-033, G02-034, G02-35, and G02-036; $b = 200 \mu\text{m}$; $T_i = 20^\circ\text{C}$.

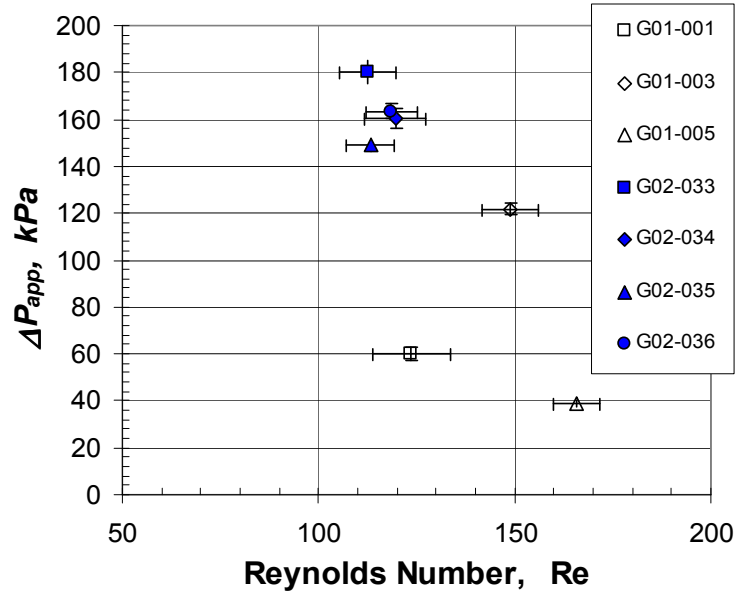


Figure 10.5: Apparent Pressure Drop vs. Reynolds Number. For $Q = 69$ mL/min; Plain = G01-001, G01-003, and G01-005; Enhanced = G02-033, G02-034, G02-35, and G02-036; $b = 200$ μm ; $T_i = 20$ $^{\circ}\text{C}$.

10.3 f_{app} and j Factors

The friction factor and Colburn j factors are reported to give the relationship between the heat transfer performance and the pressure drop. Figures 10.6, 10.7, and 10.8 all show f and j occurring for each of the microchannel heat exchanger geometries.

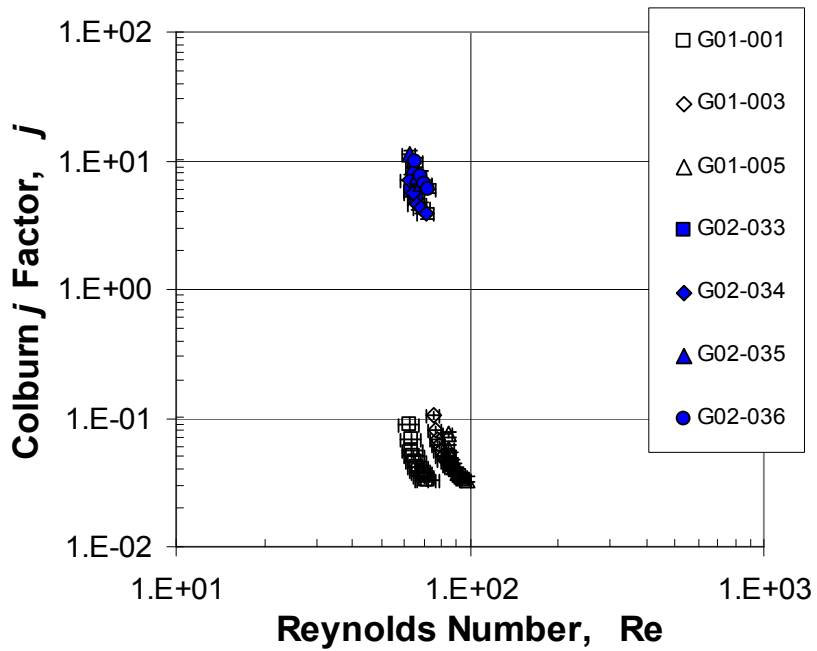
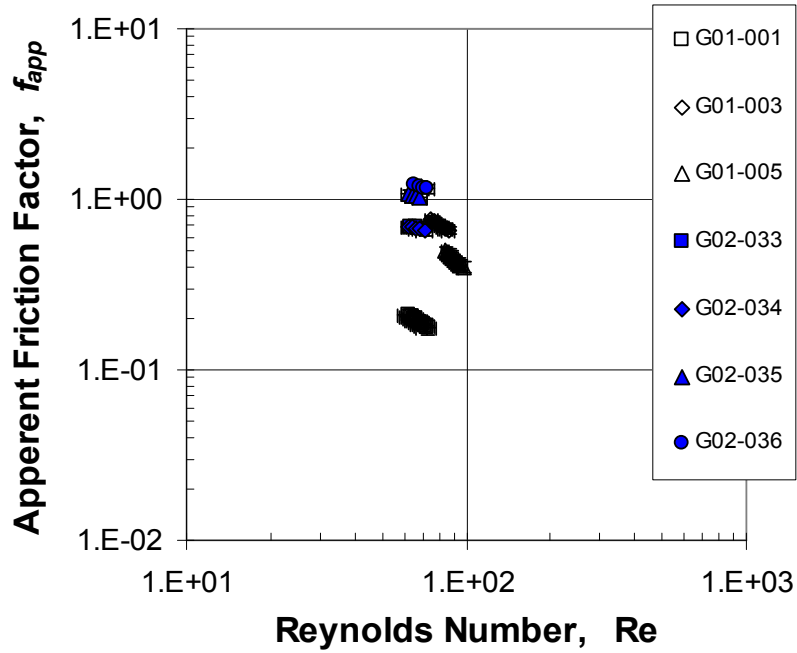


Figure 10.6: Friction and Colburn j Factors vs. Reynolds Number. For $Q = 39$ mL/min; Plain = G01-001, G01-003, and G01-005; Enhanced = G02-033, G02-034, G02-35, and G02-036; $b = 200$ μ m; $T_i = 20$ $^{\circ}$ C.

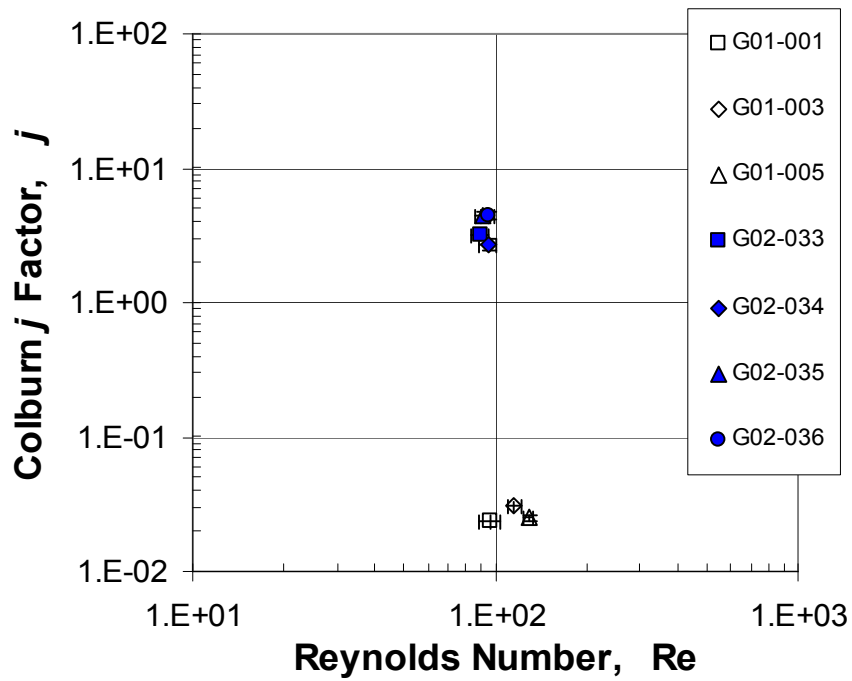
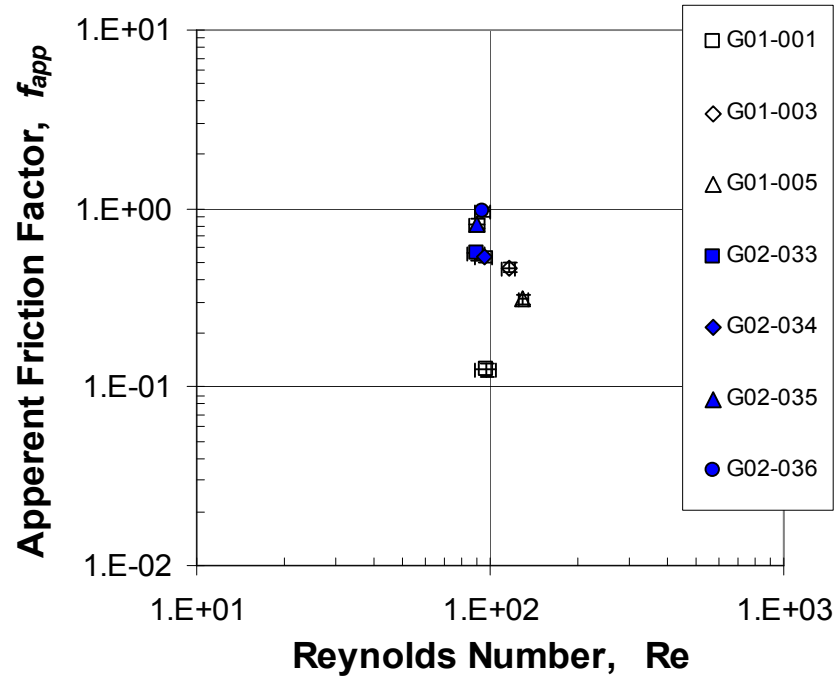


Figure 10.7: Friction and Colburn j Factors vs. Reynolds Number. For $Q = 53$ mL/min; Plain = G01-001, G01-003, and G01-005; Enhanced = G02-033, G02-034, G02-35, and G02-036; $b = 200$ μ m; $T_i = 20$ $^{\circ}$ C.

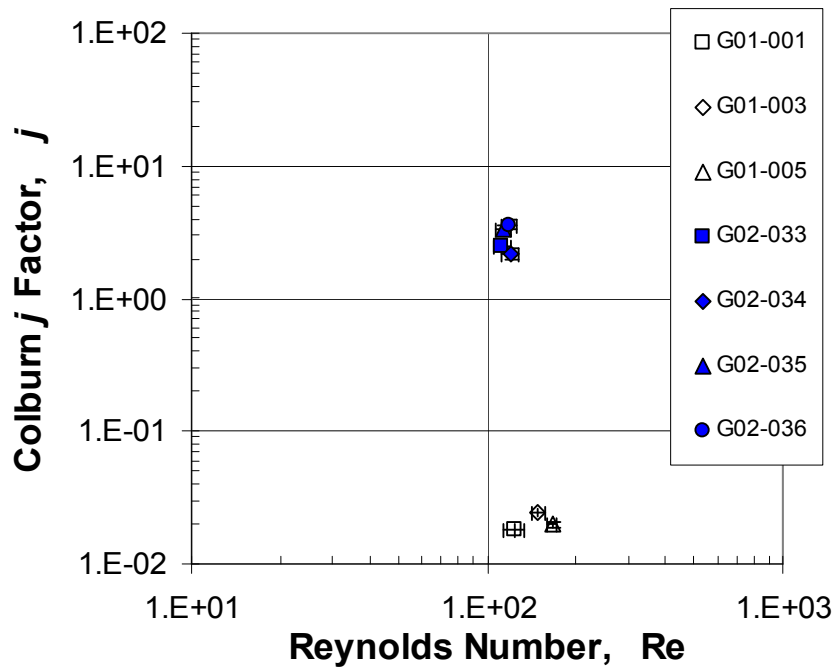
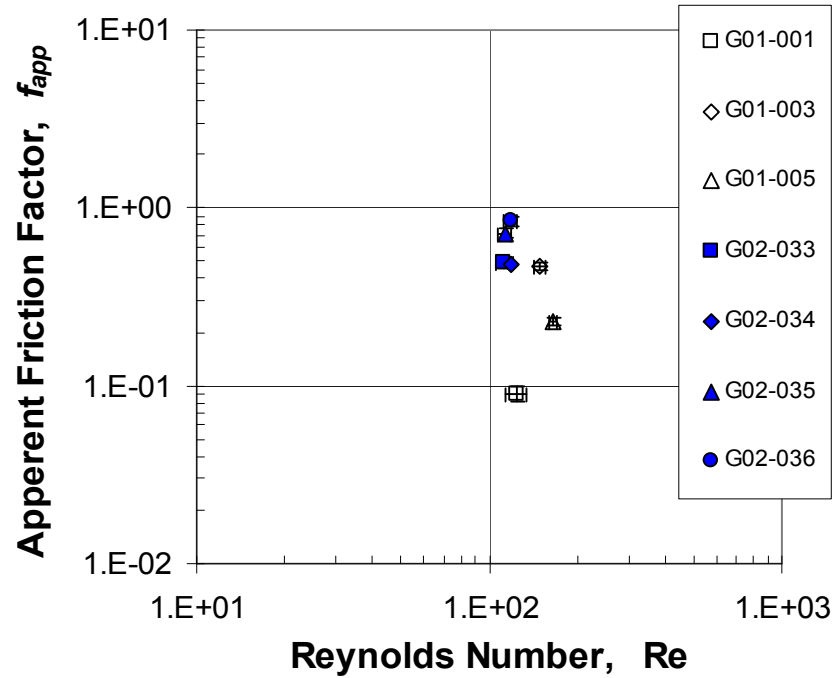


Figure 10.8: Friction and Colburn j Factors vs. Reynolds Number. For $Q = 69$ mL/min; Plain = G01-001, G01-003, and G01-005; Enhanced = G02-033, G02-034, G02-35, and G02-036; $b = 200$ μ m; $T_i = 20$ $^{\circ}$ C.

There are several general items to mention concerning the f and j Factor figures. First, all of the data exhibit the expected decreasing trend with an increasing Reynolds number. The enhanced microchannel geometries have larger f and j factors than the plain microchannels. This is expected due to the increased flow blockage and heat transfer area, respectively. Although there currently is no correlation for this geometry, it seems as if the j factors may fall upon a linear line. However, much more data and correlation work is required as the slopes may be different. These figures are presented in part for future correlation work.

10.4 Coefficient of Performance Using Pumping Flux

It can become very difficult to compare different microchannel heat exchanger geometries. There is a wide variety of geometries and boundary conditions employed in these heat exchangers. Sections 10.1 and 10.2 present some of the traditional reported parameters and they are useful in that they lend insight into some of the aspects of specific features. An overriding parameter that can measure the overall performance of the microchannel heat exchanger seems to be missing. The thermal resistance is excellent but it provides no information regarding the pressure penalty involved with the heat exchanger. A parameter that would account for both the heat flux being dissipated and the pressure drop required would be desired. Therefore, a novel parameter called the pumping power flux has been developed.

The pumping power flux is a new parameter proposed here to use in microchannel heat exchangers. It is based upon the idea of pumping power and is seen in Eq. (10.2).

$$P = \frac{\dot{m} \Delta p}{\rho} \quad (10.2)$$

where P is the pumping power. The pumping power can be manipulated to transform it into a

flux term by dividing by the free flow area of the flow. Equation (10.3) shows the formula for the pumping power flux, or the pumping flux for short.

$$P'' = \frac{\dot{m} \Delta p}{\rho A_{free}} \quad (10.3)$$

where P'' is the pumping power flux and A_{free} is the free flow area. This parameter now has the same units and meaning as the heat flux. The pumping power flux is the amount of pumping power per unit free flow area in the microchannel. Another useful form of the pumping power flux is found in Eq. (10.4) where the mass flow rate is replaced with the mass flux.

$$P'' = \frac{G \Delta p}{\rho} \quad (10.4)$$

The heat flux and pumping power flux can be related in a simple manner by considering the coefficient of performance (COP) in thermodynamics. In its simplest terms, the COP is the desired output divided by the required input as in a refrigeration system. It is the heat removed by the cycle divided by the work done by the cycle. It would be desirable to have as high a COP as possible.

For the present work, the COP will be the desired heat flux to be dissipated divided by the required pumping power flux, Eq. (10.5).

$$COP = \frac{P''}{q''} \quad (10.5)$$

Substituting in known parameters gives Eq. (10.6) and rearranging gives Eq. (10.7).

$$COP = \frac{\frac{\dot{m} \Delta p}{\rho A_{free}}}{\frac{q}{A_{HT}}} \quad (10.6)$$

$$COP = \frac{\dot{m} \Delta p}{\rho q} \frac{A_{HT}}{A_{free}} \quad (10.7)$$

The COP terms out to be a ratio of the heat transfer area to the free flow area. If one could significantly increase the heat transfer area with all others remaining unchanged, the COP would increase. This is point to the heat transfer enhancements discussed in the present work. The free flow is reduced slightly but the heat transfer area is significantly increased, as a result the COP is increased. The COPs for the three flow rates are given in Fig. 10.9, 10.10, and 10.11.

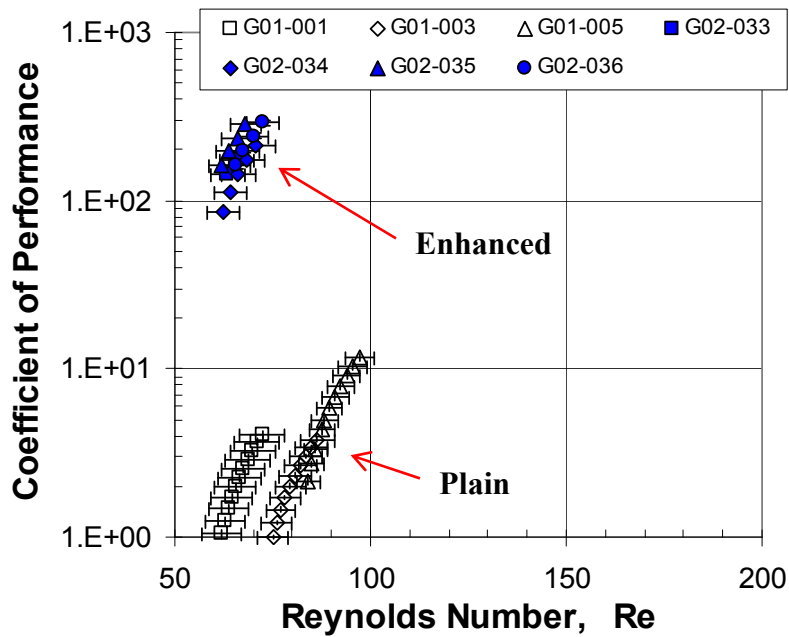


Figure 10.9: Coefficient of Performance vs. Reynolds Number. For $Q = 39$ mL/min; Plain = G01-001, G01-003, and G01-005; Enhanced = G02-033, G02-034, G02-35, and G02-036; $b = 200$ μ m; $T_i = 20$ $^{\circ}$ C.

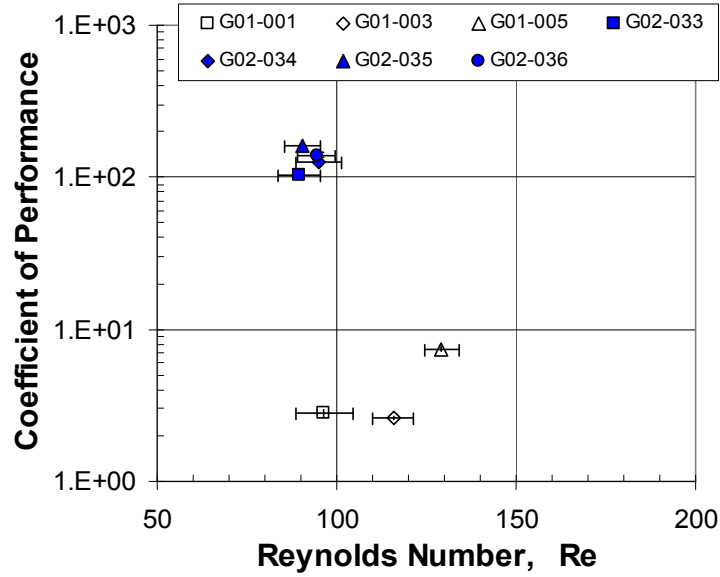


Figure 10.10: Coefficient of Performance vs. Reynolds Number. For $Q = 39$ mL/min; Plain = G01-001, G01-003, and G01-005; Enhanced = G02-033, G02-034, G02-35, and G02-036; $b = 200$ μ m; $T_i = 20$ $^{\circ}$ C.

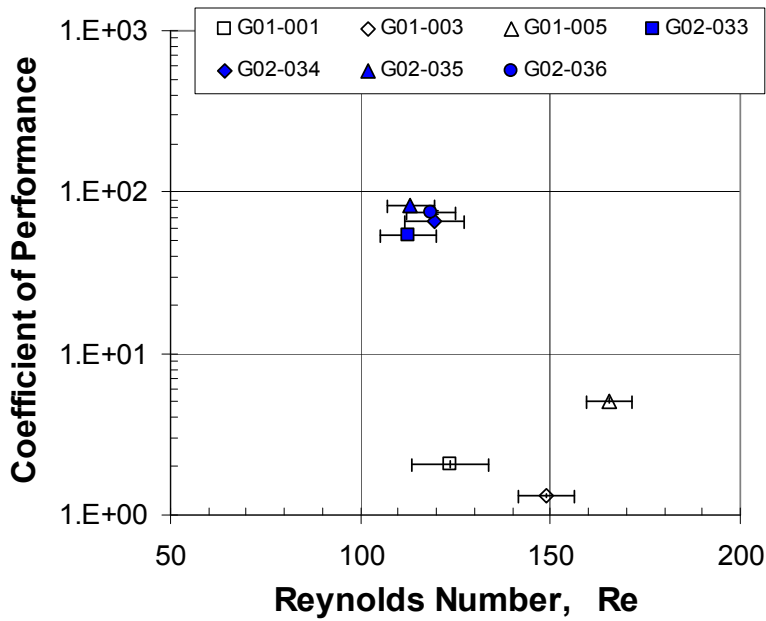


Figure 10.11: Coefficient of Performance vs. Reynolds Number. For $Q = 39$ mL/min; Plain = G01-001, G01-003, and G01-005; Enhanced = G02-033, G02-034, G02-35, and G02-036; $b = 200$ μ m; $T_i = 20$ $^{\circ}$ C.

It can be seen from the figures that the enhanced microchannels have a much higher COP than the plain microchannels. The plain microchannels have a seemingly linear relationship in a log-log plot. That relationship is also seen in the enhanced microchannels. However, the slope is much larger and allows the COPs for those cases to be several times larger than the plain microchannels at the same Reynolds numbers. With very high COPs, the enhanced microchannels actually cost less to dissipate more amount of heat even with the increase in pressure drop over the plain microchannels.

The evaluation of the enhanced microchannels is challenging. The thermal performance is increasing at the same time the pressure drop is increasing. These two competing results and can bring up an excellent point. Is the thermal benefit worth the added pressure drop? The answer is yes for the offset strip fin geometry used in the present work. Using the new COP parameter based upon the heat flux and the pumping power flux, it can be concluded that the COP is an appropriate metric flow comparing plain and enhanced microchannel heat exchangers.

An enhanced microchannel heat exchanger has been designed, fabricated and tested for thermal performance and pressure drop penalty. There is a marked improvement for heat that can be dissipated for the same footprint area. There is an increase in pressure drop for the enhanced microchannel heat exchanger. However, the coefficient of performance states that the benefits in heat transfer performance out weigh the increase in pressure drop. This enhancement technique is viable for high heat flux applications and further study is recommended to optimize the geometry.

Finally, the COP for the plain and enhanced microchannels can be compared to the COP for the previous literature. Only the previous literature that reports the heat flux and pressure drop can be used for the comparison. Figure 10.12 shows the comparison of the present work to

the available data. The open squares represent the previous literature data, the open diamond points represent the present work's plain microchannels, and the closed circles represent the present work's enhanced microchannels.

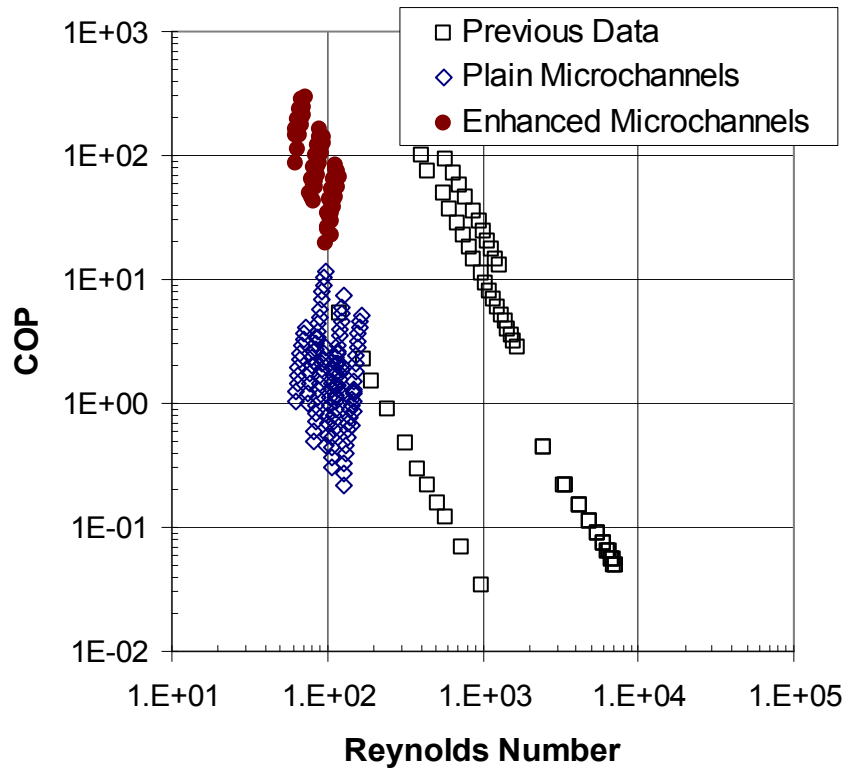


Figure 10.12: Coefficient of Performance vs. Reynolds Number. Open square points - Previous Data; Open Diamonds - Present Work Plain Microchannels; and Closed Circles - Present Work Enhanced Microchannels.

It can be seen that the plain microchannels for the present work fall into the same order of magnitude COP as the previous literature data. This validates the present work plain microchannels. It can be seen that the enhanced microchannels achieve a higher COP for a give flow rate than the plain microchannels. An also achieve that higher COP at a lower Reynolds

number as compared to the previous literature. As a result, the enhanced microchannels definitely provide an improvement over plain microchannels.

CHAPTER 11

CONCLUSIONS

The following conclusions can be drawn from the present work. In order to provide an efficient presentation, the conclusions are broken down into sub-categories that relate to the major results.

11.1 Reconciliation of Discrepancies in Literature

There are over 150 papers specifically addressing the topic of fluid flow and heat transfer in microchannels. Approximately 40 of those papers present useful data on friction factors in microchannels. A database of over 5,000 data points has been generated. The present work includes a Reynolds number range of $0.002 < Re < 5,000$ and a hydraulic diameter range of $8 < D_h < 990 \mu\text{m}$.

In order to resolve the previous discrepancies in literature regarding fluid flow and heat transfer in microchannels, a critical review of the data and experimental facilities has been conducted. The papers that do not account for the entrance and exit losses or the developing flow in the microchannel are the same papers that report significant deviation from theory. A reasonable explanation has been offered for what contributed to the discrepancies reported in previous literature. Therefore, the conventional friction factor theory is applicable for the entire range of conditions reported in the previous literature including the Reynolds numbers range of 0.01 to 3,000 and a hydraulic diameter range of 7 to 1,020 μm .

It is recommended that researchers report the non-dimensional Poiseuille number, C^* , instead of friction factor, unless the researcher is presenting the friction factor for frictional losses only. This will highlight what measurement of f the researcher is actually reporting and will be less confusing and eliminate the inappropriate use of friction factor currently occurring.

11.2 Development of an Experimental Facility

A single-phase experimental test facility has been designed and fabricated. The system is capable of delivering water to a test section with a variety of inlet temperatures and flow conditions. The range of volumetric flow rates for the facility is 1 to 300 mL/min and the range of inlet water temperatures is from 5 to 85 °C. In addition, it can provide a maximum power of 1.5 kW to the test section.

A data acquisition system is used to monitor, control, and log many parameters in the experimental facility. The raw data are collected and a calibration is applied to give highly accurate data with experimental uncertainties included. Data burst mode signal collection allows for 500 individual data points to be collected at a rate of 1.0 kHz. The mean and standard deviations of each data set are used to provide an accurate measurement of any desired parameter. The resulting experimental accuracy of the temperature measurements is ± 0.05 °C and the pressure drop is 0.14 kPa.

11.3 Uncertainty Analysis

A careful analysis of uncertainty is conducted to determine how to propagate the experimental uncertainties in the measured parameters to the calculated parameters used to characterize the thermal and hydraulic performance. This is the first time such a derivation has been attempted for microchannels.

It is demonstrated that the uncertainty in fRe is dominated by the microchannel geometry measurements. It is shown that the fRe has a seven time dependence upon microchannel width and depth measurements and only a single dependence upon the pressure drop measurement. Even a very accurate pressure drop measurement will often be overshadowed by the geometry measurement uncertainties.

The uncertainty in Nusselt number is affected by the microchannel geometry measurements. The temperature measurements are more important, especially when small temperature differences below a few degrees are encountered. The measurement errors in

temperature will be magnified eight times due to utilizing those measurements several times in calculating the Nusselt number.

11.4 Single-Phase Liquid Fluid Flow

The components that contribute to the total pressure drop occurring across a microchannel heat exchanger are identified. These components are the inlet and outlet losses, the developing flow losses, and the frictional flow losses. The effect of the developing flow is included in the form of Hagenbach factor.

New experimental data are generated to demonstrate the procedure for correcting the measured pressure drop. A plain G01-008 geometry microchannel heat exchanger is used to provide experimental evidence of the effect of the identified pressure drop components. There are 27 microchannels with a width of 200 μm , a depth of 250 μm , and a length of 10,000 μm in this heat exchanger. The microchannels occupy a 10 mm x 10 mm area that is heated using a copper resistor.

The data are corrected for inlet and exit losses and then they are corrected for developing flows. The corrected data show good agreement in value and trend with the conventional theory for laminar fluid flow for a Reynolds number range of 25 to 800.

The microchannel geometry must be carefully evaluated. There is no substitute for accurate measurements obtained through destructive measurement of the channel geometry. The profiles of the flow passage must be carefully determined while reducing the experimental data for obtaining the experimental friction factors. The nominal hydraulic diameter for the G01-008 is 222 μm whereas the hydraulic diameter based upon the measure trapezoidal profile is 227 μm . Even, this small change in hydraulic diameter is noticeable when the data are calculated.

11.5 Single-Phase Heat Transfer Enhancement

Some of the more successful enhancement techniques currently used for heat transfer augmentation have been reviewed. The applicability of single-phase enhancement techniques is

evaluated for microchannel flow, minichannel flow, and microdevices. Several passive techniques have been identified as possibilities for microchannel enhancement.

An offset strip fin enhanced microchannel heat exchanger is fabricated and tested. The results show a marked improvement in the overall thermal resistance of the enhanced microchannel heat exchanger compared to one using plain microchannels. The unit thermal resistance of the plain microchannels is approximately $0.1 \text{ } ^\circ\text{C m}^2 / \text{W}$. The unit thermal resistance of the enhanced microchannel heat exchanger at the same flow and heat transfer conditions is $0.001 \text{ } ^\circ\text{C m}^2 / \text{W}$. There is a clear decrease in the thermal resistance and this would result in better thermal performance.

Finally, a new parameter called pumping power flux is developed to aid in the evaluation and comparison of enhanced microchannel heat exchangers. Using the new COP parameter based upon the heat flux and the pumping power flux, it can be concluded that the COP and pumping power flux are an appropriate metrics for comparing plain and enhanced microchannel heat exchangers. The maximum COP for the plain microchannels is 11 where the maximum for the enhanced microchannels is 290. Therefore, the enhanced microchannel heat exchanger is substantially more effective at dissipating the same heat flux despite the increase in pressure drop.

There is a great deal of research needed to bring these proposed techniques into fruition. In some cases, the technology might not be available. However, the present work is expected to serve as a road map for microchannel, minichannel, and microdevice heat transfer enhancement.

CHAPTER 12

REFERENCES

Adams, T.M., Dowling, M.F., Abdel-Khalik, S.I., and Jeter, S.M. "Applicability of traditional turbulent single-phase forced convection correlations to non-circular microchannels," *International Journal of Heat and Mass Transfer* 42, No. 23 (1999) 4411-4415.

Allen, P.H.G. and Karayiannis, T.G., Electrohydrodynamic Enhancement of Heat Transfer and Fluid Flow, *Heat Recovery Systems & CHP*, vol. 15, no. 5, pp. 389-423, 1995.

Bailey, D.K., Ameen, T.A., Warrington, R.O. and Savoie, T.I. "Single phase forced convection heat transfer in microgeometries-a review." *Proceedings of the Intersociety Energy Conversion Engineering Conference, v 2, Environmental Impact* (1995) 301-310.

Balaras, C.A., Review of Augmentation Techniques for Heat Transfer Surfaces in Single-Phase Heat Exchangers, *Energy (Oxford)*, vol. 15, no. 10, pp. 899-906, 1990.

Baviere, R., Ayela, F., Le Person, S. and Favre-Marinet, M. "An experimental study of water flow in smooth and rough rectangular micro-channels." *International Conference on Microchannels and Minichannels* ASME Publications (2004).

Bergles, A.E., Heat Transfer Enhancement - The Encouragement and Accommodation of High Heat Fluxes, *Journal of Heat Transfer*, vol. 119, pp. 8-19, 1997.

Bergles, A.E., Jensen, M.K., and B. Shome, The Literature on Enhancement of Convective Heat and Mass Transfer, *Enhanced Heat Transfer*, vol. 4, pp. 1-6, 1996.

Bergles, A.E., Enhanced Heat Transfer: Endless Frontier, or Mature and Routine?, *Enhanced Heat Transfer*, vol. 6, pp. 79-88, 1999.

Bergles, A.E., ExHFT for Fourth Generation Heat Transfer Technology, *Experimental Thermal Fluid Science*, vol. 26, pp. 335-344, 2002.

Bondar, F. and Battaglia, F., A Computational Study on Mixing of Two-Phase Flow in Microchannels, *Proceedings of ASME International Mechanical Engineering Congress Washington, D.C., November 15–21, 2003, Paper # IMECE03-43957*, ASME Publications, 2003.

Bosch, R. Gmbh, "Trench etch process for a single-wafer RIE dry etch reactor." US Patent 4 855 017, Sept. 8, 1988.

Bucci, A., Celata, G.P., Cumo, M., Serra, E. and Zummo, G. "Water single-phase fluid flow and heat transfer in capillary tubes." *International Conference on Microchannels and Minichannels. Paper # 1037* ASME Publications 1 (2003) 319-326.

Champagne, P.R. and Bergles, A.E., Development and Testing of a Novel, Variable-Roughness Technique to Enhance, on Demand, Heat Transfer in a Single-Phase Heat Exchanger, *Journal of Enhanced Heat Transfer*, vol. 8, no. 5, pp. 341-352, 2001.

Chen, R.Y. "Flow in the entrance region at low Reynolds numbers." *Journal of Fluids Engineering* 95 (1973) 153-158.

Chung, P.M.-Y., Kawaji, M. and Kawahara, A. "Characteristics of single-phase flow in microchannels." *Proceedings of Fluids Engineering Division Summer Meeting, July 14-18, 2002, Montreal, Quebec, Canada* ASME Publications (2002) 1219-1227.

Churchill, S.W. "Friction-factor equation spans all fluid flow regimes." *Chem. Eng.* 84, no 24 (1977) 91-92.

Colburn, A.P. "A method of correlating forced convection heat transfer data and a comparison with fluid friction." *Trans. Am. Inst. Chem. Eng.* 29 (1933) 174-210.

Colebrook, C.F. "Turbulent flow in pipes with particular reference to the transition region between the smooth and rough pipe laws." *J. of the Institution of Civil Engineers, London* 11 (1938-1939) 133-156.

Colgan, E.G., Furman, B., Gaynes, M., Graham, W., LaBianca, N., Magerlein, J.H., Polastre, R.J., Rothwell, M.B., Bezama, R.J., Toy, H., Wakil, J., Zitz, J. and Schmidt, R. "A practical implementation of silicon microchannel coolers for high power chips." *Semiconductor Thermal Measurement, Modeling, and Management Symposium* (2005).

Curr, R.M., Sharma, D., and Tatchell, D.G. "Numerical Predictions of Some Three-Dimensional Boundary Layers in Ducts." *Computational Methods in Applied Mechanical Engineering* 1 (1972) 143-158.

Cuta, J.M., McDonald, C.E. and Shekarriz, A. "Forced convection heat transfer in parallel channel array microchannel heat exchanger." *American Society of Mechanical Engineers, Heat Transfer Division, Advances in Energy Efficiency, Heat/Mass Transfer Enhancement HTD*, v 338 (1996) 17-23.

Dittus, P.W. and Boelter, L.M.K. "Heat transfer in Automobile Radiators of the tubular." *Univ. Calif. Pub. Eng.* 2, no 13 (1930) 443-461.

Garimella, S.V. and Singhal, V. "Single-phase flow and heat transport and pumping considerations in microchannel heat sinks." *Heat Transfer Engineering* 25, no 1 (2004) 15-25.

Gnielinski, V. "New Equations for Heat Transfer in Turbulent Pipe and Channel Flow." *International Chemical Engineering* 16 (1976) 359-368.

Go, J.S., Design of a Microfin Array Heat Sink Using Flow-Induced Vibration to Enhance the Heat Transfer in the Laminar Flow Regime, *Sensors and Actuators A*, vol. 105, pp. 201-210, 2003.

Gui, F. and Scaringe, R.P. "Enhanced heat transfer in the entrance region of microchannels." *Proceedings of the Intersociety Energy Conversion Engineering Conference* (1995) 289-294.

Haaland, S.E. "Simple and explicit formulas for the friction factor in turbulent pipe flow." *J. of Fluids Eng* 105, no 1 (1983) 89-90.

Hausen, H. "Neue Gleichungen für die Wärmeübertragung bei freier oder erzwungener Strömung." *Allg. Waermetech* 9 (1959) 75-79.

Hessami, M.-A., Berryman, A. and Bandopdhayay, P., Heat Transfer Enhancement in an Electrically Heated Horizontal Pipe Due to Flow Pulsation, *Proceedings of ASME International Mechanical Engineering Congress Washington, D.C., November 15–21, 2003, Paper # IMECE03-55146*, ASME Publications, 2003.

Hsieh, S.-S., Lin, C.-Y., Huang, C.-F. and Tsai, H.-H. "Liquid flow in a micro-channel." *Journal of Micromechanics and Microengineering* 14, no 4 (2004) 436-445.

Hu, X. and Zhang, Y., Novel Insight and Numerical Analysis of Convective Heat Transfer Enhancement with Microencapsulated Phase Change Material Slurries: Laminar Flow in a Circular Tube with Constant Heat Flux, *International Journal of Heat and Mass Transfer*, vol. 45, no. 15, pp. 3163-3172, 2002.

Jiang, X.N., Zhou, Z.Y., Huang, X.Y. and Liu, C.Y. "Laminar flow through microchannels used for microscale cooling systems." *Proceedings of the Electronic Packaging Technology Conference, EPTC* (1997) 119-122.

Judy, J., Maynes, D., and Webb, B.W. "Characterization of frictional pressure drop for liquid flows through microchannels," *International Journal of Heat and Mass Transfer* 45, No. 17 (2002) 3477-3489.

Jung, J.-Y. and Kwak, H.-Y. "Fluid flow and heat transfer in microchannels with rectangular cross section." *International Conference on Microchannels and Minichannels, Paper # 1032 1* (2003) 291-297.

Kakaç, S., Shah, R.K. and Aung, W. *Handbook of Single-Phase Convective Heat Transfer* John Wiley & Sons: New York (1987).

Kandlikar, S.G., Fundamental Issues Related to Flow Boiling in Minichannels and Microchannels, *Experimental Thermal and Fluid Science*, vol. 26, no. 2-4, pp. 389-407, 2002.

Kandlikar, S.G., and Grande, W.J., Evolution of Microchannel Flow Passages - Thermohydraulic Performance and Fabrication Technology, *Heat Transfer Engineering*, vol. 24, no. 1, pp. 3-17, 2003.

Kandlikar, S.G., Joshi S. and Tian S., Effect of Surface Roughness on Heat Transfer and Fluid Flow Characteristics at Low Reynolds Numbers in Small Diameter Tubes, *Heat Transfer Engineering*, vol. 24, no. 3, pp. 4-16, 2003.

Kandlikar, S.G., and Grande, W.J., Evaluation of Single Phase Flow in Microchannels for High Flux Chip Cooling – Thermohydraulic Performance Enhancement and Fabrication

Technology, *Proceedings of International Conference on Microchannels and Minichannels*, CMM04-2321 ASME Publications, 2004.

Kandlikar, S.G., and Grande, W.J., Evaluation of Single Phase Flow in Microchannels for High Flux Chip Cooling – Thermohydraulic Performance Enhancement and Fabrication Technology, *Heat Transfer Engineering*, vol. 25, no. 8, pp. 1–13, 2004.

Kandlikar, S.G. and Schmitt, D. “Characterization of surface roughness effect on pressure drop in single-phase flow in minichannels and microchannels.” *Physics of Fluids* (2005).

Lee, P.S., Ho, J.C., and Xue, H. "Experimental study on laminar heat transfer in microchannel heat sink," *The Eighth Intersociety Conference on Thermal and Thermomechanical Phenomena in Electronic Systems, 30 May-1 June 2002, IITHERM 2002*. IEEE Publications (2002) 379 -386.

Lee, P.-S. and Garimella, S.V. "Experimental investigation of heat transfer in microchannels." *Proceedings of the ASME Summer Heat Transfer Conference* (2003) 391-397.

Mala, G.M., and Li, D.Q. "Flow characteristics of water in microtubes," *International Journal of Heat and Fluid Flow* 20, No. 2 (1999) 142-148.

Missaggia, L.J., Walpole, J.N., Liao, Z.L. and Phillips, R.J. "Microchannel heat sinks for two-dimensional high-power-density diode laser arrays." *IEEE Journal of Quantum Electronics* 25, no 9 (1989) 1988-1992.

Morini, G.L. "Single-phase convective heat transfer in microchannels: A review of experimental results." *International Journal of Thermal Sciences* 43, no 7 (2004) 631-651.

Nikuradse, J. "Strmungsgesetze in rauhen rohren." *V.D.I. Forschungsheft* 361 (1933) 1–22.

Owhaib, W. and Palm, B. "Experimental investigation of single-phase convective heat transfer in circular microchannels." *Experimental Thermal and Fluid Science* 28, no 2-3 (2004) 105-110.

Palm, B. "Heat transfer in microchannels." *Microscale Thermophysical Engineering* 5, no 3 (2001) 155-175.

Papautsky, I., Brazzle, J., Ameen, T. and Frazier, A.B. "Laminar fluid behavior in microchannels using micropolar fluid theory." *Sensors and Actuators, A: Physical* 73, no 1-2 (1999) 101-108.

Park, H., Pak, J.J., Son, S.Y., Lim, G. and Song, I. "Fabrication of a microchannel integrated with inner sensors and the analysis of its laminar flow characteristics." *Sensors and Actuators, A: Physical* 103, no 3 (2003) 317-329.

Peng, X.F., Wang, B.X., Peterson, G.P., and Ma, H.B. "Experimental investigation of heat transfer in flat plates with rectangular microchannels," *International Journal of Heat and Mass Transfer* 38, No. 1 (1995) 127-137.

Peng, X.F., and Peterson, G.P. "Effect of thermofluid and geometrical parameters on convection of liquids through rectangular microchannels," *International Journal of Heat and Mass Transfer* 38, no. 4 (1995) 755-758.

Peng, X. F., and Peterson, G.P., 1996, "Convective heat transfer and flow friction for water flow in microchannel structures," *International Journal of Heat and Mass Transfer* 39, no. 12 (1996) 2599-2608.

Petukhov, B.S. and Popov, V.N. "Theoretical calculation of heat exchange in turbulent flow in tubes of an incompressible fluid with variable properties." *High Temperature* 1, no 1 (1963) 69-83.

Pfund, D., Rector, D., Shekarriz, A., Popescu, A. and Welty, James "Pressure drop measurements in a microchannel." *AIChE Journal* 46, no 8 (2000) 1496-1507.

Qu, W., Mala, M., and Li, D. "Heat transfer for water in trapizoid silicon microchannels," *International Journal of Heat and Mass Transfer* Vol. 43, (2000a) 3925-3936.

Qu, W., Mala, G.M., and Li, D. "Pressure-driven water flows in trapezoidal silicon microchannels," *International Journal of Heat and Mass Transfer* 43, No. 3 (2000b) 353-364.

Qu, W. and Mudawar, I. "Experimental and numerical study of pressure drop and heat transfer in a single-phase micro-channel heat sink." *International Journal of Heat and Mass Transfer* 45, no 12 (2002) 2549-2565.

Rahman, M.M. and Gui, F. "Experimental measurements of fluid flow and heat transfer in microchannel cooling passages in a chip substrate." *Proceedings of the ASME International Electronics Packaging Conference, Sep 29-Oct 2 1993, Binghamton, NY, USA* ASME publications 4-2 (1993a) 685-692.

Rahman, M.M. and Gui, F. "Design, fabrication, and testing of microchannel heat sinks for aircraft avionics cooling." *Proceedings of the Intersociety Energy Conversion Engineering Conference* 1 (1993b) 1-6.

Rahman, M.M. "Measurements of heat transfer in microchannel heat sinks," *International Communications in Heat and Mass Transfer* 27, No. 4 (2000) 495-507.

Ravigururajan, T.S. and Drost, M.K. "Single-phase flow thermal performance characteristics of a parallel microchannel heat exchanger." *Journal of Enhanced Heat Transfer* 6, no 5 (1999) 383-393.

Reynolds, O. "On the extent and action of the heating surface for steam boilers." *Proc. Manchester Lit. Philos. Soc.* 14 (1874) 7-12.

Riddle, R.A., Contolini, R.J. and Bernhardt, A.F. "Design calculations for the microchannel heatsink." *Proceedings of the Technical Program - National Electronic Packaging and Production Conference* 1 (1991) 161-171.

Shah, R.K. and London, A.L. "Laminar Flow Forced Convection in Ducts," *Supplement 1 to Advances in Heat Transfer* Academic, New York (1978).

Sobhan, C.B. and Garimella, S.V. "A comparative analysis of studies on heat transfer and fluid flow in microchannels." *Microscale Thermophysical Engineering* 5, no 4 (2001) 293-311.

Steinke, M.E. and Kandlikar, S.G. "Control and Effect of Dissolved Air in Water During Flow Boiling in Microchannels." *International Journal of Heat and Mass Transfer* 47 (2004) 1925–1935.

Steinke, M.E. and Kandlikar, S.G. "Single-Phase, Liquid Friction Factors in Microchannels." *International Conference on Microchannels and Minichannels, Paper # ICMM05-75112* ASME Publications (2005).

Steinke, M.E. and Kandlikar, S.G. "Single-phase liquid friction factors in microchannels." *Submitted to International Conference on Microchannels and Minichannels, ICMM05-75112* ASME Publications (2005a).

Steinke, M.E. and Kandlikar, S.G. "Development of an experimental facility for investigating single-phase liquid flow in microchannels." *Submitted to International Conference on Microchannels and Minichannels, ICMM05-75070* ASME Publications (2005b).

Sturgis, J.C. and Mudawar, I., Single-Phase Heat Transfer Enhancement in a Curved, Rectangular Channel Subjected to Concave Heating, *International Journal of Heat and Mass Transfer*, vol. 42, no. 7, pp. 1255-1272, 1999.

Tao, W.Q., He, Y.L., Wang, Q.W., Qu, Z.G. and Song, F.Q., A Unified Analysis on Enhancing Single Phase Convective Heat Transfer with Field Synergy Principle, *International Journal of Heat and Mass Transfer*, vol. 45, no. 24, pp. 4871-4879, 2002.

Tso, C.P. and Mahulikar, S.P. "Multimode heat transfer in two-dimensional microchannel." *American Society of Mechanical Engineers, EEP 26-2* (1999) 1229-1233.

Tu, X. and Hrnjak, P. "Experimental investigation of single-phase flow pressure drop through rectangular microchannels." *International Conference on Microchannels and Minichannels, Paper # 1028* ASME Publications 1 (2003) 257-267.

Tuckerman, D.B., and Pease, R.F.W. "High-Performance Heat Sinking for VLSI," *IEEE Electron Device Letters* EDL-2 (1981) 126-129.

Vidmar, R.J., and Barker, R.J. "Microchannel Cooling for a High-Energy Particle Transmission Window, an RF Transmission Window, and VLSI Heat Dissipation," *IEEE Transactions on Plasma Science* 26, No. 3 (1998) 1031-1043.

Wu, H., and Cheng, P. "An experimental study of convective heat transfer in silicon microchannels with different surface conditions," *International Journal of Heat and Mass Transfer* 46, No. 14 (2003a) 2547-2556.

Wu, H., and Cheng, P. "Friction factors in smooth trapezoidal silicon microchannels with different aspect ratios," *International Journal of Heat and Mass Transfer* 46, No. 14 (2003b) 2519-2525.

Xu, B., Ooi, K.T., Wong, N.T., and Choi, W.K. "Experimental investigation of flow friction for liquid flow in microchannels," *International Communications in Heat and Mass Transfer* 27, No. 8 (2000) 1165-1176.

CHAPTER 13

APPENDIX

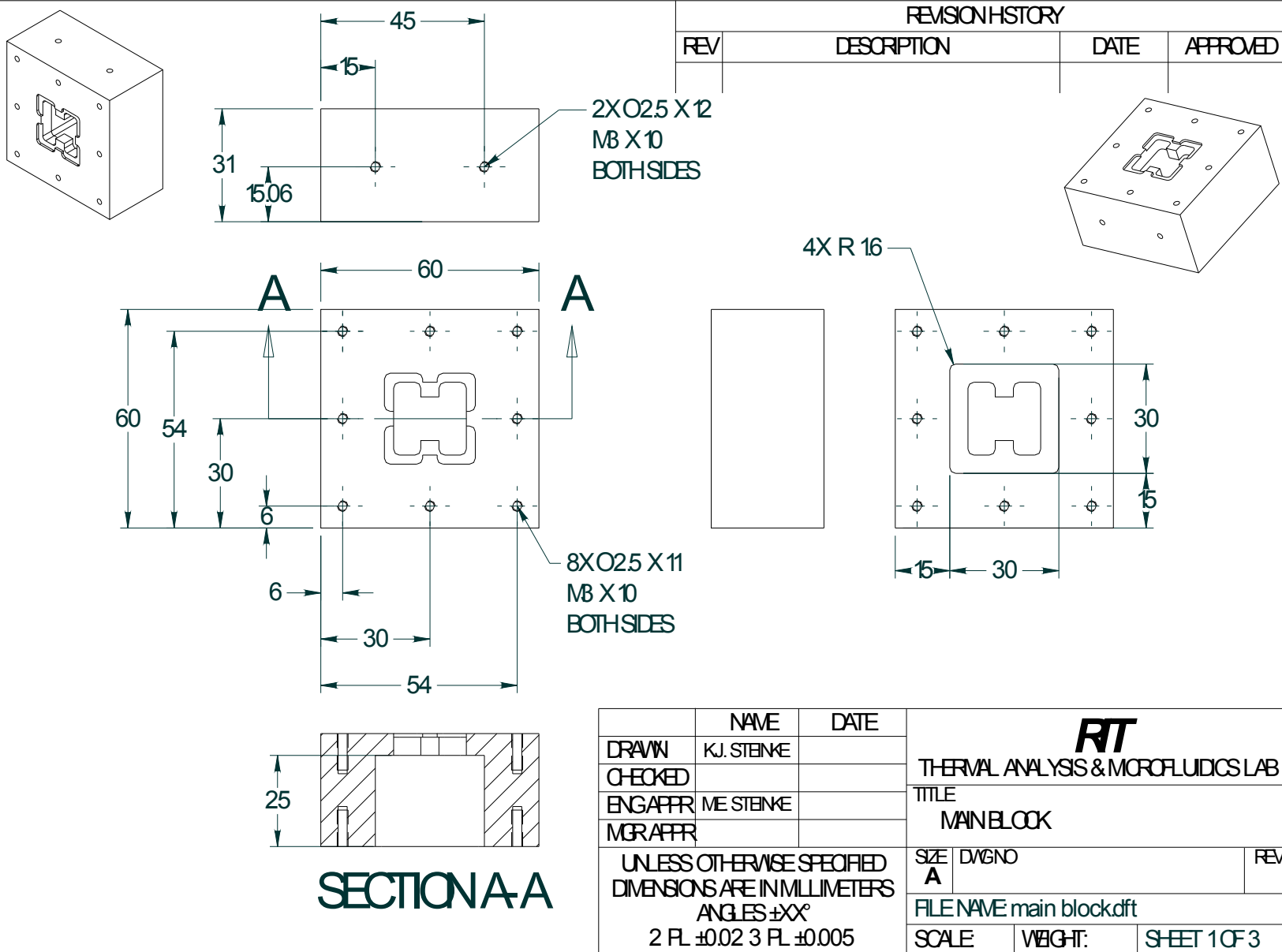
This appendix will present the details of items that did not exactly fit into the regular body of the paper. However, it is important to include these items as a matter of record. The details or drawings of the test fixtures, test sections, and the LabVIEW system will be presented.

13.1 Test Fixture Details

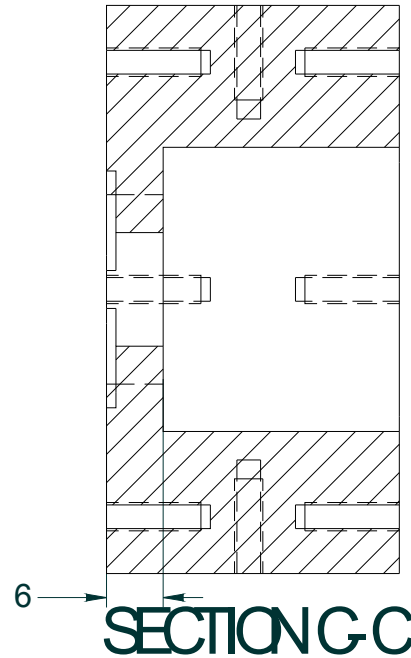
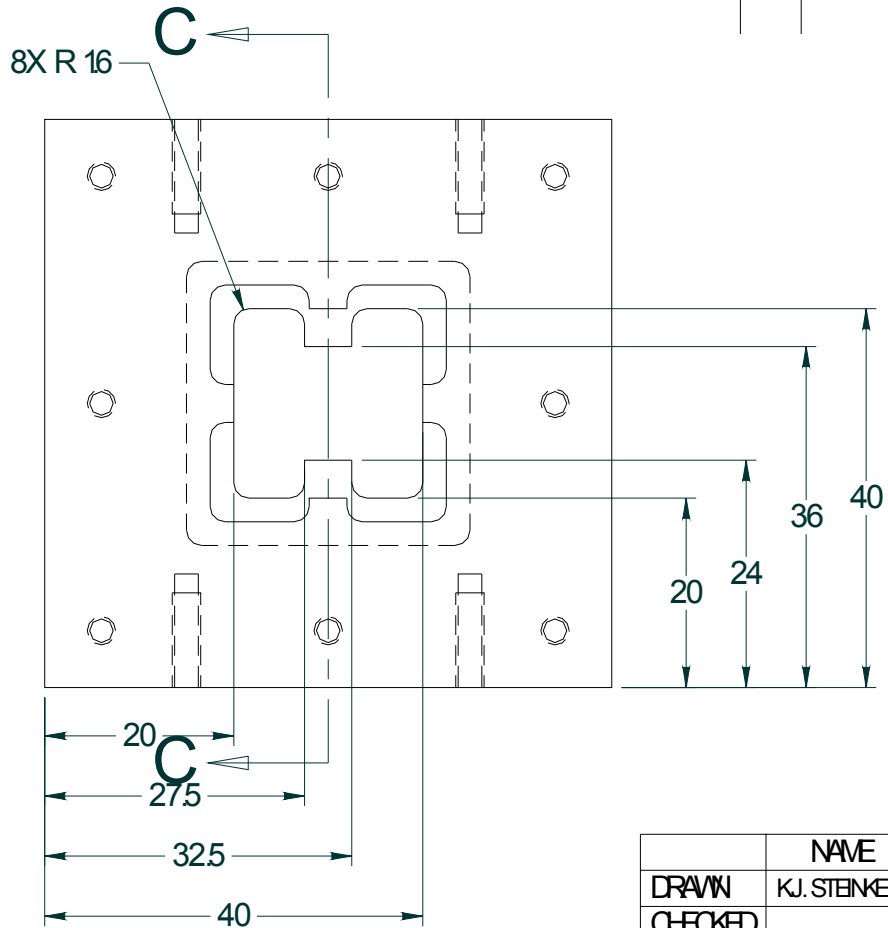
There are several details for the test fixture that are presented in this section that do not fit into the main body of the dissertation. However, it is important to present them for record keeping and future reference.

The first items are the detailed drawings of the test fixture components. First, the main block is shown. Then, the pogo probe block is presented followed by the bottom retaining plate, the X-Y stage mounting plate, and the polycarbonate retaining plate.

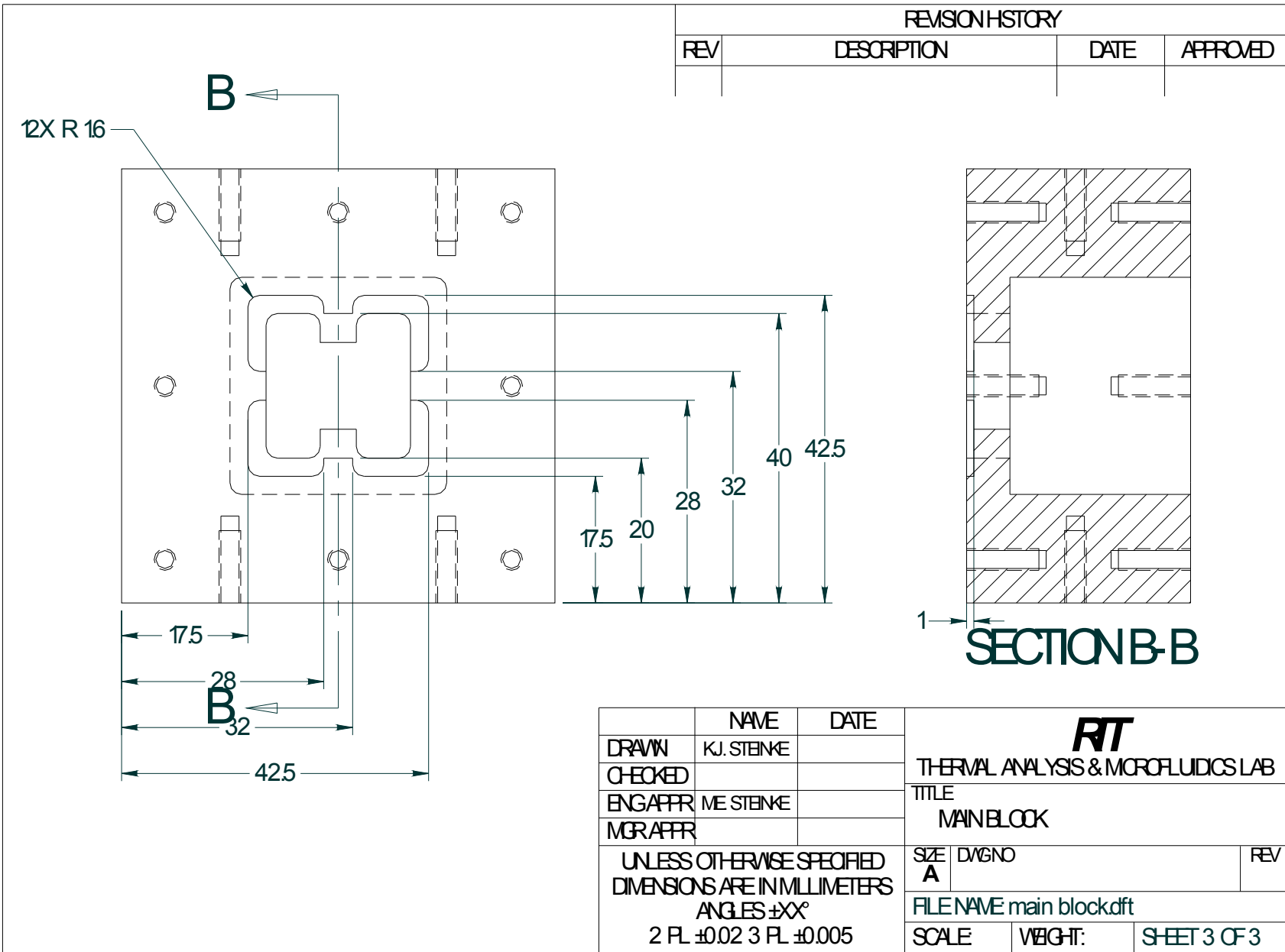
Finally, the assembly of the test fixture is depicted using some models. The progression begins with the empty pogo probe block. Then, the probes are inserted and the pogo probe block is inserted into the pogo probe block. Next, the pogo probe block is inserted into the main block. The test section is added and the Lexan retaining plate is attached. Finally, the assembled block is attached to the X-Y stage mounting plate.

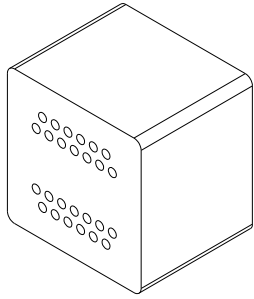


REVISION HISTORY			
REV	DESCRIPTION	DATE	APPROVED

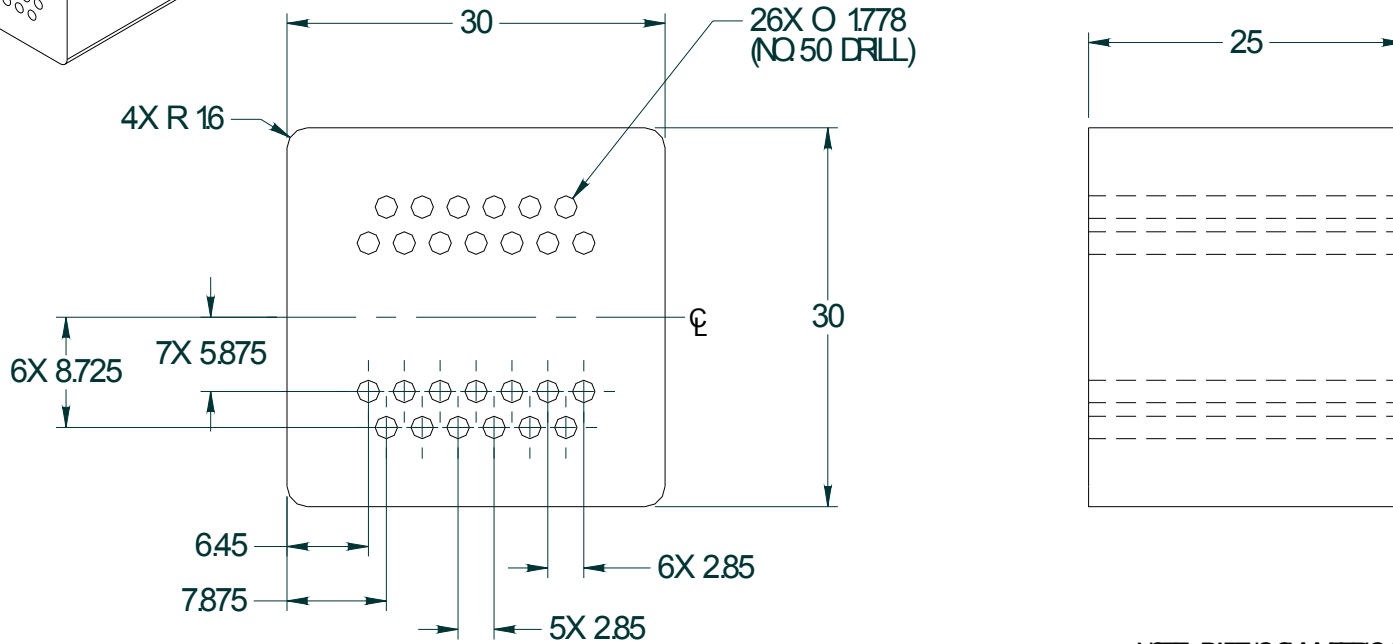


	NAME	DATE		
DRAWN	KJ. STENKE		<p style="text-align: center;">RT</p> <p style="text-align: center;">THERMAL ANALYSIS & MICROFLUIDICS LAB</p> <p style="text-align: center;">TITLE</p> <p style="text-align: center;">MAIN BLOCK</p>	
CHECKED				
ENG APPR	ME STENKE			
MGR APPR				
UNLESS OTHERWISE SPECIFIED DIMENSIONS ARE IN MILLIMETERS ANGLES ±XX° 2 FL ±0.02 3 FL ±0.005			SIZE A	REV
			FILE NAME: main_block.dft	
SCALE		WEIGHT:	SHEET 2 OF 3	



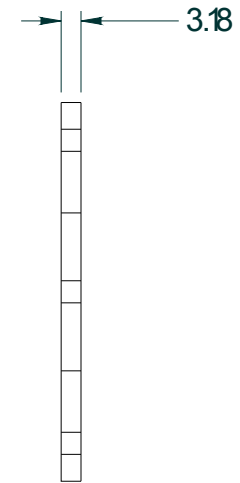
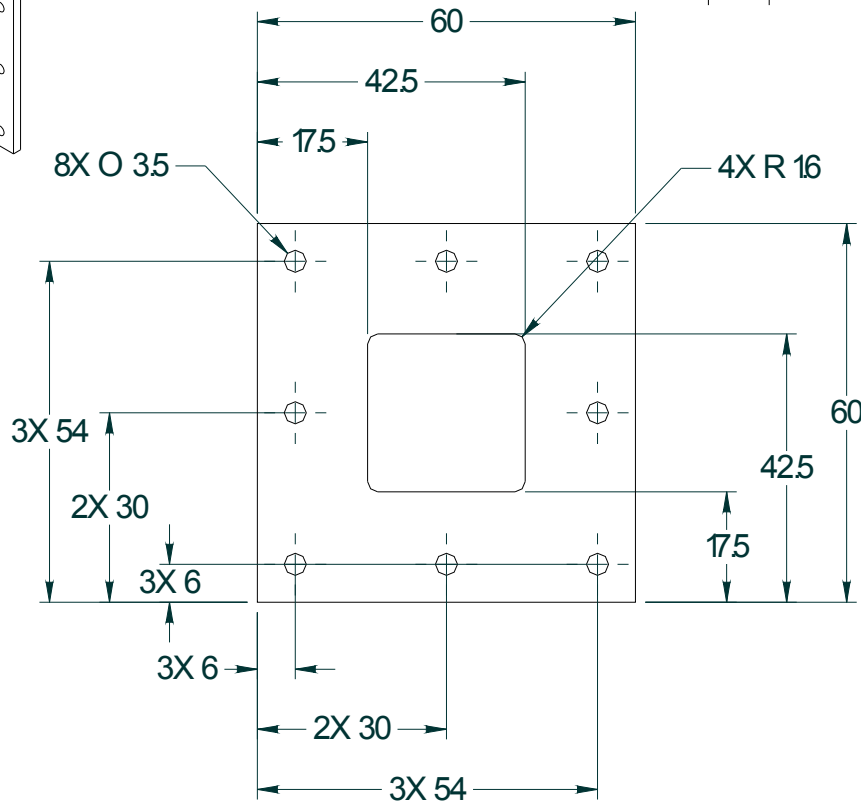
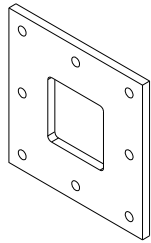


REVISION HISTORY			
REV	DESCRIPTION	DATE	APPROVED



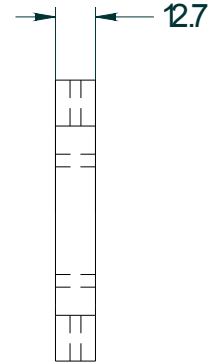
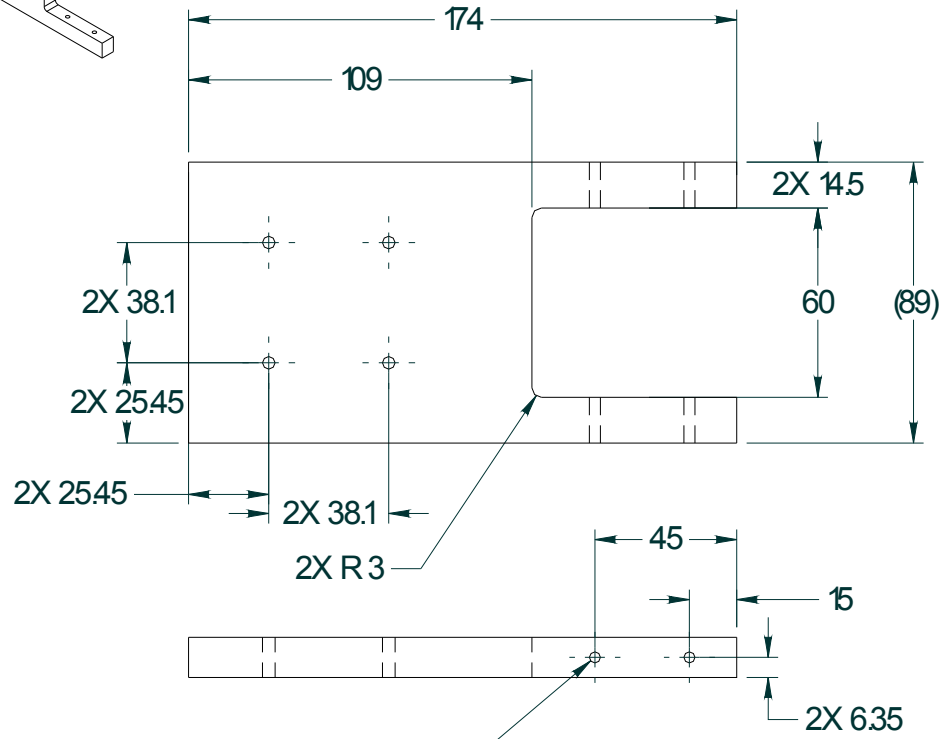
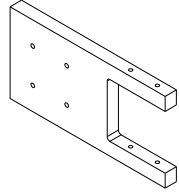
NOTE: PART IS SYMMETRIC ABOUT CENTERLINE

	NAME	DATE		
DRAWN	KJ. STENKE		THERMAL ANALYSIS & MICROFLUIDICS LAB	
CHECKED			TITLE	
ENG APPR	ME STENKE		POGO PROBE BLOCK	
MGR APPR			SIZE	REV
UNLESS OTHERWISE SPECIFIED DIMENSIONS ARE IN MILLIMETERS ANGLES ±XX° 2 FL ±0.02 3 FL ±0.005			A	
			FILE NAME: pogo probe block.dft	
SCALE		WEIGHT:	SHEET 1 OF 1	



REVISION HISTORY			
REV	DESCRIPTION	DATE	APPROVED

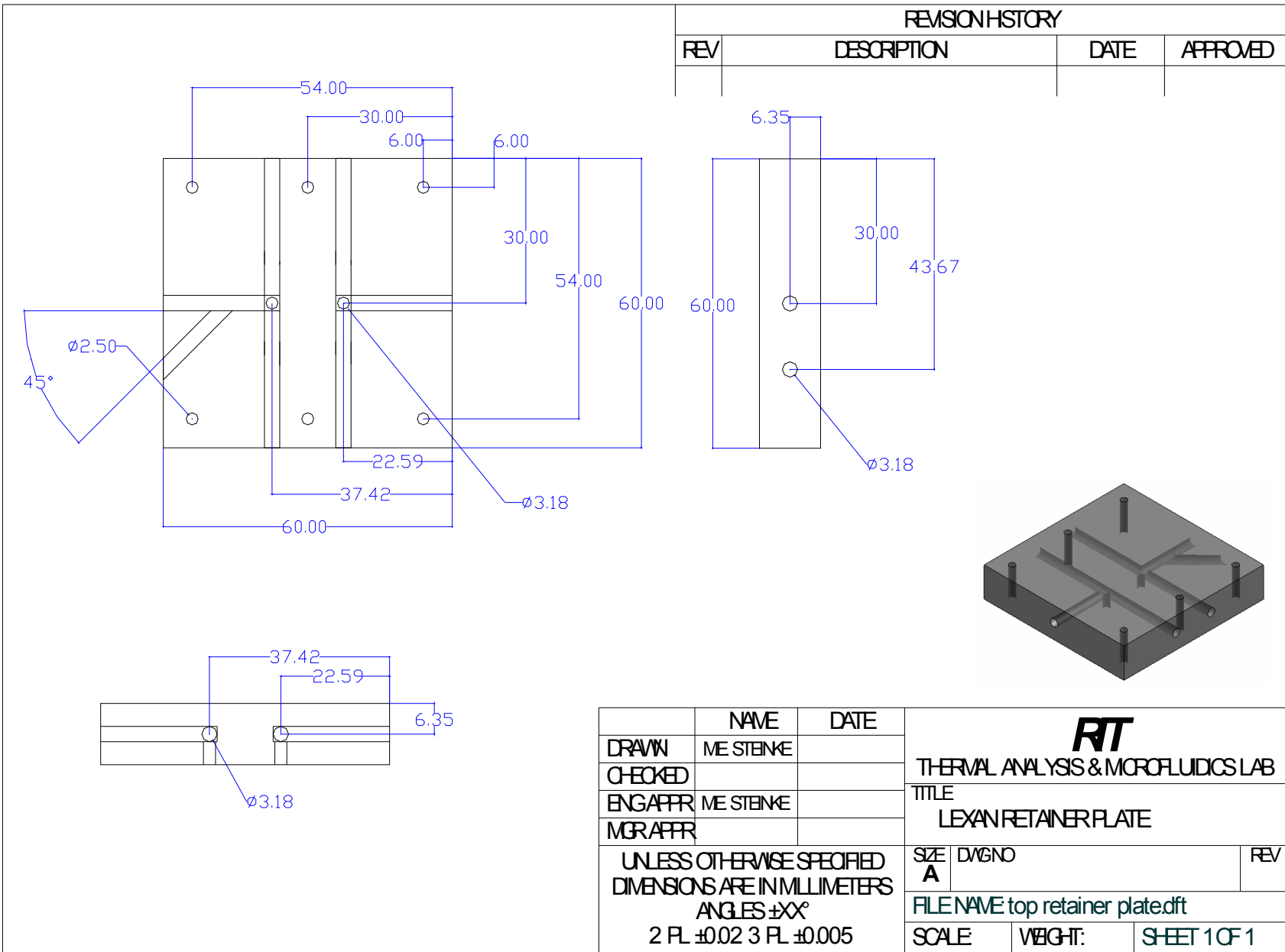
	NAME	DATE	RT THERMAL ANALYSIS & MICROFLUIDICS LAB	
DRAWN	KJ. STENKE		TITLE	
CHECKED			BOTTOM RETAINER PLATE	
ENG APPR	ME STENKE		SIZE	REV
MGR APPR			A	DWGNO
UNLESS OTHERWISE SPECIFIED DIMENSIONS ARE IN MILLIMETERS ANGLES ±XX° 2 FL ±0.02 3 FL ±0.005			FILE NAME: bottom retainer plate.dft	
SCALE		WEIGHT:	SHEET 1 OF 1	



2X Ø 3.5
THRU BOTH SIDES

REVISION HISTORY			
REV	DESCRIPTION	DATE	APPROVED

	NAME	DATE	RT THERMAL ANALYSIS & MICROFLUIDICS LAB	
DRAWN	KJ. STENKE			
CHECKED			MOUNTING PLATE	
ENG APPR	ME STENKE		SIZE	DWG NO
MGR APPR			A	REV
UNLESS OTHERWISE SPECIFIED DIMENSIONS ARE IN MILLIMETERS ANGLES ±XX° 2 FL ±0.02 3 FL ±0.005			FILE NAME: mounting_plate.DFT	
			SCALE	WEIGHT:



REVISION HISTORY			
REV	DESCRIPTION	DATE	APPROVED

NAME	DATE	RT THERMAL ANALYSIS & MICROFLUIDICS LAB	
DRAWN ME STENKE			
CHECKED		LEXAN RETAINER PLATE	
ENG APPR ME STENKE		SIZE	REV
MGR APPR		A	
UNLESS OTHERWISE SPECIFIED DIMENSIONS ARE IN MILLIMETERS ANGLES ±XX° 2 FL ±0.02 3 FL ±0.005		FILE NAME top_retainer_plate.dft	
		SCALE	WEIGHT: SHEET 1 OF 1

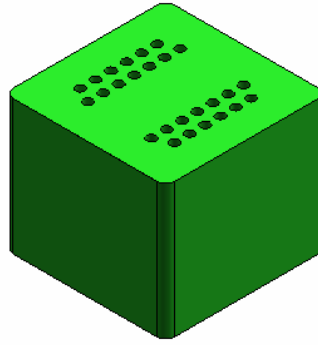


Figure 14.1.1: Empty Pogo Probe Block.

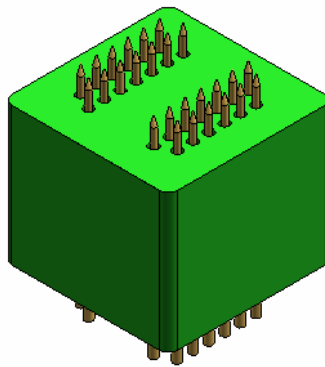


Figure 14.1.2: Pogo Probe Block with Probes.

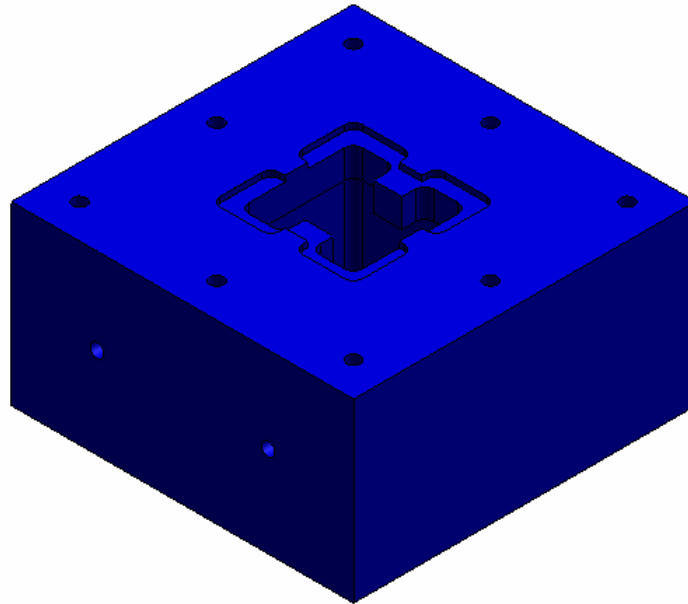


Figure 14.1.3: Empty Main Block.

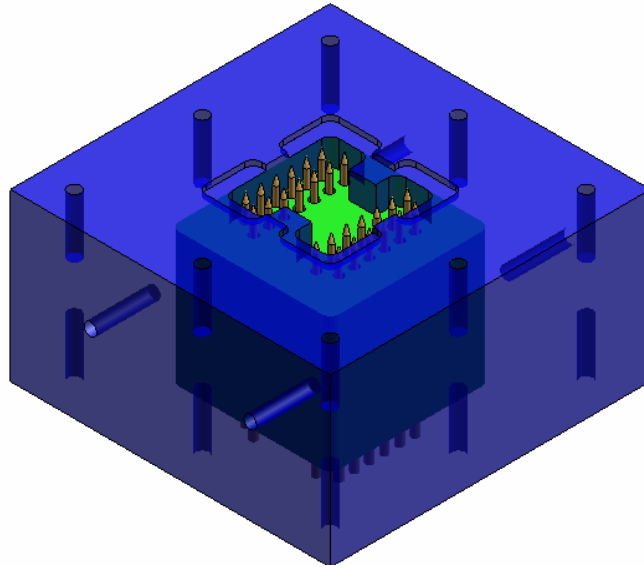


Figure 14.1.4: Main Block with Pogo Probe Block Inserted.

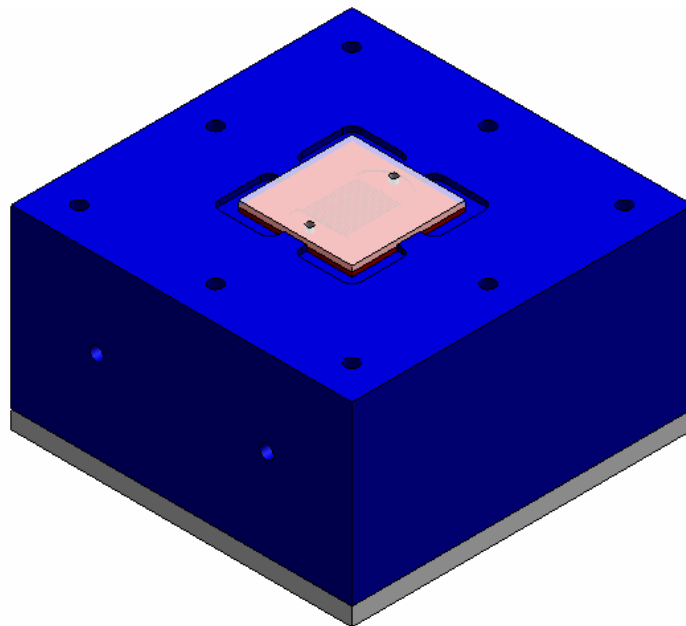


Figure 14.1.5: Main Block with Test Section Inserted and Bottom Retaining Plate.

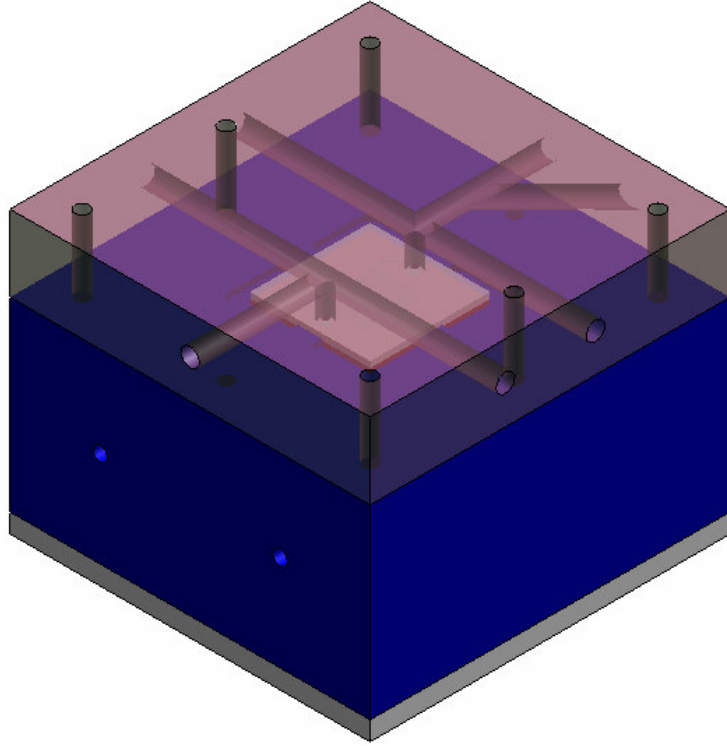


Figure 14.1.6: Assembled Main Block with Polycarbonate Retaining Plate.

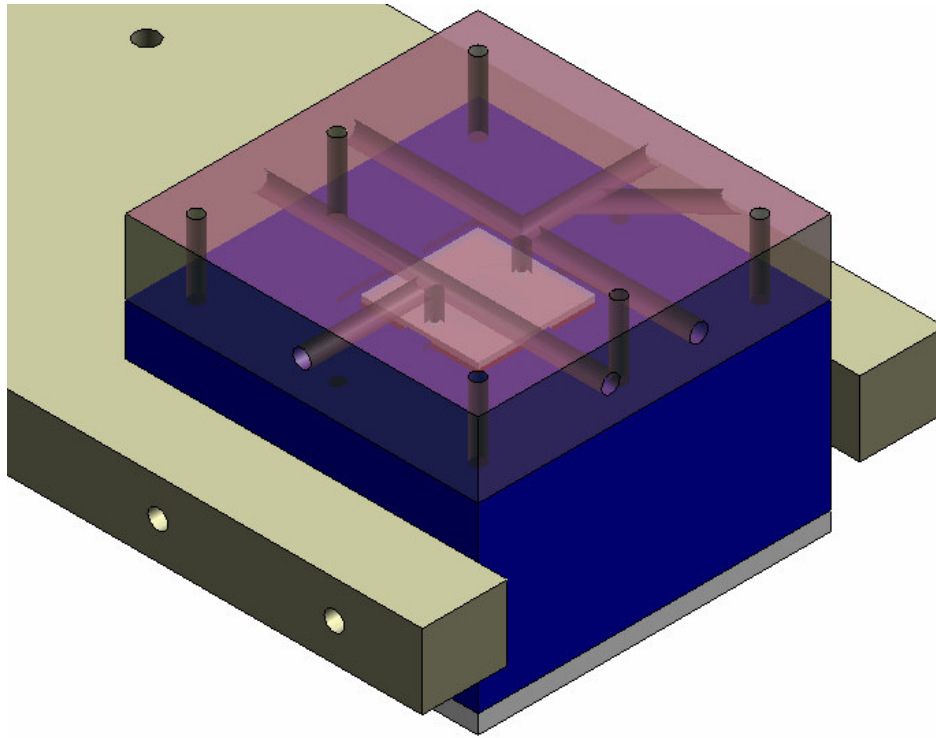


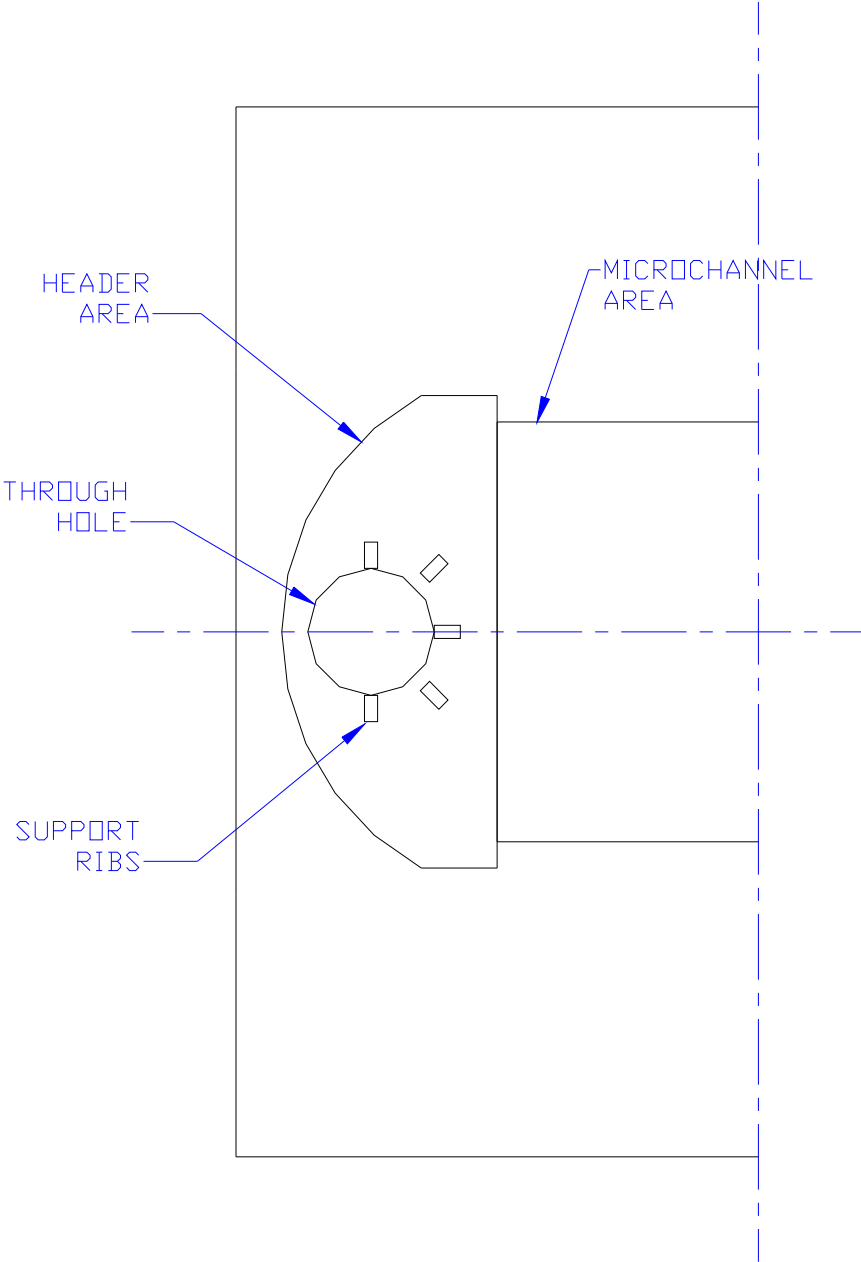
Figure 14.1.6: Assembled Main Block Mounted in X-Y Stage Mounting Plate.

13.2 Test Section Details

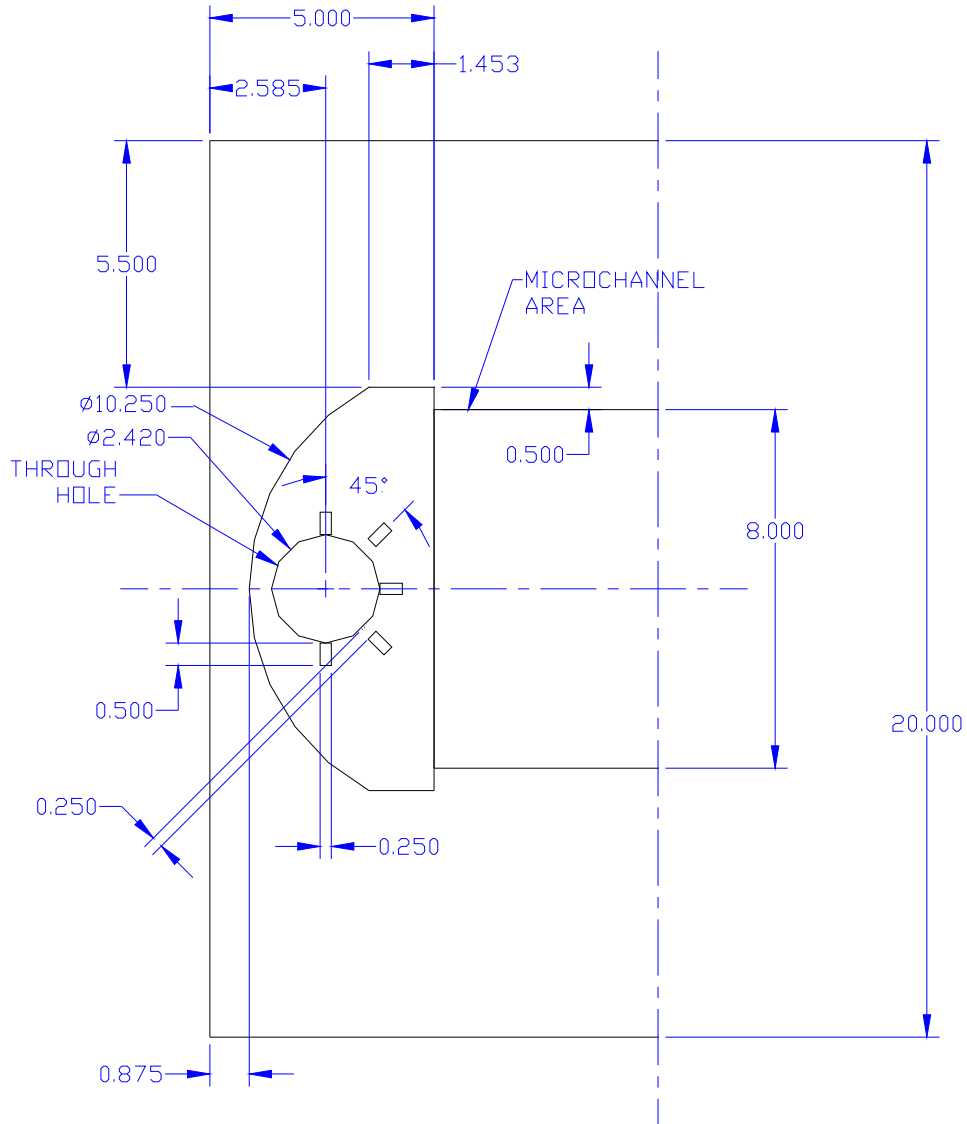
This appendix supplies information regarding the test device or in other words the test section. First, some dimensioned drawings pertaining to the test sections are presented.

Finally, the masks used to fabricate the test devices. The devices were fabricated by John Magerlein and Evan Colgan at the IBM Corp. T.J. Watson Research Laboratory. The final versions of the mask layouts were generated by Evan Colgan.

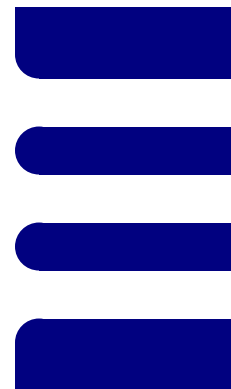
Header Details



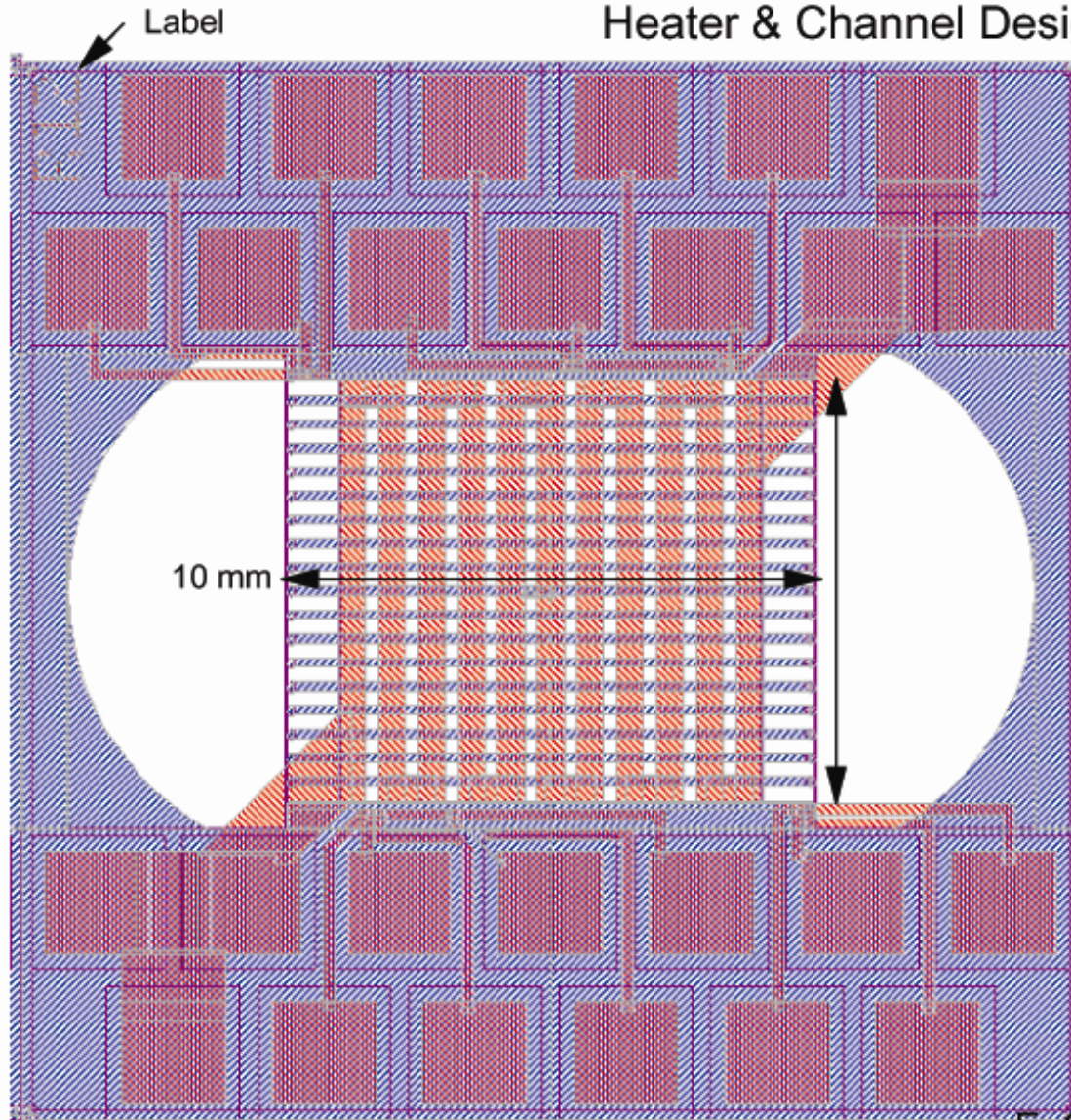
All dimensions in mm



Radius on channel inlets = 1/2 channel depth = 1/2 space between
ie... spherical ends for all channel separators



Heater & Channel Design for RIT Test Chip



Red is metal;
0.5 μm of Cu.
 ~ 0.065 Ohm/sqr.

Blue is Si not
etched on back
(white is etched)

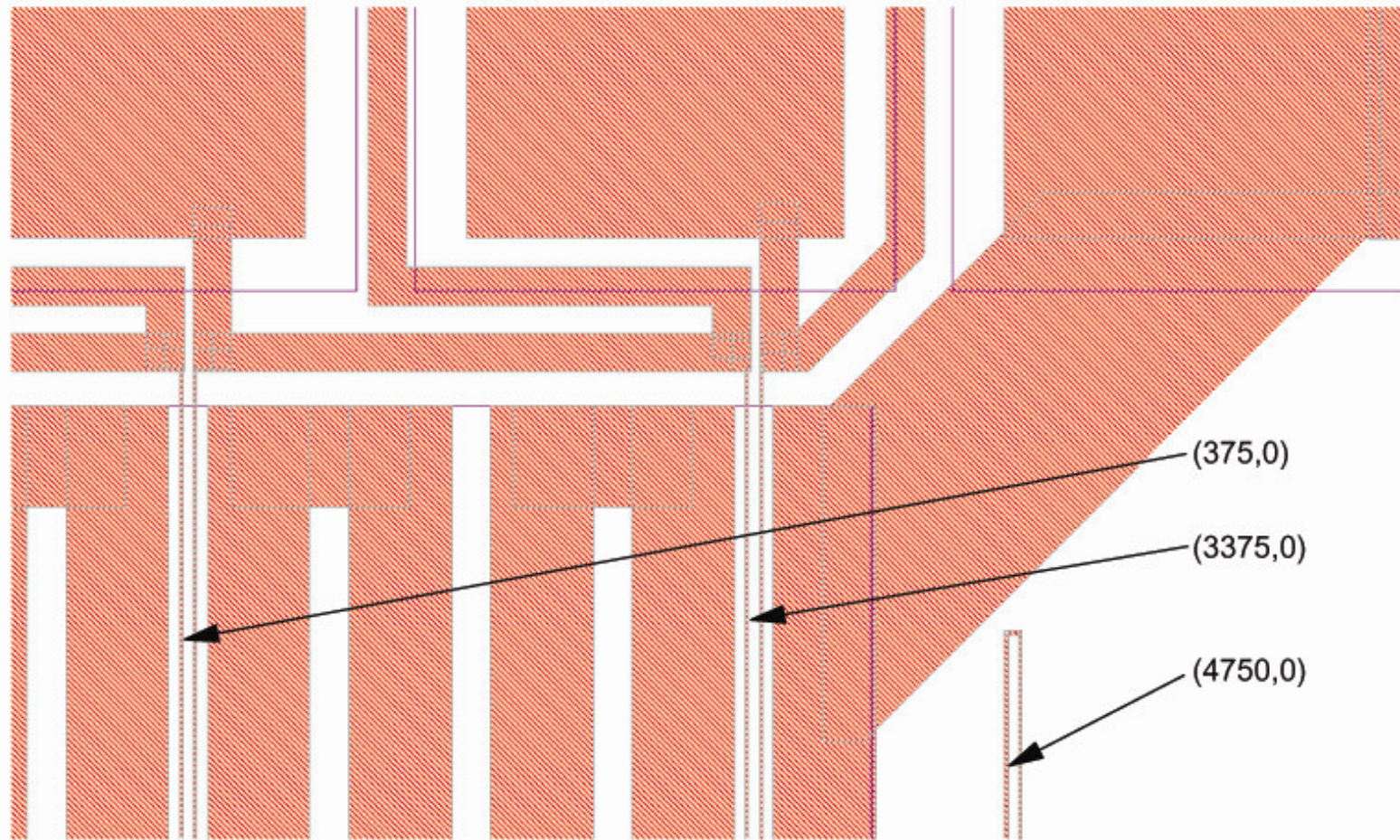
Overall chip size is
20 x 20 mm
before dicing.

Designed for 0.1"
center Pogo
probes such as
HCP-25 from
ECT.

E. Colgan

11/03

Detail of Upper Right

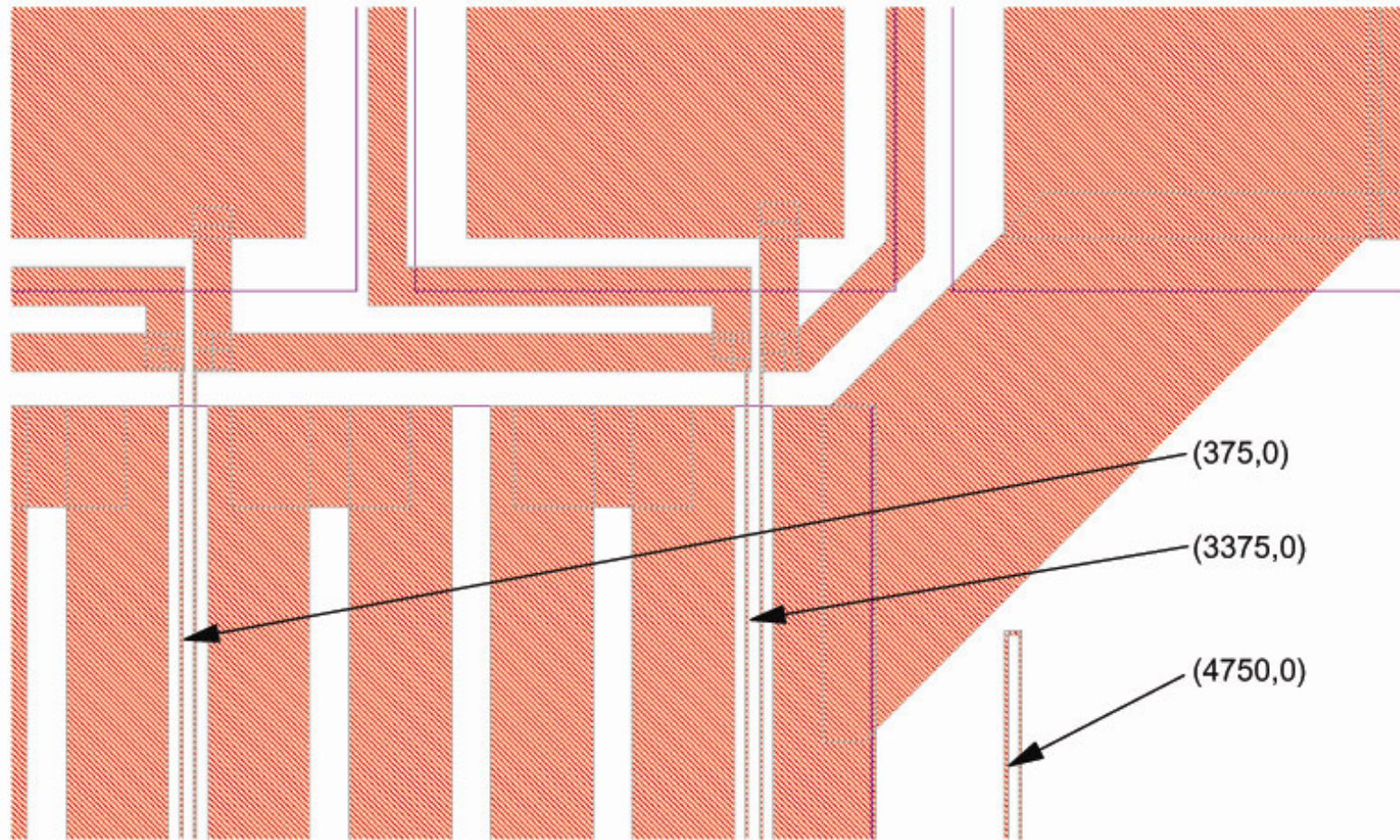


Heater Design for RIT Test Chip

E. Colgan

11/03

Detail of Upper Right

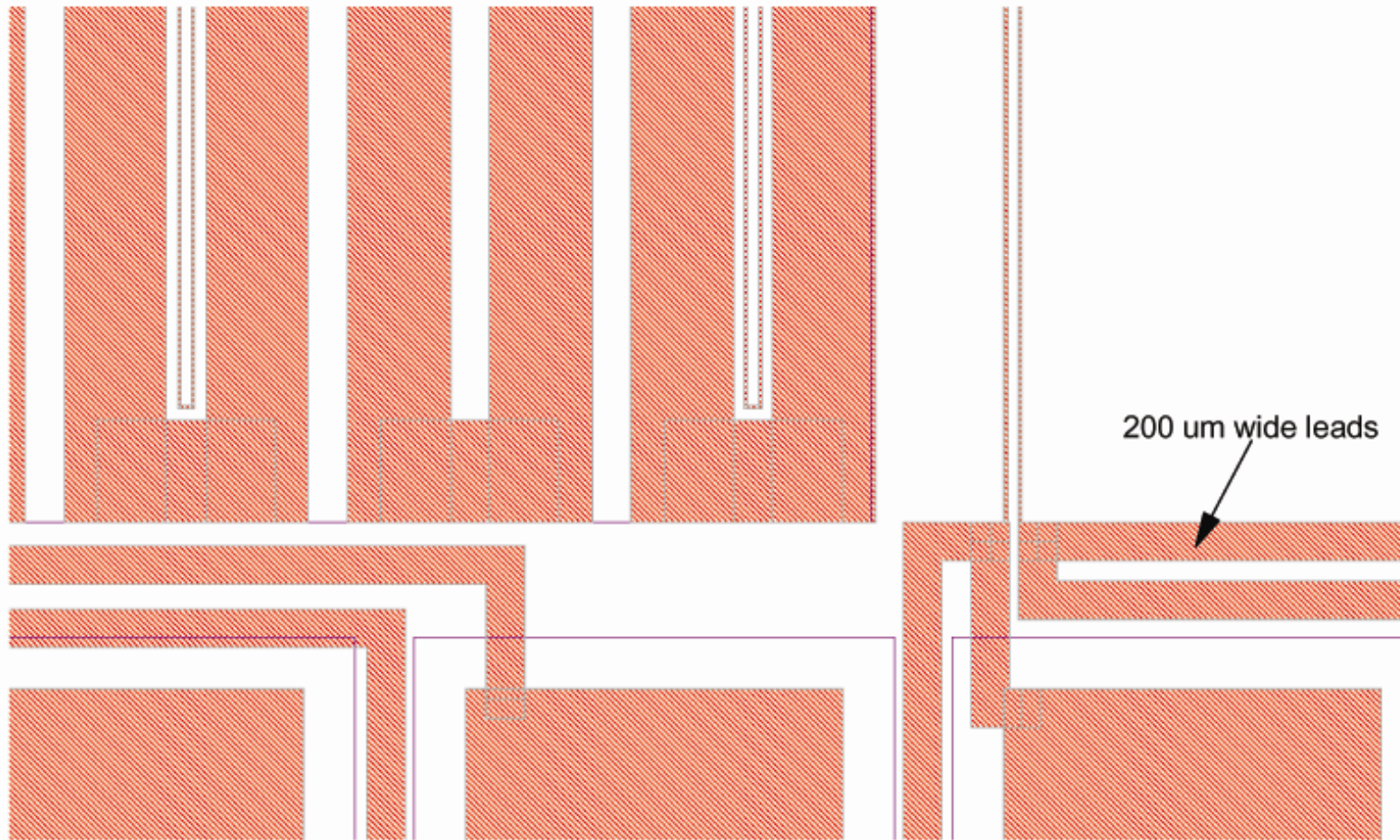


Heater Design for RIT Test Chip

E. Colgan

11/03

Detail of Lower Right

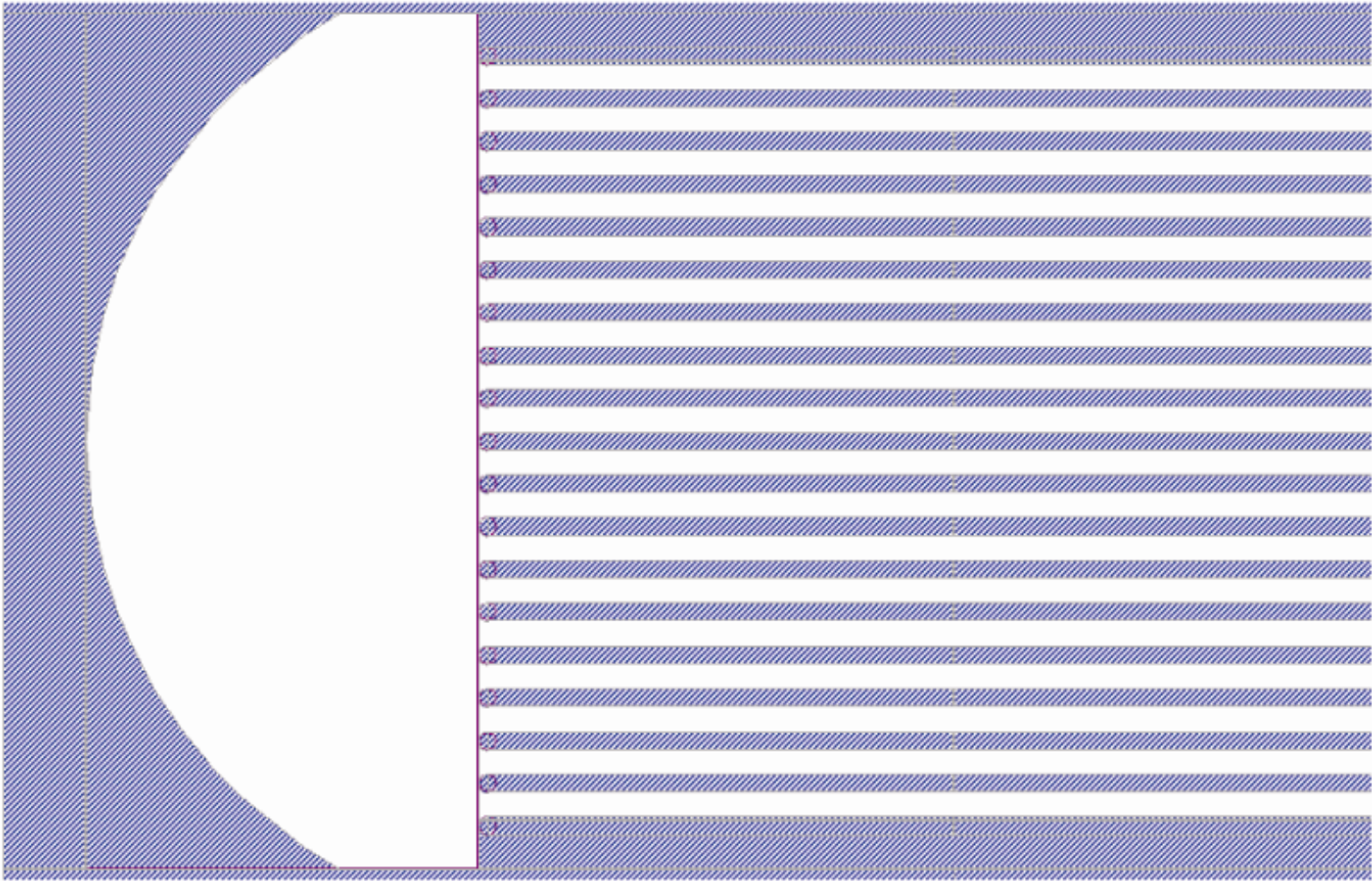


Heater Design for RIT Test Chip

E. Colgan

11/03

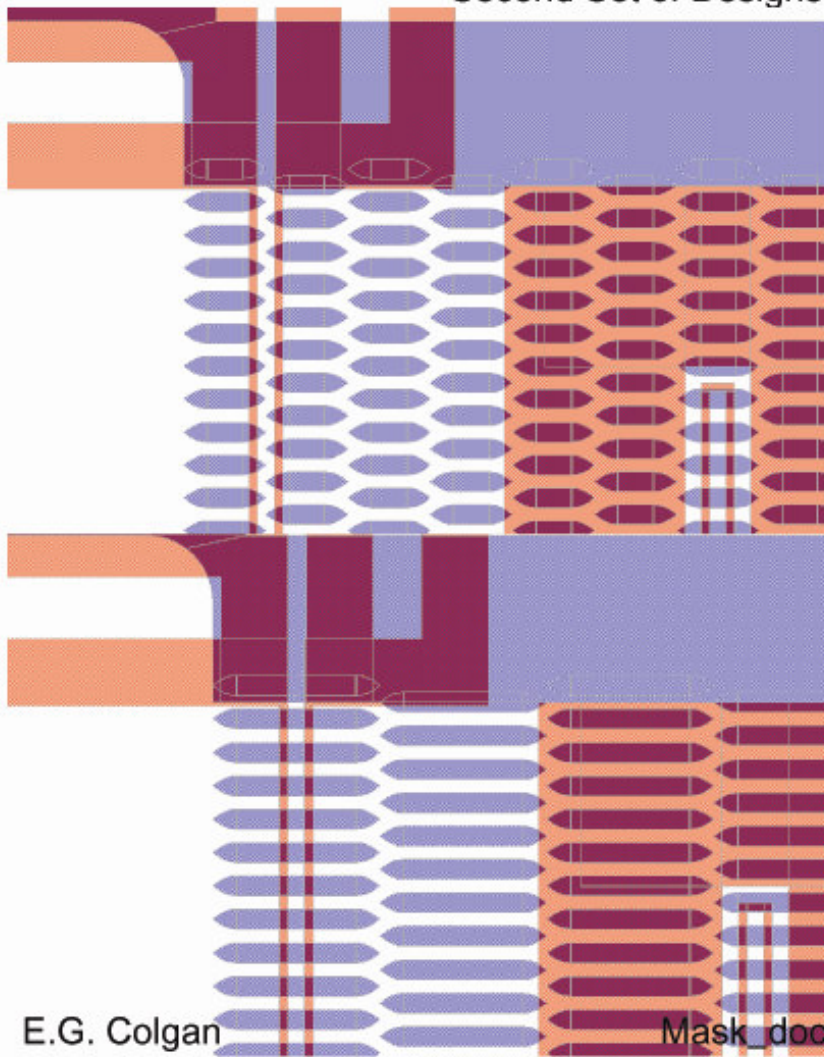
Detail of manifold on R12



E. Colgan

11/03

Second Set of Designs for RIT



R33
50 um chan/50 x 250 um fin

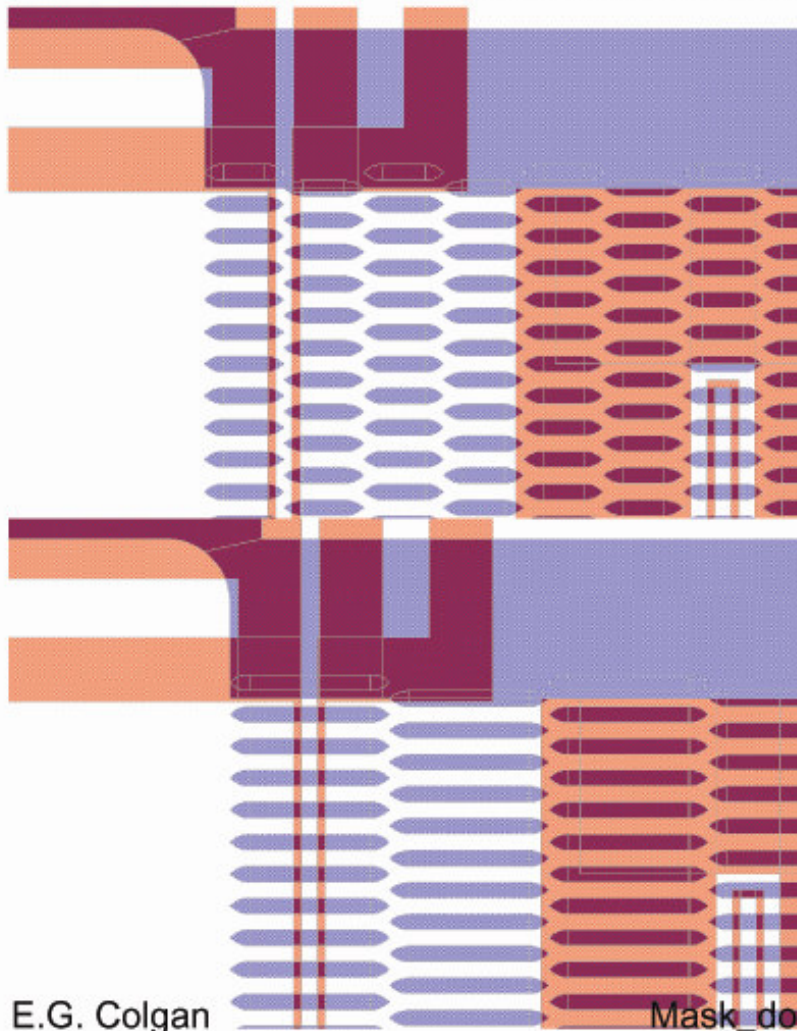
R34
50 um chan/50 x 500 um fin
-Drawn as 40/60, but >10 um
etch bias so fins narrower.

E.G. Colgan

Mask_doc_RIT2

1/05

Second Set of Designs for RIT



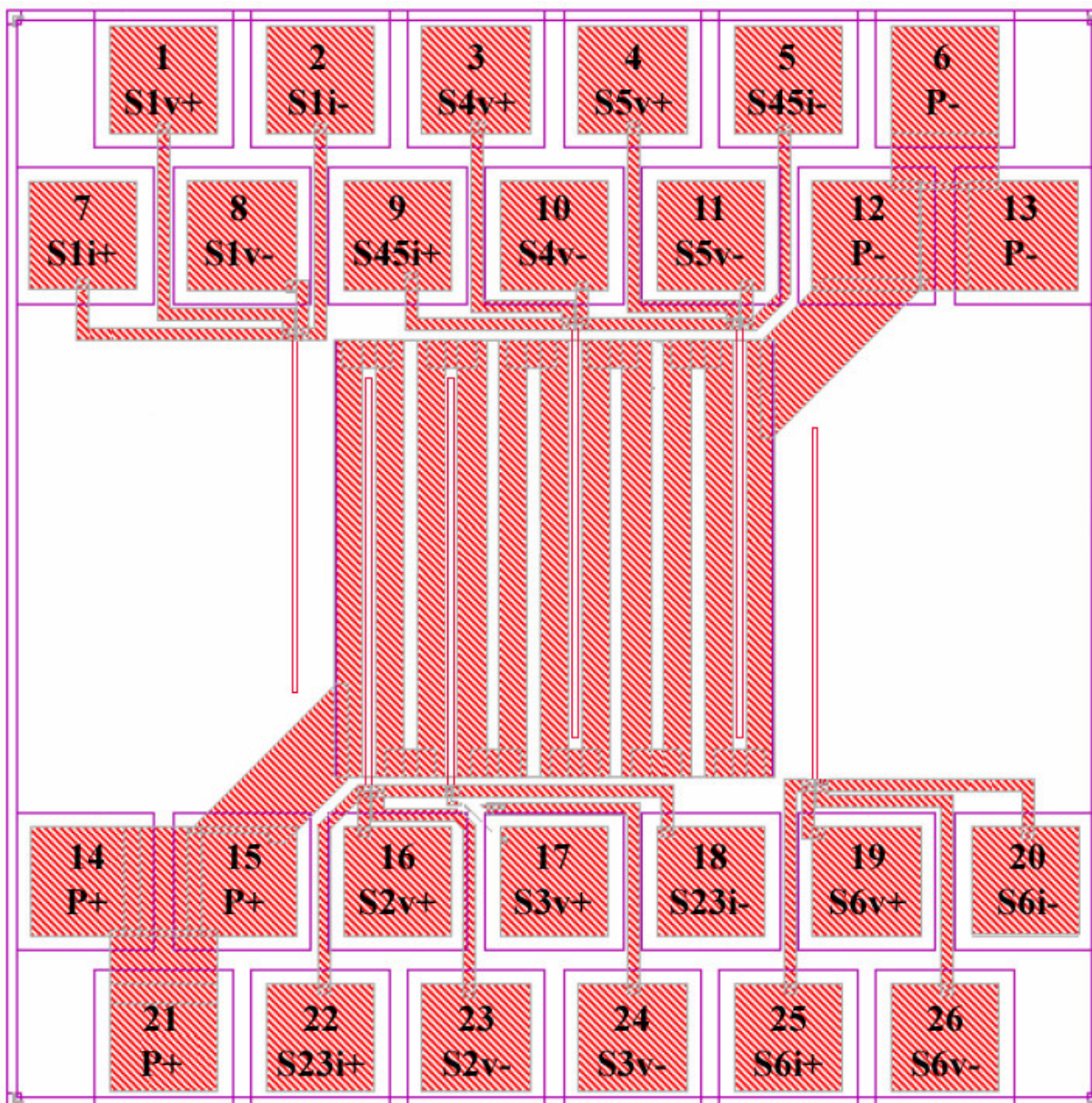
R35
60 μm chan/40 x 250 μm fin

R36
60 μm chan/40 x 500 fin
-Drawn as 50/50, but >10 μm
etch bias so fins narrower.

E.G. Colgan

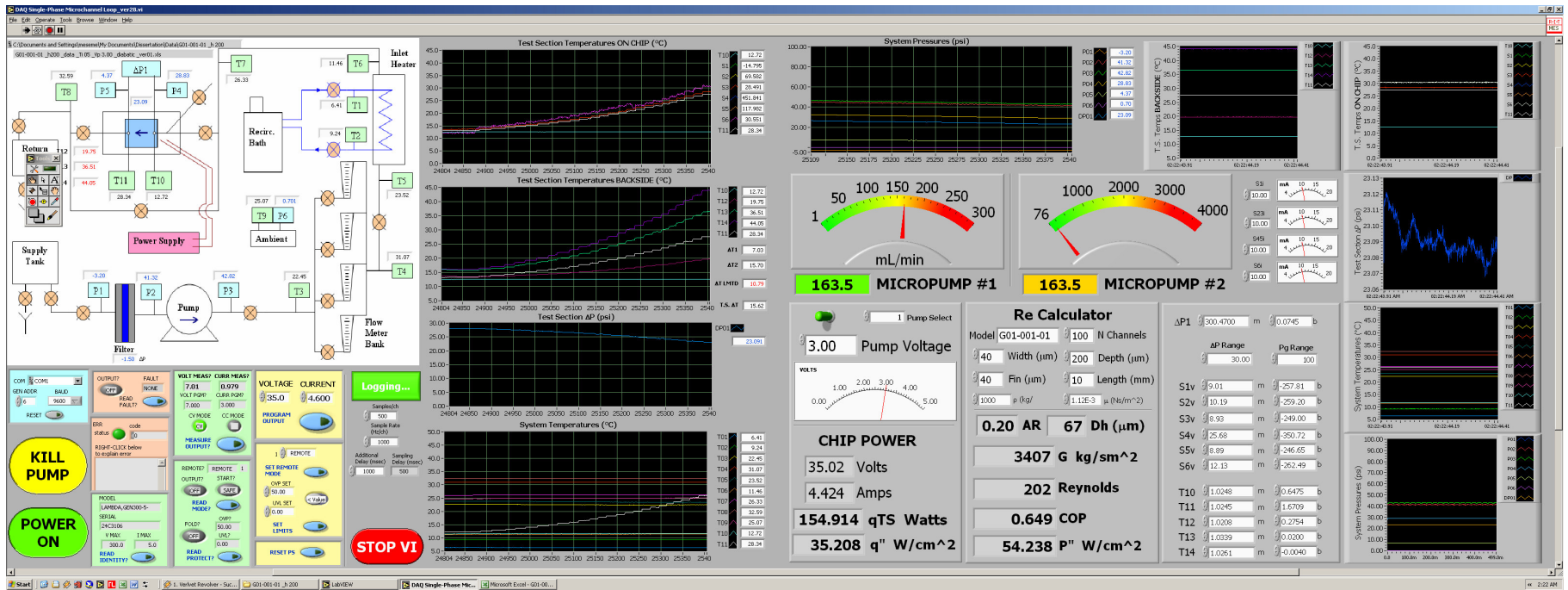
Mask_doc_RIT2

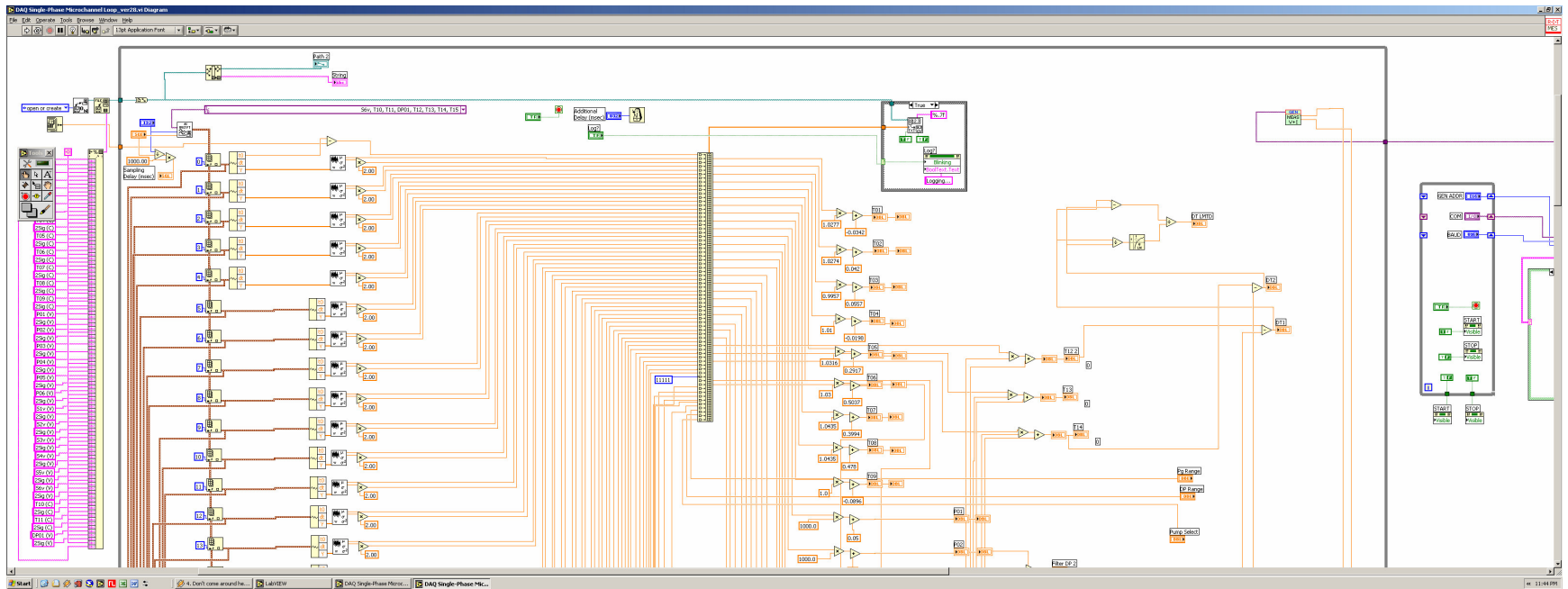
1/05

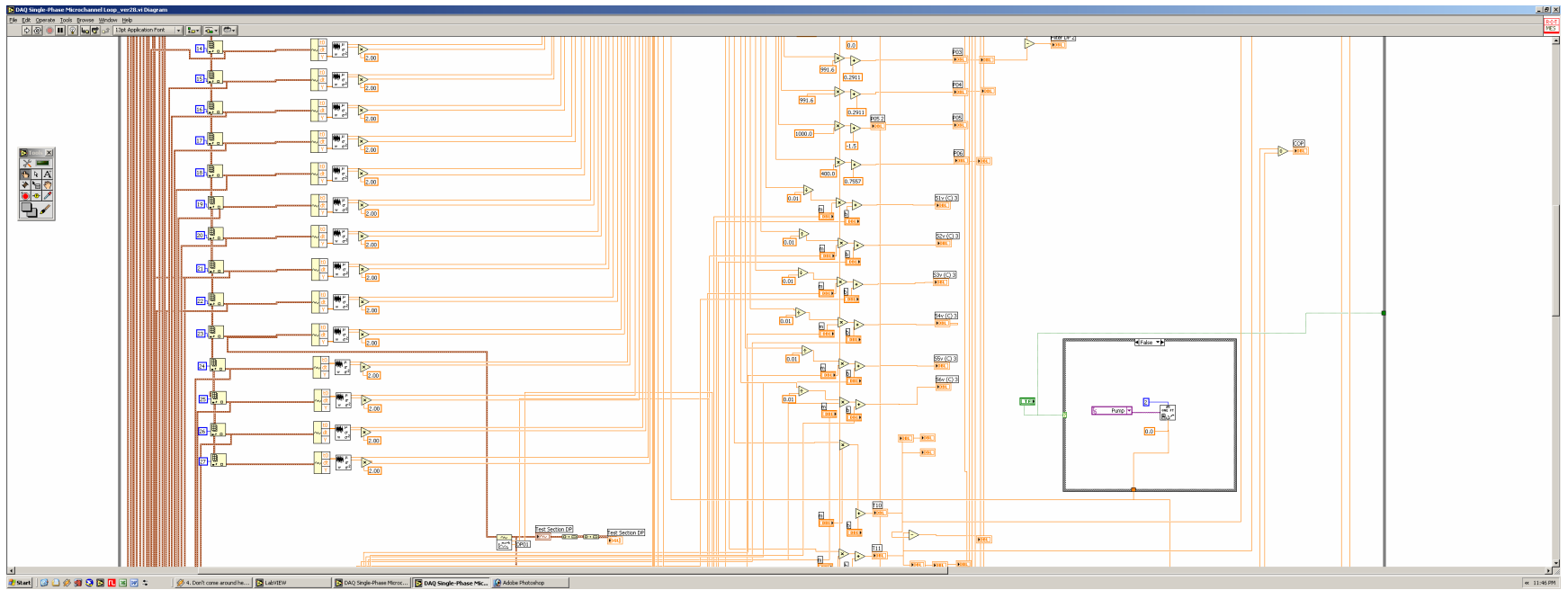


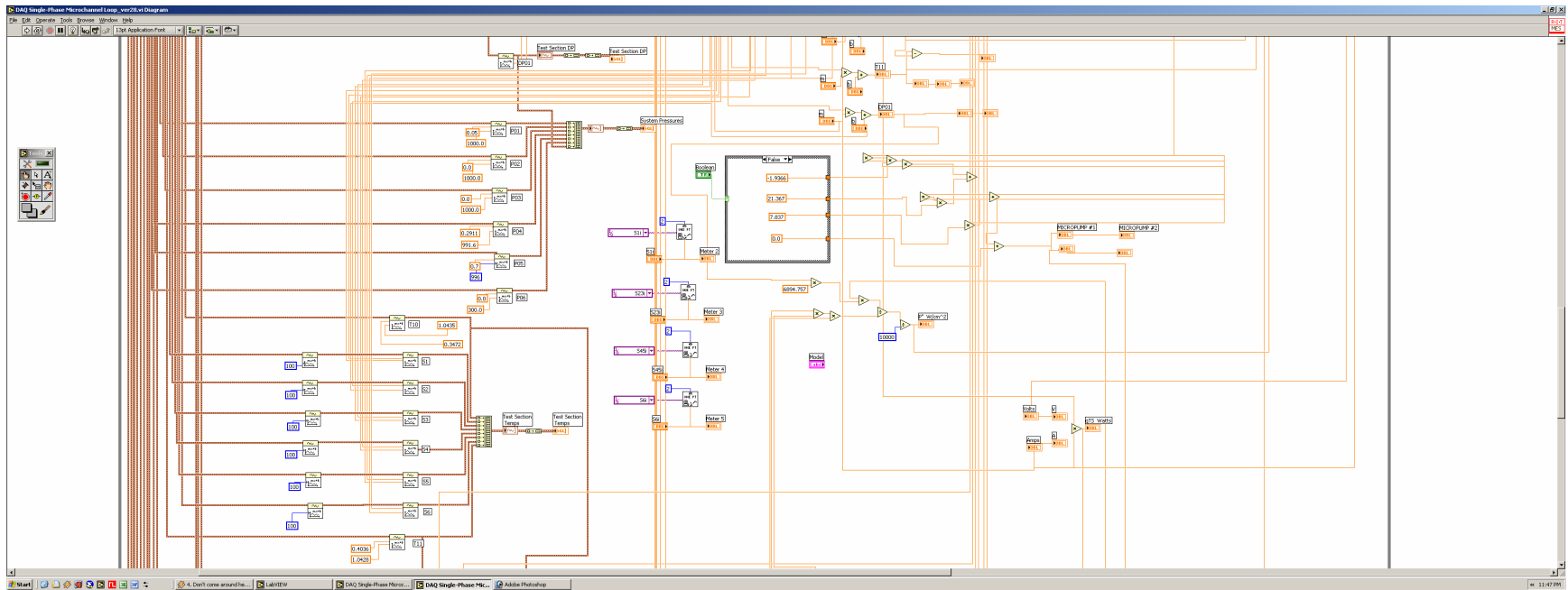
13.3 DAQ Details

This appendix supplies information regarding the data acquisition system. This includes the hardware from National Instruments as well as the LabVIEW software code. First, the LabVIEW virtual instrument (VI) is presented. The front panel is first followed by the diagram. Finally, the wiring connections are listed in a table.









Description	Identifier	Pin Outs	Wire Marker No. of Lines	Wire Color	Terminal Name Pogo Probe	Connection Pogo Probe	Terminal Block LabVIEW	Connection LabVIEW
Pogo block Power	connector	1	1	red	Power in (+)	14	-	-
		2	1	black	Power in (+)	15	-	-
		3	1	white	Power in (+)	21	-	-
		7	2	red	Power out (-)	12	-	-
		8	2	black	Power out (-)	13	-	-
		9	2	white	Power out (-)	6	-	-
Pogo Block Voltage	connector	1	1	green	S1V (+)	1		ch 0 +
		2	1	red	S1V (-)	8		ch 0 -
		3	1	black	S4V (+)	3		ch1 +
		4	1	white	S4V (-)	10		ch 1 -
		5	2	green	S2V (+)	16		ch2 +
		6	2	red	S2V (-)	23		ch2 -
		7	2	black	S3V (+)	17		ch 3 +
		8	2	white	S3V (-)	24		ch 3 -
		9	3	green	S5V (+)	4		ch 4 +
		10	3	red	S5V (-)	11		ch4 -
		11	3	black	S6V (+)	19		ch5 +
		12	3	white	S6V (-)	26		ch5 -
Pogo Block Current	connector	1	1	green	S1i (+)	7	67	ICH16
		2	1	red	S1i (-)	2	46	AGND16
		3	1	black	S45i (+)	9	32	ICH17
		4	1	white	S45i (-)	5	33	AGND17
		5	2	green	S23i (+)	22	64	ICH18
		6	2	red	S23i (-)	18	65	AGND18
		7	2	black	S6i (+)	25	29	ICH19
		8	2	white	S6i (-)	20	30	AGND19
Thermocouples	T01	-	-	-	-	-		ch31
	T02	-	-	-	-	-		ch30
	T03	-	-	-	-	-		ch29
	T04	-	-	-	-	-		ch28
	T05	-	-	-	-	-		ch27
	T06	-	-	-	-	-		ch26
	T07	-	-	-	-	-		ch07
	T08	-	-	-	-	-		ch24
	T09	-	-	-	-	-		ch23
Pressure Gages	P01	-	-	-	-	-		ch0
	P02	-	-	-	-	-		ch1
	P03	-	-	-	-	-		ch2
	P04	-	-	-	-	-		ch3
	P05	-	-	-	-	-		ch4
	↑P01	-	-	-	-	-		ch5
Pressure Gage Connector Pin Outs	ALL	1	power +	black	-	-	-	-
		2	meter +	red	-	-	-	-
		3	power -	white	-	-	-	-
		4	meter -	green	-	-	-	-
Micropump		1	power +	black/red	-	-	28	VCH4
		2	power -	white/green	-	-	62	AGND4

13.4 Uncertainty Analysis

This appendix supplies information regarding the uncertainty analysis that does not necessarily fit into the regular body of the present work. The items that will be presented include; uncertainty derivation example a calculated example, uncertainty propagation example, and the derivation of many parameter's uncertainty.

13.4.1 Uncertainty Derivation Example

The following uncertainty propagation rules are derived using partial differential equations and presented in a convenient form where the partial is actually equal to the uncertainty. For example, suppose a function is one variable divided by another. The resulting derivation would be as follows:

Function

$$z = x \cdot y$$

Take derivative

$$\partial z = x \cdot \partial y + y \cdot \partial x$$

Divide both sides by function

$$\frac{\partial z}{z} = \frac{x \cdot \partial y}{x \cdot y} + \frac{y \cdot \partial x}{x \cdot y}$$

Simplify

$$\frac{\partial z}{z} = \frac{\partial x}{x} + \frac{\partial y}{y}$$

Recast as uncertainty

$$\frac{U_z}{z} = \frac{U_x}{x} + \frac{U_y}{y}$$

Take the root means square of the uncertainty expression to eliminate signs

$$\frac{U_z}{z} = \sqrt{\left(\frac{U_x}{x}\right)^2 + \left(\frac{U_y}{y}\right)^2}$$

Now can report in standard form

$$z \pm U_z$$

13.4.2 Uncertainty Example

An example calculation of uncertainty is presented here. Let a equal the microchannel width. Suppose that three measurements of the microchannel width are made. The accuracy of the measurement device is $1.0 \mu\text{m}$.

$$a_1 = 100 \mu\text{m}, a_2 = 99 \mu\text{m}, a_3 = 101 \mu\text{m}$$

$$\text{mean of the sample set, } \mu = 100 \mu\text{m}$$

$$\text{standard deviation of the sample set, } \sigma = 1 \mu\text{m}$$

$$U = 2\sqrt{\left(\frac{B}{2}\right)^2 + \left(\frac{\sigma}{\sqrt{N}}\right)^2}$$

$$U_a = 2\sqrt{\left(\frac{\frac{1}{2} \cdot 1.0 \mu\text{m}}{2}\right)^2 + \left(\frac{1.0 \mu\text{m}}{\sqrt{3}}\right)^2}$$

$$U_a = 1.258 \mu\text{m}$$

Now, report the measurement in the standard form of uncertainty.

$$\mu \pm U_a$$

$$100 \pm 1.258 \mu\text{m}$$

13.4.3 Uncertainty Propagation

The following subsections present the propagation rules for the most common functions. The function is first defined. Then, the uncertainty is presented in the RMS form to simplify uncertainty propagation.

Single Variable

Function

$$z = x$$

Uncertainty

$$\frac{U_z}{z} = \frac{U_x}{x}$$

Single Variable Multiplied by a Constant

Function

$$z = C \cdot x$$

Uncertainty

$$\frac{U_z}{z} = \frac{U_x}{x}$$

Addition

Function

$$z = x + y$$

Uncertainty

$$U_z = [(U_x)^2 + (U_y)^2]^{1/2} \quad \text{or}$$

$$\frac{U_z}{z} = \left[\left(\frac{U_x}{x+y} \right)^2 + \left(\frac{U_y}{x+y} \right)^2 \right]^{1/2}$$

Subtraction

Function

$$z = x - y$$

Uncertainty

$$U_z = [(U_x)^2 + (U_y)^2]^{1/2} \quad \text{or}$$

$$\frac{U_z}{z} = \left[\left(\frac{U_x}{x-y} \right)^2 + \left(\frac{U_y}{x-y} \right)^2 \right]^{1/2}$$

Multiplication

Function

$$z = x \cdot y$$

Uncertainty

$$\frac{U_z}{z} = \left[\left(\frac{U_x}{x} \right)^2 + \left(\frac{U_y}{y} \right)^2 \right]^{1/2}$$

Division

Function

$$z = \frac{x}{y}$$

Uncertainty

$$\frac{U_z}{z} = \left[\left(\frac{U_x}{x} \right)^2 + \left(\frac{U_y}{y} \right)^2 \right]^{1/2}$$

Exponent

Function

$$z = x^n$$

Uncertainty

$$\frac{U_z}{z} = \left[n \cdot \left(\frac{U_x}{x} \right)^2 \right]^{1/2}$$

Natural Log

Function

$$z = \ln(x)$$

Uncertainty

$$U_z = \frac{U_x}{x} \quad \text{or} \quad \frac{U_z}{z} = \left[\left(\frac{U_x}{x \cdot \ln(x)} \right)^2 \right]^{1/2}$$

Sine

Function

$$z = \sin(x)$$

Uncertainty

$$U_z = \cos(x) \cdot U_x$$

Cosine

Function

$$z = \cos(x)$$

Uncertainty

$$U_z = -\sin(x) \cdot U_x$$

Tangent

Function

$$z = \tan(x)$$

Uncertainty

$$U_z = \sec^2(x) \cdot U_x$$

First Order Polynomial

Function

$$y = m \cdot x + b$$

Standard Deviation

$$\sigma_y = \sqrt{\frac{1}{N-2} \sum_{i=1}^n (y_i - b - m \cdot x_i)^2}$$

13.4.4 Uncertainty of Major Calculated Parameters

This section will present the derivation of the uncertainties of the calculated parameters for the present work. The calculated parameter formula will be presented followed by the derivation of the uncertainty. Finally, the result of the derivation will present the final form of the uncertainty for that parameter.

Measured Parameters

All of the following uncertainties are calculated based upon the measured parameters or variables. The measured parameters are as follows:

Table A13.1

Parameter	Symbol	Units
microchannel width	a	m
microchannel depth	b	m
microchannel fin thickness	s	m
microchannel length	L	m
flow length	x	m
volumetric flow rate	Q	$\text{m}^3 \text{s}^{-1}$
viscosity	μ	N s m^{-2}
density	ρ	kg m^{-3}
thermal conductivity	k	$\text{W m}^{-1} \text{K}^{-1}$
pressure drop	Δp	Pa
temperature	T	$^{\circ}\text{C}$
Prandtl number	Pr	-
pressure loss factor	K	-
voltage	V	V
current	I	A

Microchannel Aspect Ratio

Function

$$\alpha_c = \frac{a}{b}$$

Uncertainty

$$\frac{U_{\alpha_c}}{\alpha_c} = \left[\left(\frac{U_a}{a} \right)^2 + \left(\frac{U_b}{b} \right)^2 \right]^{1/2}$$

Fin Aspect Ratio

Function

$$\alpha_f = \frac{s}{b}$$

Uncertainty

$$\frac{U_{\alpha_f}}{\alpha_f} = \left[\left(\frac{U_s}{s} \right)^2 + \left(\frac{U_b}{b} \right)^2 \right]^{1/2}$$

Fin Spacing Ratio

Function

$$\beta = \frac{\alpha_f}{\alpha_c} = \frac{s}{a}$$

Uncertainty

$$\frac{U_{\beta}}{\beta} = \left[\left(\frac{U_s}{s} \right)^2 + \left(\frac{U_a}{a} \right)^2 \right]^{1/2}$$

Cross Sectional Area

Function

$$A_c = a \cdot b$$

Uncertainty

$$\frac{U_{A_c}}{A_c} = \left[\left(\frac{U_a}{a} \right)^2 + \left(\frac{U_b}{b} \right)^2 \right]^{1/2}$$

Wetted Perimeter

Function

$$P_w = 2 \cdot (a + b)$$

Uncertainty

$$U_{P_w} = 2 \cdot U_a + 2 \cdot U_b$$

$$\frac{U_{P_w}}{P_w} = \left[\left(\frac{U_a}{a+b} \right)^2 + \left(\frac{U_b}{a+b} \right)^2 \right]^{1/2}$$

Hydraulic Diameter

Function

$$D_h = \frac{4 \cdot A_c}{P_w}$$

Uncertainty

$$\frac{U_{D_h}}{D_h} = \left[\left(\frac{U_{A_c}}{A_c} \right)^2 + \left(\frac{U_{P_w}}{P_w} \right)^2 \right]^{1/2}$$

$$\frac{U_{D_h}}{D_h} = \left[\left(\frac{U_a}{a} \right)^2 + \left(\frac{U_b}{b} \right)^2 + \left(\frac{U_a}{a+b} \right)^2 + \left(\frac{U_b}{a+b} \right)^2 \right]^{1/2}$$

Reynolds Number

Function

$$\text{Re} = \frac{\rho \cdot \bar{V} \cdot D_h}{\mu} = \frac{\rho \cdot Q \cdot D_h}{\mu \cdot A_c}$$

Uncertainty

$$\frac{U_{\text{Re}}}{\text{Re}} = \left[\left(\frac{U_{\rho}}{\rho} \right)^2 + \left(\frac{U_{\mu}}{\mu} \right)^2 + \left(\frac{U_Q}{Q} \right)^2 + \left(\frac{U_{A_c}}{A_c} \right)^2 + \left(\frac{U_{D_h}}{D_h} \right)^2 \right]^{1/2}$$

$$\frac{U_{\text{Re}}}{\text{Re}} = \left[\left(\frac{U_{\rho}}{\rho} \right)^2 + \left(\frac{U_{\mu}}{\mu} \right)^2 + \left(\frac{U_Q}{Q} \right)^2 + \left(\frac{U_a}{a} \right)^2 + \left(\frac{U_b}{b} \right)^2 + \left(\frac{U_a}{a} \right)^2 + \left(\frac{U_b}{b} \right)^2 + \left(\frac{U_a}{a+b} \right)^2 + \left(\frac{U_b}{a+b} \right)^2 \right]^{1/2}$$

$$\frac{U_{\text{Re}}}{\text{Re}} = \left[\left(\frac{U_{\rho}}{\rho} \right)^2 + \left(\frac{U_{\mu}}{\mu} \right)^2 + \left(\frac{U_Q}{Q} \right)^2 + 2 \cdot \left(\frac{U_a}{a} \right)^2 + 2 \cdot \left(\frac{U_b}{b} \right)^2 + \left(\frac{U_a}{a+b} \right)^2 + \left(\frac{U_b}{a+b} \right)^2 \right]^{1/2}$$

Fanning Friction Factor

Function

$$f = \frac{\Delta p \cdot D_h}{2 \cdot \rho \cdot L \cdot \bar{V}^2} = \frac{\Delta p \cdot D_h \cdot A_c^2}{2 \cdot \rho \cdot L \cdot Q^2}$$

Uncertainty

$$\frac{U_f}{f} = \left[\left(\frac{U_{\rho}}{\rho} \right)^2 + \left(\frac{U_{\Delta p}}{\Delta p} \right)^2 + \left(\frac{U_L}{L} \right)^2 + 2 \cdot \left(\frac{U_Q}{Q} \right)^2 + 2 \cdot \left(\frac{U_{A_c}}{A_c} \right)^2 + \left(\frac{U_{D_h}}{D_h} \right)^2 \right]^{1/2}$$

$$\frac{U_f}{f} = \left[\left(\frac{U_\rho}{\rho} \right)^2 + \left(\frac{U_{\Delta p}}{\Delta p} \right)^2 + \left(\frac{U_L}{L} \right)^2 + 2 \cdot \left(\frac{U_Q}{Q} \right)^2 + 2 \cdot \left\{ \left(\frac{U_a}{a} \right)^2 + \left(\frac{U_b}{b} \right)^2 \right\} \right. \\ \left. + \left\{ \left(\frac{U_a}{a} \right)^2 + \left(\frac{U_b}{b} \right)^2 + \left(\frac{U_a}{a+b} \right)^2 + \left(\frac{U_b}{a+b} \right)^2 \right\} \right]^{1/2}$$

$$\frac{U_f}{f} = \left[\left(\frac{U_\rho}{\rho} \right)^2 + \left(\frac{U_{\Delta p}}{\Delta p} \right)^2 + \left(\frac{U_L}{L} \right)^2 + 2 \cdot \left(\frac{U_Q}{Q} \right)^2 + 3 \cdot \left(\frac{U_a}{a} \right)^2 \right. \\ \left. + 3 \cdot \left(\frac{U_b}{b} \right)^2 + \left(\frac{U_a}{a+b} \right)^2 + \left(\frac{U_b}{a+b} \right)^2 \right]^{1/2}$$

Poiseuille Number, $f^* \text{Re}$

Function

$$f \cdot \text{Re} = \frac{\text{Re} \cdot \Delta p \cdot D_h}{2 \cdot \rho \cdot L \cdot \bar{V}^2} = \frac{\text{Re} \cdot \Delta p \cdot D_h \cdot A_c^2}{2 \cdot \rho \cdot L \cdot Q^2}$$

Uncertainty

$$\frac{U_{f \text{Re}}}{f \text{Re}} = \left[\left(\frac{U_f}{f} \right)^2 + \left(\frac{U_{\text{Re}}}{\text{Re}} \right)^2 \right]^{1/2}$$

$$\frac{U_{f \text{Re}}}{f \text{Re}} = \left[\left\{ \left(\frac{U_\rho}{\rho} \right)^2 + \left(\frac{U_{\Delta p}}{\Delta p} \right)^2 + \left(\frac{U_L}{L} \right)^2 + 2 \cdot \left(\frac{U_Q}{Q} \right)^2 + 3 \cdot \left(\frac{U_a}{a} \right)^2 \right\} \right. \\ \left. + \left\{ 3 \cdot \left(\frac{U_b}{b} \right)^2 + \left(\frac{U_a}{a+b} \right)^2 + \left(\frac{U_b}{a+b} \right)^2 \right\} \right]^{1/2} \\ + \left[\left\{ \left(\frac{U_\rho}{\rho} \right)^2 + \left(\frac{U_\mu}{\mu} \right)^2 + \left(\frac{U_Q}{Q} \right)^2 + 2 \cdot \left(\frac{U_a}{a} \right)^2 \right\} \right. \\ \left. + \left\{ 2 \cdot \left(\frac{U_b}{b} \right)^2 + \left(\frac{U_a}{a+b} \right)^2 + \left(\frac{U_b}{a+b} \right)^2 \right\} \right]^{1/2}$$

$$\frac{U_{fRe}}{fRe} = \left[\begin{array}{l} 2 \cdot \left(\frac{U_\rho}{\rho} \right)^2 + \left(\frac{U_\mu}{\mu} \right)^2 + \left(\frac{U_{\Delta p}}{\Delta p} \right)^2 + \left(\frac{U_L}{L} \right)^2 + 3 \cdot \left(\frac{U_Q}{Q} \right)^2 + \\ 5 \cdot \left(\frac{U_a}{a} \right)^2 + 5 \cdot \left(\frac{U_b}{b} \right)^2 + 2 \cdot \left(\frac{U_a}{a+b} \right)^2 + 2 \cdot \left(\frac{U_b}{a+b} \right)^2 \end{array} \right]^{1/2}$$

Non-Dimensional Length, Hydraulic

Function

$$x^+ = \frac{x}{D_h \cdot Re}$$

Uncertainty

$$\frac{U_{x^+}}{x^+} = \left[\left(\frac{U_x}{x} \right)^2 + \left(\frac{U_{D_h}}{D_h} \right)^2 + \left(\frac{U_{Re}}{Re} \right)^2 \right]^{1/2}$$

$$\frac{U_{x^+}}{x^+} = \left[\left(\frac{U_x}{x} \right)^2 + \left\{ \left(\frac{U_a}{a} \right)^2 + \left(\frac{U_b}{b} \right)^2 + \left(\frac{U_a}{a+b} \right)^2 + \left(\frac{U_b}{a+b} \right)^2 \right\} \right]^{1/2}$$

$$\frac{U_{x^+}}{x^+} = \left[\begin{array}{l} \left\{ \left(\frac{U_\rho}{\rho} \right)^2 + \left(\frac{U_\mu}{\mu} \right)^2 + \left(\frac{U_Q}{Q} \right)^2 + 2 \cdot \left(\frac{U_a}{a} \right)^2 \right\} \\ + \left\{ 2 \cdot \left(\frac{U_b}{b} \right)^2 + \left(\frac{U_a}{a+b} \right)^2 + \left(\frac{U_b}{a+b} \right)^2 \right\} \end{array} \right]^{1/2}$$

$$\frac{U_{x^+}}{x^+} = \left[\begin{array}{l} \left(\frac{U_\rho}{\rho} \right)^2 + \left(\frac{U_\mu}{\mu} \right)^2 + \left(\frac{U_x}{x} \right)^2 + \left(\frac{U_Q}{Q} \right)^2 + 3 \cdot \left(\frac{U_a}{a} \right)^2 \\ + 3 \cdot \left(\frac{U_b}{b} \right)^2 + 2 \cdot \left(\frac{U_a}{a+b} \right)^2 + 2 \cdot \left(\frac{U_b}{a+b} \right)^2 \end{array} \right]^{1/2}$$

Non-Dimensional Length, Thermal

Function

$$x^* = \frac{x}{D_h \cdot \text{Re} \cdot \text{Pr}}$$

Uncertainty

$$\frac{U_{x^*}}{x^*} = \left[\left(\frac{U_x}{x} \right)^2 + \left(\frac{U_{D_h}}{D_h} \right)^2 + \left(\frac{U_{\text{Re}}}{\text{Re}} \right)^2 + \left(\frac{U_{\text{Pr}}}{\text{Pr}} \right)^2 \right]^{1/2}$$

$$\frac{U_{x^*}}{x^*} = \left[\left(\frac{U_x}{x} \right)^2 + \left\{ \left(\frac{U_a}{a} \right)^2 + \left(\frac{U_b}{b} \right)^2 + \left(\frac{U_a}{a+b} \right)^2 + \left(\frac{U_b}{a+b} \right)^2 \right\} \right. \\ \left. + \left\{ \left(\frac{U_\rho}{\rho} \right)^2 + \left(\frac{U_\mu}{\mu} \right)^2 + \left(\frac{U_Q}{Q} \right)^2 + 2 \cdot \left(\frac{U_a}{a} \right)^2 \right\} + \left(\frac{U_{\text{Pr}}}{\text{Pr}} \right)^2 \right. \\ \left. + \left\{ 2 \cdot \left(\frac{U_b}{b} \right)^2 + \left(\frac{U_a}{a+b} \right)^2 + \left(\frac{U_b}{a+b} \right)^2 \right\} \right]^{1/2}$$

$$\frac{U_{x^*}}{x^*} = \left[\left(\frac{U_\rho}{\rho} \right)^2 + \left(\frac{U_\mu}{\mu} \right)^2 + \left(\frac{U_x}{x} \right)^2 + \left(\frac{U_Q}{Q} \right)^2 + 3 \cdot \left(\frac{U_a}{a} \right)^2 \right. \\ \left. + 3 \cdot \left(\frac{U_b}{b} \right)^2 + 2 \cdot \left(\frac{U_a}{a+b} \right)^2 + 2 \cdot \left(\frac{U_b}{a+b} \right)^2 + \left(\frac{U_{\text{Pr}}}{\text{Pr}} \right)^2 \right]^{1/2}$$

Hydrodynamic Entrance Length

Function

$$Le_H = 0.05 \cdot D_h \cdot \text{Re}$$

Uncertainty

$$\frac{U_{Le_H}}{Le_H} = \left[\left(\frac{U_{D_h}}{D_h} \right)^2 + \left(\frac{U_{\text{Re}}}{\text{Re}} \right)^2 \right]^{1/2}$$

$$\frac{U_{Le_H}}{Le_H} = \left[\left\{ \left(\frac{U_a}{a} \right)^2 + \left(\frac{U_b}{b} \right)^2 + \left(\frac{U_a}{a+b} \right)^2 + \left(\frac{U_b}{a+b} \right)^2 \right\} + \left\{ \left(\frac{U_\rho}{\rho} \right)^2 + \left(\frac{U_\mu}{\mu} \right)^2 + \left(\frac{U_Q}{Q} \right)^2 + 2 \cdot \left(\frac{U_a}{a} \right)^2 + 2 \cdot \left(\frac{U_b}{b} \right)^2 + \left(\frac{U_a}{a+b} \right)^2 + \left(\frac{U_b}{a+b} \right)^2 \right\} \right]^{1/2}$$

$$\frac{U_{Le_H}}{Le_H} = \left[\left(\frac{U_\rho}{\rho} \right)^2 + \left(\frac{U_\mu}{\mu} \right)^2 + \left(\frac{U_Q}{Q} \right)^2 + 3 \cdot \left(\frac{U_a}{a} \right)^2 + 3 \cdot \left(\frac{U_b}{b} \right)^2 + 2 \cdot \left(\frac{U_a}{a+b} \right)^2 + 2 \cdot \left(\frac{U_b}{a+b} \right)^2 \right]^{1/2}$$

Thermal Entrance Length

Function

$$Le_T = 0.05 \cdot D_h \cdot Re \cdot Pr$$

Uncertainty

$$\frac{U_{Le_T}}{Le_T} = \left[\left(\frac{U_{D_h}}{D_h} \right)^2 + \left(\frac{U_{Re}}{Re} \right)^2 + \left(\frac{U_{Pr}}{Pr} \right)^2 \right]^{1/2} + \left[\left\{ \left(\frac{U_a}{a} \right)^2 + \left(\frac{U_b}{b} \right)^2 + \left(\frac{U_a}{a+b} \right)^2 + \left(\frac{U_b}{a+b} \right)^2 \right\} + \left\{ \left(\frac{U_\rho}{\rho} \right)^2 + \left(\frac{U_\mu}{\mu} \right)^2 + \left(\frac{U_Q}{Q} \right)^2 + 2 \cdot \left(\frac{U_a}{a} \right)^2 + 2 \cdot \left(\frac{U_b}{b} \right)^2 + \left(\frac{U_a}{a+b} \right)^2 + \left(\frac{U_b}{a+b} \right)^2 \right\} + \left(\frac{U_{Pr}}{Pr} \right)^2 \right]^{1/2}$$

$$\frac{U_{Le_T}}{Le_T} = \left[\left(\frac{U_\rho}{\rho} \right)^2 + \left(\frac{U_\mu}{\mu} \right)^2 + \left(\frac{U_Q}{Q} \right)^2 + 3 \cdot \left(\frac{U_a}{a} \right)^2 + 3 \cdot \left(\frac{U_b}{b} \right)^2 + 2 \cdot \left(\frac{U_a}{a+b} \right)^2 + 2 \cdot \left(\frac{U_b}{a+b} \right)^2 + \left(\frac{U_{Pr}}{Pr} \right)^2 \right]^{1/2}$$

fRe as a Function of Microchannel Aspect Ratio Shah & London (1978) four side heating

Function

$$f Re = 24 \left(1 - 1.3553\alpha_c + 1.9467\alpha_c^2 - 1.7012\alpha_c^3 + 0.9564\alpha_c^4 - 0.2537\alpha_c^5 \right)$$

Uncertainty

$$\frac{U_{f Re_{SL}}}{f Re_{SL}} = 0.05\% \quad \text{or} \quad U_{f Re_{SL}} = 0.0005 \cdot f Re_{SL}$$

Hagenbach Factor as a Function of x

Function

$$K(x) = (f_{app} - f_{FD}) \frac{4 \cdot x}{D_h}$$

Uncertainty

$$\frac{U_{K(x)}}{K(x)} = \left[\left(\frac{U_{D_h}}{D_h} \right)^2 + \left(\frac{U_x}{x} \right)^2 + \left(\frac{U_{(f_{app}-f_{FD})}}{f_{app} - f_{FD}} \right)^2 \right]^{1/2}$$

$$U_{f_{app}-f_{FD}} = \left[(U_{f_{app}})^2 + (U_{f_{FD}})^2 \right]^{1/2}$$

$$\frac{U_{f_{app}-f_{FD}}}{f_{app} - f_{FD}} = \left[\left(\frac{U_{f_{app}}}{f_{app} - f_{FD}} \right)^2 + \left(\frac{U_{f_{FD}}}{f_{app} - f_{FD}} \right)^2 \right]^{1/2}$$

$$\begin{aligned}
\frac{U_{\mathbf{K}(x)}}{\mathbf{K}(x)} &= \left[\left(\frac{U_{D_h}}{D_h} \right)^2 + \left(\frac{U_x}{x} \right)^2 + \left(\frac{U_{f_{app}}}{f_{app} - f_{FD}} \right)^2 + \left(\frac{U_{f_{FD}}}{f_{app} - f_{FD}} \right)^2 \right]^{1/2} \\
\frac{U_{\mathbf{K}(x)}}{\mathbf{K}(x)} &= \left[\left(\frac{U_x}{x} \right)^2 + \left(\frac{U_a}{a} \right)^2 + \left(\frac{U_b}{b} \right)^2 + \left(\frac{U_a}{a+b} \right)^2 + \left(\frac{U_b}{a+b} \right)^2 \right. \\
&\quad \left. + \left(\frac{U_{f_{app}}}{f_{app} - f_{FD}} \right)^2 + \left(\frac{U_{f_{FD}}}{f_{app} - f_{FD}} \right)^2 \right]^{1/2} \\
\frac{U_{\mathbf{K}(x)}}{\mathbf{K}(x)} &= \left[\left(\frac{U_x}{x} \right)^2 + \left(\frac{U_a}{a} \right)^2 + \left(\frac{U_b}{b} \right)^2 + \left(\frac{U_a}{a+b} \right)^2 + \left(\frac{U_b}{a+b} \right)^2 + \left(\frac{U_{f_{FD}}}{f_{app} - f_{FD}} \right)^2 \right. \\
&\quad \left. + \left\{ \frac{f_{app} \left[\left(\frac{U_\rho}{\rho} \right)^2 + \left(\frac{U_{\Delta p}}{\Delta p} \right)^2 + \left(\frac{U_L}{L} \right)^2 + 2 \cdot \left(\frac{U_Q}{Q} \right)^2 + 3 \cdot \left(\frac{U_a}{a} \right)^2 \right]^{1/2} + 3 \cdot \left(\frac{U_b}{b} \right)^2 + \left(\frac{U_a}{a+b} \right)^2 + \left(\frac{U_b}{a+b} \right)^2}{f_{app} - f_{FD}} \right\}^2 \right]^{1/2} \\
\frac{U_{\mathbf{K}(x)}}{\mathbf{K}(x)} &= \left[\left(\frac{U_x}{x} \right)^2 + \left(\frac{U_a}{a} \right)^2 + \left(\frac{U_b}{b} \right)^2 + \left(\frac{U_a}{a+b} \right)^2 + \left(\frac{U_b}{a+b} \right)^2 + \left(\frac{U_{f_{FD}}}{f_{app} - f_{FD}} \right)^2 \right. \\
&\quad \left. + \left\{ \left(\frac{U_\rho}{\rho} \right)^2 + \left(\frac{U_{\Delta p}}{\Delta p} \right)^2 + \left(\frac{U_L}{L} \right)^2 + 2 \cdot \left(\frac{U_Q}{Q} \right)^2 + 3 \cdot \left(\frac{U_a}{a} \right)^2 \right\} \cdot \left(\frac{f_{app}}{f_{app} - f_{FD}} \right)^2 \right. \\
&\quad \left. + \left\{ 3 \cdot \left(\frac{U_b}{b} \right)^2 + \left(\frac{U_a}{a+b} \right)^2 + \left(\frac{U_b}{a+b} \right)^2 \right\} \right]^{1/2}
\end{aligned}$$

Fully Developed Hagenbach Factor

Function

$$\mathbf{K}(\infty) = \begin{pmatrix} 0.6796 + 1.2197 \cdot \alpha_c + 3.3089 \cdot \alpha_c^2 - 9.5921 \cdot \alpha_c^3 \\ + 8.9089 \cdot \alpha_c^4 - 2.9959 \cdot \alpha_c^5 \end{pmatrix}$$

Uncertainty

$$\frac{U_{\mathbf{K}(\infty)}}{\mathbf{K}(\infty)} = 0.04\%$$

fRe Ratio, C*

Δp_{total}

Function

$$\Delta p_{\text{microchannel}} = \Delta p_{\text{total}} - \frac{\rho \cdot \bar{V}^2}{2} [K_i + K_o + \mathbf{K}(x)]$$

$$\Delta p_{\text{microchannel}} = \Delta p_{\text{total}} - \frac{\rho \cdot Q^2}{2 \cdot A_c^2} [K_i + K_o + \mathbf{K}(x)]$$

Uncertainty

$$\frac{U_{K_i + K_o + \mathbf{K}(x)}}{K_i + K_o + \mathbf{K}(x)} = \left[\left(\frac{U_{K_i}}{K_i + K_o + \mathbf{K}(x)} \right)^2 + \left(\frac{U_{K_o}}{K_i + K_o + \mathbf{K}(x)} \right)^2 + \left(\frac{U_{\mathbf{K}(x)}}{K_i + K_o + \mathbf{K}(x)} \right)^2 \right]^{1/2}$$

$$\frac{U_{\frac{\rho \cdot \bar{V}^2}{2} [K_i + K_o + \mathbf{K}(x)]}}{\frac{\rho \cdot Q^2}{2 \cdot A_c^2} [K_i + K_o + \mathbf{K}(x)]} = \left[\left(\frac{U_{\rho}}{\rho} \right)^2 + 2 \cdot \left(\frac{U_Q}{Q} \right)^2 + 2 \cdot \left(\frac{U_{A_c}}{A_c} \right)^2 + \left(\frac{U_{K_i + K_o + \mathbf{K}(x)}}{K_i + K_o + \mathbf{K}(x)} \right)^2 \right]^{1/2}$$

$$\frac{U \frac{\rho \bar{V}^2}{2} [K_i + K_o + \mathbf{K}(x)]}{\frac{\rho \cdot Q^2}{2 \cdot A_c^2} [K_i + K_o + \mathbf{K}(x)]} = \left[\left(\frac{U_\rho}{\rho} \right)^2 + 2 \cdot \left(\frac{U_Q}{Q} \right)^2 + 2 \cdot \left(\left[\left(\frac{U_a}{a} \right)^2 + \left(\frac{U_b}{b} \right)^2 \right]^{1/2} \right)^2 \right. \\ \left. + \left[\left(\frac{U_{K_i}}{K_i + K_o + \mathbf{K}(x)} \right)^2 + \left(\frac{U_{K_o}}{K_i + K_o + \mathbf{K}(x)} \right)^2 \right]^{1/2} \right]^2 \\ \left. + \left[\left(\frac{U_{\mathbf{K}(x)}}{K_i + K_o + \mathbf{K}(x)} \right)^2 \right] \right]^{1/2}$$

$$\frac{U \frac{\rho \bar{V}^2}{2} [K_i + K_o + \mathbf{K}(x)]}{\frac{\rho \cdot Q^2}{2 \cdot A_c^2} [K_i + K_o + \mathbf{K}(x)]} = \left[\left(\frac{U_\rho}{\rho} \right)^2 + 2 \cdot \left(\frac{U_Q}{Q} \right)^2 + 2 \cdot \left(\frac{U_a}{a} \right)^2 + 2 \cdot \left(\frac{U_b}{b} \right)^2 \right]^{1/2} \\ + \left(\frac{U_{K_i}}{K_i + K_o + \mathbf{K}(x)} \right)^2 + \left(\frac{U_{K_o}}{K_i + K_o + \mathbf{K}(x)} \right)^2 \\ + \left(\frac{U_{\mathbf{K}(x)}}{K_i + K_o + \mathbf{K}(x)} \right)^2$$

$$U_{\Delta p_{microchannel}} = U_{\Delta p_{total}} + U \frac{\rho \cdot Q^2}{2 \cdot A_c^2} [K_i + K_o + \mathbf{K}(x)]$$

$$\frac{U_{\Delta p_{\text{microchannel}}}}{\Delta p_{\text{microchannel}}} = \left[\left(\frac{U_{\Delta p_{\text{total}}}}{\Delta p_{\text{total}} - \frac{\rho \cdot Q^2}{2 \cdot A_c^2} [K_i + K_o + K(x)]} \right)^2 + \left\{ \frac{\rho \cdot Q^2}{2 \cdot A_c^2} [K_i + K_o + K(x)] \right\} \cdot \left[\left(\frac{U_\rho}{\rho} \right)^2 + 2 \cdot \left(\frac{U_Q}{Q} \right)^2 + 2 \cdot \left(\frac{U_a}{a} \right)^2 + 2 \cdot \left(\frac{U_b}{b} \right)^2 \right]^{1/2} + \left(\frac{U_{K_i}}{K_i + K_o + K(x)} \right)^2 + \left(\frac{U_{K_o}}{K_i + K_o + K(x)} \right)^2 + \left(\frac{U_{K(x)}}{K_i + K_o + K(x)} \right)^2 \right]^2 \cdot \left[\frac{\rho \cdot Q^2}{2 \cdot A_c^2} [K_i + K_o + K(x)] \right]^{1/2}$$

$$\frac{U_{\Delta p_{\text{microchannel}}}}{\Delta p_{\text{microchannel}}} = \left[\left(\frac{U_{\Delta p_{\text{total}}}}{\Delta p_{\text{total}} - \frac{\rho \cdot Q^2}{2 \cdot A_c^2} [K_i + K_o + K(x)]} \right)^2 + \left(\left\{ \frac{\rho \cdot Q^2}{2 \cdot A_c^2} [K_i + K_o + K(x)] \right\} \cdot \left(\left(\frac{U_\rho}{\rho} \right)^2 + 2 \cdot \left(\frac{U_Q}{Q} \right)^2 + 2 \cdot \left(\frac{U_a}{a} \right)^2 + 2 \cdot \left(\frac{U_b}{b} \right)^2 + \left(\frac{U_{K_i}}{K_i + K_o + K(x)} \right)^2 + \left(\frac{U_{K_o}}{K_i + K_o + K(x)} \right)^2 + \left(\frac{U_{K(x)}}{K_i + K_o + K(x)} \right)^2 \right) \right]^2 \right]^{1/2}$$

$$\frac{U_{\Delta p_{\text{microchannel}}}}{\Delta p_{\text{microchannel}}} = \left[\left(\frac{U_{\Delta p_{\text{total}}}}{\Delta p_{\text{total}} - \frac{\rho \cdot Q^2}{2 \cdot A_c^2} [K_i + K_o + K(x)]} \right)^2 + \left(\frac{\frac{\rho \cdot Q^2}{2 \cdot A_c^2} [K_i + K_o + K(x)]}{\Delta p_{\text{total}} - \frac{\rho \cdot Q^2}{2 \cdot A_c^2} [K_i + K_o + K(x)]} \cdot \left(\left(\frac{U_\rho}{\rho} \right)^2 + 2 \cdot \left(\frac{U_Q}{Q} \right)^2 + 2 \cdot \left(\frac{U_a}{a} \right)^2 + 2 \cdot \left(\frac{U_b}{b} \right)^2 + \left(\frac{U_{K_i}}{K_i + K_o + K(x)} \right)^2 + \left(\frac{U_{K_o}}{K_i + K_o + K(x)} \right)^2 + \left(\frac{U_{K(x)}}{K_i + K_o + K(x)} \right)^2 \right) \right]^{1/2}$$

fRe with $\Delta p_{\text{microchannel}}$ not Δp_{total}

$$\frac{U_{fRe}}{fRe} = \left[\begin{aligned} & 2 \cdot \left(\frac{U_\rho}{\rho} \right)^2 + \left(\frac{U_\mu}{\mu} \right)^2 + \left(\frac{U_L}{L} \right)^2 + 3 \cdot \left(\frac{U_Q}{Q} \right)^2 + 5 \cdot \left(\frac{U_a}{a} \right)^2 + 5 \cdot \left(\frac{U_b}{b} \right)^2 \\ & + 2 \cdot \left(\frac{U_a}{a+b} \right)^2 + 2 \cdot \left(\frac{U_b}{a+b} \right)^2 + \left(\frac{U_\rho}{\rho} \right)^2 + 2 \cdot \left(\frac{U_Q}{Q} \right)^2 + 2 \cdot \left(\frac{U_a}{a} \right)^2 \\ & + 2 \cdot \left(\frac{U_b}{b} \right)^2 + \left(\frac{U_{K_i}}{K_i + K_o + K(x)} \right)^2 + \left(\frac{U_{K_o}}{K_i + K_o + K(x)} \right)^2 \\ & + \left(\frac{U_{K(x)}}{K_i + K_o + K(x)} \right)^2 + \left(\frac{U_{\Delta p_{total}}}{\Delta p_{total} - \frac{\rho \cdot Q^2}{2 \cdot A_c^2} [K_i + K_o + K(x)]} \right)^2 \end{aligned} \right]^{1/2}$$

$$\frac{U_{fRe}}{fRe} = \left[\begin{aligned} & 3 \cdot \left(\frac{U_\rho}{\rho} \right)^2 + \left(\frac{U_\mu}{\mu} \right)^2 + \left(\frac{U_L}{L} \right)^2 + 5 \cdot \left(\frac{U_Q}{Q} \right)^2 + 7 \cdot \left(\frac{U_a}{a} \right)^2 + 7 \cdot \left(\frac{U_b}{b} \right)^2 \\ & + 2 \cdot \left(\frac{U_a}{a+b} \right)^2 + 2 \cdot \left(\frac{U_b}{a+b} \right)^2 + \left(\frac{U_{K_i}}{K_i + K_o + K(x)} \right)^2 \\ & + \left(\frac{U_{K_o}}{K_i + K_o + K(x)} \right)^2 + \left(\frac{U_{K(x)}}{K_i + K_o + K(x)} \right)^2 \\ & + \left(\frac{U_{\Delta p_{total}}}{\Delta p_{total} - \frac{\rho \cdot Q^2}{2 \cdot A_c^2} [K_i + K_o + K(x)]} \right)^2 \end{aligned} \right]^{1/2}$$

f_{Re} with $\Delta p_{\text{microchannel}}$ not Δp_{total} including $K(x)$

$$\frac{U_{f_{Re}}}{f_{Re}} = \left[\begin{aligned} & 3 \cdot \left(\frac{U_{\rho}}{\rho} \right)^2 + \left(\frac{U_{\mu}}{\mu} \right)^2 + \left(\frac{U_L}{L} \right)^2 + 5 \cdot \left(\frac{U_Q}{Q} \right)^2 + 7 \cdot \left(\frac{U_a}{a} \right)^2 + 7 \cdot \left(\frac{U_b}{b} \right)^2 \\ & + 2 \cdot \left(\frac{U_a}{a+b} \right)^2 + 2 \cdot \left(\frac{U_b}{a+b} \right)^2 + \left(\frac{U_{K_i}}{K_i + K_o + K(x)} \right)^2 \\ & + \left(\frac{U_{K_o}}{K_i + K_o + K(x)} \right)^2 + \left(\frac{U_{K(x)}}{K_i + K_o + K(x)} \right)^2 \\ & + \left(\frac{U_{\Delta p_{total}}}{\Delta p_{total} - \frac{\rho \cdot Q^2}{2 \cdot A_c^2} [K_i + K_o + K(x)]} \right)^2 \end{aligned} \right]^{1/2}$$

$$\frac{U_{K(x)}}{K(x)} = \left[\begin{aligned} & \left(\frac{U_x}{x} \right)^2 + \left(\frac{U_a}{a} \right)^2 + \left(\frac{U_b}{b} \right)^2 + \left(\frac{U_a}{a+b} \right)^2 + \left(\frac{U_b}{a+b} \right)^2 + \left(\frac{U_{f_{FD}}}{f_{app} - f_{FD}} \right)^2 \\ & + \left\{ \left(\frac{U_{\rho}}{\rho} \right)^2 + \left(\frac{U_{\Delta p}}{\Delta p} \right)^2 + \left(\frac{U_L}{L} \right)^2 + 2 \cdot \left(\frac{U_Q}{Q} \right)^2 + 3 \cdot \left(\frac{U_a}{a} \right)^2 \right\} \cdot \left(\frac{f_{app}}{f_{app} - f_{FD}} \right)^2 \\ & + \left\{ 3 \cdot \left(\frac{U_b}{b} \right)^2 + \left(\frac{U_a}{a+b} \right)^2 + \left(\frac{U_b}{a+b} \right)^2 \right\} \end{aligned} \right]^{1/2}$$

$$\begin{aligned}
& \left[3 \cdot \left(\frac{U_\rho}{\rho} \right)^2 + \left(\frac{U_\mu}{\mu} \right)^2 + \left(\frac{U_L}{L} \right)^2 + 5 \cdot \left(\frac{U_Q}{Q} \right)^2 + 7 \cdot \left(\frac{U_a}{a} \right)^2 + 7 \cdot \left(\frac{U_b}{b} \right)^2 \right. \\
& + 2 \cdot \left(\frac{U_a}{a+b} \right)^2 + 2 \cdot \left(\frac{U_b}{a+b} \right)^2 + \left(\frac{U_{K_i}}{K_i + K_o + \mathbf{K}(x)} \right)^2 \\
& + \left(\frac{U_{K_o}}{K_i + K_o + \mathbf{K}(x)} \right)^2 + \left. \left(\frac{U_{\Delta p_{total}}}{\Delta p_{total} - \frac{\rho \cdot Q^2}{2 \cdot A_c^2} [K_i + K_o + \mathbf{K}(x)]} \right)^2 \right]^{1/2} \\
\frac{U_{fRe}}{fRe} = & \left(\left[\left(\frac{U_x}{x} \right)^2 + \left(\frac{U_a}{a} \right)^2 + \left(\frac{U_b}{b} \right)^2 + \left(\frac{U_a}{a+b} \right)^2 + \left(\frac{U_b}{a+b} \right)^2 + \left(\frac{U_{f_{FD}}}{f_{app} - f_{FD}} \right)^2 \right. \right. \\
& + \left. \left. \mathbf{K}(x) \cdot \left[\left(\frac{U_\rho}{\rho} \right)^2 + \left(\frac{U_{\Delta p}}{\Delta p} \right)^2 + \left(\frac{U_L}{L} \right)^2 + 2 \cdot \left(\frac{U_Q}{Q} \right)^2 + 3 \cdot \left(\frac{U_a}{a} \right)^2 \right] \right. \right. \\
& \left. \left. + \left[3 \cdot \left(\frac{U_b}{b} \right)^2 + \left(\frac{U_a}{a+b} \right)^2 + \left(\frac{U_b}{a+b} \right)^2 \right] \cdot \left(\frac{f_{app}}{f_{app} - f_{FD}} \right)^2 \right] \right. \\
& \left. \left. \frac{\phantom{\left[\left(\frac{U_x}{x} \right)^2 + \left(\frac{U_a}{a} \right)^2 + \left(\frac{U_b}{b} \right)^2 + \left(\frac{U_a}{a+b} \right)^2 + \left(\frac{U_b}{a+b} \right)^2 + \left(\frac{U_{f_{FD}}}{f_{app} - f_{FD}} \right)^2 \right. + \mathbf{K}(x) \cdot \left[\left(\frac{U_\rho}{\rho} \right)^2 + \left(\frac{U_{\Delta p}}{\Delta p} \right)^2 + \left(\frac{U_L}{L} \right)^2 + 2 \cdot \left(\frac{U_Q}{Q} \right)^2 + 3 \cdot \left(\frac{U_a}{a} \right)^2 \right] + \left[3 \cdot \left(\frac{U_b}{b} \right)^2 + \left(\frac{U_a}{a+b} \right)^2 + \left(\frac{U_b}{a+b} \right)^2 \right] \cdot \left(\frac{f_{app}}{f_{app} - f_{FD}} \right)^2}}{K_i + K_o + \mathbf{K}(x)} \right. \right. \\
& \left. \left. \right)^2 \right)^{1/2}
\end{aligned}$$

$$\frac{U_{fRe}}{fRe} = \left[\begin{aligned} & 3 \cdot \left(\frac{U_\rho}{\rho} \right)^2 + \left(\frac{U_\mu}{\mu} \right)^2 + \left(\frac{U_L}{L} \right)^2 + 5 \cdot \left(\frac{U_Q}{Q} \right)^2 + 7 \cdot \left(\frac{U_a}{a} \right)^2 + 7 \cdot \left(\frac{U_b}{b} \right)^2 + 2 \cdot \left(\frac{U_a}{a+b} \right)^2 \\ & + 2 \cdot \left(\frac{U_b}{a+b} \right)^2 + \left(\frac{U_{K_i}}{K_i + K_o + K(x)} \right)^2 + \left(\frac{U_{K_o}}{K_i + K_o + K(x)} \right)^2 + \left(\frac{U_{\Delta p_{total}}}{\Delta p_{total} - \frac{\rho \cdot Q^2}{2 \cdot A_c^2} [K_i + K_o + K(x)]} \right)^2 \\ & + \frac{K(x)^2}{(K_i + K_o + K(x))^2} \left\{ \left(\frac{U_x}{x} \right)^2 + \left(\frac{U_a}{a} \right)^2 + \left(\frac{U_b}{b} \right)^2 + \left(\frac{U_a}{a+b} \right)^2 + \left(\frac{U_b}{a+b} \right)^2 + \left(\frac{U_{f_{FD}}}{f_{app} - f_{FD}} \right)^2 \right. \\ & \left. + \left\{ \left(\frac{U_\rho}{\rho} \right)^2 + \left(\frac{U_{\Delta p}}{\Delta p} \right)^2 + \left(\frac{U_L}{L} \right)^2 + 2 \cdot \left(\frac{U_Q}{Q} \right)^2 + 3 \cdot \left(\frac{U_a}{a} \right)^2 \right\} \cdot \left(\frac{f_{app}}{f_{app} - f_{FD}} \right)^2 \right. \\ & \left. + \left\{ 3 \cdot \left(\frac{U_b}{b} \right)^2 + \left(\frac{U_a}{a+b} \right)^2 + \left(\frac{U_b}{a+b} \right)^2 \right\} \cdot \left(\frac{f_{app}}{f_{app} - f_{FD}} \right)^2 \right\} \end{aligned} \right]^{1/2}$$

$$\left[\begin{aligned}
& 3 \cdot \left(\frac{U_\rho}{\rho} \right)^2 + \left(\frac{U_\mu}{\mu} \right)^2 + \left(\frac{U_L}{L} \right)^2 + 5 \cdot \left(\frac{U_Q}{Q} \right)^2 + 7 \cdot \left(\frac{U_a}{a} \right)^2 + 7 \cdot \left(\frac{U_b}{b} \right)^2 + 2 \cdot \left(\frac{U_a}{a+b} \right)^2 \\
& + 2 \cdot \left(\frac{U_b}{a+b} \right)^2 + \left(\frac{U_{K_i}}{K_i + K_o + K(x)} \right)^2 + \left(\frac{U_{K_o}}{K_i + K_o + K(x)} \right)^2 \\
& + \left(\frac{U_{\Delta p_{total}}}{\Delta p_{total} - \frac{\rho \cdot Q^2}{2 \cdot A_c^2} [K_i + K_o + K(x)]} \right)^2 + \left(\frac{\frac{\rho \cdot Q^2}{2 \cdot A_c^2} [K_i + K_o + K(x)]}{\Delta p_{total} - \frac{\rho \cdot Q^2}{2 \cdot A_c^2} [K_i + K_o + K(x)]} \right)^2 \\
& + \left(\left(\frac{U_\rho}{\rho} \right)^2 + 2 \cdot \left(\frac{U_Q}{Q} \right)^2 + 2 \cdot \left(\frac{U_a}{a} \right)^2 + 2 \cdot \left(\frac{U_b}{b} \right)^2 \right. \\
& \quad \left. + \left(\frac{U_{K_i}}{K_i + K_o + K(x)} \right)^2 + \left(\frac{U_{K_o}}{K_i + K_o + K(x)} \right)^2 \right. \\
& \quad \left. + \left(\frac{U_{K(x)}}{K_i + K_o + K(x)} \right)^2 \right)^2 \\
& + \frac{K(x)^2}{(K_i + K_o + K(x))^2} \left\{ \left(\frac{U_x}{x} \right)^2 + \left(\frac{U_a}{a} \right)^2 + \left(\frac{U_b}{b} \right)^2 + \left(\frac{U_a}{a+b} \right)^2 + \left(\frac{U_b}{a+b} \right)^2 + \left(\frac{U_{f_{FD}}}{f_{app} - f_{FD}} \right)^2 \right. \\
& \quad \left. + \left[\left(\frac{U_\rho}{\rho} \right)^2 + \left(\frac{U_{\Delta p}}{\Delta p} \right)^2 + \left(\frac{U_L}{L} \right)^2 + 2 \cdot \left(\frac{U_Q}{Q} \right)^2 + 3 \cdot \left(\frac{U_a}{a} \right)^2 \right] \cdot \left(\frac{f_{app}}{f_{app} - f_{FD}} \right)^2 \right. \\
& \quad \left. + 3 \cdot \left(\frac{U_b}{b} \right)^2 + \left(\frac{U_a}{a+b} \right)^2 + \left(\frac{U_b}{a+b} \right)^2 \right\}
\end{aligned} \right]^{1/2}$$

Heat Transfer Power

Function

$$q = V \cdot I$$

Uncertainty

$$\frac{U_q}{q} = \left[\left(\frac{U_V}{V} \right)^2 + \left(\frac{U_I}{I} \right)^2 \right]^{1/2}$$

Heat Transfer, Average h in General Form

Function

$$q = \bar{h} \cdot A_{HT} \cdot \Delta T$$

Uncertainty

$$\frac{U_q}{q} = \left[\left(\frac{U_{\bar{h}}}{\bar{h}} \right)^2 + \left(\frac{U_{A_{HT}}}{A_{HT}} \right)^2 + \left(\frac{U_{\Delta T}}{\Delta T} \right)^2 \right]^{1/2}$$

Heat Transfer Coefficient, Average

Function

$$\bar{h} = \frac{q}{A_{HT} \cdot \Delta T}$$

Uncertainty

$$\frac{U_{\bar{h}}}{\bar{h}} = \left[\left(\frac{U_q}{q} \right)^2 + \left(\frac{U_{A_{HT}}}{A_{HT}} \right)^2 + \left(\frac{U_{\Delta T}}{\Delta T} \right)^2 \right]^{1/2}$$

General form with no specific ΔT or A_{HT} defined

$$\frac{U_{\bar{h}}}{\bar{h}} = \left[\left(\frac{U_V}{V} \right)^2 + \left(\frac{U_I}{I} \right)^2 + \left(\frac{U_{\Delta T}}{\Delta T} \right)^2 + \left(\frac{U_{A_{HT}}}{A_{HT}} \right)^2 \right]^{1/2}$$

Nusselt, Laminar Average h

Function

$$\bar{Nu} = \frac{\bar{h} \cdot D_h}{k_f}$$

Uncertainty

$$\frac{U_{\bar{Nu}}}{\bar{Nu}} = \left[\left(\frac{U_{D_h}}{D_h} \right)^2 + \left(\frac{U_{k_f}}{k_f} \right)^2 + \left(\frac{U_{\bar{h}}}{\bar{h}} \right)^2 \right]^{1/2}$$

$$\frac{U_{\bar{Nu}}}{\bar{Nu}} = \left[\left(\frac{U_{k_f}}{k_f} \right)^2 + \left(\frac{U_a}{a} \right)^2 + \left(\frac{U_b}{b} \right)^2 + \left(\frac{U_a}{a+b} \right)^2 + \left(\frac{U_b}{a+b} \right)^2 + \left(\frac{U_{\bar{h}}}{\bar{h}} \right)^2 \right]^{1/2}$$

Nusselt Number Ratio, A^*

Function

$$A^* = \frac{(Nu)_{\text{exp}}}{(Nu)_{\text{theory}}}$$

Uncertainty

$$\frac{U_{A^*}}{A^*} = \left[\left(\frac{U_{Nu_{\text{exp}}}}{Nu_{\text{exp}}} \right)^2 + \left(\frac{U_{Nu_{\text{theory}}}}{Nu_{\text{theory}}} \right)^2 \right]^{1/2}$$

Colburn j Factor

Function

$$j = \frac{Nu \cdot \text{Pr}^{1/3}}{\text{Re}}$$

Uncertainty

$$\frac{U_j}{j} = \left[\left(\frac{U_{Nu}}{Nu} \right)^2 + \frac{1}{3} \cdot \left(\frac{U_{\text{Pr}}}{\text{Pr}} \right)^2 + \left(\frac{U_{\text{Re}}}{\text{Re}} \right)^2 \right]^{1/2}$$

$$\frac{U_j}{j} = \left[\left(\frac{U_{Nu}}{Nu} \right)^2 + \frac{1}{3} \cdot \left(\frac{U_{Pr}}{Pr} \right)^2 + \left(\frac{U_\rho}{\rho} \right)^2 + \left(\frac{U_\mu}{\mu} \right)^2 + \left(\frac{U_Q}{Q} \right)^2 + 2 \cdot \left(\frac{U_a}{a} \right)^2 \right. \\ \left. + 2 \cdot \left(\frac{U_b}{b} \right)^2 + \left(\frac{U_a}{a+b} \right)^2 + \left(\frac{U_b}{a+b} \right)^2 \right]^{1/2}$$

$$\frac{U_j}{j} = \left[\left(\frac{U_\rho}{\rho} \right)^2 + \left(\frac{U_\mu}{\mu} \right)^2 + \left(\frac{U_Q}{Q} \right)^2 + 2 \cdot \left(\frac{U_a}{a} \right)^2 + 2 \cdot \left(\frac{U_b}{b} \right)^2 + \left(\frac{U_a}{a+b} \right)^2 \right. \\ \left. + \left(\frac{U_b}{a+b} \right)^2 + \frac{1}{3} \cdot \left(\frac{U_{Pr}}{Pr} \right)^2 + \left(\frac{U_{Nu}}{Nu} \right)^2 \right]^{1/2}$$

Log Mean Temperature Difference

Function

$$\Delta T_{LMTD} = \frac{(T_s - T_i) - (T_s - T_o)}{\ln \left(\frac{T_s - T_i}{T_s - T_o} \right)}$$

$$\Delta T_{LMTD} = \frac{\Delta T_2 - \Delta T_1}{\ln \left(\frac{\Delta T_2}{\Delta T_1} \right)}$$

Uncertainty

$$\text{Let } B = \ln \left(\frac{\Delta T_2}{\Delta T_1} \right)$$

$$\frac{U_{\Delta T_{LMTD}}}{\Delta T_{LMTD}} = \left[\left(\frac{U_{\Delta T_2 - \Delta T_1}}{\Delta T_2 - \Delta T_1} \right)^2 + \left(\frac{U_B}{B} \right)^2 \right]^{1/2}$$

$$\frac{U_B}{B} = \left[\left(\frac{U_{\frac{\Delta T_2}{\Delta T_1}}}{\frac{\Delta T_2}{\Delta T_1} \cdot \ln\left(\frac{\Delta T_2}{\Delta T_1}\right)} \right)^2 \right]^{1/2}$$

$$U_{\Delta T_2 - \Delta T_1} = \left[(U_{\Delta T_2})^2 + (U_{\Delta T_1})^2 \right]^{1/2}$$

$$\frac{U_{\Delta T_2 - \Delta T_1}}{\Delta T_2 - \Delta T_1} = \frac{1}{\Delta T_2 - \Delta T_1} \left[(U_{\Delta T_2})^2 + (U_{\Delta T_1})^2 \right]^{1/2}$$

$$\frac{U_{\Delta T_2 - \Delta T_1}}{\Delta T_2 - \Delta T_1} = \left[\frac{(U_{\Delta T_2})^2}{(\Delta T_2 - \Delta T_1)^2} + \frac{(U_{\Delta T_1})^2}{(\Delta T_2 - \Delta T_1)^2} \right]^{1/2}$$

$$\frac{U_{\Delta T_2 - \Delta T_1}}{\Delta T_2 - \Delta T_1} = \left[\left(\frac{U_{\Delta T_2}}{\Delta T_2 - \Delta T_1} \right)^2 + \left(\frac{U_{\Delta T_1}}{\Delta T_2 - \Delta T_1} \right)^2 \right]^{1/2}$$

$$\frac{U_{\Delta T_{LMTD}}}{\Delta T_{LMTD}} = \left[\left(\left[\left(\frac{U_{\Delta T_2}}{\Delta T_2 - \Delta T_1} \right)^2 + \left(\frac{U_{\Delta T_1}}{\Delta T_2 - \Delta T_1} \right)^2 \right]^{1/2} \right)^2 + \left(\left[\left(\frac{U_{\frac{\Delta T_2}{\Delta T_1}}}{\frac{\Delta T_2}{\Delta T_1} \cdot \ln\left(\frac{\Delta T_2}{\Delta T_1}\right)} \right)^2 \right]^{1/2} \right)^2 \right]^{1/2}$$

$$\frac{U_{\Delta T_{LMTD}}}{\Delta T_{LMTD}} = \left[\left(\frac{U_{\Delta T_2}}{\Delta T_2 - \Delta T_1} \right)^2 + \left(\frac{U_{\Delta T_1}}{\Delta T_2 - \Delta T_1} \right)^2 + \left(\frac{U_{\frac{\Delta T_2}{\Delta T_1}}}{\frac{\Delta T_2}{\Delta T_1} \cdot \ln \left(\frac{\Delta T_2}{\Delta T_1} \right)} \right)^2 \right]^{1/2} \quad \text{*** general form}$$

In terms of constant surface temperature, T

$$\frac{U_{\Delta T_{LMTD}}}{\Delta T_{LMTD}} = \left[\left(\frac{U_{T_s - T_i}}{(T_s - T_i) - (T_s - T_o)} \right)^2 + \left(\frac{U_{T_s - T_{oi}}}{(T_s - T_i) - (T_s - T_o)} \right)^2 + \left(\frac{U_{\frac{T_s - T_i}{T_i - T_o}}}{\frac{(T_s - T_i)}{(T_s - T_o)} \cdot \ln \left(\frac{(T_s - T_i)}{(T_s - T_o)} \right)} \right)^2 \right]^{1/2}$$

In terms of constant heat flux, H1

$$\frac{U_{\Delta T_{LMTD}}}{\Delta T_{LMTD}} = \left[\left(\frac{U_{T_{so} - T_i}}{(T_{s,i} - T_i) - (T_{s,o} - T_o)} \right)^2 + \left(\frac{U_{T_{si} - T_o}}{(T_{s,i} - T_i) - (T_{s,o} - T_o)} \right)^2 + \left(\frac{U_{\frac{T_{si} - T_i}{T_{so} - T_o}}}{\frac{(T_{s,i} - T_i)}{(T_{s,o} - T_o)} \cdot \ln \left(\frac{(T_{s,i} - T_i)}{(T_{s,o} - T_o)} \right)} \right)^2 \right]^{1/2}$$

Heat Transfer Area; single channel

Function

$$A_{HT} = a \cdot L + 2 \cdot b \cdot L$$

Uncertainty

$$\frac{U_{aL}}{a \cdot L} = \left[\left(\frac{U_a}{a} \right)^2 + \left(\frac{U_L}{L} \right)^2 \right]^{1/2}$$

$$\frac{U_{bL}}{b \cdot L} = \left[\left(\frac{U_b}{b} \right)^2 + \left(\frac{U_L}{L} \right)^2 \right]^{1/2}$$

$$U_{A_{HT}} = \left[(U_{aL})^2 + 2 \cdot (U_{bL})^2 \right]^{1/2}$$

$$U_{A_{HT}} = \left[\left(a \cdot L \cdot \left[\left(\frac{U_a}{a} \right)^2 + \left(\frac{U_L}{L} \right)^2 \right]^{1/2} \right)^2 + 2 \cdot \left(b \cdot L \cdot \left[\left(\frac{U_b}{b} \right)^2 + \left(\frac{U_L}{L} \right)^2 \right]^{1/2} \right)^2 \right]^{1/2}$$

$$U_{A_{HT}} = \left[a^2 \cdot L^2 \left(\frac{U_a}{a} \right)^2 + a^2 \cdot L^2 \left(\frac{U_L}{L} \right)^2 + 2 \cdot b^2 \cdot L^2 \left(\frac{U_b}{b} \right)^2 + 2 \cdot b^2 \cdot L^2 \left(\frac{U_L}{L} \right)^2 \right]^{1/2}$$

$$\frac{U_{A_{HT}}}{A_{HT}} = \frac{1}{a \cdot L + 2 \cdot b \cdot L} \left[a^2 \cdot L^2 \left(\frac{U_a}{a} \right)^2 + a^2 \cdot L^2 \left(\frac{U_L}{L} \right)^2 + 2 \cdot b^2 \cdot L^2 \left(\frac{U_b}{b} \right)^2 + 2 \cdot b^2 \cdot L^2 \left(\frac{U_L}{L} \right)^2 \right]^{1/2}$$

$$\frac{U_{A_{HT}}}{A_{HT}} = \left[\frac{a^2 \cdot L^2}{(a \cdot L + 2 \cdot b \cdot L)^2} \left(\frac{U_a}{a} \right)^2 + \frac{a^2 \cdot L^2}{(a \cdot L + 2 \cdot b \cdot L)^2} \left(\frac{U_L}{L} \right)^2 \right. \\ \left. + \frac{2 \cdot b^2 \cdot L^2}{(a \cdot L + 2 \cdot b \cdot L)^2} \left(\frac{U_b}{b} \right)^2 + \frac{2 \cdot b^2 \cdot L^2}{(a \cdot L + 2 \cdot b \cdot L)^2} \left(\frac{U_L}{L} \right)^2 \right]^{1/2}$$

$$\frac{U_{A_{HT}}}{A_{HT}} = \left[\frac{a^2 \cdot L^2}{(L \cdot (a + 2 \cdot b))^2} \left(\frac{U_a}{a} \right)^2 + \frac{a^2 \cdot L^2}{(L \cdot (a + 2 \cdot b))^2} \left(\frac{U_L}{L} \right)^2 \right. \\ \left. + \frac{2 \cdot b^2 \cdot L^2}{(L \cdot (a + 2 \cdot b))^2} \left(\frac{U_b}{b} \right)^2 + \frac{2 \cdot b^2 \cdot L^2}{(L \cdot (a + 2 \cdot b))^2} \left(\frac{U_L}{L} \right)^2 \right]^{1/2}$$

$$\frac{U_{A_{HT}}}{A_{HT}} = \left[\frac{a^2}{(a + 2 \cdot b)^2} \left(\frac{U_a}{a} \right)^2 + \frac{a^2}{(a + 2 \cdot b)^2} \left(\frac{U_L}{L} \right)^2 \right. \\ \left. + \frac{2 \cdot b^2}{(a + 2 \cdot b)^2} \left(\frac{U_b}{b} \right)^2 + \frac{2 \cdot b^2}{(a + 2 \cdot b)^2} \left(\frac{U_L}{L} \right)^2 \right]^{1/2}$$

Heat Transfer Area; multiple channels

Function

$$A_{HT} = (a \cdot L + 2 \cdot b \cdot L) \cdot n$$

Uncertainty

$$U_{A_{HT,m}} = n \cdot U_{A_{HT}}$$

Heat Transfer Area, multiple channels with Fin Efficiency

Function

$$A_{HT,\eta} = (a + 2 \cdot \eta \cdot b) \cdot n \cdot L$$

Uncertainty

$$\frac{U_{AHT,\eta}}{A_{HT,\eta}} = \left[\left(\frac{U_L}{L} \right)^2 + \left(\frac{U_{(a+2\eta \cdot b)}}{a+2\eta \cdot b} \right)^2 \right]^{1/2}$$

$$\frac{U_{\eta \cdot b}}{\eta \cdot b} = \left[\left(\frac{U_\eta}{\eta} \right)^2 + \left(\frac{U_b}{b} \right)^2 \right]^{1/2}$$

$$U_{a+2\eta \cdot b} = \left[(U_a)^2 + 2 \cdot (U_{\eta \cdot b})^2 \right]^{1/2}$$

$$U_{a+2\eta \cdot b} = \left[(U_a)^2 + 2 \cdot \left(\eta \cdot b \left[\left(\frac{U_\eta}{\eta} \right)^2 + \left(\frac{U_b}{b} \right)^2 \right]^{1/2} \right)^2 \right]^{1/2}$$

$$U_{a+2\eta \cdot b} = \left[(U_a)^2 + 2 \left(\eta^2 \cdot b^2 \left\{ \left(\frac{U_\eta}{\eta} \right)^2 + \left(\frac{U_b}{b} \right)^2 \right\} \right) \right]^{1/2}$$

$$U_{a+2\eta \cdot b} = \left[(U_a)^2 + 2 \cdot \eta^2 \cdot b^2 \left(\frac{U_\eta}{\eta} \right)^2 + 2 \cdot \eta^2 \cdot b^2 \left(\frac{U_b}{b} \right)^2 \right]^{1/2}$$

$$\frac{U_{a+2\eta \cdot b}}{a+2\eta \cdot b} = \frac{1}{a+2\eta \cdot b} \left[(U_a)^2 + 2 \cdot \eta^2 \cdot b^2 \left(\frac{U_\eta}{\eta} \right)^2 + 2 \cdot \eta^2 \cdot b^2 \left(\frac{U_b}{b} \right)^2 \right]^{1/2}$$

$$\frac{U_{a+2\eta \cdot b}}{a+2\eta \cdot b} = \left[\frac{(U_a)^2}{(a+2\eta \cdot b)^2} + \frac{2 \cdot \eta^2 \cdot b^2}{(a+2\eta \cdot b)^2} \left(\frac{U_\eta}{\eta} \right)^2 + \frac{2 \cdot \eta^2 \cdot b^2}{(a+2\eta \cdot b)^2} \left(\frac{U_b}{b} \right)^2 \right]^{1/2}$$

$$\frac{U_{a+2\eta \cdot b}}{a+2\eta \cdot b} = \left[\left(\frac{U_a}{a+2\eta \cdot b} \right)^2 + 2 \cdot \left(\frac{\eta \cdot b \cdot U_\eta}{\eta \cdot (a+2\eta \cdot b)} \right)^2 + 2 \cdot \left(\frac{\eta \cdot b \cdot U_b}{b \cdot (a+2\eta \cdot b)} \right)^2 \right]^{1/2}$$

$$\frac{U_{a+2\eta \cdot b}}{a+2\eta \cdot b} = \left[\left(\frac{U_a}{a+2\eta \cdot b} \right)^2 + 2 \cdot \left(\frac{b \cdot U_\eta}{(a+2\eta \cdot b)} \right)^2 + 2 \cdot \left(\frac{\eta \cdot U_b}{(a+2\eta \cdot b)} \right)^2 \right]^{1/2}$$

$$\frac{U_{A_{HT},\eta}}{A_{HT,\eta}} = \left[\left(\frac{U_L}{L} \right)^2 + \left\{ \left[\left(\frac{U_a}{a+2\cdot\eta\cdot b} \right)^2 + 2 \cdot \left(\frac{b\cdot U_\eta}{a+2\cdot\eta\cdot b} \right)^2 \right]^{1/2} \right\}^2 \right]^{1/2}$$

$$\frac{U_{A_{HT},\eta}}{A_{HT,\eta}} = \left[\left(\frac{U_L}{L} \right)^2 + \left(\frac{U_a}{a+2\cdot\eta\cdot b} \right)^2 + 2 \cdot \left(\frac{b\cdot U_\eta}{a+2\cdot\eta\cdot b} \right)^2 \right]^{1/2}$$

$$\frac{U_{A_{HT},\eta}}{A_{HT,\eta}} = \left[\left(\frac{U_L}{L} \right)^2 + \left(\frac{U_a}{a+2\cdot\eta\cdot b} \right)^2 + 2 \cdot \left(\frac{\eta\cdot U_b}{a+2\cdot\eta\cdot b} \right)^2 \right]^{1/2}$$

Heat Transfer Coefficient; general

Function

$$\bar{h} = \frac{q}{A_{HT} \cdot \Delta T_{LMTD}}$$

Uncertainty

$$\frac{U_{\bar{h}}}{\bar{h}} = \left[\left(\frac{U_q}{q} \right)^2 + \left(\frac{U_{A_{HT}}}{A_{HT}} \right)^2 + \left(\frac{U_{\Delta T_{LMTD}}}{\Delta T_{LMTD}} \right)^2 \right]^{1/2}$$

$$\frac{U_{\bar{h}}}{\bar{h}} = \left[\left\{ \left[\left(\frac{U_V}{V} \right)^2 + \left(\frac{U_I}{I} \right)^2 \right]^{1/2} \right\}^2 + \left(\frac{U_{A_{HT}}}{A_{HT}} \right)^2 \right]^{1/2}$$

$$\frac{U_{\bar{h}}}{\bar{h}} = \left[\left\{ \left(\frac{U_{\Delta T_2}}{\Delta T_2 - \Delta T_1} \right)^2 + \left(\frac{U_{\Delta T_1}}{\Delta T_2 - \Delta T_1} \right)^2 + \left(\frac{U_{\frac{\Delta T_2}{\Delta T_1}}}{\frac{\Delta T_2}{\Delta T_1} \cdot \ln \left(\frac{\Delta T_2}{\Delta T_1} \right)} \right)^2 \right\}^{1/2} \right]^2 \right]^{1/2}$$

$$\frac{U_{\bar{h}}}{\bar{h}} = \left[\left(\frac{U_V}{V} \right)^2 + \left(\frac{U_I}{I} \right)^2 + \left(\frac{U_{A_{HT}}}{A_{HT}} \right)^2 + \left(\frac{U_{\Delta T_2}}{\Delta T_2 - \Delta T_1} \right)^2 + \left(\frac{U_{\Delta T_1}}{\Delta T_2 - \Delta T_1} \right)^2 \right]^{1/2} + \left(\frac{U_{\frac{\Delta T_2}{\Delta T_1}}}{\frac{\Delta T_2}{\Delta T_1} \cdot \ln \left(\frac{\Delta T_2}{\Delta T_1} \right)} \right)^2$$

Heat Transfer Coefficient; H1, multiple channels, with fin efficiency, LMTD

Function

$$\bar{h} = \frac{q}{A_{HT} \cdot \Delta T_{LMTD}}$$

Uncertainty

$$\frac{U_{\bar{h}}}{\bar{h}} = \left[\left(\frac{U_q}{q} \right)^2 + \left(\frac{U_{A_{HT}}}{A_{HT}} \right)^2 + \left(\frac{U_{\Delta T_{LMTD}}}{\Delta T_{LMTD}} \right)^2 \right]^{1/2}$$

$$\frac{U_{\bar{h}}}{\bar{h}} = \left[\left(\frac{U_V}{V} \right)^2 + \left(\frac{U_I}{I} \right)^2 + \left[\left(\frac{U_L}{L} \right)^2 + \left(\frac{U_a}{a + 2 \cdot \eta \cdot b} \right)^2 + 2 \cdot \left(\frac{b \cdot U_\eta}{a + 2 \cdot \eta \cdot b} \right)^2 \right]^{1/2} + 2 \cdot \left(\frac{\eta \cdot U_b}{a + 2 \cdot \eta \cdot b} \right)^2 \right]^2 + \left[\left(\frac{U_{T_{so}-T_i}}{(T_{s,i} - T_i) - (T_{s,o} - T_o)} \right)^2 + \left(\frac{U_{T_{si}-T_o}}{(T_{s,i} - T_i) - (T_{s,o} - T_o)} \right)^2 \right]^{1/2} + \left[\frac{U_{\frac{T_{si}-T_i}{T_{so}-T_o}}}{\left(\frac{T_{s,i} - T_i}{T_{s,o} - T_o} \right) \cdot \ln \left(\frac{T_{s,i} - T_i}{T_{s,o} - T_o} \right)} \right]^2 \right]^2$$

$$\frac{U_{\bar{h}}}{\bar{h}} = \left[\left(\frac{U_V}{V} \right)^2 + \left(\frac{U_I}{I} \right)^2 + \left(\frac{U_L}{L} \right)^2 + \left(\frac{U_a}{a + 2 \cdot \eta \cdot b} \right)^2 + 2 \cdot \left(\frac{b \cdot U_\eta}{a + 2 \cdot \eta \cdot b} \right)^2 + 2 \cdot \left(\frac{\eta \cdot U_b}{a + 2 \cdot \eta \cdot b} \right)^2 + \left(\frac{U_{T_{si}-T_i}}{(T_{s,i} - T_i) - (T_{s,o} - T_o)} \right)^2 + \left(\frac{U_{T_{so}-T_o}}{(T_{s,i} - T_i) - (T_{s,o} - T_o)} \right)^2 + \left(\frac{U_{\frac{T_{si}-T_i}{T_{so}-T_o}}}{\left(\frac{T_{s,i} - T_i}{T_{s,o} - T_o} \right) \cdot \ln \left(\frac{T_{s,i} - T_i}{T_{s,o} - T_o} \right)} \right)^2 \right]^{1/2}$$

Nusselt Number; laminar, H1, average heat transfer coefficient, multiple channels, with fin efficiency, LMTD

Function

$$\bar{Nu} = \frac{\bar{h} \cdot D_h}{k_f}$$

Uncertainty

$$\frac{U_{\bar{Nu}}}{\bar{Nu}} = \left[\left(\frac{U_{D_h}}{D_h} \right)^2 + \left(\frac{U_k}{k_f} \right)^2 + \left(\frac{U_{\bar{h}}}{\bar{h}} \right)^2 \right]^{1/2}$$

$$\frac{U_{\bar{Nu}}}{\bar{Nu}} = \left[\left(\frac{U_k}{k_f} \right)^2 + \left(\frac{U_a}{a} \right)^2 + \left(\frac{U_b}{b} \right)^2 + \left(\frac{U_a}{a+b} \right)^2 + \left(\frac{U_b}{a+b} \right)^2 \right]^{1/2} + \left[\left(\frac{U_V}{V} \right)^2 + \left(\frac{U_I}{I} \right)^2 + \left(\frac{U_L}{L} \right)^2 + \left(\frac{U_a}{a+2 \cdot \eta \cdot b} \right)^2 + 2 \cdot \left(\frac{b \cdot U_\eta}{(a+2 \cdot \eta \cdot b)} \right)^2 + 2 \cdot \left(\frac{\eta \cdot U_b}{(a+2 \cdot \eta \cdot b)} \right)^2 + \left(\frac{U_{T_{so}-T_o}}{(T_{s,i} - T_i) - (T_{s,o} - T_o)} \right)^2 + \left(\frac{U_{T_{si}-T_i}}{(T_{s,i} - T_i) - (T_{s,o} - T_o)} \right)^2 + \left(\frac{U_{\frac{T_{si}-T_i}{T_{so}-T_o}}}{\left(\frac{T_{s,i} - T_i}{T_{s,o} - T_o} \right) \cdot \ln \left(\frac{T_{s,i} - T_i}{T_{s,o} - T_o} \right)} \right)^2 \right]^{1/2} \Bigg]^2$$

$$\frac{U_{\bar{Nu}}}{\bar{Nu}} = \left[\begin{aligned} & \left(\frac{U_k}{k_f} \right)^2 + \left(\frac{U_a}{a} \right)^2 + \left(\frac{U_b}{b} \right)^2 + \left(\frac{U_a}{a+b} \right)^2 + \left(\frac{U_b}{a+b} \right)^2 \\ & + \left(\frac{U_V}{V} \right)^2 + \left(\frac{U_I}{I} \right)^2 + \left(\frac{U_L}{L} \right)^2 + \left(\frac{U_a}{a+2 \cdot \eta \cdot b} \right)^2 \\ & + 2 \cdot \left(\frac{b \cdot U_\eta}{(a+2 \cdot \eta \cdot b)} \right)^2 + 2 \cdot \left(\frac{\eta \cdot U_b}{(a+2 \cdot \eta \cdot b)} \right)^2 \\ & + \left(\frac{U_{T_{so}-T_o}}{(T_{s,i} - T_i) - (T_{s,o} - T_o)} \right)^2 + \left(\frac{U_{T_{si}-T_i}}{(T_{s,i} - T_i) - (T_{s,o} - T_o)} \right)^2 \\ & + \left(\frac{U_{\frac{T_{si}-T_i}{T_{so}-T_o}}}{\left(\frac{T_{s,i} - T_i}{T_{s,o} - T_o} \right) \cdot \ln \left(\frac{T_{s,i} - T_i}{T_{s,o} - T_o} \right)} \right)^2 \end{aligned} \right]^{1/2}$$